

**Co-Cured Composite Joint Strength Investigation Based on  
Behavior Characterization of the  $[0/\pm\theta/90]_s$  Family**

A Thesis  
Presented to  
The Academic Faculty

by

**Xinyuan Tan**

In Partial Fulfillment  
of the Requirements for the Degree  
Doctor of Philosophy

School of Aerospace Engineering  
Georgia Institute of Technology  
December 2008

# Co-Cured Composite Joint Strength Investigation Based on Behavior Characterization of the $[0/\pm\theta/90]_s$ Family

Approved by:

Dr. Erian Armanios  
(School of Aerospace Engineering), Advisor

Dr. Nico F. Declercq  
(School of Mechanical Engineering, GT Lorraine)

Dr. D. Stefan Dancila  
(Dancila LLC)

Dr. W. Steven Johnson  
(School of Mechanical Engineering)

Dr. Rami Haj-Ali  
(School of Civil Engineering)

Date Approved: 23 October 2008

# ACKNOWLEDGEMENTS

I would like to express my gratitude and appreciation to those that made this possible.

My family. For respecting and supporting my choices in life. For encouraging and believing in me as I explore my potential. Giving me a peace of mind to enjoy each day in strength and confidence.

My thesis advisor and many other teachers. For teaching me the importance of learning and the skills I need to continue on this path. For showing me the significance of one's belief and the strength I need to live up to it. I will remember well the lesson from my thesis advisor to always have the confidence to identify my role and work hard at whatever comes my way.

I would also like to acknowledge Dr. Rami Haj-Ali (Professor), Dr. Bo-Siou Wei (Graduate student) and Mr. Shane Johnson (Graduate student), from the School of Civil Engineering, Georgia Institute of Technology, for their assistance and the use of the Infrared Thermoelastic Stress Analysis equipment.

Special thanks also goes to Robert Haynes, a graduate student in the Aerospace Composite Laboratory, for patiently reviewing my dissertation.

This work was sponsored by the National Rotorcraft Technology Center through the Georgia Institute of Technology Rotorcraft Center of Excellence. This support is gratefully acknowledged. The generous donation of the IM7/8551-7 graphite/epoxy material system from Hexcel is also greatly appreciated.

Finally, my friends and other administrative staff. For pulling me along the way. For making everyday lighter than it seems. For reminding me that I never walk alone.

Thank you.

# TABLE OF CONTENTS

<b>ACKNOWLEDGEMENTS</b> . . . . .	<b>iii</b>
<b>LIST OF TABLES</b> . . . . .	<b>viii</b>
<b>LIST OF FIGURES</b> . . . . .	<b>xii</b>
<b>SUMMARY</b> . . . . .	<b>xviii</b>
<b>I INTRODUCTION</b> . . . . .	<b>1</b>
1.1 Literature Survey . . . . .	3
1.2 Composite Joints . . . . .	4
1.2.1 Mechanically Fastened Joints . . . . .	5
1.2.2 Selection Criteria For Mechanically Fastened Joints . . . . .	6
1.2.3 Analysis of Mechanically Fastened Joints . . . . .	8
1.2.4 Bonded Joints . . . . .	12
1.2.5 Selection Criteria For Bonded Joints . . . . .	13
1.2.6 Analysis of Bonded Joints . . . . .	16
1.3 Non-conventional Joints and Their Analysis . . . . .	20
1.3.1 Single Nested Overlap (SNO) Joint . . . . .	20
1.3.2 SNO Joint: Strength Comparison . . . . .	22
1.3.3 Bonded Wavy Composite Lap Joint . . . . .	22
1.3.4 Wavy Joint: Static Strength . . . . .	22
1.3.5 Wavy Joint: Fatigue Study . . . . .	23
1.4 Non-destructive Testing . . . . .	23
1.4.1 Acoustic Emission . . . . .	25
1.4.2 Infrared Thermoelastic Stress Analysis Technique . . . . .	29
1.5 Fatigue of Composites . . . . .	31
1.6 Edge Delamination in Composites . . . . .	32
<b>II QUASI-STATIC STRENGTH CHARACTERIZATION AND FAILURE MODES OF <math>[0/\pm\theta/90]_S</math> FAMILY OF COMPOSITE JOINTS</b> . . . . .	<b>35</b>
2.1 Three Observed Failure Modes . . . . .	35
2.2 Three Categorized Failure Types . . . . .	37



2.2.1	Dominant Cohesive Failure . . . . .	39
2.2.2	Dominant Adherend Failure . . . . .	39
2.2.3	Mixed Type Failure . . . . .	39
2.3	Quasi-static Failure Type Comparison for $[0]_8$ and $[0/\pm\theta/90]_s$ Family of Joints . . . . .	40
2.3.1	Straight Laminates . . . . .	40
2.3.2	Single Lap Joints . . . . .	40
2.3.3	Single Nested Overlap Joints . . . . .	42
2.4	Quasi-static Strength Comparison for the $[0]_8$ and $[0/\pm\theta/90]_s$ Family of Joints . . . . .	42
2.4.1	Static Strength Indicator I: Stacking Sequence Static Effectiveness Factor . . . . .	46
2.4.2	Static Strength Indicator II: Joint Static Effectiveness Factor . . . . .	48
2.5	Statistical Inference of Single Panel vs. Multiple Panels . . . . .	49
2.6	Chapter Summary . . . . .	49

### III FATIGUE STRENGTH CHARACTERIZATION AND FAILURE MODES OF $[0/\pm\theta/90]_s$ FAMILY OF COMPOSITE JOINTS . . . . . 51

3.1	Power Fitted S-N Curves: Frequency = 5 Hz, R = 0.1 and Fatigue run-out = $1 \times 10^6$ cycles . . . . .	51
3.2	Fatigue Failure Type Comparison for the $[0]_8$ and $[0/\pm\theta/90]_s$ Family of Joints . . . . .	53
3.2.1	Straight Laminates . . . . .	53
3.2.2	Single Lap Joints . . . . .	53
3.2.3	Single Nested Overlap Joints . . . . .	56
3.3	Fatigue Strength Comparison for the $[0]_8$ and $[0/\pm\theta/90]_s$ Family of Joints . . . . .	56
3.3.1	Fatigue Strength Indicator I: Stacking Sequence Fatigue Effectiveness Factor . . . . .	58
3.3.2	Fatigue Strength Indicator II: Joint Fatigue Effectiveness Factor . . . . .	61
3.4	Quasi-static and Fatigue Strength Comparison for the $[0]_8$ and $[0/\pm\theta/90]_s$ Family of Joints . . . . .	63
3.4.1	Fatigue Strength Indicator III: Fatigue-to-static Joint Effectiveness Factor . . . . .	63
3.5	Chapter Summary . . . . .	65

<b>IV</b>	<b>QUASI-STATIC ACOUSTIC EMISSION COUNT PEAKS OBSERVED AS FATIGUE LIMIT INDICATOR . . . . .</b>	<b>66</b>
4.1	Quasi-static Cumulative AE Count Peaks . . . . .	67
4.2	Observed Fatigue Limit Indicators for the $[0/\pm\theta/90]_s$ Family . . . . .	69
4.2.1	Straight Laminates . . . . .	70
4.2.2	Single Lap Joints . . . . .	70
4.2.3	Single Nested Overlap Joints . . . . .	70
4.3	Difference in Rate of Damage Accumulation under Quasi-static and Fatigue with Increased Frequency . . . . .	73
4.4	Conditions for Quasi-static Cumulative AE Count Peaks as Fatigue Limit Indicators . . . . .	75
4.5	Chapter Summary . . . . .	78
<b>V</b>	<b>FATIGUE DAMAGE INITIATION AND PROPAGATION OF THE <math>[0/\pm 45/90]_S</math> AND <math>[45/0/-45/90]_S</math> . . . . .</b>	<b>79</b>
5.1	First Approach: Damage Type Comparison with Quasi-static Cumulative AE Count Peaks . . . . .	80
5.1.1	Damage Type Comparison at 5 Hz: $[0/\pm 45/90]_s$ . . . . .	80
5.1.2	Damage Type Comparison at 10 Hz: $[45/0/-45/90]_s$ . . . . .	85
5.2	Damage Types Correlated to Fatigue Limit Indicators . . . . .	88
5.3	Second Approach: Damage propagation with Infrared Thermoelastic Stress Analysis Techniques . . . . .	90
5.3.1	Damage propagation at Frequency = 5 Hz and R = 0.2: Graphite/epoxy $[0/\pm 45/90]_s$ . . . . .	90
5.4	Chapter Summary . . . . .	91
<b>VI</b>	<b>STRENGTH STUDY OF QUASI-ISOTROPIC LAY-UP WITH REDUCED EDGE DELAMINATION . . . . .</b>	<b>94</b>
6.1	Effect of Stacking Sequence on Free-edge Delamination . . . . .	94
6.1.1	Quasi-static Comparison of Free-Edge Delamination in Straight Laminates . . . . .	95
6.1.2	Effect of Minimized Edge Delamination on Strength under Monotonic and Cyclic Loading . . . . .	99
6.2	IR-TSA Damage Monitoring for S2-glass/epoxy $[45/90/-45/0]_s$ . . . . .	100
6.3	Effect of Specimen Width in $[45/90/-45/0]_s$ Free-edge Delamination Minimized Lay-up . . . . .	105

6.4 Chapter Summary . . . . .	114
<b>VII CONCLUSION AND RECOMMENDATIONS FOR FUTURE WORK</b>	<b>115</b>
7.1 Conclusions . . . . .	115
7.2 Recommendations for Future Work . . . . .	117
<b>APPENDIX A — EQUIPMENT SETUP AND COUPON MANUFACTURING . . . . .</b>	<b>118</b>
<b>APPENDIX B — SUMMARY OF ULTIMATE STRENGTH FOR QUASI-STATIC TEST SPECIMENS . . . . .</b>	<b>128</b>
<b>APPENDIX C — SUMMARY OF ACOUSTIC EMISSION COUNTS UNDER QUASI-STATIC LOADING . . . . .</b>	<b>144</b>
<b>APPENDIX D — SUMMARY OF FATIGUE TEST SPECIMENS . . .</b>	<b>163</b>
<b>REFERENCES . . . . .</b>	<b>182</b>
<b>INDEX . . . . .</b>	<b>191</b>

# LIST OF TABLES

1	Summary of advantages and disadvantages of bonded and bolted composite-to-metal joints in aircraft applications [50] . . . . .	5
2	Material properties for graphite/epoxy (Hexcel IM7/8551-7) . . . . .	35
3	Summary of UTS for IM7/8551-7 $[0]_8$ and $[0/\pm\theta/90]_s$ with UTS of $[0/\pm\theta/90]_s$ as a percentage of $[0]_8$ . . . . .	45
4	p-values (1-way ANOVA): To test for significant differences in mean UTS values between $[0/\pm 30/90]_s$ , $[0/\pm 45/90]_s$ and $[0/\pm 60/90]_s$ . . . . .	46
5	Static strength indicator I for IM7/8551-7 $[0/\pm\theta/90]_s$ . . . . .	47
6	Static strength indicator II for IM7/8551-7 $[0]_8$ and $[0/\pm\theta/90]_s$ . . . . .	48
7	Comparison of Single Panel (Cao and Dancila [13, 12]) and Multiple Panels Monotonic Loading Results . . . . .	50
8	Summary of fatigue limit for IM7/8551-7 $[0]_8$ and $[0/\pm\theta/90]_s$ with fatigue limit of $[0/\pm\theta/90]_s$ as a percentage of $[0]_8$ . . . . .	58
9	Fatigue strength indicator I for IM7/8551-7 $[0/\pm\theta/90]_s$ . . . . .	60
10	Fatigue strength indicator II for IM7/8551-7 $[0]_8$ and $[0/\pm\theta/90]_s$ . . . . .	62
11	Quasi-static and fatigue failure type comparison for IM7/8551-7 $[0]_8$ and $[0/\pm\theta/90]_s$ . . . . .	63
12	Fatigue strength indicator III for IM7/8551-7 $[0]_8$ and $[0/\pm\theta/90]_s$ . . . . .	64
13	Straight laminates: Quasi-static cumulative AE count peaks for IM7/8551-7 $[0]_8$ and $[0/\pm\theta/90]_s$ . . . . .	67
14	Single lap joints: Quasi-static cumulative AE count peaks for IM7/8551-7 $[0]_8$ and $[0/\pm\theta/90]_s$ . . . . .	68
15	Single nested overlap joints: Quasi-static cumulative AE count peaks for IM7/8551-7 $[0]_8$ and $[0/\pm\theta/90]_s$ . . . . .	68
16	Quasi-static cumulative AE count peaks for IM7/8551-7 $[45/0/-45/90]_s$ straight laminates, single lap and single nested overlap joints . . . . .	73
17	Straight laminates: Damage type comparison at fatigue frequency of 5 Hz for IM7/8551-7 $[0/\pm 45/90]_s$ at AE count peaks and fatigue limit . . . . .	81
18	Single lap joints: Damage type comparison at fatigue frequency of 5 Hz for IM7/8551-7 $[0/\pm 45/90]_s$ at AE count peaks and fatigue limit . . . . .	83
19	Single nested overlap joints: Damage type comparison at fatigue frequency of 5 Hz for IM7/8551-7 $[0/\pm 45/90]_s$ at AE count peaks and fatigue limit . . . . .	84
20	Straight laminates: Damage type comparison at fatigue frequency of 10 Hz for IM7/8551-7 $[45/0/-45/90]_s$ at AE count peaks and fatigue limit . . . . .	86

21	Single lap joints: Damage type comparison at fatigue frequency of 10 Hz for IM7/8551-7 [45/0/ – 45/90] <sub>s</sub> at AE count peaks and fatigue limit . . . . .	87
22	Single nested overlap joints: Damage type comparison at fatigue frequency of 10 Hz for IM7/8551-7 [45/0/ – 45/90] <sub>s</sub> at AE count peaks and fatigue limit	88
23	Fatigue limit comparison for IM7/8551-7 [45/90/ – 45/0] <sub>s</sub> and [0/ ± 45/90] <sub>s</sub> joints . . . . .	100
24	Material properties for S2-glass/epoxy (Cytec S2/E773FR) . . . . .	104
25	UTS for S2/E773FR [0/ ± 45/90] <sub>s</sub> . . . . .	104
26	MTS tuning parameters: PIDF load control values . . . . .	119
27	Nomenclature used for lay-up and configuration identification . . . . .	127
28	Straight laminates (IM7/8551-7 [0] <sub>8</sub> ): Summary of quasi-static test specimens	129
29	Single lap joints (IM7/8551-7 [0] <sub>8</sub> ): Summary of quasi-static test specimens	129
30	SNO joints (IM7/8551-7 [0] <sub>8</sub> ): Summary of quasi-static test specimens . . .	130
31	Straight laminates (IM7/8551-7 [0/ ± 30/90] <sub>s</sub> ): Summary of quasi-static test specimens . . . . .	130
32	Single lap joints (IM7/8551-7 [0/ ± 30/90] <sub>s</sub> ): Summary of quasi-static test specimens . . . . .	131
33	SNO joints (IM7/8551-7 [0/ ± 30/90] <sub>s</sub> ): Summary of quasi-static test specimens	131
34	Straight laminates (IM7/8551-7 [0/ ± 45/90] <sub>s</sub> ): Summary of quasi-static test specimens . . . . .	132
35	Single lap joints (IM7/8551-7 [0/ ± 45/90] <sub>s</sub> ): Summary of quasi-static test specimens . . . . .	133
36	SNO joints (IM7/8551-7 [0/ ± 45/90] <sub>s</sub> ): Summary of quasi-static test specimens	134
37	Straight laminates (IM7/8551-7 [0/ ± 60/90] <sub>s</sub> ): Summary of quasi-static test specimens . . . . .	135
38	Single lap joints (IM7/8551-7 [0/ ± 60/90] <sub>s</sub> ): Summary of quasi-static test specimens . . . . .	135
39	SNO joints (IM7/8551-7 [0/ ± 60/90] <sub>s</sub> ): Summary of quasi-static test specimens	136
40	Straight laminates (IM7/8551-7 [45/0/ – 45/90] <sub>s</sub> ): Summary of quasi-static test specimens . . . . .	136
41	Single lap joints (IM7/8551-7 [45/0/ – 45/90] <sub>s</sub> ): Summary of quasi-static test specimens . . . . .	137
42	SNO joints (IM7/8551-7 [45/0/ – 45/90] <sub>s</sub> ): Summary of quasi-static test specimens . . . . .	137

43	Straight laminates (S2/E773FR $[0/\pm 45/90]_s$ ): Summary of quasi-static test specimens . . . . .	138
44	Single lap joints (S2/E773FR $[0/\pm 45/90]_s$ ): Summary of quasi-static test specimens . . . . .	139
45	SNO joints (S2/E773FR $[0/\pm 45/90]_s$ ): Summary of quasi-static test specimens	140
46	Straight laminates (1.0 inch width IM7/8551-7 $[45/90/-45/0]_s$ ): Summary of quasi-static test specimens . . . . .	141
47	Straight laminates (1.5 inch width IM7/8551-7 $[45/90/-45/0]_s$ ): Summary of quasi-static test specimens . . . . .	141
48	Straight laminates (2.0 inch width IM7/8551-7 $[45/90/-45/0]_s$ ): Summary of quasi-static test specimens . . . . .	142
49	Single lap joints (1.0 inch width IM7/8551-7 $[45/90/-45/0]_s$ ): Summary of quasi-static test specimens . . . . .	142
50	SNO joints (1.0 inch width IM7/8551-7 $[45/90/-45/0]_s$ ): Summary of quasi-static test specimens . . . . .	143
51	Straight laminates (IM7/8551-7 $[0]_8$ ): Summary of fatigue test specimens at 5 Hz with fatigue run-out at $1 \times 10^6$ cycles . . . . .	164
52	Single lap joints (IM7/8551-7 $[0]_8$ ): Summary of fatigue test specimens at 5 Hz with fatigue run-out at $1 \times 10^6$ cycles . . . . .	165
53	SNO joints (IM7/8551-7 $[0]_8$ ): Summary of fatigue test specimens at 5 Hz with fatigue run-out at $1 \times 10^6$ cycles . . . . .	166
54	Straight laminates (IM7/8551-7 $[0/\pm 30/90]_s$ ): Summary of fatigue test specimens at 5 Hz with fatigue run-out at $1 \times 10^6$ cycles . . . . .	167
55	Single lap joints (IM7/8551-7 $[0/\pm 30/90]_s$ ): Summary of fatigue test specimens at 5 Hz with fatigue run-out at $1 \times 10^6$ cycles . . . . .	167
56	SNO joints (IM7/8551-7 $[0/\pm 30/90]_s$ ): Summary of fatigue test specimens at 5 Hz with fatigue run-out at $1 \times 10^6$ cycles . . . . .	168
57	Straight laminates (IM7/8551-7 $[0/\pm 45/90]_s$ ): Summary of fatigue test specimens at 5 Hz with fatigue run-out at $1 \times 10^6$ cycles . . . . .	169
58	Single lap joints (IM7/8551-7 $[0/\pm 45/90]_s$ ): Summary of fatigue test specimens at 5 Hz with fatigue run-out at $1 \times 10^6$ cycles . . . . .	170
59	SNO joints (IM7/8551-7 $[0/\pm 45/90]_s$ ): Summary of fatigue test specimens at 5 Hz with fatigue run-out at $1 \times 10^6$ cycles . . . . .	171
60	Straight laminates (IM7/8551-7 $[0/\pm 60/90]_s$ ): Summary of fatigue test specimens at 5 Hz with fatigue run-out at $1 \times 10^6$ cycles . . . . .	172
61	Single lap joints (IM7/8551-7 $[0/\pm 60/90]_s$ ): Summary of fatigue test specimens at 5 Hz with fatigue run-out at $1 \times 10^6$ cycles . . . . .	172

62	SNO joints (IM7/8551-7 $[0/\pm 60/90]_s$ ): Summary of fatigue test specimens at 5 Hz with fatigue run-out at $1 \times 10^6$ cycles . . . . .	173
63	Straight laminates (IM7/8551-7 $[45/0/-45/90]_s$ ): Summary of fatigue test specimens at 10 Hz with fatigue run-out at $1 \times 10^7$ cycles . . . . .	173
64	Single lap joints (IM7/8551-7 $[45/0/-45/90]_s$ ): Summary of fatigue test specimens at 10 Hz with fatigue run-out at $1 \times 10^7$ cycles . . . . .	174
65	SNO joints (IM7/8551-7 $[45/0/-45/90]_s$ ): Summary of fatigue test specimens at 10 Hz with fatigue run-out at $1 \times 10^7$ cycles . . . . .	174
66	Straight laminates (S2/E773FR $[0/\pm 45/90]_s$ ): Summary of fatigue test specimens at 5 Hz with fatigue run-out at $1 \times 10^6$ cycles . . . . .	175
67	Single lap joints (S2/E773FR $[0/\pm 45/90]_s$ ): Summary of fatigue test specimens at 5 Hz with fatigue run-out at $1 \times 10^6$ cycles . . . . .	176
68	SNO joints (S2/E773FR $[0/\pm 45/90]_s$ ): Summary of fatigue test specimens at 5 Hz with fatigue run-out at $1 \times 10^6$ cycles . . . . .	177
69	Straight laminates (1.0 inch width IM7/8551-7 $[45/90/-45/0]_s$ ): Summary of fatigue test specimens at 5 Hz with fatigue run-out at $1 \times 10^6$ cycles . . .	178
70	Straight laminates (1.5 inch width IM7/8551-7 $[45/90/-45/0]_s$ ): Summary of fatigue test specimens at 5 Hz with fatigue run-out at $1 \times 10^6$ cycles . . .	179
71	Straight laminates (2.0 inch width IM7/8551-7 $[45/90/-45/0]_s$ ): Summary of fatigue test specimens at 5 Hz with fatigue run-out at $1 \times 10^6$ cycles . . .	179
72	Single lap joints (1.0 inch width IM7/8551-7 $[45/90/-45/0]_s$ ): Summary of fatigue test specimens at 5 Hz with fatigue run-out at $1 \times 10^6$ cycles . . . .	180
73	SNO joints (1.0 inch width IM7/8551-7 $[45/90/-45/0]_s$ ): Summary of fatigue test specimens at 5 Hz with fatigue run-out at $1 \times 10^6$ cycles . . . . .	181

# LIST OF FIGURES

1	Geometric configuration for the straight laminate, single lap and single nested overlap joints . . . . .	2
2	Stress concentration around a fastener hole in composites <i>Figure taken from Hart-Smith (1987) [47]</i> . . . . .	8
3	Modes of failure for single-hole bolted composite joints <i>Figure taken from Hart-Smith (1987) [47]</i> . . . . .	9
4	Static failure modes due to various bolt clamp-up <i>Figure taken from Crews (1981) [26]</i> . . . . .	9
5	A two-dimensional illustration of the single shear and double shear configurations <i>Figure taken from Oplinger (1996) [73]</i> . . . . .	12
6	Adhesive fillets in (a)co-cured and (b)adhesively bonded joints <i>Figure taken from Ashcroft, Gilmore and Shaw [3] (1996)</i> . . . . .	13
7	Shear stress distribution in adhesive with fully developed plastic and elastic zones <i>Figure taken from Composite Materials for Aircraft Structures (1986) [50]</i>	16
8	Types of adhesively bonded joints commonly used <i>Figure taken from Engineered Materials Handbook -Composites (1987) [47]</i>	17
9	Shear load in adherend-adhesive in adhesively bonded joints <i>Figure taken from Engineered Materials Handbook -Composites (1987) [47]</i>	17
10	Failure modes for bonded composite joints <i>Figure taken from Heslehurst and Hart-Smith (2002) [49]</i> . . . . .	18
11	Rigid adherend model: Finite element model with different adherend deformations <i>Figure taken from MIL Handbook 17 volume 3 (2002) [27]</i> . . . . .	19
12	Nested joint concept evolving from single lap joint . . . . .	21
13	Dimensions and geometry of single lap and wavy joint <i>figure taken from Zeng and Sun (2004) [113]</i> . . . . .	23
14	Three observed failure modes in straight laminates, single lap and single nested overlap joints <i>Adherend fracture and cohesive fracture sketch taken from Heslehurst and Hart-Smith [49]</i> . . . . .	36
15	Three categorized failure types observed in straight laminates, single lap and single nested overlap joints <i>Adherend fracture and cohesive fracture sketch taken from Heslehurst and Hart-Smith [49]</i> . . . . .	38



16	Straight laminates: Quasi-static failure modes for IM7/8551-7 $[0]_8$ and $[0/\pm\theta/90]_s$ <i>Adherend fracture sketch taken from Heslehurst and Hart-Smith [49]</i> . . . .	41
17	Single lap joints: Quasi-static failure modes for IM7/8551-7 $[0]_8$ and $[0/\pm\theta/90]_s$ <i>Cohesive fracture sketch taken from Heslehurst and Hart-Smith [49]</i> . . . .	43
18	Single nested overlap joints: Quasi-static failure modes for IM7/8551-7 $[0]_8$ and $[0/\pm\theta/90]_s$ <i>Adherend fracture and cohesive fracture sketch taken from Heslehurst and Hart-Smith [49]</i> . . . . .	44
19	UTS values for $[0]_8$ , $[0/\pm 30/90]_s$ , $[0/\pm 45/90]_s$ and $[0/\pm 60/90]_s$ straight laminates, single lap and single nested overlap joints . . . . .	45
20	Straight laminates: Fatigue failure modes for IM7/8551-7 $[0]_8$ and $[0/\pm\theta/90]_s$ (frequency = 5 Hz, R = 0.1 and fatigue run-out = $1 \times 10^6$ cycles) <i>Adherend fracture sketch taken from Heslehurst and Hart-Smith [49]</i> . . . .	54
21	Single lap joints: Fatigue failure modes for IM7/8551-7 $[0]_8$ and $[0/\pm\theta/90]_s$ (frequency = 5 Hz, R = 0.1 and fatigue run-out = $1 \times 10^6$ cycles) <i>Cohesive fracture sketch taken from Heslehurst and Hart-Smith [49]</i> . . . .	55
22	Single nested overlap joints: Fatigue failure modes for IM7/8551-7 $[0]_8$ and $[0/\pm\theta/90]_s$ (frequency = 5 Hz, R = 0.1 and fatigue run-out = $1 \times 10^6$ cycles) <i>Adherend fracture and cohesive fracture sketch taken from Heslehurst and Hart-Smith [49]</i> . . . . .	57
23	S-N curve on a linear scale and a semi-logarithmic scale for IM7/8551-7 $[0]_8$ and $[0/\pm\theta/90]_s$ . . . . .	59
24	Fatigue limit values for $[0]_8$ , $[0/\pm 30/90]_s$ , $[0/\pm 45/90]_s$ and $[0/\pm 60/90]_s$ straight laminates, single lap and single nested overlap joints . . . . .	60
25	Scatter plot of quasi-static AE count peaks (onset of AE events, first AE count peak, second AE count peak and third AE count peak) for IM7/8551-7 $[0]_8$ and $[0/\pm\theta/90]_s$ . . . . .	68
26	Straight laminates: FL indicators and S-N curve on a linear scale (frequency = 5 Hz, R = 0.1 and fatigue run-out = $1 \times 10^6$ cycles) and observed fatigue limit indicators for IM7/8551-7 $[0/\pm\theta/90]_s$ and $[0]_8$ . . . . .	71
27	Single lap joints: FL indicators and S-N curve on a linear scale (frequency = 5 Hz, R = 0.1 and fatigue run-out = $1 \times 10^6$ cycles) and observed fatigue limit indicators for IM7/8551-7 $[0/\pm\theta/90]_s$ and $[0]_8$ . . . . .	72
28	Single nested overlap joints: FL indicators and S-N curve on a linear scale (frequency = 5 Hz, R = 0.1 and fatigue run-out = $1 \times 10^6$ cycles) and observed fatigue limit indicators for IM7/8551-7 $[0/\pm\theta/90]_s$ and $[0]_8$ . . . . .	74

29	Semi-logarithmic S-N curve for IM7/8551-7 [45/0/ - 45/90] <sub>s</sub> straight laminates, single lap and single nested overlap joints (Frequency = 10 Hz, R = 0.1, Fatigue run-out = $1 \times 10^7$ cycles) . . . . .	75
30	Constant amplitude tension-tension S-N curve on a linear scale for IM7/8551-7 [45/0/ - 45/90] <sub>s</sub> . . . . .	76
31	Damage types at AE count peaks and at fatigue limit (frequency = 5 Hz, R = 0.1, fatigue run-out = $1 \times 10^6$ ) for IM7/8551-7 [0/ $\pm$ 45/90] <sub>s</sub> straight laminates <i>The damage types illustrated have been highlighted to enhance clarity.</i> . . . .	82
32	Damage types at AE count peaks and at fatigue limit (frequency = 5 Hz, R = 0.1, fatigue run-out = $1 \times 10^6$ ) for IM7/8551-7 [0/ $\pm$ 45/90] <sub>s</sub> single lap joints <i>The damage types illustrated have been highlighted to enhance clarity.</i> . . . .	84
33	Damage types at AE count peaks and at fatigue limit (frequency = 5 Hz, R = 0.1, fatigue run-out = $1 \times 10^6$ ) for IM7/8551-7 [0/ $\pm$ 45/90] <sub>s</sub> single nested overlap joints <i>The damage types illustrated have been highlighted to enhance clarity.</i> . . . .	85
34	Damage types at AE count peaks and at fatigue limit (frequency = 10 Hz, R = 0.1, fatigue run-out = $1 \times 10^7$ ) for IM7/8551-7 [45/0/ - 45/90] <sub>s</sub> straight laminates <i>The damage types illustrated have been highlighted to enhance clarity.</i> . . . .	87
35	Damage types at AE count peaks and at fatigue limit (frequency = 10 Hz, R = 0.1, fatigue run-out = $1 \times 10^7$ <i>The damage types illustrated have been highlighted to enhance clarity.</i> ) for IM7/8551-7 [45/0/ - 45/90] <sub>s</sub> single lap joints . . . . .	88
36	Damage types at AE count peaks and at fatigue limit (frequency = 10 Hz, R = 0.1, fatigue run-out = $1 \times 10^7$ ) for IM7/8551-7 [45/0/ - 45/90] <sub>s</sub> single nested overlap joints <i>The damage types illustrated have been highlighted to enhance clarity.</i> . . . .	89
37	Infrared TSA images showing fatigue damage propagation for IM7/8551-7 straight laminates, single lap and single nested overlap joint (frequency = 5 Hz, R = 0.2) . . . . .	92
38	Opening and closing midplane modes for the optimized and minimized edge delamination stacking sequence, respectively . . . . .	96
39	Quasi-static tensile strength comparison for [45/90/ - 45/0] <sub>s</sub> , [0/ $\pm$ 45/90] <sub>s</sub> and [45/0/ - 45/90] <sub>s</sub> <i>Standard deviation of quasi-static tests plotted as error bars</i> . . . . .	97
40	Quasi-static failure mode comparison for IM7/8551-7 (IM7/8551-7) [45/90/ - 45/0] <sub>s</sub> , [0/ $\pm$ 45/90] <sub>s</sub> and [45/0/ - 45/90] <sub>s</sub> <i>Adherend fracture sketch taken from Heslehurst and Hart-Smith [49]</i> . . . .	98

41	UTS comparison of IM7/8551-7 $[45/90/-45/0]_s$ and $[0/\pm 45/90]_s$ straight laminates, single lap and SNO joints <i>Standard deviation of quasi-static tests plotted as error bars</i> . . . . .	101
42	Fatigue limit comparison of IM7/8551-7 $[45/90/-45/0]_s$ and $[0/\pm 45/90]_s$ straight laminates, single lap and SNO joints on a linear and a semi-logarithmic scale . . . . .	101
43	Quasi-static failure mode comparison for IM7/8551-7 (IM7/8551-7) $[45/90/-45/0]_s$ and $[0/\pm 45/90]_s$ <i>Adherend fracture and cohesive fracture sketch taken from Heslehurst and Hart-Smith [49]</i> . . . . .	102
44	Fatigue failure mode comparison for IM7/8551-7 (IM7/8551-7) $[45/90/-45/0]_s$ and $[0/\pm 45/90]_s$ <i>Adherend fracture and cohesive fracture sketch taken from Heslehurst and Hart-Smith [49]</i> . . . . .	103
45	Straight laminates: Infrared TSA images showing fatigue damage propagation comparison and fatigue failure modes between $[0/\pm 45/90]_s$ and $[45/90/-45/0]_s$ S2/E773FR cycled at a frequency of 5 Hz and a R of 0.2 .	106
46	Single lap joints: Infrared TSA images showing fatigue damage propagation comparison and fatigue failure modes between $[0/\pm 45/90]_s$ and $[45/90/-45/0]_s$ S2/E773FR cycled at a frequency of 5 Hz and a R of 0.2 . . . . .	107
47	Single nested overlap joints: Infrared TSA images showing fatigue damage propagation comparison and fatigue failure modes between $[0/\pm 45/90]_s$ and $[45/90/-45/0]_s$ S2/E773FR cycled at a frequency of 5 Hz and a R of 0.2 .	108
48	UTS comparison of IM7/8551-7 1.0 inch, 1.5 inch and 2.0 inch wide $[45/90/-45/0]_s$ straight laminates <i>Standard deviation of quasi-static tests plotted as error bars</i> . . . . .	110
49	S-N curve on a linear scale and a semi-logarithmic scale for IM7/8551-7 1.0 inch, 1.5 inch and 2.0 inch wide $[45/90/-45/0]_s$ straight laminates . . . . .	111
50	Quasi-static failure mode comparison for IM7/8551-7 (IM7/8551-7) 1.0 inch, 1.5 inch and 2.0 inch width $[45/90/-45/0]_s$ straight laminates <i>Adherend fracture sketch taken from Heslehurst and Hart-Smith [49]</i> . . . . .	112
51	Fatigue failure mode comparison for 1.0 inch, 1.5 inch and 2.0 inch width IM7/8551-7 (IM7/8551-7) $[45/90/-45/0]_s$ straight laminates under cyclic loading at frequency of 5 Hz, R of 0.1 and fatigue run-out at $1 \times 10^6$ cycles <i>Adherend fracture sketch taken from Heslehurst and Hart-Smith [49]</i> . . . . .	113
52	AE workstation and MTS servo-hydraulic testing machine setup . . . . .	120
53	IR camera and MTS servo-hydraulic testing machine setup . . . . .	121
54	<i>National</i> digital microscope . . . . .	121
55	Curing cycle for IM7/8551-7 and S2-glass/E773FR . . . . .	122

56	Co-cured composite joint mold . . . . .	123
57	<i>American Autoclave</i> with a 20x36 inches horizontal workspace . . . . .	124
58	Development of peel stresses due to eccentricity in single lap joints . . . . .	125
59	Fiberglass tabs of different thickness to reduce eccentricity in load path . . .	125
60	Specimen labeling . . . . .	126
61	Straight laminates (IM7/8551-7 [0] <sub>8</sub> ): Quasi-static acoustic emission <i>Onset of AE damage is a computed average based on all accepted quasi-static test specimens . . . . .</i>	145
62	Single lap joints (IM7/8551-7 [0] <sub>8</sub> ): Quasi-static acoustic emission <i>Onset of AE damage is a computed average based on all accepted quasi-static test specimens . . . . .</i>	146
63	SNO joints (IM7/8551-7 [0] <sub>8</sub> ): Quasi-static acoustic emission <i>Onset of AE damage is a computed average based on all accepted quasi-static test specimens . . . . .</i>	147
64	Straight laminates (IM7/8551-7 [0/±30/90] <sub>s</sub> ): Quasi-static acoustic emission <i>Onset of AE damage is a computed average based on all accepted quasi-static test specimens . . . . .</i>	148
65	Single lap joints (IM7/8551-7 [0/±30/90] <sub>s</sub> ): Quasi-static acoustic emission <i>Onset of AE damage is a computed average based on all accepted quasi-static test specimens . . . . .</i>	149
66	SNO joints (IM7/8551-7 [0/±30/90] <sub>s</sub> ): Quasi-static acoustic emission <i>Onset of AE damage is a computed average based on all accepted quasi-static test specimens . . . . .</i>	150
67	Straight laminates (IM7/8551-7 [0/±45/90] <sub>s</sub> ): Quasi-static acoustic emission <i>Onset of AE damage is a computed average based on all accepted quasi-static test specimens . . . . .</i>	151
68	Single lap joints (IM7/8551-7 [0/±45/90] <sub>s</sub> ): Quasi-static acoustic emission <i>Onset of AE damage is a computed average based on all accepted quasi-static test specimens . . . . .</i>	152
69	SNO joints (IM7/8551-7 [0/±45/90] <sub>s</sub> ): Quasi-static acoustic emission <i>Onset of AE damage is a computed average based on all accepted quasi-static test specimens . . . . .</i>	153
70	Straight laminates (IM7/8551-7 [0/±60/90] <sub>s</sub> ): Quasi-static acoustic emission <i>Onset of AE damage is a computed average based on all accepted quasi-static test specimens . . . . .</i>	154
71	Single lap joints (IM7/8551-7 [0/±60/90] <sub>s</sub> ): Quasi-static acoustic emission <i>Onset of AE damage is a computed average based on all accepted quasi-static test specimens . . . . .</i>	155

72	SNO joints (IM7/8551-7 $[0/\pm 60/90]_s$ ): Quasi-static acoustic emission <i>Onset of AE damage is a computed average based on all accepted quasi-static test specimens . . . . .</i>	156
73	Straight laminates (IM7/8551-7 $[45/0/-45/90]_s$ ): Quasi-static acoustic emission <i>Onset of AE damage is a computed average based on all accepted quasi-static test specimens . . . . .</i>	157
74	Single lap joints (IM7/8551-7 $[45/0/-45/90]_s$ ): Quasi-static acoustic emission <i>Onset of AE damage is a computed average based on all accepted quasi-static test specimens . . . . .</i>	158
75	SNO joints (IM7/8551-7 $[45/0/-45/90]_s$ ): Quasi-static acoustic emission <i>Onset of AE damage is a computed average based on all accepted quasi-static test specimens . . . . .</i>	159
76	Straight laminates (S2/E773FR $[0/\pm 45/90]$ ): Quasi-static acoustic emission <i>Onset of AE damage is a computed average based on all accepted quasi-static test specimens . . . . .</i>	160
77	Single lap joints (S2/E773FR $[0/\pm 45/90]$ ): Quasi-static acoustic emission <i>Onset of AE damage is a computed average based on all accepted quasi-static test specimens . . . . .</i>	161
78	Straight laminates (S2/E773FR $[0/\pm 45/90]$ ): Quasi-static acoustic emission <i>Onset of AE damage is a computed average based on all accepted quasi-static test specimens . . . . .</i>	162

# SUMMARY

Joints provide a path for transfer of load and are important components in an assembly of structures, particularly in translating joint strength improvements directly to significant cost savings. These cost savings are more evident in composite joints since manufacturing of more complex single piece components results in a reduction of both part count and labor. An improvement in joint strength for co-cured composite joints through minimized free-edge delamination was investigated for a quasi-isotropic  $[0/\pm 45/90]_s$  lay-up based on the quantitative assessments of the quasi-static and fatigue strength and qualitative understanding of the fatigue damage initiation and propagation for the  $[0/\pm \theta/90]_s$  family of co-cured composite joints. A previously proposed co-cured joint concept, the Single Nested Overlap (SNO) joint, was compared against a Straight Laminate (SL) and a single lap joint. The SL represents a “perfect” joint and serves as an upper bound whereas the single lap joint represents the simplest generic joint and is the base design for the SNO joint concept. Three categorized failure types, which represent the predominant failure modes in the SL, single lap, and SNO joints, along with two different fatigue strength indicators were used for quasi-static and fatigue strength comparison. With fatigue run-out defined at  $1 \times 10^6$  cycles, the fatigue damage initiation and propagation at high loadings was monitored with an Infrared Thermoelastic Stress Analysis (IR-TSA) technique, while a damage type comparison was used at low loadings. Quasi-static Acoustic Emission (AE) counts were observed to be Fatigue Limit (FL) indicators for  $[0/\pm \theta/90]_s$  SL and SNO joints. The validity of these FL indicators was also assessed in the comparison of damage types.

# CHAPTER I

## INTRODUCTION

Joints provide a path for transfer of load and are important components in an assembly of structures, particularly in translating joint strength improvements directly to significant cost savings. These cost savings are more evident in composite joints since manufacturing of more complex single piece components results in a reduction of both part count and labor. This work investigates the improvement of co-cured composite joint strength through minimized edge delamination based on quantitative assessments of the quasi-static and fatigue strength and qualitative understanding of the damage initiation and propagation during fatigue.

Among the two types of composite joints, mechanically fastened joints are more convenient for disassembly, inspection, repairs, and replacement but develop regions of high stress concentrations around fastener holes, which increase susceptibility to matrix cracking and delaminations. Adhesively bonded joints, however, are prone to manufacturing defects, storage conditions and service conditions, which results in considerable scatter in joint strength evaluation. In this investigation, the strength improvement of a previously proposed co-cured joint concept, the Single Nested Overlap (SNO) joint (Figure 1c), is compared against the Straight Laminate (SL) (Figure 1a) and the single lap joint (Figure 1b). The SL represents a “perfect” joint and serves as an upper bound while the single lap joint represents the simplest generic joint and is the base design for the SNO joint concept. The SNO joint is modified from the single lap joint through an overlapping/interleafing of adjoining top/bottom adherend plies to provide multiple interfaces for load transfer, which lead to a reversal of the peel stress.

A systematic investigation of the quasi-static and fatigue behavior of this previously conceived SNO joint is conducted in this research. In particular, the behavior of the  $[0/\pm\theta/90]_s$  family is studied and an improvement in joint strength is proposed based on observations. A literature survey pertaining to earlier work conducted on co-cured composite joints and

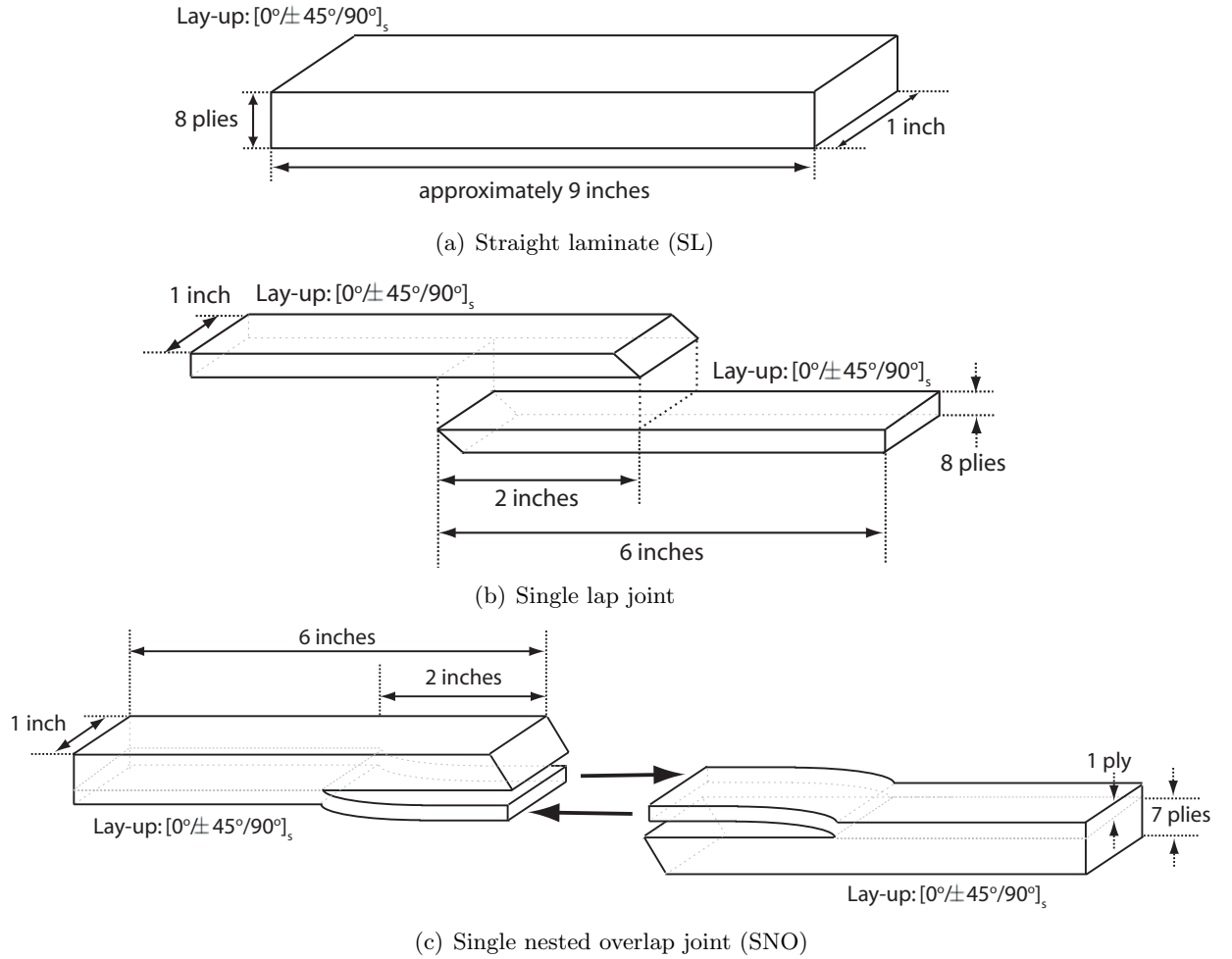


**Figure 1:** Geometric configuration for the straight laminate, single lap and single nested overlap joints



related assessment tools is provided in Chapter 1. Chapters 2 and 3 discuss the failure modes necessary to compare the strength of the SL, single lap, and SNO joints under monotonic and cyclic loading, respectively. Various indicators are used to quantify the fatigue strength comparison. An observation of quasi-static cumulative AE count peaks as fatigue limit predictors is explored in Chapter 4 with further discussion of their applicability in Chapter 5. Chapter 5 also includes two different approaches to studying fatigue damage initiation and progression at high and low stress levels. Building upon the presented work, an improvement in joint strength is investigated in Chapter 6. The conclusions and future work are summarized in Chapter 7.

## ***1.1 Literature Survey***

With the increasing cost of energy sources to consumers and the burden of depleting resources to the environment, the importance of reducing structural weight with alternative materials in engineering applications is growing quickly. Composite materials are attractive, particularly in the aerospace industry, because they offer significant improvements in strength-to-weight and stiffness-to-weight ratios compared to metals. However, the sustainability of these strength and stiffness benefits under long term service conditions is harder to predict than for metals because of the pronounced difference in damage initiation and damage propagation. Unlike metals, composites failure tend to be more brittle and the fatigue damage mechanisms are significantly more complex because of the variety and interaction of their different damage types.

The subject of this study is co-cured composite joints. Joints are important elements within an assembly of structures because they provide a path for transfer of load but they also represent weaknesses in the structure and are often sites of damage initiation. Co-cured composite joints reduce part count and manufacturing cost but non-destructive evaluation techniques for reliable assessment of their strength and stiffness are lacking. This study addresses the importance of the physical understanding of co-cured composite joint failure mechanism for strength characterization and joint improvement techniques. Non-destructive testing techniques, such as acoustic emission and infrared thermoelastic

stress analysis, are used in conjunction with quasi-static and fatigue loading for damage monitoring and strength assessment. Finally, based on the understood damage mechanism, a joint improvement study was conducted to further improve the joint strength of a co-cured SNO joint proposed earlier [24, 23, 22].

This chapter begins with an introduction to composite joints and non-conventional co-cured composite joints to explain the motivation for this study. Following that, some of the non-destructive testing techniques applicable to composites are discussed with specific focus on the two techniques adopted in this study, acoustic emission analysis and infrared thermoelastic stress analysis, to emphasize the importance of these two techniques in strength and damage assessment of co-cured composite joints. A brief outline of fatigue and damage evolution of composites and a summary of the work done on the study of edge delamination in composites is presented to underline the significance of the current joint improvement study through minimization of edge delamination.

## ***1.2 Composite Joints***

As compared to metal components, composites are more flexible in accommodating larger and more complex one-piece components in the manufacturing process, which allows for an efficient reduction in part count. This reduction could amount to significant savings in labor hours and cost, particularly in the aerospace industry where more than six million parts from over a thousand vendors are assembled with approximately half a million rivets and three million fasteners for a Boeing 747. However, due to the lack of load carrying members in the through-the-thickness direction, metal joints are still preferred in applications with significant through-the-thickness stresses and/or concentrated loads. For example, on the F/A-18, titanium fittings are joined to the graphite/epoxy skin for each of the half-wing before attachment to the fuselage to allow for higher bolt bearing loads in the the wing-to-fuselage attachment.

The subject of this investigation is co-cured composite joints, which is an alternative to mechanically fastened joints that reduces cost and increases durability. A summary of the advantages and disadvantages of bonded and bolted joints taken from Hoskin and Baker

**Table 1:** Summary of advantages and disadvantages of bonded and bolted composite-to-metal joints in aircraft applications [50]

<i>Bonded Joints</i>	<b>Advantages</b>	<b>Disadvantages</b>
	<ol style="list-style-type: none"> <li>1. No stress concentrations in adherends</li> <li>2. Stiff connection</li> <li>3. Excellent fatigue properties</li> <li>4. No fretting problems</li> <li>5. Sealed against corrosion</li> <li>6. Smooth surface contour</li> <li>7. Relatively light weight</li> <li>8. Damage tolerant</li> </ol>	<ol style="list-style-type: none"> <li>1. Limits to thickness that can be joined with simple joint configurations</li> <li>2. Inspection difficult</li> <li>3. Prone to environmental degradation</li> <li>4. Requires high level of process control</li> <li>5. Sensitive to peel and through-thickness stresses</li> <li>6. Residual stress problems when joining dissimilar materials</li> <li>7. Cannot be disassembled</li> </ol>
<i>Bolted Joints</i>	<b>Advantages</b>	<b>Disadvantages</b>
	<ol style="list-style-type: none"> <li>1. Positive connection</li> <li>2. No thickness limitations</li> <li>3. Simple process</li> <li>4. Simple inspection procedure</li> <li>5. Simple joint configuration</li> <li>6. Not environmentally sensitive</li> <li>7. Provides through-thickness reinforcement (not sensitive to peel stress)</li> <li>8. No residual stress problems</li> <li>9. Can be disassembled</li> </ol>	<ol style="list-style-type: none"> <li>1. Considerable stress concentration</li> <li>2. Relatively compliant connection</li> <li>3. Relatively poor fatigue properties</li> <li>4. Hole formation may cause damage to composite</li> <li>5. Prone to fretting</li> <li>6. Prone to corrosion</li> </ol>

(1986) [50] is provided in Table 1. In the following sections, mechanically fastened and bonded joints are briefly discussed based on their selection criteria and analysis methods. A number of good literature reviews of composite joints, available in the literature, are Hart-Smith (1973, 1977, 1980, 1987) [41, 42, 43, 47], Oplinger (1980, 1996) [72, 73] and Poon and Xiong (1996) [76].

### 1.2.1 Mechanically Fastened Joints

Fastener holes are typically drilled using tungsten carbide tipped bits under controlled pressure at a low feed rate so as to avoid delamination in the composite laminate. Bolts are then used to fasten the two parts together. The drill exit surface can also be coated with a layer of film adhesive to further prevent delamination. For stress and strength analysis of both single- and multi-fasteners in metals, two-dimensional analysis have been adequately established in the literature [104, 83, 78, 65, 33, 75, 109, 87, 108, 73, 10, 60, 61, 51, 59, 52].

However, similar success with bolted composite joints may not be inferred since the material properties of metals are distinctively different from that of composites. For example, the lack of yielding in composites makes bolted composite joints more sensitive to edge distances and hole spacings than their metal counterparts.

The analysis of mechanically fastened joints is usually divided into single row and multi-row designs. A single row of fasteners is used on non critical, lightly loaded joints (e.g. airframe bearings), while multi-row designs that have more rows of fasteners to distribute load transfer more efficiently, are used on highly loaded joints (e.g. root joint of a wing or a control surface). Various factors affect the stress state in a bolted joint, including the dimensions of the planar geometry, loading conditions, degree of material anisotropy, bolt-hole clearance, bolt flexibility and friction between the laminates [52]. Load sharing in these joints depends strongly on (i)the number of bolts, (ii)the diameter of bolts, (iii)the material of bolts and (iv)the stiffness of joining members [27].

Oplinger (1996) [73] gives a detailed review on bolted joints, summarizing the available two-dimensional and three-dimensional stress analysis methods for single row and multi-row joints since the mid 60's. Hart-Smith (1987) [47] provides a thorough review on both bonded and mechanically fastened joints, addressing their shear load transfer mechanism, their key characteristics and analysis. A review on the development of analytical tools in mechanically fastened joints can be found in Poon and Xiong (1996) [76], while MIL-Handbook 17F [27], volume 3, Chapter 6: *Structural Behavior of Joints* presents the state of the art practices in aircraft industry and succinctly summarizes the key factors that govern the behavior of mechanically fastened joints in composite structures.

### **1.2.2 Selection Criteria For Mechanically Fastened Joints**

The use of mechanical fastening methods to join parts of a big assembly together provides an added convenience when it comes to disassembly, inspection, repair or replacement. Additionally, joint design for a thick composite laminate still remains simpler for a mechanically fastened joint as compared to a bonded joint, where multiple steps or scarfs are required to increase the contact surface for sufficient through-the-thickness strength.

The difference in material properties between metals and composites determines the differences in joint strength, failure mechanism and failure modes. Composites are brittle and lack the ductility of metals to smoothen out stress peaks that develop around the fastener holes. The stress concentration around a fastener hole for a composite laminate based on Hart-Smith’s [47] semi-empirical model is illustrated in Figure 2. These fastener holes cut through the main load-carrying fibers in the composite laminate and, unlike metals, results in significant load redistributions due to matrix cracks and delaminations around the fastener holes. Furthermore, an absence of fibers in the through-the-thickness direction implies that the resulting through-the-thickness strength is totally dependant on the matrix. As such, specialized fasteners have to be used in composite joints as opposed to rivets, which are typically used in metal joints. Composite failures are also progressive, implying that the harder to predict non-linear material responses have to be taken into consideration, particularly at the contact between the bolt and fastener hole, bringing about the need to consider multiple failure modes in composite joints.

The location and failure mode are important in the analysis and design of mechanically fastened joints as well, because their effects are factored into the failure criterion. A variety of failure modes for single-hole bolted joints are illustrated in Figure 3. For fiber dominated in-plane failure modes, net section failure of a composite is the most common. Bearing stresses, which are stresses acting on the joint face directly as a result of the force applied by the fastener, may also cause the laminate to fail right before the bolt or by pull-through. Shear-out may precede bearing failure depending on hole spacing, edge distances, and lay-up [27] but can generally be corrected with a larger edge distance for each fastener. Delaminations are commonly present, though not a primary cause of failure, and bolt failure should also be considered. Failure modes are also influenced by the bolt clamp-up [26]. Figure 4 illustrates the various static failure modes accompanying the type of bolt clamp-up. The “brooming” characteristic near the hole in Figure 4a shows a typical bearing failure from a pin bearing. Figure 4b shows the failure modes from a moderate bolt clamp-up, including a combination of shearout under the washer and bearing failure beyond the washer. For high bolt clamp-up, the typical shearout-tension-bearing failure mode is shown in Figure 4c.

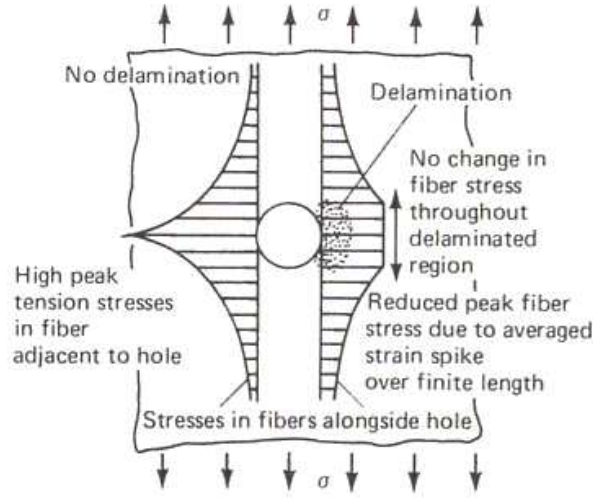


**Figure 2:** Stress concentration around a fastener hole in composites  
*Figure taken from Hart-Smith (1987) [47]*

Appropriate choice of mechanical fastener will help prevent premature failure of composite bolted joints. Alloy steel or cadmium, the common plating used on fasteners are not compatible with carbon-fiber reinforced composites because of galvanic corrosion [74]. Therefore, titanium alloy(6AL-4V) is commonly used as a fastener material with carbon-fiber reinforced composites.

### 1.2.3 Analysis of Mechanically Fastened Joints

The most common analysis method is the Empirical Correlation Factor, which is a ply-level failure criterion at a characteristic distance away from the edge of the fastener hole. This characteristic length is a laminate material property that accounts for two experimental observation, (i)the strength of laminates with a hole is greater than the ratio of the unnotched strength to the theoretical stress concentration for an open hole, and (ii)this strength is a function of the hole diameter and decreases with increasing hole diameter.

Two general approaches, Whitney and Nuismer [103] and Hart-Smith [43], form the basis for estimation of the Empirical Correlation Factor in fiber dominated in-plane modes (e.g. net-section failures). The difference between experimental results and analytical results is more pronounced because of the non-linearity of composites. While neither of these theories cover the scope of all possible cases, these two general approaches complements each other

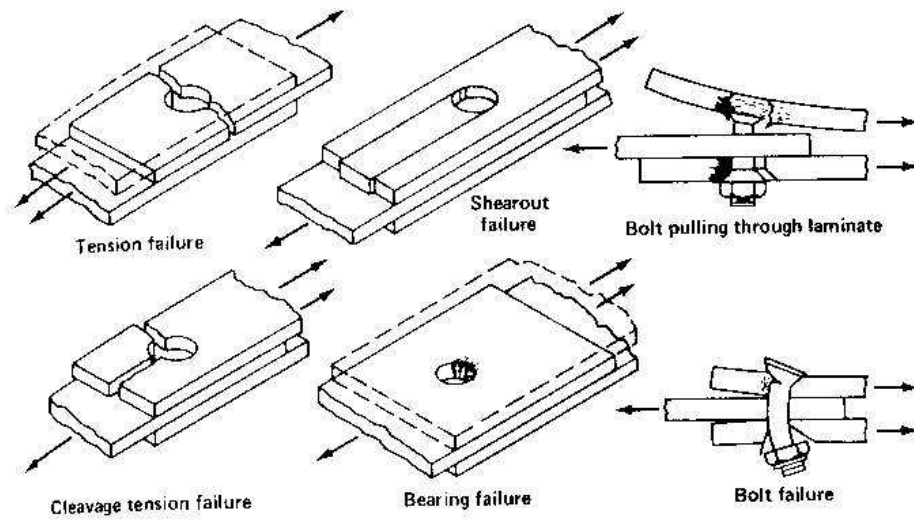


**Figure 3:** Modes of failure for single-hole bolted composite joints  
*Figure taken from Hart-Smith (1987) [47]*

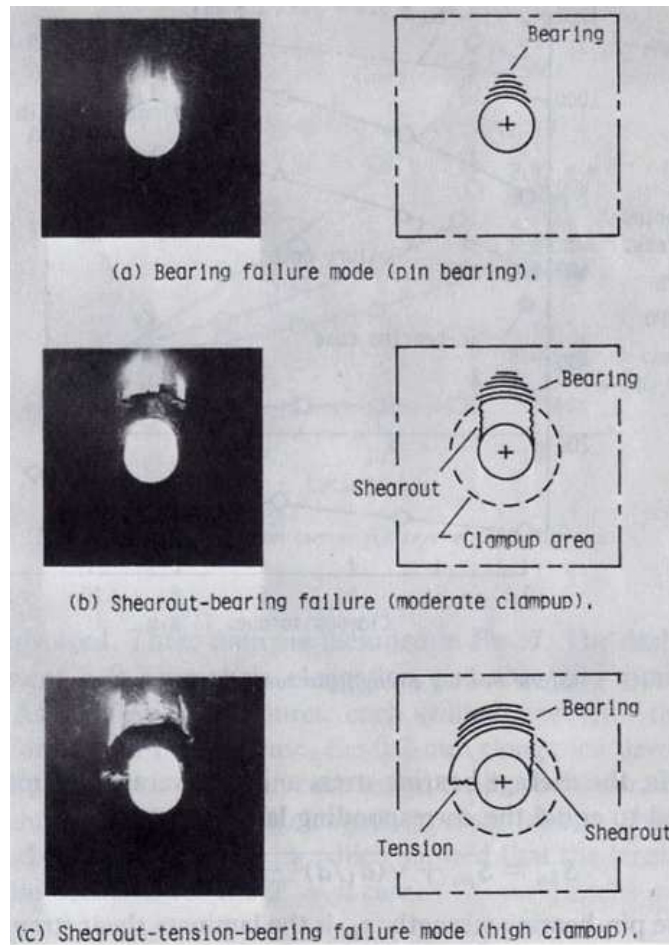


**Figure 4:** Static failure modes due to various bolt clamp-up  
*Figure taken from Crews (1981) [26]*

and have both been successfully integrated in hardware applications [47]. The characteristic offset approach, developed by Whitney and Nuismer (1974) [103], assumed a linear elastic region that was applicable to a characteristic softened zone adjacent to the fastener hole. There were, however, considerable variations in results with changes in bearing stresses. The other approach, Hart-Smith's hypothesis (1977, 1980, 1982, 1987) [42, 43, 45, 46], assumed that the amount of stress concentration relief was proportional to the intensity of the original elastic stress concentration. This allowed for simple calculation of residual stress concentration for other geometries that were not tested. Nelson et al. (1983) [67] were able to successfully predict the strength of highly loaded multi-row bolted composite joints from single-hole test specimens using this approach. Another common method is the half-cosine function distribution [102, 107, 19, 20, 18], which was used to approximate the pressure distribution around fastener holes for bearing loaded bolts. This method is limited by the error due to the non-linear contact between the bolt and the fastener hole.

For multi-bolt joint stress analysis, the crucial load distribution among the bolts or the most highly loaded bolt is determined first, typically with finite element analysis, before subsequent detailed stress analysis. This approach was presented by Ramkumar et al. (1986) [78] and was limited to specific bolt patterns that conformed to the loaded hole element geometry and one-dimensional analysis that resulted in equal load distributions on an entire row of bolts when the row was perpendicular to the direction of loading. This approach also did not account for the interaction between bolts that are placed closely together. Madenci et al. (1998) [61] developed a boundary collocation technique for single lap joints with multi-row fasteners to overcome these limitations. The contact stresses, contact region, and bolt load distribution were obtained as part of the solution procedure. This method was highly sensitive to the number of bolts, their location with respect to each other, and the free boundaries. This approach was later extended to thermal loading on double lap joints [59] but convergence inconsistencies remained and the approach was limited to specific configurations. A two-stage iterative analysis based on a variational formulation with the complex potential theory was proposed by Xiong and Poon (1994) [108] on single lap and double lap joints. This approach was later modified by Kradinov et al. (2001) [52]



to a single step analysis without the associative iterative process. The modified approach successfully accounted for the contact phenomenon and interaction among the bolts.

For two-dimensional stress analysis of mechanically fastened joints [75, 73, 87], the contact region is confined to the area near the surfaces of the joint, as illustrated in Figure 5 but the through-the-thickness pressure distribution is not taken into consideration. Two-dimensional analysis is limited by non-uniform contact stress distribution due to the interlaminar stresses at the free edges, secondary bending in single lap joints, and the bending of the bolt. Two-dimensional finite element models are limited by the effect of stacking sequence [109, 33, 104, 83, 65, 62, 77] and clamp-up force. The former can have up to a 10-20% effect on joint strength, while the latter can affect laminate failure by suppressing the delamination failure mode and thus changing the fastener head restraint. Some two-dimensional finite element models in the literature include the Lagrangian Multiplier Method [109], the Transformation Matrix Method [33, 104, 83] and the Inverse Method [65, 62, 77]. The Lagrangian multiplier method satisfies the contact conditions, but increases the total number of unknowns in the system of equations [100]. The Transformation Matrix Method is limited in its applications because of the need to match contact nodes, and it also requires costly iterative procedures, whereas the contact area has to be prescribed for the Inverse Method.

Three-dimensional analysis addresses some of these limitations. Marshall et al. (1989) [63] and Lee and Chen (1991) [54] investigated the contact stress on the fastener hole by assuming a uniform through-the-thickness contact surface without the effects of friction and clearance on the contact region. Chen and Yeh (1990), [21] implemented the Transformation Matrix Method on three-dimensional contact problems, accounting for the more complicated deformable surface rather than a curve in two-dimensional analysis. Ireman(1998) [51] developed a three-dimensional finite element model to determine the non-uniform through-the-thickness stress distribution of an isolated region on a composite joint in the vicinity of the fastener hole. Contact, friction, pre-tension, bolt type, stacking sequence, clearance, and lateral support were considered for a bolted composite single lap joint with experimental validation. There were, however, various sources that could account for the differences in

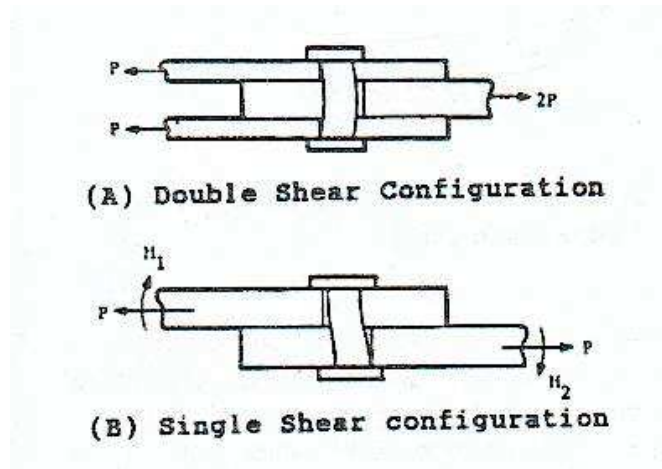


**Figure 5:** A two-dimensional illustration of the single shear and double shear configurations  
*Figure taken from Oplinger (1996) [73]*

the validation because of the multiple parameters included in the model.

#### 1.2.4 Bonded Joints

There are two different kinds of bonded joints, adhesively bonded joints and co-cured joints (co-bond joint). The former are manufactured using a two step procedure where the composite laminates are first cured and then bonded together by means of adhesive. The latter, however, combine both the composite laminate curing and adhesive bonding in a single step, typically in the form of a preimpregnated (or prepreg for short) which contains resin embedded among the composite fibers. Most prepreg holds more resin than required in the finished product, which eventually forms the layer of adhesive that bonds the two adherends during the cure cycle. Excess resin will be bled off into the bleeder. An additional layer of adhesive can also be included in the co-curing process to reinforce the joint. This difference in manufacturing process results in a less distinct adhesive fillet at the end of the lap adherend in the co-cured joint because of the inter-diffusion of adhesive and composite resins, as illustrated in Figure 6 [3].

MIL-Handbook 17F [27], volume 3, Chapter 6: *Structural Behavior of Joints* provides a thorough summary on the issues concerning bonded joints, particularly the various parameters that affect joint designs, analytical and numerical solutions for stress distribution and structural behavior of bonded joints. Hart-Smith (1987) [47] presents an extensive review

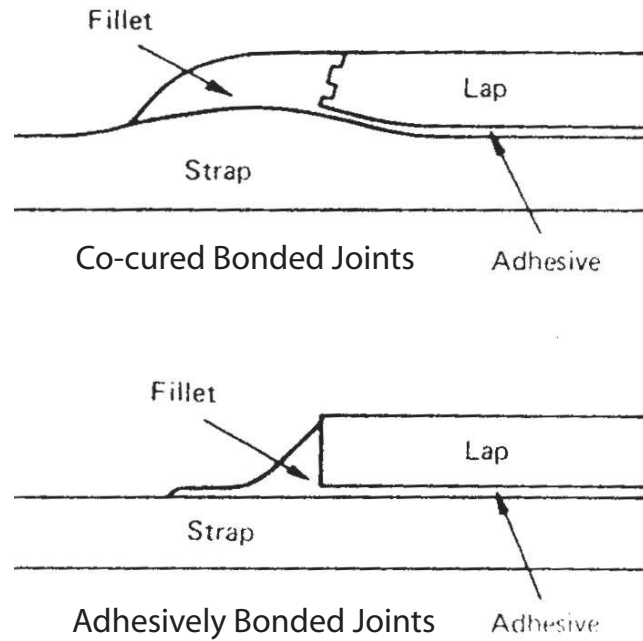


**Figure 6:** Adhesive fillets in (a)co-cured and (b)adhesively bonded joints  
*Figure taken from Ashcroft, Gilmore and Shaw [3] (1996)*

on the fundamentals of bonded joints, the various analytical methods for stress analysis and the elastic-plastic modeling of the adhesive layer. Williams and Scardino (1987) [105] discuss the selection criteria for adhesive, including technical descriptions, and recommend usage conditions for commonly used adhesives in a detailed review.

### 1.2.5 Selection Criteria For Bonded Joints

With the capability to manufacture complex one-piece components, bonded joints can significantly reduce the part count and weight in structural assemblies. However, there may be added inconvenience and excessive material waste when an entire part, instead of a component, needs to be replaced because of the damage type and location.

Comparing bonded joints to mechanically fastened joints, stress concentration is less severe in bonded joint because the load carrying capability of fibers is not compromised with fastener holes. This also leaves more material available for load transfer in bonded

joints. Tailoring joint designs, such as ply tapering, and choosing the ductility of the adhesive layer can also reduce stress concentrations, resulting in a relatively uniform stress distribution, which further improves the strength and fatigue life performance of bonded composite joints. Hence, bonded joints are, theoretically, more structurally efficient than mechanically fastened joints.

Although the adhesive layer is typically weaker in strength compared to its adjoining composite adherend and does not have through-the-thickness reinforcing components, it is important in determining the strength of bonded joints because load is mainly transferred through it. The adhesive layer is ideally designed to  $\geq 50\%$  of the adherend strength to compensate for manufacturing imperfections. The adhesives used in bonded joints usually have lower moduli than the matrix in the composite adherend in order to better handle the high local load arising from joint geometry. This load transfer efficiency, along with the likelihood of manufacturing imperfections between the adhesive-adherend interface, accounts for the high amount of scatter observed in strength evaluation and are often the limiting cause of bond strength. The ductility in adhesives will reduce the effect of shear stresses on the joint, while the brittleness makes it more susceptible to peeling. As such, a higher load transfer efficiency can be achieved through an increase in the overlapping adherend-adhesive area. This increase reaches a theoretical limit when the plastic and elastic zones, illustrated in Figure 7, are fully developed [50]. Figure 8 shows some commonly used adhesively bonded joint designs. Loading between the adherend-adhesive bond peaks at the end of the overlapped region as a result of compatibility of deformation. Figure 9 illustrates this shear loading in the adherend-adhesive interface in adhesively bonded joints [47]. The peak stresses at the end of the overlapped region can be reduced through tapering of plies to alleviate geometry change.

Similar to bolt material compatibility in mechanically fastened joints, the selection of a suitable adhesive to resist corrosion, moisture, and temperature in the service environment and ensure failure in the adherend is important in bonded joints. One of the factors to consider in adhesive selection is the local peak load as the joint geometry changes. Williams (1987) [105] discusses in details various resin systems and recommends adhesive selection

criteria based on operating stresses, environmental conditions, and application practicality. Other secondary factors for adhesive consideration are surface preparation, inadequate fit of adherends, void formation during bonding, and possible joint distortion due to thermal stresses.

Epoxy adhesives are good for composite structure assembling and repairing because of their high bond strength. Their ability to withstand a hostile environment makes them particularly good candidates for aerospace applications. However, large scale production with epoxy adhesives are inefficient because of sensitivity to surface treatments (e.g. poor wetting on certain surfaces) and a lengthy curing process. There are a wide range of epoxy resin systems available through modification of select properties with additives. The more commonly used ones in aerospace applications are the high shear strength, heat-cured, two-part systems toughened with rubber to improve the peel strength. The pot life (period between time of mixing the resin and curing agent to the time where the increase in viscosity renders the adhesive useless) for mixes ranges from 2 hours to several days while the shelf life of film adhesives is much longer [105]. The rubber-base adhesives have low shear strength and high peel strength in comparison to glassy systems and are often used in applications that have a large region for bonding.

Another important criterion is bond defects, which include voids, porosity, and thickness variations in the resin bonding layer [27]. These pose a major problem because non-destructive evaluation techniques do not offer reliable means of assessing interfacial strength between the bond and the adherends. Defects can be introduced indirectly through poor adhesion between bonding surfaces from the residue left on the bonding surface as release film is removed from the adherend. Porosity in the bond can result in catastrophic failure under the presence of significant peel stresses. Inappropriate surface preparation is the most common cause of bond defects.

Types of failure observed in a fiber-reinforce composite system includes fiber fracture, matrix cracking, matrix crazing, fiber buckling, fiber-matrix debonding, and delaminations. Heslehurt and Hart-Smith (2002) [49] identified two major types of failure modes in adhesively bonded joints: the adherend failure modes, such as adherend fracture in the far

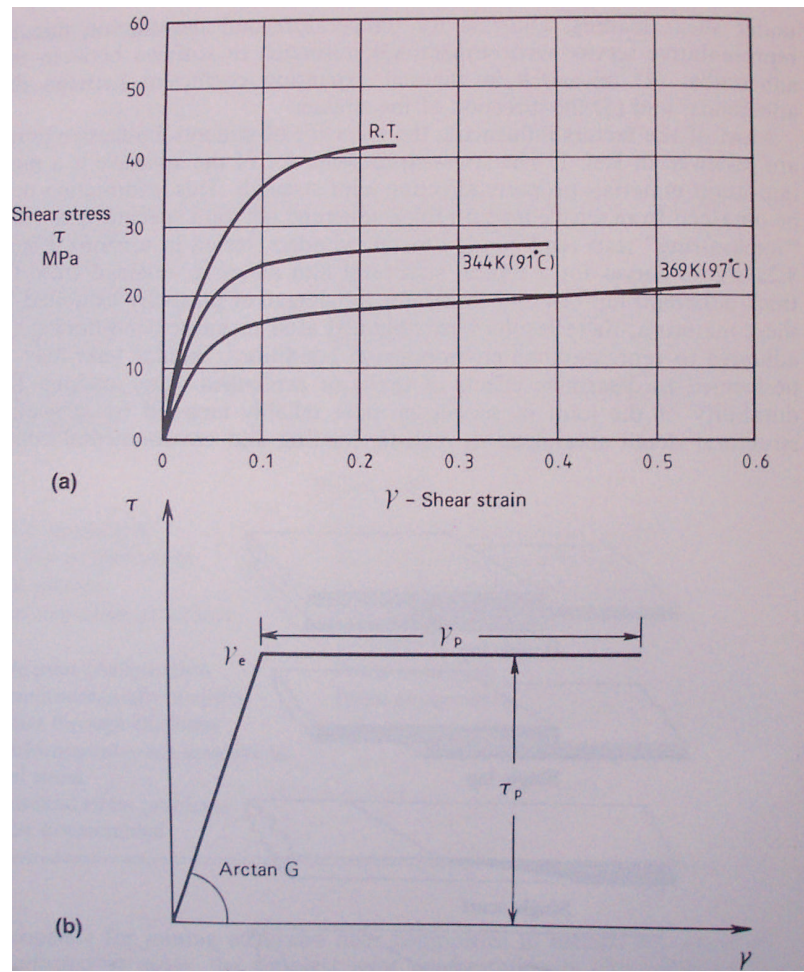


**Figure 7:** Shear stress distribution in adhesive with fully developed plastic and elastic zones  
*Figure taken from Composite Materials for Aircraft Structures (1986) [50]*

field and composite adherend interlaminar fracture, and the adhesive failure modes, such as cohesive fracture under shear and under peel, adhesive bondline fracture under shear, and under peel. These failure modes are illustrated in Figure 10.

### 1.2.6 Analysis of Bonded Joints

The most simple method is the load over area formulation, which only takes into account the average shear stresses in the bond layer. Hart-Smith neglected through-the-thickness effects and formulated one dimensional models with variations in the axial direction. Other commonly used approaches of this method are modified from the closed form and classical series solutions proposed by Volkersen (1938) [101] and Goland (1944) [36] and have been successfully applied to joint designs on aircraft components [27].

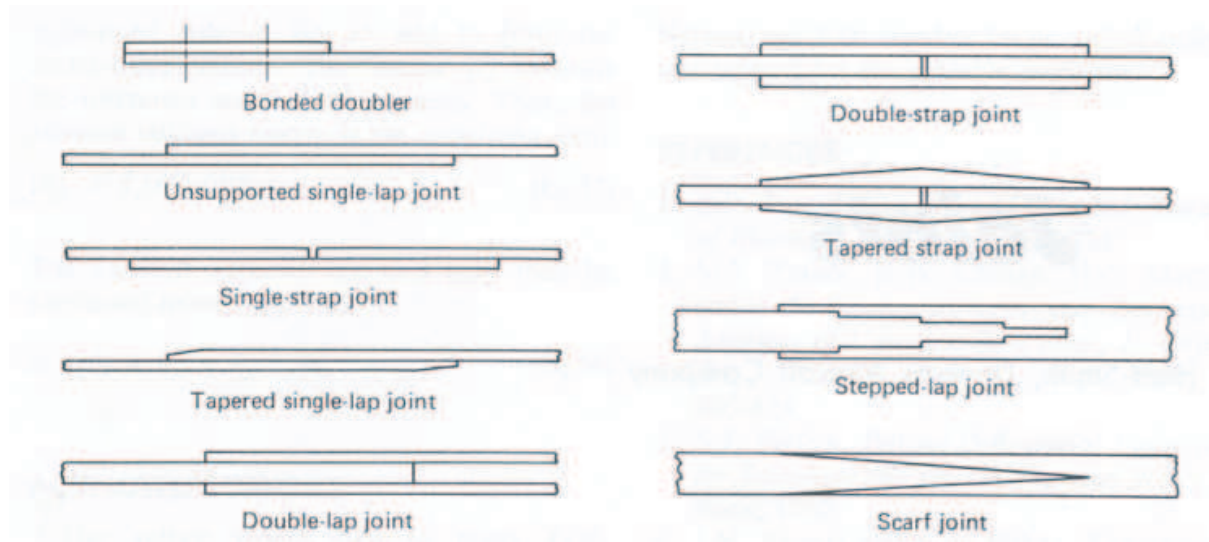


**Figure 8:** Types of adhesively bonded joints commonly used

*Figure taken from Engineered Materials Handbook -Composites (1987) [47]*

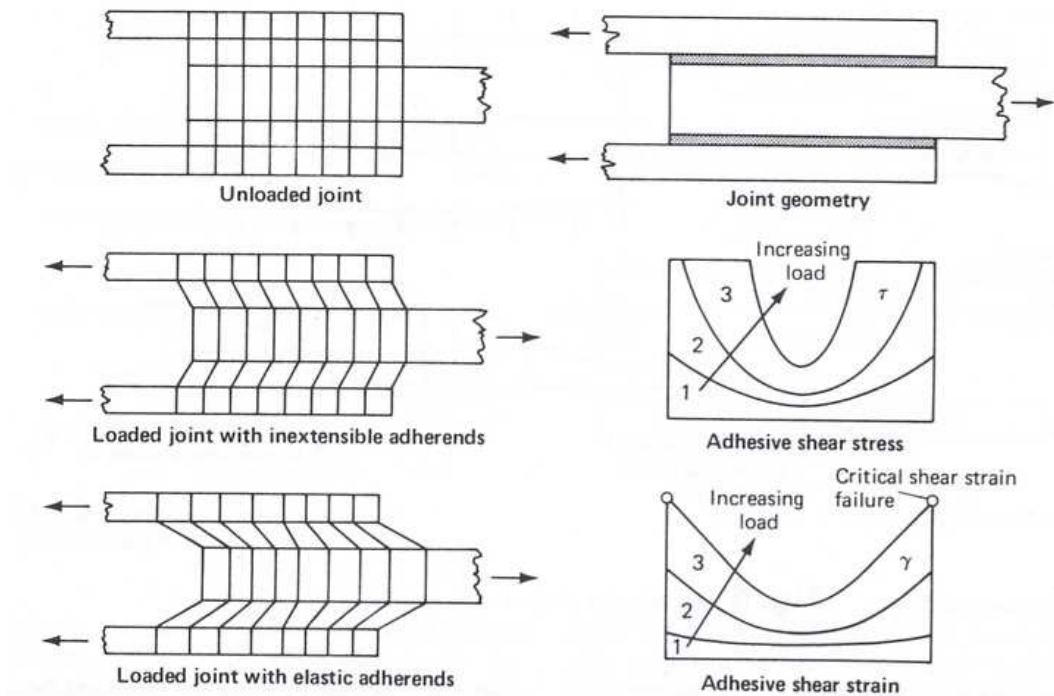


**Figure 9:** Shear load in adherend-adhesive in adhesively bonded joints

*Figure taken from Engineered Materials Handbook -Composites (1987) [47]*



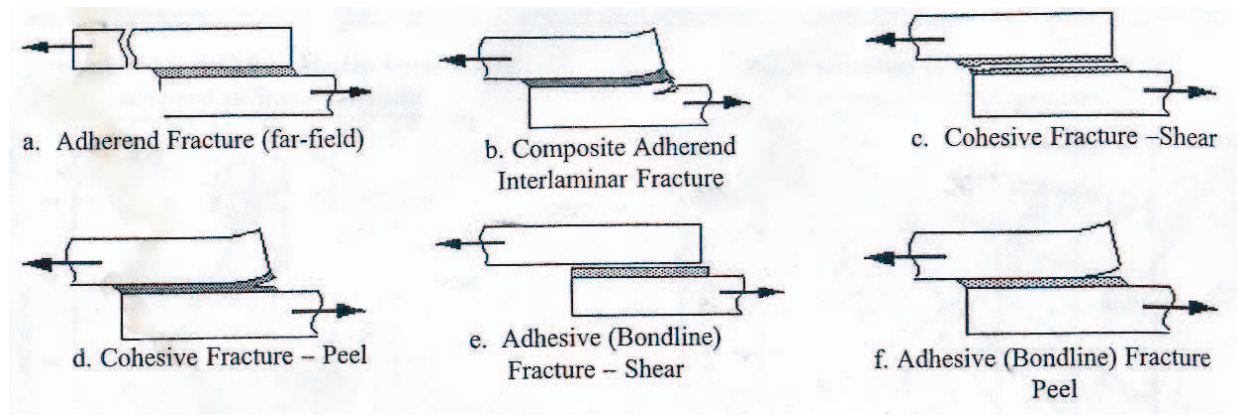


**Figure 10:** Failure modes for bonded composite joints  
*Figure taken from Heslehurst and Hart-Smith (2002) [49]*

The joint can also be modeled as a rigid adherend, where neighboring points on the upper and lower adherend align vertically and slide horizontally with respect to each other as the joint is loaded, resulting in a linear distribution of resultant axial stresses. Two cases of different adherend deformability have been considered [27], as shown in Figure 11. The difference between two deformable adherends and only one deformable adherend is an unequal shear strain increase at the tip of the rigid adherend in the latter case.

Other analytical models include the elastic-plastic adhesive shear model proposed by Hart-Smith (1972) [39]. This method has an equivalent elastic-perfectly plastic response for the stress-strain curve of the adhesive layer to predict the mechanical response of adhesively bonded joints. The primary parameter in determining joint strength is the strain energy to shear failure in the adhesive layer as long as peel stresses are kept to a minimum through tapering [47]. Only a relatively simple one-dimensional stress analysis is required even for complicated joint geometries [44]. A modification of the elastic-plastic adhesive shear model, the bilinear model, was applied to double lap joints in a later paper [40]. In comparing the bilinear model and the elastic-plastic model, the former has the advantage of representing all load levels with a single model whereas the latter needs to be adjusted based on the ultimate loads.



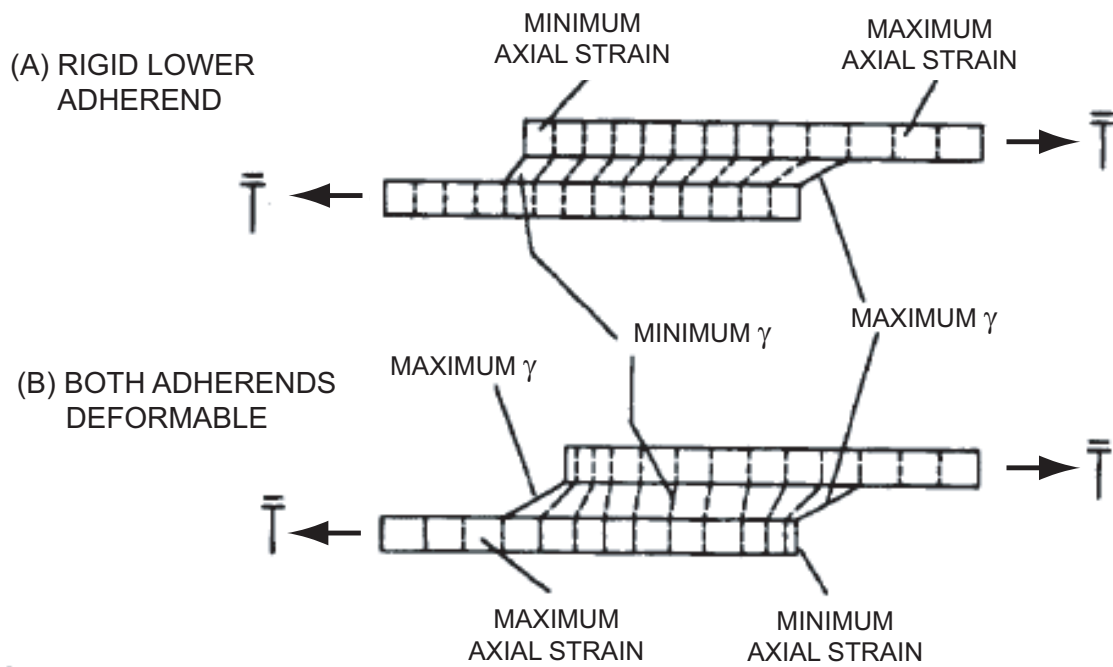


**Figure 11:** Rigid adherend model: Finite element model with different adherend deformations

*Figure taken from MIL Handbook 17 volume 3 (2002) [27]*

### ***1.3 Non-conventional Joints and Their Analysis***

Non-conventional joint improvement concepts have been developed through an understanding of the fundamental mechanisms responsible for composite joint failure. In a single lap joint, where the load transfer mechanism is effected through the interlaminar peel and shear stresses, the distributions within the overlap region follow a boundary layer form. Both the single nested overlap joint and the wavy lap joint covered in this section are co-cure composite joint improvement concepts aimed at addressing the cause of these boundary layer type interlaminar stress distributions. The improvement is achieved through a reduction or reversal of the peel stresses and a redistribution of the intensity of both the transverse normal and shear stress over the entire length of the overlap.

#### **1.3.1 Single Nested Overlap (SNO) Joint**

Coates and Armanios (2000, 2001) [24, 23, 22] proposed a nested concept to provide multiple interfaces for load transfer. The Single Nested Overlap (SNO) joint is a co-cured joint derived from the single lap joint through an overlapping/interleafing of adjoining top/bottom adherend plies. Nesting leads to a reduction and ultimately a reversal of peel stress. An illustration of the load transfer mechanism of this SNO joint concept evolving from a single lap joint is depicted in Figure 12. The transverse normal or peel stress distribution is a finite element result obtained from ABAQUS and is plotted over the co-cured length of the joint or the shaded region of the SNO joint as shown. This distribution shows a typical boundary layer behavior. For the single lap joint referred to as Unmodified in Figure 12, the stress is positive leading to a separation or peel of the joint. This is due to the moment generated by the eccentric lines of action of the applied tensile loads. The transverse normal stress in the SNO joint is negative leading to a significant improvement in static strength. Multiple nested layers, interleaving multiple plies from each adherend, was also investigated in Coates and Armanios (2001) [25]. It was concluded that there was minimal improvement in quasi-static strength for multiple nested layers as compared to the single layer to justify the increase in manufacturing effort required.

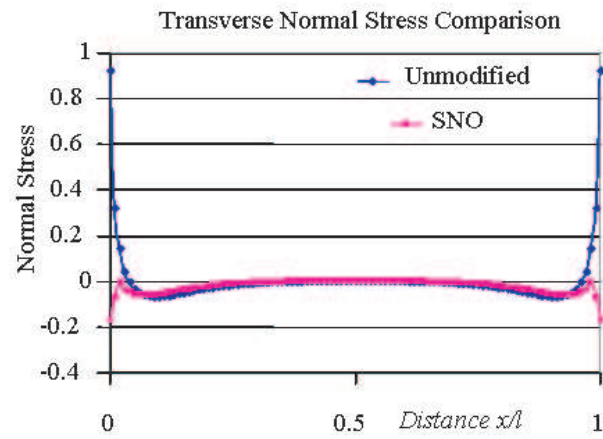
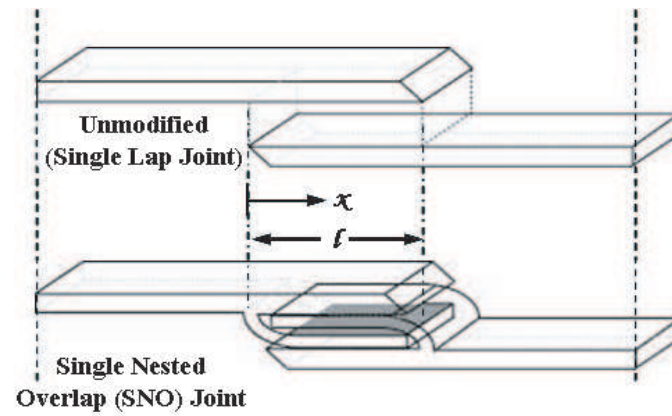


**Figure 12:** Nested joint concept evolving from single lap joint

### 1.3.2 SNO Joint: Strength Comparison

Coates and Armanios (2000, 2001) [24, 23, 22] reported a static strength improvement of 23% and a fatigue limit of 150% for graphite/epoxy T300/8551-7 SNO joint over the single lap joint. Constant amplitude tension-tension fatigue was carried out under a frequency of 5 Hz and a stress ratio of 0.1.

Cao and Dancila (2005) [15, 16] verified the static ultimate failure strength improvement of SNO joints with non-destructive evaluation techniques, such as optical microscopy, X-ray radiography and Acoustic Emission (AE). Three joint configurations, namely the straight laminate, the single lap joint and the SNO joint were used to ascertain the improvement of the SNO joint over a single lap joint. They concluded that for graphite/epoxy IM7/8551-7 with quasi-isotropic lay-up, the SNO joint retained 97% of the strength of a straight laminate whereas the single lap joint retained 76% under quasi-static loading. These results were obtained from a single manufactured panel of specimens. Clustering was applied to parametric AE histories for waveform characterization of specific failure type. Although successful identification of failure types were limited by the complexity in failure mechanisms and their interactions, AE counts and cumulative AE counts were concluded to be representative of the elastic energy released during quasi-static loading.

### 1.3.3 Bonded Wavy Composite Lap Joint

A wavy lap joint design, depicted in Figure 13, was proposed by Zeng and Sun (2000) [110, 112] to eliminate the load eccentricity in single lap joint through a reversal of the peel stress.

### 1.3.4 Wavy Joint: Static Strength

The static strength of graphite/epoxy T300/E767HM single lap and wavy joint was compared [113, 111]. The single lap and wavy lap joints were manufactured with an additional layer of FM73M adhesive. The average static strength of the single lap and wavy lap joint was 10.4 kN and 19.4 kN, respectively. Cohesive fracture was dominant in the single lap joint whereas significant plastic deformation in the adhesive layer prior to a sudden failure

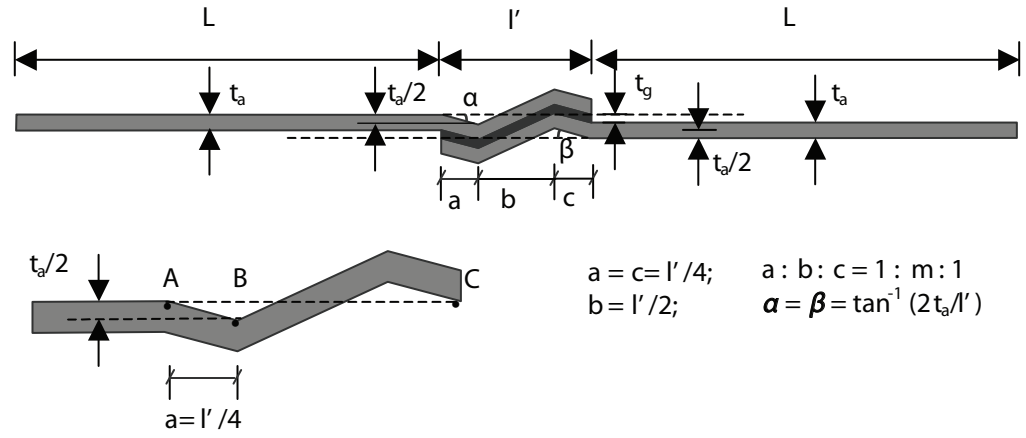


**Figure 13:** Dimensions and geometry of single lap and wavy joint  
figure taken from Zeng and Sun (2004) [113]

was observed in the wavy lap joint.

### 1.3.5 Wavy Joint: Fatigue Study

The wavy lap joint showed improvement over the single lap joint under various constant amplitude tension-tension sinusoidal cyclic loading at a stress ratio of 0.1 and frequency of 6 Hz. The effect of increased frequency was concluded to have a direct correlation to the increase in fatigue life. Fatigue crack propagation dominated failure of single lap joints whereas cyclic degradation and creep damage accumulation in the adhesive accounted for the fatigue failure of wavy lap joints. Significant loss in stiffness was observed for single lap and wavy lap joints, due to crack growth and adhesive layer degradation, respectively [113].

The fatigue properties of the co-cured SNO joint is extensively studied in this investigation to establish the observed failure modes and damage propagation for the graphite/epoxy IM7/8551-7  $[0/\pm\theta/90]_s$  family. Based on those observations, the nesting concept is further improved by reducing edge delaminations.

## 1.4 Non-destructive Testing

Non-destructive testing utilizes tools to evaluate the structural integrity of service components through detection of failure without compromising the structural integrity of service components. Of particular importance are tools that enable inspection of less accessible

parts within a structure or within a laminate. The non-destructive techniques briefly covered here are limited to those commonly used for evaluation of composite defects. Due to the complexity of part geometries and location of parts, inspection of composites in aircraft relies strongly on non-destructive testing techniques such as ultrasonic, X-ray radiography, optical interferometry, and acoustic emission. The more common methods for detection of internal delamination and free-edge matrix cracking are ultrasonic C-scan and X-ray radiography, respectively.

Ultrasonic technique utilizes either a pulse-echo or through-transmission mode to measure defects, such as delamination, debonding, and impact damage in the part. Microprocessors are typically used to process these measurements and also to display a C-scan image. This technique allows estimation of internal defect size, shape, and orientation with higher accuracy compared to other non-destructive methods but requires sufficient scanning time and presents difficulties when inspecting irregularly shaped or rough parts. Some modifications to the conventional immersed pulse-echo ultrasonic technique include non-contact techniques, such as laser ultrasonic and air-coupled ultrasonic, that enable quicker inspection of curved surfaces in more hostile environments. The former uses lasers to emit and detect ultrasonic waves while the latter depends on high voltage transmission of the emitting transducer and high sensitivity of the receiving transducer.

X-ray radiographic images are generated on film based on the exposure of varying degrees of radiation that passes through the part due to material absorption. This method allows inspection of internal defects with minimal preparation but requires strict radiation containment measures, is slow, and does not measure the depth of the defect.

Unlike ultrasonic and X-ray radiography that detect internal defects in structures, conventional optical interferometry is typically used to measure surface deformations or to provide the shape of defects. Using the resonant vibration of the part, the shape of the defect is determined from the interference fringe pattern between top and bottom surfaces of the part under the same resonance mode. The depth of the defect is then located using the resonant frequencies of the two surfaces.

A common optical interferometry method is Moire interferometry, which measures in-plane displacements primarily for flat surfaces to obtain the engineering strain on the specimen surface. The measured data are contours of fringe patterns for the in-plane displacements. This method is also widely practiced in the microelectronics industry to measure thermally induced deformation of electronic packages. The resolution of the deformation measurement is limited by the sensitivity of the system and the contrast of the interference fringes.

In this study, two non-destructive testing methods, namely the acoustic emission (AE) technique and the infrared thermoelastic stress analysis (IR-TSA) technique are used to access the co-cured composite joint strength under quasi-static and fatigue loading. Some background on these two techniques is discussed in the following.

#### **1.4.1 Acoustic Emission**

Acoustic Emission is the elastic energy released by materials as they undergo deformation or fracture. Uses of AE as a nondestructive tool include monitoring structural integrity, characterizing material behavior, and detecting leaks. The two main differences between AE and most other nondestructive methods are: (i) AE detects the energy that is released by the specimen rather than supplying a source of energy, and (ii) AE is capable of tracking dynamic processes as the structure degrades [64]. A piezoelectric transducer, typically placed on the surface of the specimen, is used to convert stress waves into electrical signals. The convenience of AE in real-time monitoring makes it an attractive nondestructive evaluation tool.

There are two general approaches to AE analysis. The parametric approach is a more conventional approach which converts mechanical vibrations into analog signals. A number of parameters, such as amplitude, counts, rise time, duration, and energy, can be extracted from each AE event and are studied for damage correlation. The location of damage can be identified based on the difference in time of signal arrival from multiple mounted sensors through cluster analysis, while successful identification of failure type, such as fiber fracture or matrix cracking, has been inferred through amplitude distribution studies. However,

the complexity of failure mechanisms, the interaction of damage types, the wave propagation phenomena in composites, and the scatter observed in local microstructure, results in significant overlaps of parametric AE signals, undermining the application of parametric AE analysis in damage source identification, particularly for single parameter filtering. The transient approach counteracts this limitation in parametric AE studies by utilizing pattern recognition and classification methods on fully digitalized AE waveforms for specific damage type identification. Apart from the need for more sophisticated equipment to handle the increased data volume for a full waveform analysis, a significant amount of data is also necessary for classification.

#### *1.4.1.1 Parametric AE Analysis*

Parametric AE analysis has been used for damage location under both quasi-static and fatigue loading, based on the difference in arrival times of AE events between two sensors on a specimen. This damage detection and location is differentiated into damage initiation and damage progression in some studies. Identification of the major failure modes is also commonly used. Bakuckas et al. (1994) [7] applied this to titanium matrix composite (SCS-6/Timetal-21S TMC) under quasi-static loading. Successful correlations were established between observed damage progression mechanisms and AE amplitude for dominant failure mode specimens, and subsequently was used as a basis for multiple failure mode specimens. For composite materials, Awerbuch et al. (1989) [5] applied parametric AE analysis for identification of major failure modes and for detection and location of damage initiation and progression of cross-ply AE4/3502 graphite/epoxy laminates under quasi-static loading. They were able to determine the far-field stress and strain for damage initiation based on count rate, cumulative counts or cumulative events curves but not the fracture stress or fracture site.

Parametric AE analysis is also used as a damage parameter and failure criterion for fatigue life prediction of composites. Bourchak et al. (2007) [11] proposed the AE energy as a damage parameter to account for the material response in fatigue life prediction of composites as opposed to Palmgren-Miner rule, which assumes the same fatigue effect within



a block of loading in a variable amplitude spectrum. Correlation was observed for stress-strain curves, ultrasonic C-scans and microscopic analysis of specimens under both quasi-static and fatigue loading.

Other applications of parametric AE analysis also include damage characterization of composites. Ely and Hill (1995) [32] used source location as a filter criterion for failure type characterization of fiber breakage and longitudinal fiber splitting, addressing the importance of signal attenuation necessary for appropriate characterization. Signal attenuation is the reduction in signal amplitude due to propagation from source to sensor and can be caused by material damping due to manufacturing, environmental and loading history, structural geometry, scattering, and diffraction. Signal attenuation was also helpful in further characterizing the two failure types since fiber breakage and longitudinal fiber splitting represented a stationary and moving source, respectively.

Some of the primary concerns with parametric AE analysis under fatigue includes difficulty in separating out noises from the elastic waves generated as a result of damage accumulation and computational effort required for the significant amount of fatigue data.

Friction AE due to the rubbing of new fractured surfaces is a source of noises in fatigue AE analysis. Awerbuch and Ghaffari (1988) [6] identified a FRiction Emission Threshold (FRET) and a reliable range of loading applicable for FRET, using several AE events, such as event amplitude, duration, energy, and counts to monitor the progression of matrix splitting in double edge notched unidirectional AS/3501-6 graphite/epoxy system. The FRET threshold was restricted to higher loading and lower number of cycles to failure as friction AE became more significant than damage accumulation AE at lower loadings, limiting the practicality of this methodology because the higher loadings are also accompanied by a high amount of scatter.

#### *1.4.1.2 Transient AE Analysis*

Broadband transducers are often used for transient AE analysis because they have a wider frequency range, which allows for a more accurate transient description. Some proposed

signal processing methods for AE signal identification include classification and multi-parameter filtering of AE waveform, pattern recognition of AE waveform with neural network, finite element modeling, and the frequency response technique.

A neural network is a good tool for pattern recognition, classification, and optimization of transient AE analysis because of the significant amount of data involved. The application of a neural network for AE pattern recognition of composite failure mechanism was suggested by Fowler et al. (1989) [34]. Subsequently, Ativitavas et al. (2006) [4] achieved successful identification of some damage types for pultruded fiber-reinforced polymer composites using backpropagation with a two level neural network system. The verification of damage types were conducted with scanning electron microscopy.

To further develop AE for in-flight monitoring, a neural network is also used with transient AE analysis for detection and identification of failure modes and their progression. Bhat et al. (2003) [8] used supervised and unsupervised training of artificial neural network to characterize AE data of carbon fiber-reinforced plastic with noise under fatigue. AE signals for fiber failure, fiber/matrix debond and matrix cracks were successfully identified and classified. This work was extended with significant success in characterizing AE signals under noisy environment for the detection and identification of failure modes and their progression [9].

In addition to the neural network approach, Dzenis and Qian (2001) [29] used a combination of transient AE classification and multi-parameter filtering on the AE damage evolution histories of graphite/epoxy composites under quasi-static loading to identify and locate damage types. Three characteristic AE waveforms were identified for two micro-damages, matrix cracks, and fiber breakage, and a collective measurement of macro-damage, comprising of delaminations or longitudinal splitting of unidirectional plies. This hybrid method was postulated to be a viable option for fatigue damage histories where a full transient AE analysis was impractical or prohibitive because multi-parameter filtering only required parametric AE data.

The frequency response technique on transient AE waveform can also be used to detect and monitor damage in composite laminates. Awerbuch et al. (1989) [5] first proposed the

use of the following sequence. The specimen is excited to an optimal frequency range specific to the structure and material system and a receiver records the signals propagating through the pulser-receiver path. AE events of the transmitted signal, such as peak amplitude, arrival time, shift in frequency components and area under the frequency response curve, are processed and monitored for changes. They concluded that the frequency response technique was sensitive to internal damage stage, such as amplitude attenuation, downward shift in the resonance frequencies, and decrease in the area under the frequency response curve. However, the preliminary results they obtained indicated that this technique was not sufficiently sensitive to the dominant failure mode observed in cross-ply graphite/epoxy laminates. Leone et al. (2008) [55] concluded the application of the frequency response technique with AE waveform analysis for qualitative determination of the severity of damage ahead of a notch tip on a full-scale honeycomb sandwich graphite/epoxy composite fuselage.

Based on previous work [95, 98] and the conclusion drawn by Cao and Dancila (2005) [15, 16], quasi-static cumulative AE count peaks were observed to be fatigue limit predictors for graphite/epoxy IM7/8551-7  $[0/\pm 45/90]_s$  straight laminates and SNO joints. The significance of the accumulated damage measured by quasi-static AE counts on fatigue was further investigated.

#### **1.4.2 Infrared Thermoelastic Stress Analysis Technique**

Infrared Thermoelastic Stress Analysis Technique (IR-TSA) is a non-contact technique for full-field mapping of surface stresses using an infrared camera that detects changes in surface temperature of a stressed body. An infrared camera is used to measure small changes in surface temperatures resulting from the elastic strain energy generated as the specimen deforms. It has been successfully used as a non-destructive testing tool both qualitatively and quantitatively. Some difficulties with thermoelastic stress analysis of fiber-reinforced polymer composites include nonlinear effects, such as viscoelasticity and plasticity, which may affect mean stress or test frequency. The anisotropy of composite systems may also result in non-uniform heat conduction.

Quantitative thermoelastic stress analysis is subject to various limitations in order for

the thermoelastic theories to apply, such as cycling orthotropic composites to achieve adiabatic conditions. Dulieu-Barton et al. (2006) [28] studied the localized effect of heating on surface temperature variations and proposed a correction factor to calibrate the Deltatherm detector based on decoupling of the infrared thermoelastic response due to surface temperature and stress changes. The Deltatherm detector is a thermoelastic measurement system that counts the total number of photons per unit area and time and decoupling to ensure that the thermoelastic signal measures only changes due to stresses. This process successfully eliminates the effect of localized heating for aluminum and fiber-reinforced polymer composites, quantifying the stresses for damage progression. El-Hajjar et al. (2004) [31] presented a solution for the sum of direct surface strain components on the surface of thick pultruded composites by assuming the thin surface layer responsible for the thermoelastic effect as transversely isotropic. The results were verified with finite element analysis and applied on pultruded composites with circular cut-outs and edge cracks. This method was extended to the calculation of mixed-mode stress intensity factors for cracked laminated and pultruded composite specimens in Haj-Ali et al. (2008) [38], further demonstrating the effective application of IR-TSA for generation of full-field surface strains indirectly.

IR-TSA was also successfully used to experimentally measure the onset and growth of damage in different composite systems. Mackin and Roberts (2000) [57] presented stress maps and damage images of several brittle constituent composites by measuring the thermoelastic and dissipational thermal signatures during cyclic loading, obtaining a qualitative picture of stress distribution and a quantitative measure of the damage in terms of a modified stress concentration factor at locations of concentrated stress. This method was further applied to model the detection of sub-surface cracks in a 3-layer system of laminated polymer membrane [58] but limited to sub-surface layers that have different thermoelastic properties from the surface layer. Gyekenyesi and Morscher (2004) [37] applied this method to define the stress profile of ceramic matrix composites with significant stress concentrations in high temperature gas turbines applications and used acoustic emissions and destructive sectioning to illustrate the extent of matrix cracking at the notch roots.

Despite the success of IR-TSA in various composite systems, IR-TSA has not been used

to monitor the growth of damage in composite joints. In addition to damage monitoring, the capability of IR-TSA in identifying failure modes occurring in composite joints was also validated in this study.

## ***1.5 Fatigue of Composites***

With the fatigue damage mechanics of composites vastly different from that of isotropic materials, the durability and sustainable performance of composites under fatigue requires different analytical tools as compared to metals. The fatigue behavior of metals are typically well characterized, with a gradual growth stage, an approximately linear growth stage, and a final stage, where small cracks coalesce to form larger cracks leading to failure. Damage in fiber-reinforced composites under fatigue, however, starts earlier with different damage types growing in the damage zones at various rates. As such, the loss of stiffness in fiber-reinforced composites is gradual, accompanied by a continuous redistribution of stress and reduction of stress concentrations. Due to the lower conductivity of composites compared to metals, strength concerns arising from local overheating under high frequency ( $\geq 10$ ) cyclic loading, are more significant than metals. Tension fatigue in composites is less susceptible to damage, whereas compression fatigue is more prone to local delaminations which compromise the fatigue strength severely.

As with all engineering regimes, the study of fatigue of composites begins with the physical understanding based on a fundamental characteristic property or response. Reifsnider [79, 80] in his overview on fatigue damage of composites defined damage mechanics to include changes in stiffness, strength, and life of composite laminates, emphasizing the importance of a collective condition for fatigue damage in composites. He defined a “characteristic damage state” that determined the state of stress and strength of an unnotched laminate, analogous to the single crack study for a homogenous material. Various frameworks for modeling of fatigue behavior were proposed. Among them, Talreja [88] proposed the fatigue life diagram, which categorized fatigue of composites into three regions based on the progressive nature of the damage mechanism. This study was then further developed in Talreja [92, 94] and Gamstedt and Talreja [35].

With the eventual goal of life predictive tools for fatigue of composites, analytical and finite element models on fatigue damage mechanics and fatigue damage evolution were developed. Two main approaches were undertaken by researchers in studying the fatigue damage mechanics, namely micromechanics and Continuum Damage Mechanics (CDM) based modeling, to mathematically describe the elastic coefficients of the damage state as a function of the loading and change in damage. The micromechanics approach assumed a Representative Volume Element (RVE) as a basis for the continuum material while the CDM approach based its model on physical observations of damage growth and material response, typically by assuming a nature of damage and its effect on the elastic coefficients. Some of the researchers that contributed to the micromechanics based modeling include Hashin [48] and Tsai et al. [99], while some of the researchers that contributed to the CDM approach include Nairn [66], Talreja [91, 90] and Reifsnider and Stinchcomb [82]. There were also models, such as the synergistic damage mechanics approach proposed by Talreja [93], that combined these two approaches in order to counteract the limitations of each.

The current work focuses on the physical understanding of the damage mechanism of the  $[0/\pm\theta/90]_s$  SNO joint in comparison to the  $[0/\pm\theta/90]_s$  straight laminates and  $[0/\pm\theta/90]_s$  single lap joints. Based on this physical understanding, a joint improvement study to minimize free-edge delamination in quasi-isotropic straight laminates and SNO joints, was conducted.

## ***1.6 Edge Delamination in Composites***

Delamination between adjacent layers is a commonly observed damage type in fiber-reinforced composite materials subjected to tension loading. Some delaminations initiate along the edge of the specimen as a result of high interlaminar stresses and between adjacent layers that have significant mismatch in Poisson ratios, such as between angled and  $90^\circ$  plies. Edge delamination was documented as a stable fracture process in laminates under tension in 1970s by Lackman and Pagano (1974) [53], Rybicki et al. (1977) [84], and Reifsnider et al. (1977) [81].

O'Brien (1982, 1985) [68, 69] proposed a delamination prediction model using the strain

energy release rate to characterize interlaminar fracture behavior of composites. A simple expression was developed for the total strain energy release rate, while the strain energy release rate components for Mode I, II, and III were estimated from finite element analysis and crack closure techniques. Delamination initiating from edge delamination [68] and from matrix ply cracks parallel to fibers in a ply [69] were investigated for a variety of lay-ups and the influence of these two factors on the laminate tensile stiffness and strength were studied. O'Brien also proposed a quasi-static tensile strength prediction tool for quasi-isotropic graphite/epoxy T300/5208 specimens with equal percentages of  $0^\circ$ ,  $90^\circ$  and  $\pm 45^\circ$  plies based on delamination resistance curve and strain energy release rate [71]. Successful prediction was obtained for laminates with different thickness and stacking sequences given the delamination growth history of one laminate. Edge delamination was concluded to reduce laminate stiffness and tensile strength under quasi-static loading but will not cause premature laminate failures. The experiments were conducted in a closed-loop hydraulic testing machine under a strain controlled mode.

These results were incorporated into a fatigue life prediction methodology for composite laminates under tension fatigue [70], but the technique was limited to one dominant damage mechanism because of the complexity associated with the interaction of multiple damage modes. The same problem was investigated with three dimensional finite element analysis by Salpekar and O'Brien (1991,1993) [86, 85]. Chan et al. (1987) [17] proposed a delamination prediction tool through computation of strain energy release rate using fracture mechanics and identification of critical delamination site with sublaminates modeling and finite element analysis. In particular, an inner layer manufacturing technique and a special  $90^\circ$  hybrid technique successfully suppressed and delayed delamination, respectively. The former technique includes an additional high strain ductile adhesive layer at the critical interface of the laminate, while the latter technique reduced the mismatch in stiffness along the direction normal to the free edge by replacing the  $90^\circ$  ply in the parent laminate with a softer glass/epoxy ply. Wisnom et al. (2008) [106] demonstrated the importance of free edge delamination in failure criteria for reliable prediction of thickness and stacking sequence effects.

Armanios and Rehfield (1989) [1] developed a simple sublamine model based on transverse shear deformation theory to analyze mixed mode edge delamination specimen and provided closed form estimates of strain energy release rate components for Mode I, II, and III. The simplicity of this model allows preliminary design analysis to be evaluated quickly and economically. The characteristic roots controlling the behavior of edge delamination specimen were also provided. Armanios et al. (1989) [1, 2] proposed that edge delamination in symmetric laminates was determined by the resultant peel stress moment at the midplane and thus, a closing mode at the midplane would suppress Mode I opening, thereby reducing edge delamination. Li and O'Brien (1997) [56] developed a sublamine model including hygrothermal effects for the characterization of Mode III fracture toughness to analyze laminates with midplane edge delamination under torsional load. The hygrothermal, bending-twist coupling, and extension-twist coupling effects on the strain energy release rate were investigated for symmetric, asymmetric and antisymmetric laminates. The hygrothermal and Mode I effects on antisymmetric laminates  $[\pm\theta/(\theta - 90)/\theta]_n$  with varying number of plies,  $n$ , were also concluded.

Significant contributions have been made in understanding the formation and growth of delamination in composite laminates and its effect on the stiffness and quasi-static strength. The current study focuses on understanding the growth of delamination in co-cured composite joints under quasi-static and cyclic loading, its effect on quasi-static, fatigue strength, and failure modes.



## CHAPTER II

# QUASI-STATIC STRENGTH CHARACTERIZATION AND FAILURE MODES OF $[0/\pm\theta/90]_S$ FAMILY OF COMPOSITE JOINTS

A family of IM7/8551-7  $[0/\pm\theta/90]_S$  stacking sequences, including  $[0/\pm30/90]_S$ ,  $[0/\pm45/90]_S$ , and  $[0/\pm60/90]_S$ , were tested at a monotonic loading rate of 50 N/s. The IM7/8551-7  $[0]_8$  was also studied for comparison. The material properties for the graphite/epoxy, characterized based on ASTM standards, are listed in Table 2.

### 2.1 *Three Observed Failure Modes*

Three types of failure modes, depending on the difference between the fiber and matrix strength of the material system, were observed in the  $[0/\pm\theta/90]_S$  SL, single lap, and SNO joints. Figure 14 illustrates these three failure modes. As defined in Heslehurst and Hart-Smith (2002) [49], adherend fracture was a dominant fiber fracture whereas cohesive fracture was a matrix fracture either by peel or shear stresses. The third failure mode, interface failure, was a proposed failure mode based on the physical state of observed failure and was characterized by fiber failure initiating from the overlap joint length.

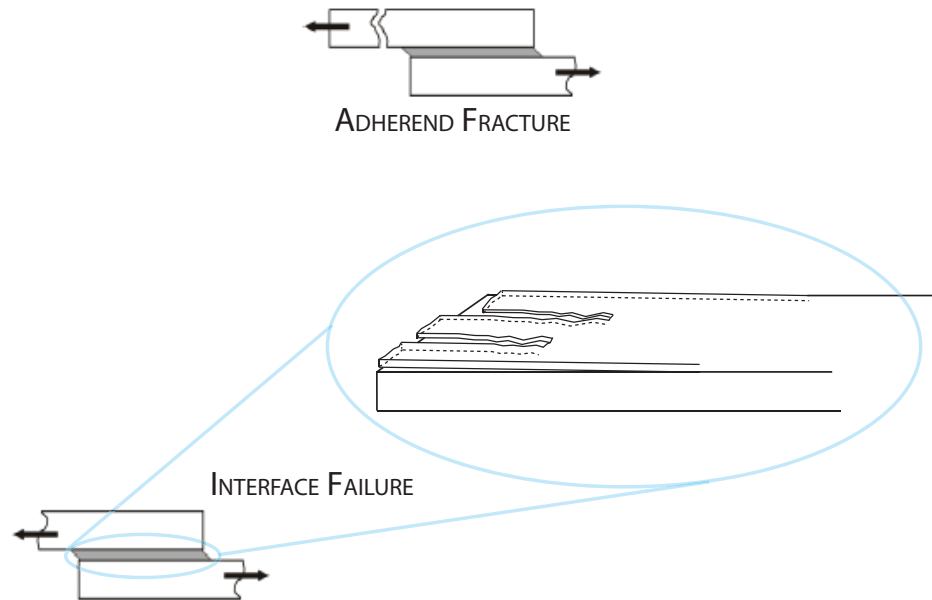
**Table 2:** Material properties for graphite/epoxy (Hexcel IM7/8551-7)

$E_{11}$	$E_{22}$	Ply Thickness	$G_{12} = G_{13}$	$\nu_{12} = \nu_{13}$
141.2 GPa	7.2 GPa	0.16 mm	3.9 GPa	0.30

*ASTM D 3039-0012 for the tensile properties*

*ASTM D 3518-9413 (reapproved 2001) for the shear properties*

### FIBER-DOMINATED FAILURE MODES :



### MATRIX-DOMINATED FAILURE MODE :

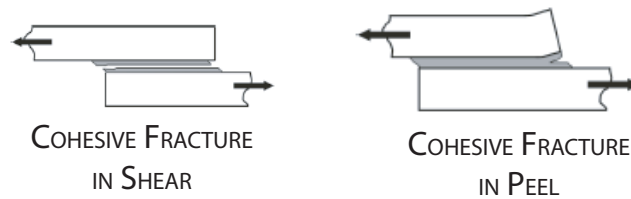


**Figure 14:** Three observed failure modes in straight laminates, single lap and single nested overlap joints

*Adherend fracture and cohesive fracture sketch taken from Heslehurst and Hart-Smith [49]*

## 2.2 *Three Categorized Failure Types*

A predominant failure type was observed for the  $[0/\pm\theta/90]_s$  SL, single lap, and SNO joints, ranging from the fiber-dominated failure type observed in the  $[0/\pm\theta/90]_s$  SL, to the mixed fiber- and matrix- dominated failure type observed in the  $[0/\pm\theta/90]_s$  SNO joints, and the matrix-dominated failure type observed in the  $[0/\pm\theta/90]_s$  single lap joints. These observed predominant failure types were categorized into dominant adherend failure, mixed type failure, and dominant cohesive failure, respectively.

Mixed type failure, predominantly observed in the  $[0/\pm\theta/90]_s$  SNO joints, was characterized by a mixture of adherend fracture or cohesive fracture with/without accompanying interface fiber failure within the overlap joint length or extending into the adherend adjacent to the overlap length. This mixed type behavior was observed to be more sensitive to loading conditions, exhibiting a range of failure modes (either adherend fracture or cohesive fracture with/without interface failure) under monotonic, high cyclic, or low cyclic loading. In contrast, the adherend fracture and cohesive fracture exhibited predominantly in the  $[0/\pm\theta/90]_s$  SL and the  $[0/\pm\theta/90]_s$  single lap joints, respectively, remained the same under monotonic or cyclic loading. The terms “dominant” and “non-dominant” will be used in the categorized failure types to differentiate between this sensitivity to loading. The adherend fracture and cohesive fracture observed predominantly in the  $[0/\pm\theta/90]_s$  SL and the  $[0/\pm\theta/90]_s$  single lap joints will be referred to as dominant adherend failure and dominant cohesive failure, respectively; the adherend fracture and cohesive fracture observed predominantly in the  $[0/\pm\theta/90]_s$  SNO joints will be referred to as non-dominant adherend failure and non-dominant cohesive failure, respectively. The three categorized failure types are illustrated in Figure 15.

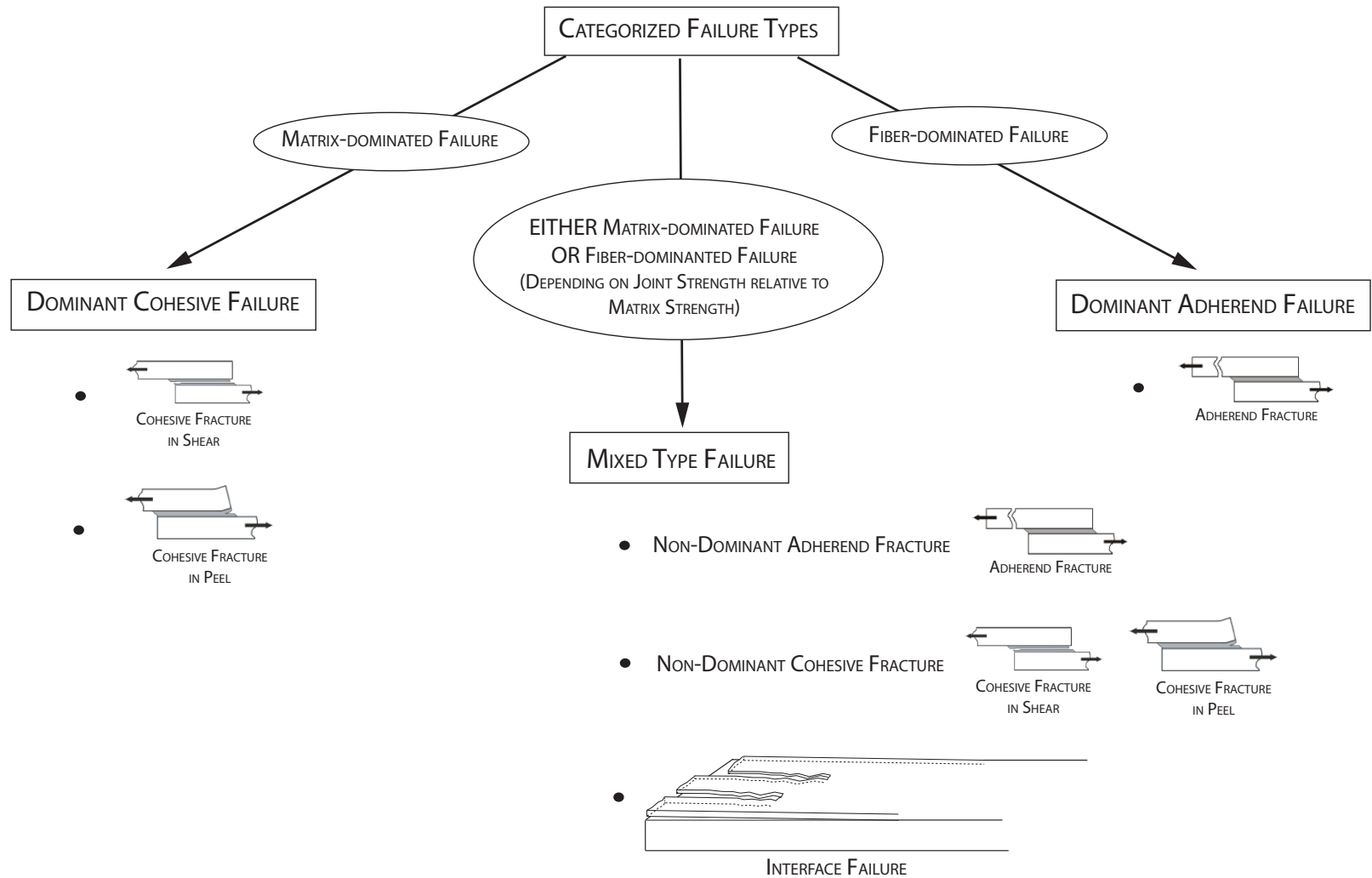


**Figure 15:** Three categorized failure types observed in straight laminates, single lap and single nested overlap joints  
*Adherend fracture and cohesive fracture sketch taken from Heslehurst and Hart-Smith [49]*

### **2.2.1 Dominant Cohesive Failure**

When the matrix strength is significantly lower than the shear and peel stresses at the onset of joint failure, dominant cohesive fracture occurs. The overlap length either shears or peels off cleanly along the joint interface, indicating that the overlap region is the weakest part of the joint. The occurrence of this mode in this study was largely dependent on the strength of the matrix system since the joints were co-cured without any additional layer of adhesive. This mode was observed predominantly in the IM7/8551-7  $[0/\pm\theta/90]_s$  single lap joints.

### **2.2.2 Dominant Adherend Failure**

When the matrix strength is significantly higher than the shear and peel stresses at the onset of joint failure, dominant adherend fracture occurs. Loading is “perfectly” transferred across the joint through the matrix in the overlap length onto the fibers and the fibers were loaded till ultimate fracture. This mode was observed predominantly in the IM7/8551-7  $[0/\pm\theta/90]_s$  SL.

### **2.2.3 Mixed Type Failure**

When the matrix strength is similar to the shear and peel stresses at the onset of joint failure, the exhibited failure type becomes more sensitive to loading conditions. This mixed type behavior is characterized by interface fiber failure, non-dominant cohesive fracture and non-dominant adherend fracture. When non-dominant adherend fracture is observed, there is an increase in joint strength as the weakest part of the joint shifts from the overlap length to the adherends immediately adjacent to the overlap length. However, when non-dominant cohesive fracture is observed, the increase in joint strength is ambiguous as the weakest part of the joint remains within the overlap length. The addition of interface failure along with non-dominant cohesive fracture typically indicates some improvement in joint strength, as part of the loading is transferred across the joint through the interfaced layers in the overlap length. This mode was observed predominantly in the IM7/8551-7  $[0/\pm\theta/90]_s$  SNO joints.

## 2.3 *Quasi-static Failure Type Comparison for $[0]_8$ and $[0/\pm\theta/90]_s$ Family of Joints*

Figures 16, 17, and 18 show the quasi-static failure modes for the  $[0]_8$  and  $[0/\pm\theta/90]_s$  SL, single lap, and SNO joints, respectively. The predominant failure features across the SL, single lap, and SNO joints were compared but the initiators leading to ultimate failure could not be ascertained from these figures. In particular, free-Edge Delamination (ED) in the  $90^\circ/90^\circ$  interface was observed for the  $[0/\pm\theta/90]_s$  SL, especially the the  $[0/\pm 45/90]_s$  lay-up. Some amount of ED in the  $90^\circ/90^\circ$  interface initiating from the fractured location was also observed for some of the failed  $[0/\pm 45/90]_s$  SNO joints.

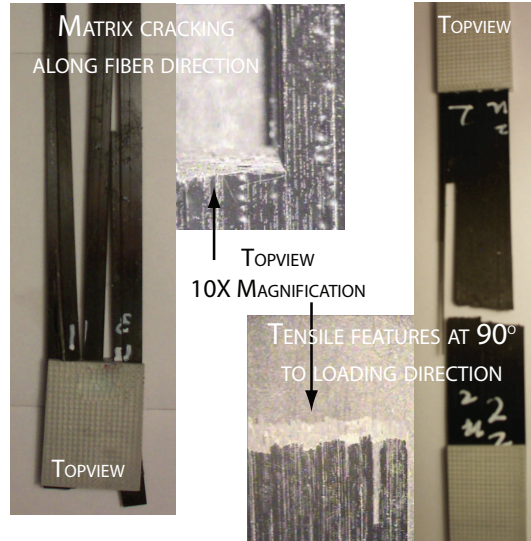
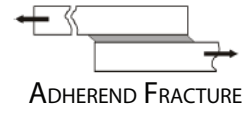
### 2.3.1 Straight Laminates

All the SL failed under dominant adherend failure. For the  $[0]_8$  SL, matrix cracking along the fiber direction was observed all through through the thickness (Figure 16a). Apart from the fiber fracture at the fractured location, a significant amount of ED in the  $90^\circ/90^\circ$  interface initiating from the fractured location was also observed in the  $[0/\pm\theta/90]_s$  SL. Fiber fracture at the fractured location included tensile features along the  $0^\circ$  and  $90^\circ$  fibers and shearing features along the  $\theta^\circ$  fibers (Figure 16b). Among the  $[0/\pm\theta/90]_s$  SL family, ED in the  $90^\circ/90^\circ$  interface was particularly prominent in the  $[0/\pm 45/90]_s$  SL.

### 2.3.2 Single Lap Joints

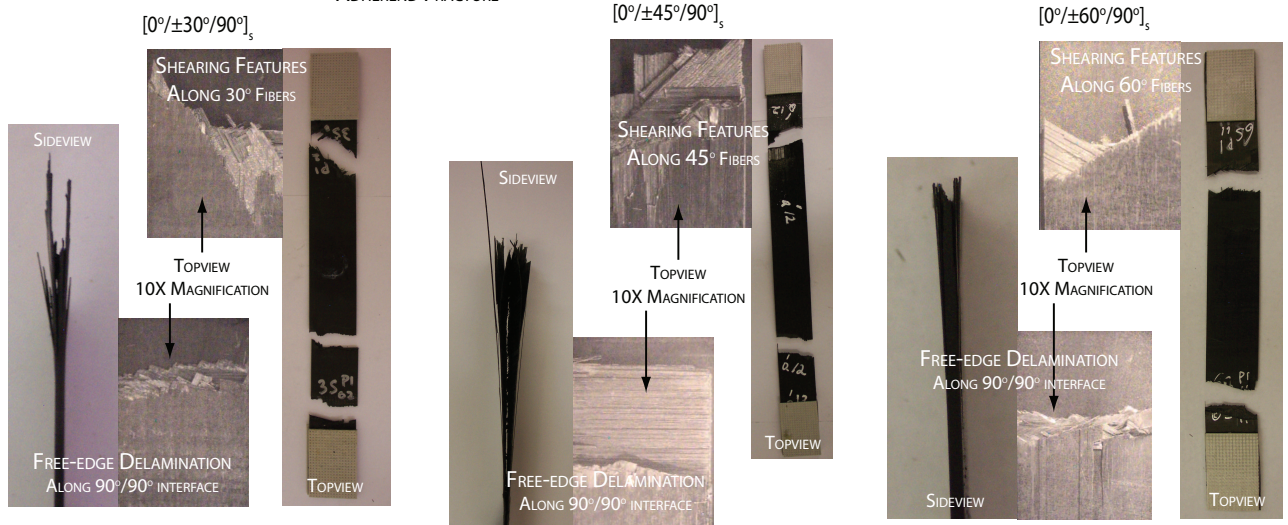
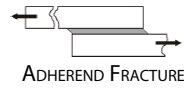
The  $[0]_8$  single lap joints failed under mixed type failure, exhibiting non-dominant cohesive fracture with significant amount of interface failure and fiber splitting within the overlap length and along the adherends of the joint, respectively (Figure 17a). The  $[0/\pm\theta/90]_s$  family of single lap joints failed predominantly under dominant cohesive failure, exhibiting cohesive fracture either in shearing or peeling (Figure 17b). Although the mechanism is rather different for each, a distinction has not been made in the results because of the possible influence of manufacturing defects. Apart from the cohesive fracture, no other significant failure types were observed in the adherends. For a minority of the tested  $[0/\pm 45/90]_s$  single lap joints (2 out of 13), adherend fracture was also observed. Unlike the  $[0/\pm\theta/90]_s$  SL, ED in the  $90^\circ/90^\circ$  interface was not observed in the adherends or within

CATEGORIZED FAILURE TYPE:  
DOMINANT ADHEREND FAILURE



(a) IM7/8551-7  $[0]_s$  straight laminates

CATEGORIZED FAILURE TYPE:  
DOMINANT ADHEREND FAILURE



(b) IM7/8551-7  $[0/\pm\theta/90]_s$  straight laminates

**Figure 16:** Straight laminates: Quasi-static failure modes for IM7/8551-7  $[0]_s$  and  $[0/\pm\theta/90]_s$

*Adherend fracture sketch taken from Heslehurst and Hart-Smith [49]*

the overlap length.

### 2.3.3 Single Nested Overlap Joints

The  $[0]_8$  SNO joints failed under mixed type failure, exhibiting non-dominant cohesive fracture with significant interface failure (Figure 18a). All the  $[0/\pm\theta/90]_s$  SNO joints failed under non-dominant adherend failure as compared to the dominant cohesive failure observed in the  $[0/\pm\theta/90]_s$  single lap joints. Similar to the  $[0/\pm\theta/90]_s$  SL, fiber fracture at the fractured location included tensile features along the  $0^\circ$  and  $90^\circ$  fibers and shearing features along the  $\theta^\circ$  fibers (Figure 18b). Some amount of ED in the  $90^\circ/90^\circ$  interface initiating from the fractured location was observed for some of the failed  $[0/\pm45/90]_s$  specimens. However, unlike the SL, the delamination did not extend across the entire width of the specimen and was observed more as delamination along the sides of the adherends. No additional failure types or ED in the  $90^\circ/90^\circ$  interface were observed in the adherends or overlap length of  $[0/\pm30/90]_s$  and  $[0/\pm60/90]_s$  SNO joints due to the limited number of specimens tested.

## 2.4 *Quasi-static Strength Comparison for the $[0]_8$ and $[0/\pm\theta/90]_s$ Family of Joints*

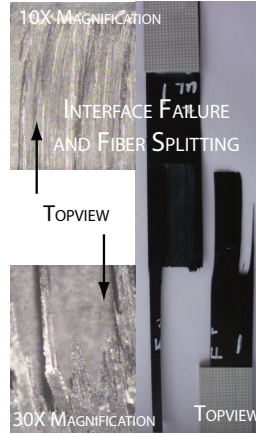
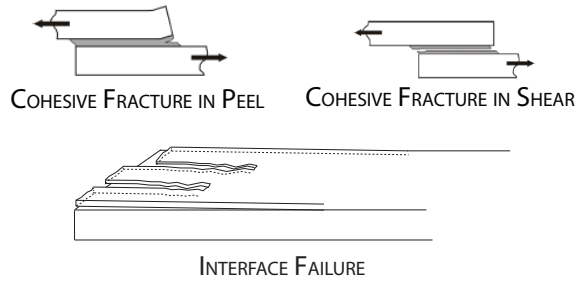
A minimum of five specimens for each stacking sequence were tested to ultimate failure. The Average Ultimate Tensile Stress (UTS), the Maximum, the Minimum, the Standard Deviation and the Coefficient of Variation (CV) for the SL, single lap and SNO joints of  $[0]_8$  and  $[0/\pm\theta/90]_s$  lay-up are provided in Appendix B. The UTS values for  $[0]_8$  and  $[0/\pm\theta/90]_s$  SL, single lap, and SNO joints are provided in Table 3. A graphical representation of the UTS values is provided in Figure 19.

Two static strength indicators, namely the stacking sequence static effectiveness factor and the joint static effectiveness factor, were used to characterize the static behavior of the  $[0]_8$  and  $[0/\pm\theta/90]_s$  SL, single lap and SNO joints. Strength indicators were used to compare and assess these joints as part of the research objective to conduct a systematic investigation of the quasi-static and fatigue behavior of the earlier proposed SNO joint. Similarly, ultimate fracture was defined as the desired level of strength loss.



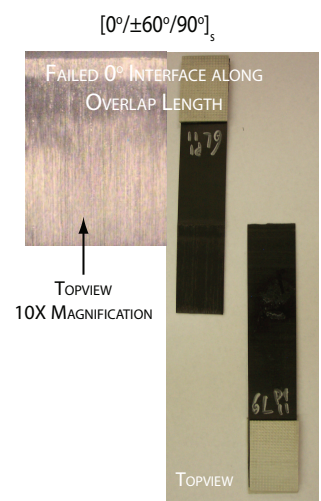
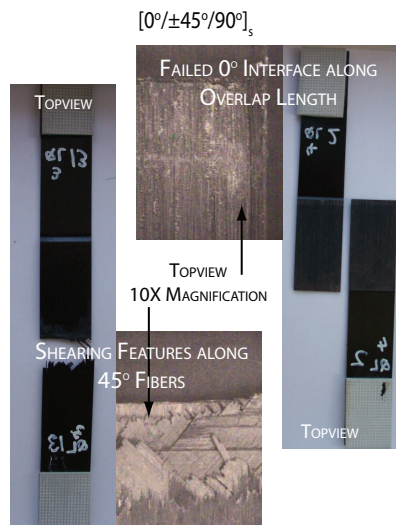
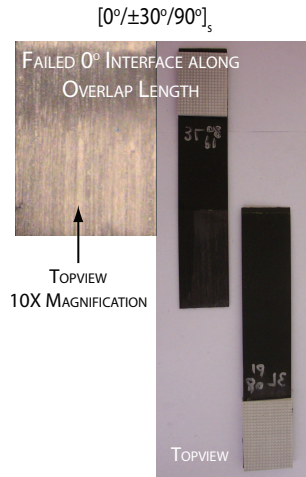
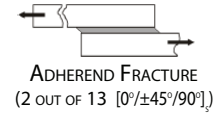
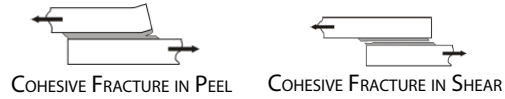
CATEGORIZED FAILURE TYPE:

NON-DOMINANT COHESIVE FAILURE AND INTERFACE FAILURE



(a) IM7/8551-7  $[0]_s$  single lap joints

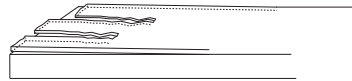
CATEGORIZED FAILURE TYPE:  
DOMINANT COHESIVE FAILURE



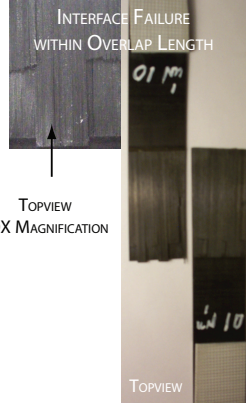
(b) IM7/8551-7  $[0/\pm\theta/90]_s$  single lap joints

**Figure 17:** Single lap joints: Quasi-static failure modes for IM7/8551-7  $[0]_s$  and  $[0/\pm\theta/90]_s$   
*Cohesive fracture sketch taken from Heslehurst and Hart-Smith [49]*

CATEGORIZED FAILURE TYPE:  
NON-DOMINANT COHESIVE FAILURE AND INTERFACE FAILURE

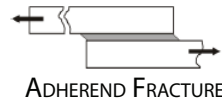


INTERFACE FAILURE



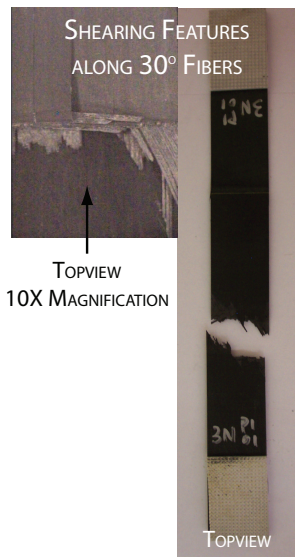
(a) IM7/8551-7  $[0]_8$  single nested overlap joints

CATEGORIZED FAILURE TYPE:  
NON-DOMINANT ADHEREND FAILURE

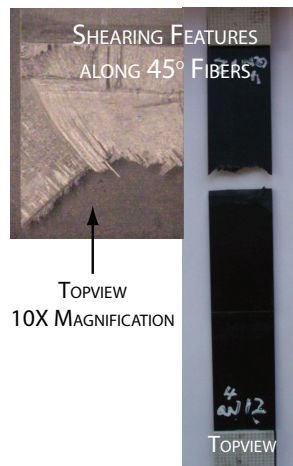


ADHEREND FRACTURE

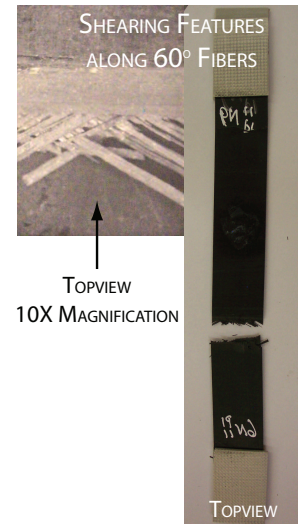
$[0^\circ/\pm 30^\circ/90^\circ]_s$



$[0^\circ/\pm 45^\circ/90^\circ]_s$



$[0^\circ/\pm 60^\circ/90^\circ]_s$



(b) IM7/8551-7  $[0/\pm\theta/90]_s$  single nested overlap joints

**Figure 18:** Single nested overlap joints: Quasi-static failure modes for IM7/8551-7  $[0]_8$  and  $[0/\pm\theta/90]_s$

*Adherend fracture and cohesive fracture sketch taken from Heslehurst and Hart-Smith [49]*

**Table 3:** Summary of UTS for IM7/8551-7  $[0]_8$  and  $[0/\pm\theta/90]_s$  with UTS of  $[0/\pm\theta/90]_s$  as a percentage of  $[0]_8$

	$[0]_8$	$[0/\pm 30/90]_s$	$[0/\pm 45/90]_s$	$[0/\pm 60/90]_s$
<b>SL</b>	2108.07	805.35	718.32	698.05
<b>Single lap joints</b>	770.42	549.17	628.33	560.29
<b>SNO joints</b>	1151.72	605.70	650.95	629.21

*UTS values are in MPa.*

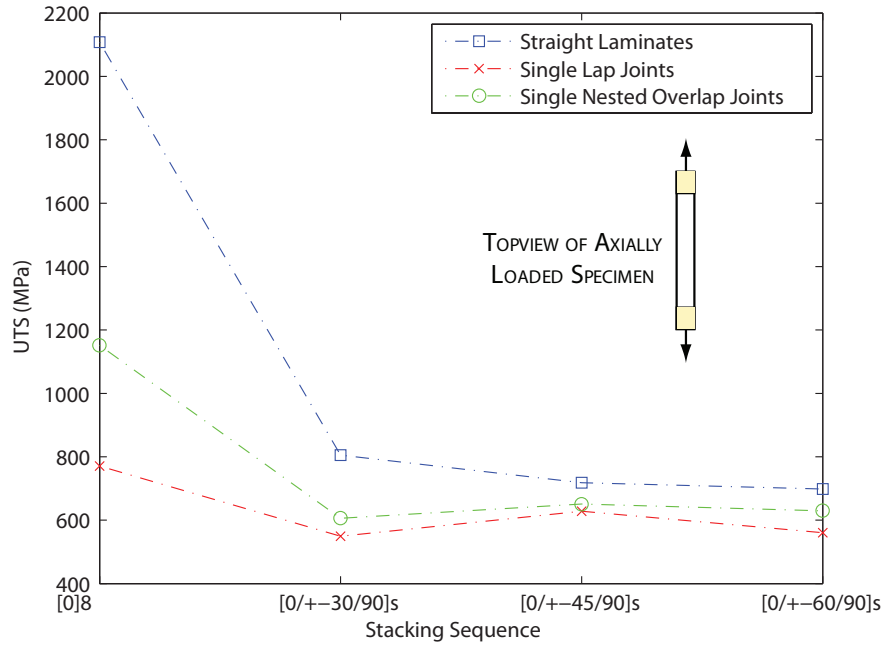


**Figure 19:** UTS values for  $[0]_8$ ,  $[0/\pm 30/90]_s$ ,  $[0/\pm 45/90]_s$  and  $[0/\pm 60/90]_s$  straight laminates, single lap and single nested overlap joints

These indicators represent two different ways of quantifying the percentage of load carrying fibers and therefore, the amount of fiber-dominated failure. The stacking sequence effectiveness factor differentiates between fiber-dominated and non-fiber-dominated fracture. In fiber-dominated adherend fracture, the stacking sequence effectiveness factor represents a proportion of fibers aligned with the loading direction. In matrix-dominated and mixed type failure, such as the comparison of single lap and SNO joints, both the stacking sequence and the joint effectiveness factors measure a level of fiber contribution, which increases both the quasi-static and fatigue strength of the joint.

While not immediately obvious from Figure 19, the mean UTS values across the  $[0/\pm$

**Table 4:** p-values (1-way ANOVA): To test for significant differences in mean UTS values between  $[0/\pm 30/90]_s$ ,  $[0/\pm 45/90]_s$  and  $[0/\pm 60/90]_s$

Mean UTS values for $[0/\pm \theta/90]_s$	
SL	0.0365
Single lap joint	0.000025
SNO joint	0.000015

$\theta/90]_s$  family for the three configurations were significantly different based on a 1-way analysis of variance (ANOVA). The p-values for the null hypothesis that the mean UTS across the  $[0/\pm \theta/90]_s$  family for each of the three configurations are indistinguishable are summarized in Table 4. Since the p-values were smaller than the critical p-value of 0.05, there was sufficient evidence to reject the null hypothesis. Although the mean UTS for each configuration and each  $[0/\pm \theta/90]_s$  family lay-up was different, there was no conclusive evidence that the  $[0/\pm 45/90]_s$  will always yield a higher UTS value than the  $[0/\pm 30/90]_s$  or  $[0/\pm 60/90]_s$ , as observed in the trend in Table 3.

#### 2.4.1 Static Strength Indicator I: Stacking Sequence Static Effectiveness Factor

The first static strength indicator  $SS_I$ , in Eq. (1), compares the static effectiveness of the  $[0/\pm \theta/90]_s$  stacking sequence relative to the  $[0]_8$  in carrying uniaxial loading. The computed  $SS_I$  for the  $[0/\pm 30/90]_s$ ,  $[0/\pm 45/90]_s$  and  $[0/\pm 60/90]_s$  SL, single lap, and SNO joints are provided in Table 5.

$$SS_I = \frac{UTS^{[0/\pm \theta/90]_s}}{UTS^{[0]_8}} \times 100\% \quad (1)$$

where:

$SS_I$  denotes stacking sequence static effectiveness factor; and

$UTS^{[0/\pm \theta/90]_s}$  denotes ultimate tensile strength for the  $[0/\pm \theta/90]_s$  SL, single lap or SNO joint; and

$UTS^{[0]_8}$  denotes ultimate tensile strength of the  $[0]_8$  SL, single lap or SNO joint.

**Table 5:** Static strength indicator I for IM7/8551-7  $[0/\pm\theta/90]_s$ 

<b>Stacking Sequence Static Effectiveness Factor: <math>SS_I</math></b>			
	$[0/\pm 30/90]_s$	$[0/\pm 45/90]_s$	$[0/\pm 60/90]_s$
<b>SL</b>	38	34	33
<b>Single lap joints</b>	71	82	73
<b>SNO joints</b>	53	57	55

*Static strength improvement values are in %.*

A sharp drop in UTS was observed in the SL between the  $[0]_8$  and  $[0/\pm\theta/90]_s$  (Figure 19), with the stacking sequence static effectiveness factor for  $[0/\pm 30/90]_s$ ,  $[0/\pm 45/90]_s$ , and  $[0/\pm 60/90]_s$  at 38%, 34%, and 33% of the  $[0]_8$  UTS (Table 5), respectively. The  $[0/\pm\theta/90]_s$  SL family UTS showed a steady decrease within 30-40% of the  $[0]_8$  UTS as  $\theta$  increased to reflect the percentage reduction in load carrying fibers along the axially loaded direction. As  $\theta$  varied for SL, a minimum of 25% of the  $[0]_8$  UTS, which was the percentage of  $0^\circ$  fibers, should be expected. For the single lap and SNO joints, a less significant drop in UTS strength between the  $[0/\pm\theta/90]_s$  and  $[0]_8$  was observed. The stacking sequence static effectiveness factor for  $[0/\pm 30/90]_s$ ,  $[0/\pm 45/90]_s$ , and  $[0/\pm 60/90]_s$  single lap joints were at 71%, 82%, and 73% of the  $[0]_8$  UTS (Table 5), respectively while that for the SNO joints were at 53%, 57%, and 55% of the  $[0]_8$  UTS (Table 5), respectively.

The dominant adherend failure observed in SL accounted for the low stacking sequence static effectiveness in  $[0/\pm\theta/90]_s$  SL as compared to  $[0]_8$ . However, as the dominant failure mechanism shifted from a fiber-dominated failure type in SL to a more matrix-dominated failure type in single lap and SNO joints, the stacking sequence static effectiveness in the  $[0/\pm\theta/90]_s$  family increased significantly. In the matrix-dominated failure observed in single lap joints, the stacking sequence static effectiveness factor was the highest. In the SNO joints, where a mix of fiber- and matrix- dominated failure, the non-dominant adherend failure was observed, the stacking sequence static effectiveness factor was approximately 50%, halfway between the SL and the single lap joints.

A steadily decreasing mean UTS with increasing  $\theta$  in the  $[0/\pm\theta/90]_s$  family should only be inferred for fiber-dominated failure type, such as  $[0/\pm\theta/90]_s$  SL, whereas a projected

**Table 6:** Static strength indicator II for IM7/8551-7  $[0]_8$  and  $[0/\pm\theta/90]_s$ 

<b>Joint Static Effectiveness Factor: <math>SS_{II}</math></b>				
	$[0]_8$	$[0/\pm 30/90]_s$	$[0/\pm 45/90]_s$	$[0/\pm 60/90]_s$
<b>Single lap joints</b>	37	68	87	80
<b>SNO joints</b>	55	75	91	90

*Static strength improvement values are in %.*

range of mean UTS could be inferred for matrix-dominated and mixed type failure, such as  $[0/\pm\theta/90]_s$  family of single lap and SNO joints.

#### 2.4.2 Static Strength Indicator II: Joint Static Effectiveness Factor

The second static strength indicator  $SS_{II}$ , in Eq. (2), compares the static effectiveness of the single lap or SNO joint relative to the SL or “perfect joint”. The computed  $SS_{II}$  for the  $[0]_8$ ,  $[0/\pm 30/90]_s$ ,  $[0/\pm 45/90]_s$  and  $[0/\pm 60/90]_s$  SL, single lap and SNO joints are provided in Table 6.

$$SS_{II} = \frac{UTS^{JOINT}}{UTS^{PERFECT}} \times 100\% \quad (2)$$

where:

$SS_{II}$  denotes joint static effectiveness factor; and

$UTS^{JOINT}$  denotes ultimate tensile strength for the single lap or SNO joint; and

$UTS^{PERFECT}$  denotes ultimate tensile strength of the SL.

The SNO joints showed an increase in joint static effectiveness over the single lap joints for both the  $[0]_8$  and  $[0/\pm\theta/90]_s$  family, due to an increased in fiber-dominated failure. Although both the  $[0]_8$  single lap and  $[0]_8$  SNO joints failed under non-dominant cohesive failure with interface failure, the more significant interface failure observed in  $[0]_8$  SNO joints resulted in an increase of approximately 18% in joint static effectiveness (Table 6: Single lap joints 37% and SNO joints 55%). The increase in fiber-dominated failure from the dominant cohesive failure observed in the  $[0/\pm\theta/90]_s$  single lap joints to the non-dominant adherend

failure observed in the  $[0/\pm\theta/90]_s$  SNO joints accounted for an increase of approximately 5-10% in joint static effectiveness (Table 6). The more significant improvement in joint static effectiveness factor in the  $[0]_8$  SNO joints as compared to the  $[0/\pm\theta/90]_s$  SNO joints could be attributed to an increase in the amount of load carrying fibers in the  $[0]_8$ .

## ***2.5 Statistical Inference of Single Panel vs. Multiple Panels***

The results presented in this study were based on specimens taken from multiple panels [98]. Table 7 summarizes a comparison for the  $[0/\pm 45/90]_s$  SL, single lap, and SNO joints made against the results from Cao and Dancila [13, 12], which were taken from a single panel. The multiple panels result was a representation of a mean of four specimens from each tested under monotonic loading while the single panel results was for five specimens from one panel.

For the SL and the single lap joints, there was only a 5% variation in mean UTS for the multiple panels results due to the consistency observed in the failure mode. A higher 13% variation was noted in the SNO joints as a result of the added complexity due to multiple overlapped interfaces and manufacturing variability.

With respect to the UTS of a “perfect” joint, Cao and Dancila [13, 12] concluded that single lap and SNO joints retain 76% and 97% of the UTS of a perfect joint, respectively. Taking into consideration the variation in manufacturing and failure types (such as delamination, matrix cracking, and fiber fracture) across multiple panels, the corresponding results from the current investigation shows 87% and 91% of the UTS of a perfect joint for single lap joints and SNO joints, respectively. Based on a 1-way ANOVA, there was no significant difference in the mean UTS of test specimens from single panel and from multiple panels for IM7/8551-7  $[0/\pm 45/90]_s$  SL, single lap and SNO joints [95].

## ***2.6 Chapter Summary***

Three failure types were observed for the  $[0/\pm\theta/90]_s$  family, ranging from fiber-dominated adherend fracture in the SL, to matrix-dominated cohesive fracture in the single lap joints, to a mix of both fiber-dominated and matrix-dominated fracture in the SNO joints. The

**Table 7:** Comparison of Single Panel (Cao and Dancila [13, 12]) and Multiple Panels Monotonic Loading Results

	<b>Straight Laminate</b>		<b>Single Lap Joint</b>		<b>SNO Joint</b>	
	Multiple	Single	Multiple	Single	Multiple	Single
<b>Average (MPa)</b>	718.32	762.50	628.33	582.60	650.95	743.00
<b>Standard Deviation (MPa)</b>	32.489	37.063	39.421	30.022	84.816	51.976
<b>Coefficient of Variation (%)</b>	4.52	4.85	6.27	5.15	13.03	7.00
<b>Strength w.r.t. Perfect Joint (%)</b>		-	87.4	76.4	90.6	97.4

nesting concept resulted in an increase in fiber-dominated behavior for the SNO joints compared to the single lap joints, which led to a more effective joint, illustrated by the joint static effectiveness factor. Both the stacking sequence static effectiveness factor and the joint static effectiveness factor are a measure of level of fiber activity in the failure mode. The former also approximates the proportion of fibers aligned along the loading direction. The fracture state illustrated in the failure mode figures only captured the predominant failure features under monotonic loading, but the initiators leading to ultimate fracture could not be ascertained from these figures. In comparing the UTS, the multiple panel results showed negligible difference of 1% in standard deviation for single lap joints and a 6% difference in standard deviation for the SNO joints. The former was attributed to the consistency of the observed dominant cohesive fracture, while the increase in scatter for the latter was attributed to the increase in complexity for the fiber-dominated non-dominant adherend fracture. Based on a 1-way ANOVA, there was no significant difference in the mean UTS of test specimens from single panel and from multiple panels under monotonic loading.



## CHAPTER III

### FATIGUE STRENGTH CHARACTERIZATION AND FAILURE MODES OF $[0/\pm\theta/90]_S$ FAMILY OF COMPOSITE JOINTS

Constant amplitude tension-tension S-N curves at a frequency of 5 Hz and a stress ratio (R) of 0.1 were generated for the IM7/8551-7  $[0/\pm\theta/90]_S$  family, including  $[0/\pm 30/90]_S$ ,  $[0/\pm 45/90]_S$ , and  $[0/\pm 60/90]_S$ . The S-N curve for IM7/8551-7  $[0]_S$  was also studied for comparison. Fatigue run-out was defined at  $1 \times 10^6$  cycles. The fatigue strength characterization of the IM7/8551-7  $[0/\pm\theta/90]_S$  family were then assessed through three different, but not independent, indicators [95, 97, 98] to illustrate the improvement of the SNO joint in comparison to the single lap joint.

#### ***3.1 Power Fitted S-N Curves: Frequency = 5 Hz, R = 0.1 and Fatigue run-out = $1 \times 10^6$ cycles***

The constant amplitude tension-tension S-N curves were generated with a minimum of eight data points at a frequency of 5 Hz, a R of 0.1, and a fatigue run-out of  $1 \times 10^6$  cycles. The Maximum cyclic Load level ( $L_{max}$ ), the Maximum cyclic Stress level ( $S_{max}$ ), and the Number of cycles to Failure ( $N_f$ ) for each individual fatigued specimen are provided in Appendix D. Weighted non-linear least square based power curve fits and the coefficient of determination ( $r^2$ ) obtained from the Matlab curve fitting toolbox for the IM7/8551-7  $[0]_S$ ,  $[0/\pm 30/90]_S$ ,  $[0/\pm 45/90]_S$  and  $[0/\pm 60/90]_S$  SL, single lap, and SNO joints are given in Eqs. 3-6a, b, and c, respectively.

IM7/8551-7  $[0]_S$

$$SL : S_{max} = 1852.0 N_f^{-0.0230}, \quad r^2 = 0.9227 \quad (3a)$$

$$Lap : S_{max} = 975.3 N_f^{-0.09959}, \quad r^2 = 0.9768 \quad (3b)$$

$$SNO : S_{max} = 1498.0 N_f^{-0.1065}, \quad r^2 = 0.9908 \quad (3c)$$

IM7/8551-7  $[0/\pm 30/90]_s$

$$SL : S_{max} = 674.3 N_f^{-0.02983}, \quad r^2 = 0.8795 \quad (4a)$$

$$Lap : S_{max} = 568.8 N_f^{-0.09327}, \quad r^2 = 0.9368 \quad (4b)$$

$$SNO : S_{max} = 1393.0 N_f^{-0.1230}, \quad r^2 = 0.7023 \quad (4c)$$

IM7/8551-7  $[0/\pm 45/90]_s$

$$SL : S_{max} = 745.4 N_f^{-0.0280}, \quad r^2 = 0.3364 \quad (5a)$$

$$Lap : S_{max} = 719.7 N_f^{-0.1058}, \quad r^2 = 0.9775 \quad (5b)$$

$$SNO : S_{max} = 1057.0 N_f^{-0.1008}, \quad r^2 = 0.9773 \quad (5c)$$

IM7/8551-7  $[0/\pm 60/90]_s$

$$SL : S_{max} = 610.6 N_f^{-0.0275}, \quad r^2 = 0.3850 \quad (6a)$$

$$Lap : S_{max} = 1136.0 N_f^{-0.1540}, \quad r^2 = 0.9936 \quad (6b)$$

$$SNO : S_{max} = 1193.0 N_f^{-0.1191}, \quad r^2 = 0.9756 \quad (6c)$$

The S-N curve for the  $[0/\pm 45/90]_s$  SL, single lap, and SNO joints were generated with at least twenty four data points each in order to obtain a reliable S-N curve. Subsequent S-N curves for the  $[0/\pm 30/90]_s$  and  $[0/\pm 60/90]_s$  SL, single lap and SNO joints were generated with a minimum of eight data points. For the curve fitting methods used, there was no significant loss in the  $r^2$  of the fitted curve as long as the smaller set of data points were taken over a wide range of loading. The  $r^2$  for the  $[0/\pm 45/90]_s$  and  $[0/\pm 60/90]_s$  SL were particularly low because the fitted curve was forced to correctly account for the specimens that did not fracture. Although there was insufficient evidence to conclude that the mean UTS from single panel and from multiple panels under monotonic loading were different, a significant amount of scatter near the FL was observed under cyclic loading, indicating the extent of scatter under fatigue for the IM7/8551-7 material system.

### **3.2 *Fatigue Failure Type Comparison for the $[0]_8$ and $[0/\pm\theta/90]_s$ Family of Joints***

Figures 20, 21, and 22 show the fatigue failure modes for the  $[0]_8$  and  $[0/\pm\theta/90]_s$  SL, single lap, and SNO joints, respectively. As with the quasi-static failure types, predominant failure features across the SL, single lap, and SNO joints were compared but damage initiators and critical damage mechanisms could not be ascertained from these post fracture figures. ED in the  $90^\circ/90^\circ$  interface was also more prominent in  $[0/\pm 45/90]_s$  SL and some of the  $[0/\pm 45/90]_s$  SNO joints that failed under non-dominant adherend failure.

#### **3.2.1 Straight Laminates**

All the SL failed under dominant adherend failure. A significant amount of fiber splitting along the fiber direction was observed all through the thickness of the  $[0]_8$  SL, particularly at higher loading (Figure 20a). In the  $[0/\pm\theta/90]_s$  SL, similar failure type under monotonic loading was observed, including tensile features along the  $0^\circ$  and  $90^\circ$  fibers and shearing features along the  $\theta^\circ$  fibers at the fractured location (Figure 20b). More significant ED in the  $90^\circ/90^\circ$  interface was observed for  $[0/\pm 45/90]_s$  at lower loading than at higher loading. Some amount of ED in the  $90^\circ/90^\circ$  interface initiating from the fractured location was also observed for the  $[0/\pm 30/90]_s$  and  $[0/\pm 60/90]_s$  SL, but the minimal number of tested specimens limits the conclusion of a more predominant behavior at lower and higher loadings.

#### **3.2.2 Single Lap Joints**

The  $[0]_8$  single lap joints failed under mixed type failure, with non-dominant cohesive failure at lower loadings and increased interface failure at higher loadings (Figure 21a). All the  $[0/\pm\theta/90]_s$  single lap joints failed cleanly under dominant cohesive failure within the overlap length with no discernable differences under both high and low loadings (Figure 21b). ED in the  $90^\circ/90^\circ$  interface was not observed in the adherend or overlap length from post-mortem examination of the single lap specimens.

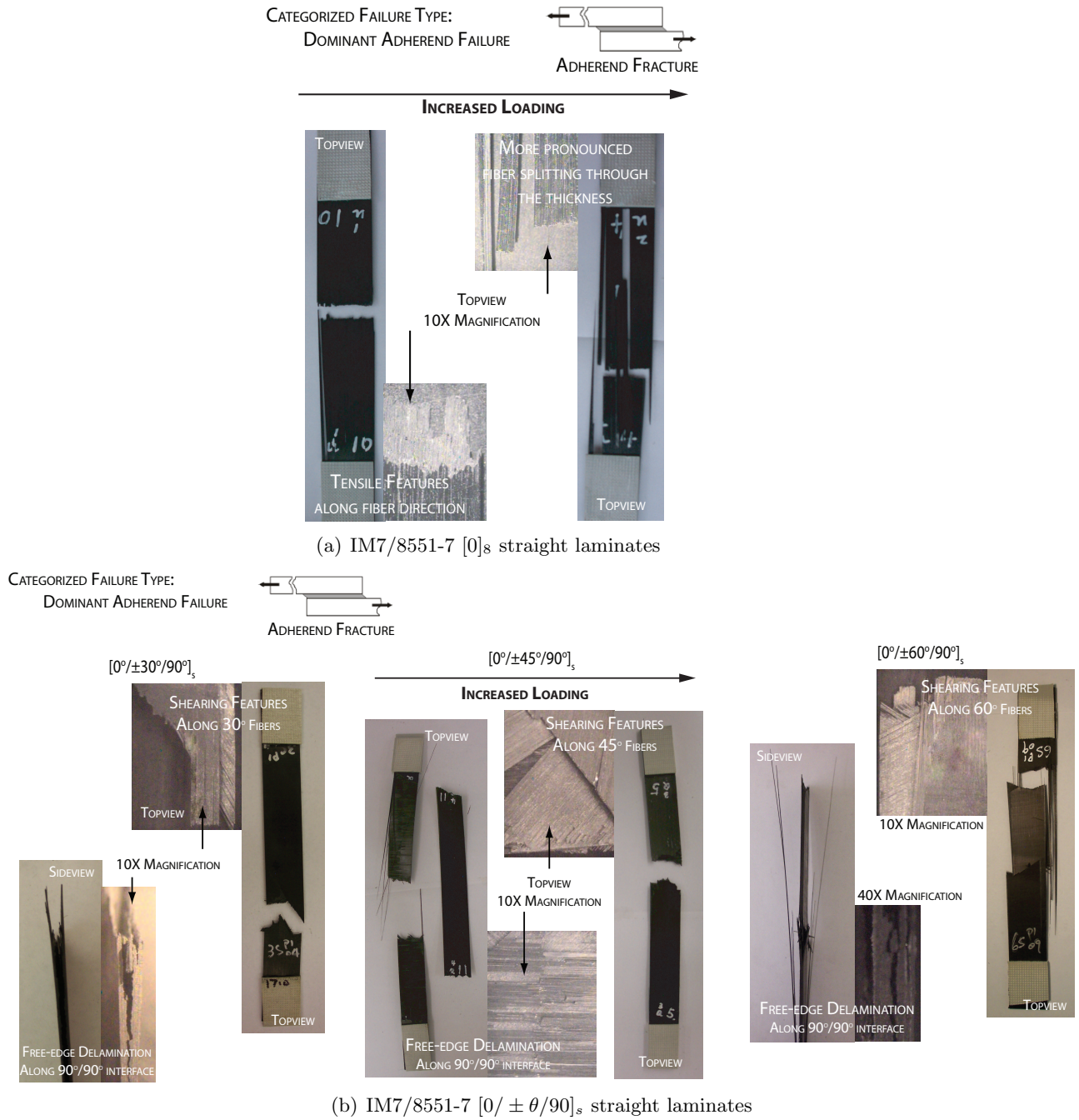
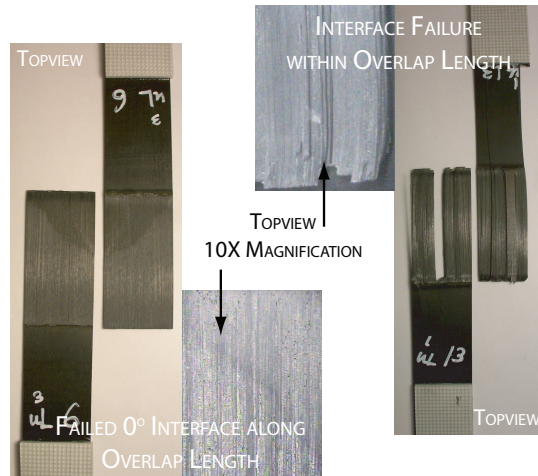
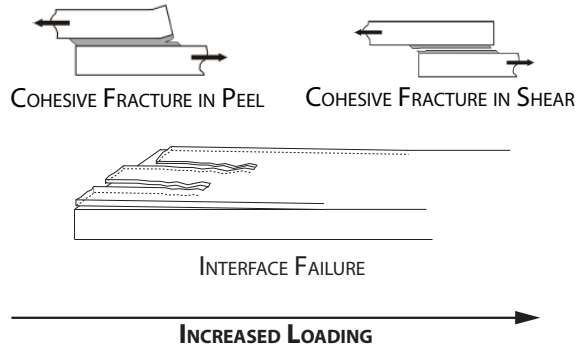


**Figure 20:** Straight laminates: Fatigue failure modes for IM7/8551-7  $[0]_s$  and  $[0/\pm\theta/90]_s$  (frequency = 5 Hz,  $R = 0.1$  and fatigue run-out =  $1 \times 10^6$  cycles)  
Adherend fracture sketch taken from Heslehurst and Hart-Smith [49]

# CATEGORIZED FAILURE TYPE:

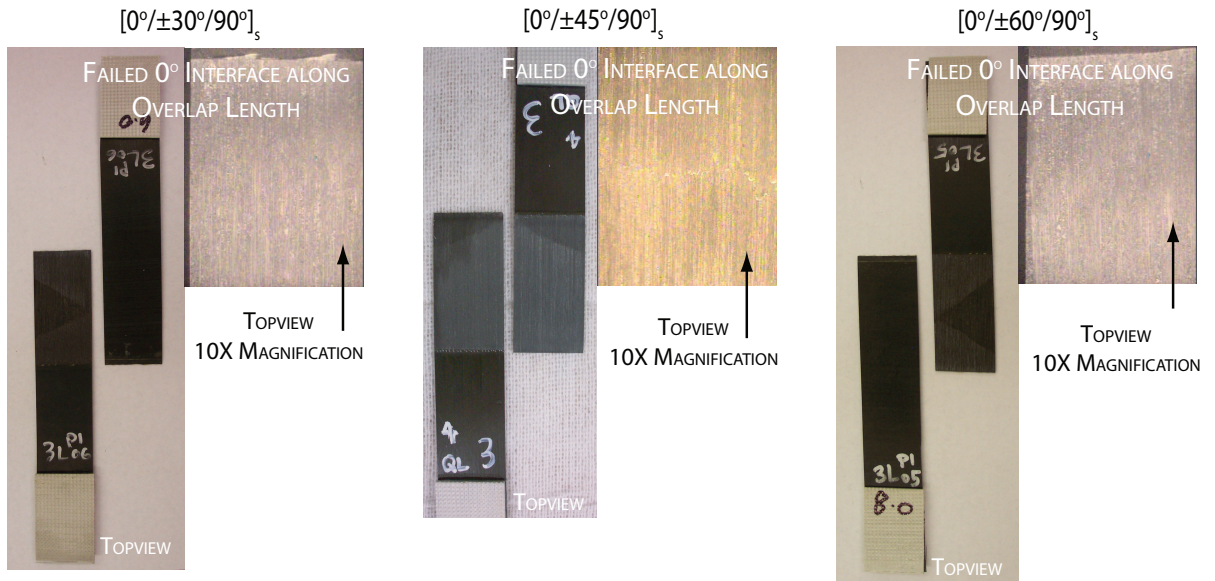
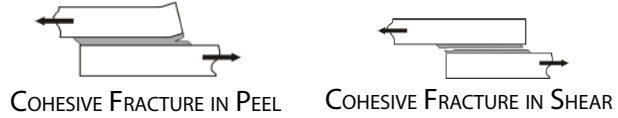
## NON-DOMINANT COHESIVE FAILURE AND INTERFACE FAILURE



(a) IM7/8551-7  $[0]_8$  Single lap joints

# CATEGORIZED FAILURE TYPE:

## DOMINANT COHESIVE FAILURE



(b) IM7/8551-7  $[0/\pm\theta/90]_s$  Single lap joints

**Figure 21:** Single lap joints: Fatigue failure modes for IM7/8551-7  $[0]_8$  and  $[0/\pm\theta/90]_s$  (frequency = 5 Hz, R = 0.1 and fatigue run out =  $1 \times 10^6$  cycles)  
*Cohesive fracture sketch taken from Heslehurst and Hart-Smith [49]*

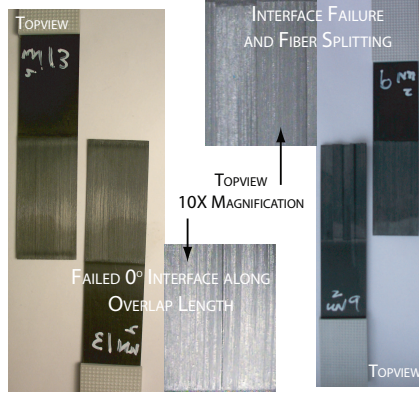
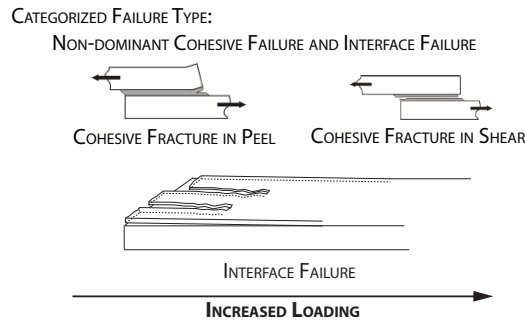
### 3.2.3 Single Nested Overlap Joints

The  $[0]_8$  SNO joints failed under mixed type failure with non-dominant cohesive failure and increasing amount of interface failure under increasing cyclic load (Figure 22a). The  $[0/\pm\theta/90]_s$  SNO joints failed predominantly under mixed type failure with non-dominant cohesive failure and interface failure. For the  $[0/\pm 45/90]_s$  SNO joints, this non-dominant cohesive failure with interface failure was observed mostly at lower loadings with the failure type shifting to non-dominant adherend failure at higher loadings. Similar to the SL, the minimal number of tested specimens for the  $[0/\pm 30/90]_s$  and  $[0/\pm 60/90]_s$  SNO joints limited discernable predominant behavior observed at lower and higher loadings. Some amount of ED in the  $90^\circ/90^\circ$  interface initiating from the fractured location was observed for some of the  $[0/\pm 45/90]_s$  SNO joints that failed under non-dominant adherend failure. Similar to the quasi-static case, this delamination did not extend across the entire width of the specimen and was observed as delamination along the sides of the adherends. However, no additional failure types or ED in the  $90^\circ/90^\circ$  interface were observed in the adherends or overlap length of  $[0/\pm 30/90]_s$  and  $[0/\pm 60/90]_s$  SNO joints due to a limited number of specimens tested.

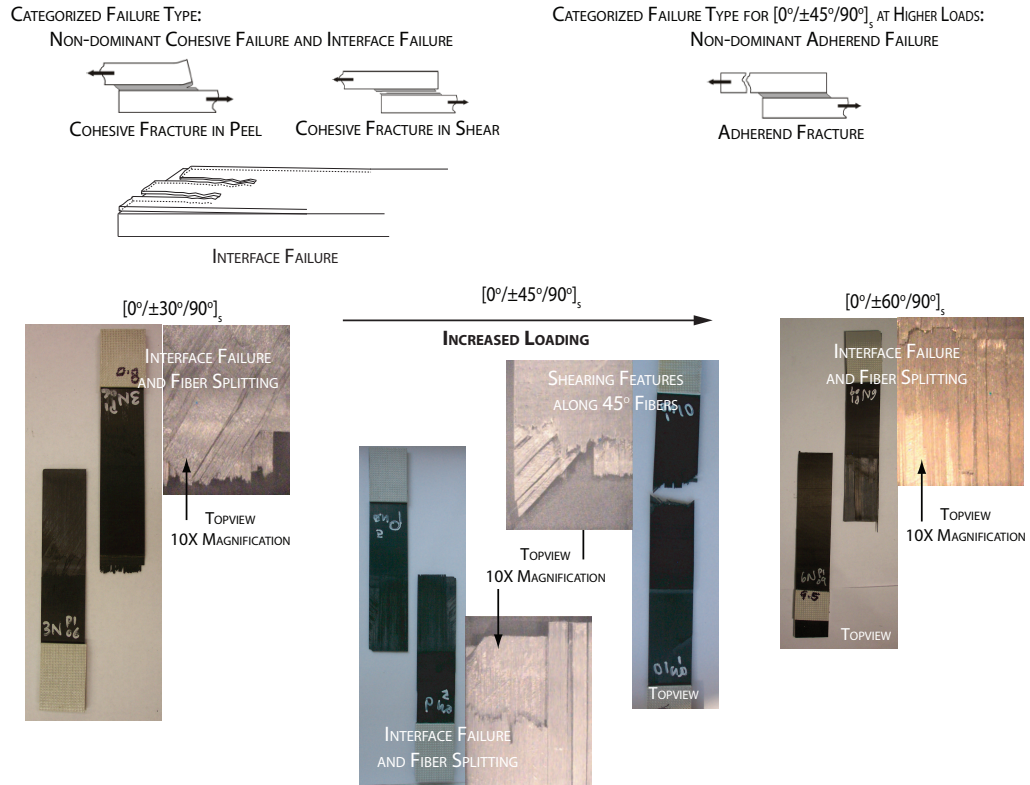
### 3.3 *Fatigue Strength Comparison for the $[0]_8$ and $[0/\pm\theta/90]_s$ Family of Joints*

Fatigue Limit (FL) is defined as the lowest stress level within fatigue run-out, where the SL, single lap, or SNO joint does not fracture. It is analogous to the endurance limit defined for metals. The S-N curve for IM7/8551-7 SL, single lap, and SNO joints with the  $[0]_8$ ,  $[0/\pm 30/90]_s$ ,  $[0/\pm 45/90]_s$ , and  $[0/\pm 60/90]_s$  lay-up, along with their power curve fits, are illustrated on a linear and a semi-logarithmic scale in Figures 23a, b, c and d, respectively. The FL is better illustrated on the linear scale S-N curves.

These S-N curves showed that for the same  $N_f$ , SL can withstand the highest maximum stress, followed by the SNO, and then the single lap joints. In the  $[0/\pm 30/90]_s$  and  $[0/\pm 60/90]_s$  (Figure 23b and d), the fitted S-N curve for SNO joints indicated improved stress endurance at low  $N_f$  compared to the SL. This was a curve fitting error due to a



(a) IM7/8551-7  $[0]_s$  Single nested overlap joints



(b) IM7/8551-7  $[0/\pm\theta/90]_s$  Single nested overlap joints

**Figure 22:** Single nested overlap joints: Fatigue failure modes for IM7/8551-7  $[0]_s$  and  $[0/\pm\theta/90]_s$  (frequency = 5 Hz, R = 0.1 and fatigue run-out =  $1 \times 10^6$  cycles)  
*Adherend fracture and cohesive fracture sketch taken from Heslehurst and Hart-Smith [49]*

**Table 8:** Summary of fatigue limit for IM7/8551-7  $[0]_8$  and  $[0/\pm\theta/90]_s$  with fatigue limit of  $[0/\pm\theta/90]_s$  as a percentage of  $[0]_8$

	$[0]_8$	$[0/\pm 30/90]_s$	$[0/\pm 45/90]_s$	$[0/\pm 60/90]_s$
<b>SL</b>	1300	450	475	420
<b>Single lap joints</b>	250	160	150	140
<b>SNO joints</b>	350	250	250	240

*Fatigue limit values are in MPa.*

smaller set of data points used.

The FL values estimated from the S-N curve fits for the  $[0]_8$  and  $[0/\pm\theta/90]_s$  are provided in Table 8, and a graphical representation of this FL trend is provided in Figure 24. The FL for the SL, representing the “perfect” joint, was the highest in all the stacking sequences tested, with a more distinct peak in the  $[0]_8$  SL as all the fibers were utilized for loading (Figure 24). Additionally, the FL of the SNO joint was also observed to be consistently higher than the FL of the single lap joint in all the stacking sequences, similar to the UTS trend. This was because both UTS and FL were characterization of strength based on failure modes.

### 3.3.1 Fatigue Strength Indicator I: Stacking Sequence Fatigue Effectiveness Factor

The first fatigue strength indicator  $FS_I$ , in Eq. (7), compares the fatigue effectiveness of the  $[0/\pm\theta/90]_s$  stacking sequence relative to the  $[0]_8$  in carrying uniaxial loading under cyclic loading. The computed  $FS_I$  for the  $[0/\pm 30/90]_s$ ,  $[0/\pm 45/90]_s$  and  $[0/\pm 60/90]_s$  SL, single lap, and SNO joints are provided in Table 9.

$$FS_I = \frac{FL^{[0/\pm\theta/90]_s}}{FL^{[0]_8}} \times 100\% \quad (7)$$

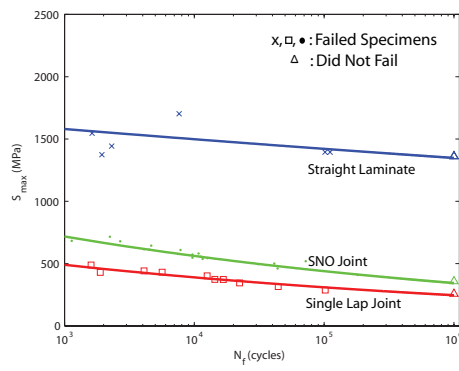
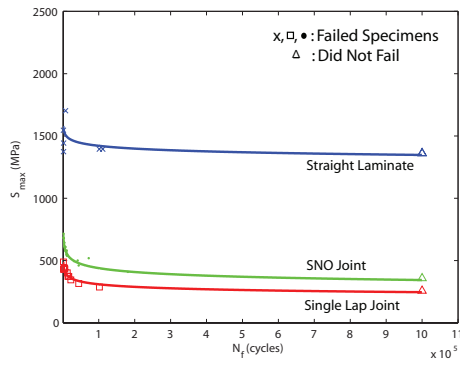
where:

$FS_I$  denotes stacking sequence static effectiveness factor; and

$FL^{[0/\pm\theta/90]_s}$  denotes fatigue limit for the  $[0/\pm\theta/90]_s$  SL, single lap or SNO joint; and

$FL^{[0]_8}$  denotes fatigue limit of the  $[0]_8$  SL, single lap or SNO joint.





#### Straight Laminate

$$S_{\max} \text{ (MPa)} = 1852.0 N_f^{-0.0230}$$

$$r^2 = 0.9227$$

#### SNO Joint

$$S_{\max} \text{ (MPa)} = 1498.0 N_f^{-0.1065}$$

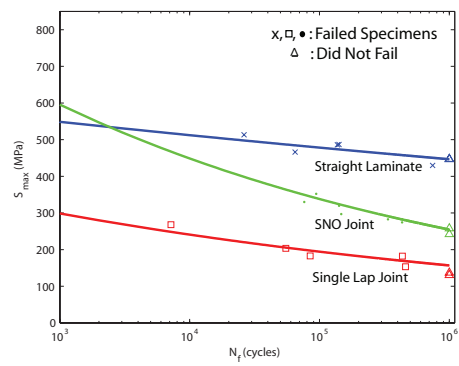
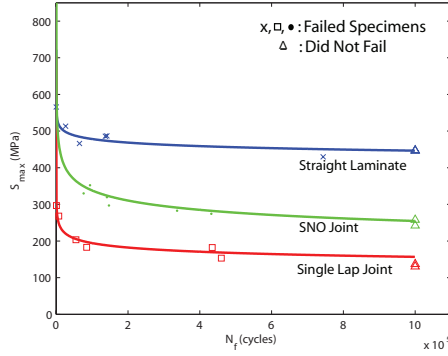
$$r^2 = 0.9908$$

#### Single Lap Joint

$$S_{\max} \text{ (MPa)} = 975.3 N_f^{-0.09959}$$

$$r^2 = 0.9768$$

(a)  $[0]_8$  SL, single lap and SNO joints



#### Straight Laminate

$$S_{\max} \text{ (MPa)} = 674.3 N_f^{-0.02983}$$

$$r^2 = 0.8795$$

#### SNO Joint

$$S_{\max} \text{ (MPa)} = 1393.0 N_f^{-0.1230}$$

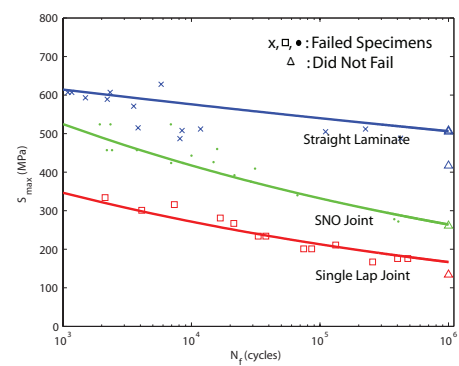
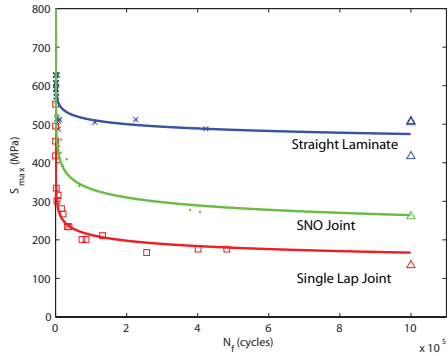
$$r^2 = 0.7023$$

#### Single Lap Joint

$$S_{\max} \text{ (MPa)} = 568.8 N_f^{-0.09327}$$

$$r^2 = 0.9368$$

(b)  $[0/\pm 30/90]_s$  SL, single lap and SNO joints



#### Straight Laminate

$$S_{\max} \text{ (MPa)} = 745.4 N_f^{-0.0280}$$

$$r^2 = 0.3364$$

#### SNO Joint

$$S_{\max} \text{ (MPa)} = 1057.0 N_f^{-0.1008}$$

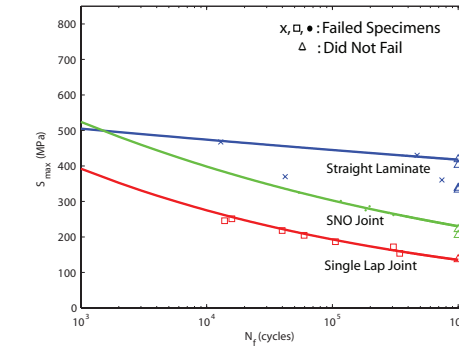
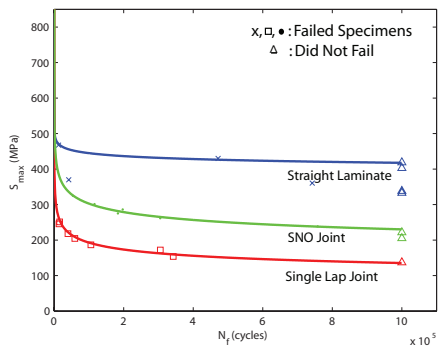
$$r^2 = 0.9773$$

#### Single Lap Joint

$$S_{\max} \text{ (MPa)} = 719.7 N_f^{-0.1058}$$

$$r^2 = 0.9775$$

(c)  $[0/\pm 45/90]_s$  SL, single lap and SNO joints



#### Straight Laminate

$$S_{\max} \text{ (MPa)} = 610.6 N_f^{-0.0275}$$

$$r^2 = 0.3850$$

#### SNO Joint

$$S_{\max} \text{ (MPa)} = 1193.0 N_f^{-0.1191}$$

$$r^2 = 0.9756$$

#### Single Lap Joint

$$S_{\max} \text{ (MPa)} = 1136.0 N_f^{-0.1540}$$

$$r^2 = 0.9936$$

(d)  $[0/\pm 60/90]_s$  SL, single lap and SNO joints

**Figure 23:** S-N curve on a linear scale and a semi-logarithmic scale for IM7/8551-7  $[0]_8$  and  $[0/\pm \theta/90]_s$

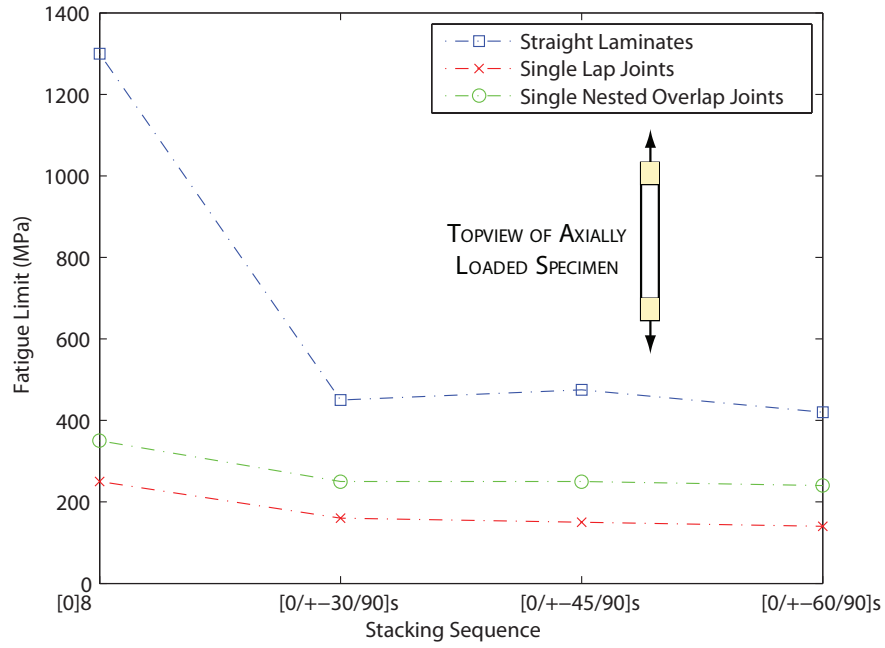


**Figure 24:** Fatigue limit values for  $[0]_8$ ,  $[0/\pm 30/90]_s$ ,  $[0/\pm 45/90]_s$  and  $[0/\pm 60/90]_s$  straight laminates, single lap and single nested overlap joints

**Table 9:** Fatigue strength indicator I for IM7/8551-7  $[0/\pm \theta/90]_s$

Stacking Sequence Fatigue Effectiveness Factor: $FS_I$			
	$[0/\pm 30/90]_s$	$[0/\pm 45/90]_s$	$[0/\pm 60/90]_s$
<b>SL</b>	35	37	32
<b>Single lap joints</b>	64	60	56
<b>SNO joints</b>	71	71	69

*Fatigue strength improvement values are in %.*

The stacking sequence fatigue effectiveness of  $[0/\pm \theta/90]_s$  family with respect to the  $[0]_8$  SL, single lap, and SNO joints was approximately 30-40%, 55-65%, and 70-80%, respectively (Table 9). Unlike the empirical data obtained for the UTS values, the FL values were approximations obtained from curve fits.

Similar to the UTS trend, when fiber-dominated failure, such as dominant adherend failure, was observed in the SL, the stacking sequence effectiveness factor was dependent on the proportion of fibers aligned along the loading direction. In the case of fiber-dominated failure observed in the  $[0/\pm \theta/90]_s$  SL, the stacking sequence effectiveness factor under

static and fatigue was consistently lowest, between 30-40% (Static: Table 5 and Fatigue: Table 9). However, when matrix-dominated or mixed type failure resulted, the stacking sequence effectiveness factor was no longer a proportion of the fiber aligned along the loading direction. In the case of the single lap and SNO joints, the stacking sequence effectiveness order of these two joint configurations were reversed under static and under fatigue. The static effectiveness factor indicated that dominant cohesive failure exhibited by the  $[0/\pm\theta/90]_s$  single lap joints was higher in effectiveness than non-dominant adherend failure exhibited by the  $[0/\pm\theta/90]_s$  SNO joints, whereas the fatigue effectiveness factor indicated that dominant cohesive failure exhibited by the  $[0/\pm\theta/90]_s$  single lap joints was lower in effectiveness than non-dominant cohesive failure and interface failure exhibited by the  $[0/\pm\theta/90]_s$  SNO joints.

This observation suggests that among non-fiber-dominated failure (i.e. matrix-dominated or mixed type failure) mixed type failure, such as that exhibited in SNO joints, tends to outperform the matrix-dominated failure in single lap joints.

### 3.3.2 Fatigue Strength Indicator II: Joint Fatigue Effectiveness Factor

The second fatigue strength indicator  $FS_{II}$ , in Eq. (8), compares the fatigue effectiveness of the single lap or SNO joint relative to the SL or “perfect joint”. The computed  $FS_{II}$  for the  $[0/\pm 30/90]_s$ ,  $[0/\pm 45/90]_s$ ,  $[0/\pm 60/90]_s$ , and  $[0]_8$ , single lap, and SNO joints are provided in Table 10.

$$FS_{II} = \frac{FL^{JOINT}}{FL^{PERFECT}} \times 100\% \quad (8)$$

where:

$FS_{II}$  denotes joint fatigue effectiveness factor; and

$FL^{JOINT}$  fatigue limit for either the SNO or single lap joint; and

$FL^{PERFECT}$  denotes fatigue limit for the SL.

**Table 10:** Fatigue strength indicator II for IM7/8551-7  $[0]_8$  and  $[0/\pm\theta/90]_s$ 

<b>Joint Fatigue Effectiveness Factor: <math>FS_{II}</math></b>				
	$[0]_8$	$[0/\pm 30/90]_s$	$[0/\pm 45/90]_s$	$[0/\pm 60/90]_s$
<b>Single lap joints</b>	19	36	32	33
<b>SNO joints</b>	27	56	53	57
<i>Fatigue strength improvement values are in %.</i>				

Improvement in joint effectiveness is significantly affected by the amount of fiber-dominated activity observed in the failure modes. As with the joint static effectiveness, fiber-dominated failure resulted in increased joint effectiveness over matrix-dominated failure, with the SNO joints showing an increase in joint fatigue effectiveness over the single lap joints for both the  $[0]_8$  and  $[0/\pm\theta/90]_s$  family (Static: Table 6 and Fatigue: Table 10). An increase of approximately 10% was observed for the  $[0]_8$  SNO joints, whereas a higher increase of approximately 20-25% was observed for the  $[0/\pm\theta/90]_s$  SNO joints.

In comparing the improvement in joint effectiveness of the  $[0]_8$  SNO joints over the  $[0]_8$  single lap under static and fatigue, a higher improvement of 18% observed in the static effectiveness was due to a comparison between the non-dominant adherend failure exhibited in SNO joints and the dominant cohesive failure exhibited in single lap joints. The more moderate improvement of 8% observed in the fatigue effectiveness was due to a difference in intensity of fiber-dominated failure since both the SNO and single lap joints exhibited non-dominant cohesive failure and interface failure.

Unlike in the  $[0]_8$  SNO joints, where the static improvement in joint effectiveness was higher than the fatigue improvement in joint effectiveness, the  $[0/\pm\theta/90]_s$  SNO joints indicated a higher improvement of 15-20% in joint fatigue effectiveness compared to the 5-10% improvement in joint static effectiveness over the single lap joints. This was a result of the increase in fiber-dominated failure in the  $[0/\pm\theta/90]_s$  SNO joints failing under non-dominant cohesive failure with interface failure compared to the  $[0/\pm\theta/90]_s$  single lap joints failing under dominant cohesive failure.

**Table 11:** Quasi-static and fatigue failure type comparison for IM7/8551-7  $[0]_8$  and  $[0/\pm\theta/90]_s$

<b>Straight Laminates</b>		
	$[0]_8$	$[0/\pm\theta/90]_s$
<i>Quasi-static</i>	Dominant adherend failure	Dominant adherend failure
<i>Fatigue</i>	Dominant adherend failure	Dominant adherend failure
<b>Single Lap Joints</b>		
	$[0]_8$	$[0/\pm\theta/90]_s$
<i>Quasi-static</i>	Non-dominant cohesive failure with interface failure	Dominant cohesive failure
<i>Fatigue</i>	Non-dominant cohesive failure with interface failure	Dominant cohesive failure
<b>Single Nested Overlap Joints</b>		
	$[0]_8$	$[0/\pm\theta/90]_s$
<i>Quasi-static</i>	Non-dominant cohesive failure with interface failure	Non-dominant adherend failure
<i>Fatigue</i>	Non-dominant cohesive failure with interface failure	Non-dominant cohesive failure with interface failure ( $[0/\pm45/90]_s$ at high loadings: Non-dominant adherend failure)

### 3.4 *Quasi-static and Fatigue Strength Comparison for the $[0]_8$ and $[0/\pm\theta/90]_s$ Family of Joints*

A summary of the categorized failure type for the  $[0]_8$  and  $[0/\pm\theta/90]_s$  SL, single lap, and SNO joints under monotonic and cyclic loading is provided in Table 11. With the exception of the  $[0/\pm\theta/90]_s$  SNO joints, whose failure type was non-dominant adherend failure under monotonic loading but shifted to non-dominant cohesive failure with interface failure under cyclic loading, all the  $[0]_8$  and  $[0/\pm\theta/90]_s$  SL, single lap joints, and the  $[0]_8$  SNO joints failed similarly under quasi-static and fatigue.

#### 3.4.1 **Fatigue Strength Indicator III: Fatigue-to-static Joint Effectiveness Factor**

The third fatigue strength indicator  $FS_{III}$ , in Eq. (9), measures the fatigue endurance of the joint compared to its static ultimate strength. The computed  $FS_{III}$  for the  $[0/\pm30/90]_s$ ,

**Table 12:** Fatigue strength indicator III for IM7/8551-7  $[0]_8$  and  $[0/\pm\theta/90]_s$ 

<b>Fatigue-to-Static Joint Effectiveness Factor: <math>FS_{III}</math></b>				
	$[0]_8$	$[0/\pm 30/90]_s$	$[0/\pm 45/90]_s$	$[0/\pm 60/90]_s$
<b>SL</b>	67	56	66	60
<b>Single lap joints</b>	32	29	23	25
<b>SNO joints</b>	30	41	38	38
<i>Fatigue strength improvement values are in %.</i>				

$[0/\pm 45/90]_s$ ,  $[0/\pm 60/90]_s$ , and  $[0]_8$ , SL, single lap, and SNO joints are provided in Table 12.

$$FS_{III} = \frac{FL^{JOINT}}{UTS^{JOINT}} \times 100\% \quad (9)$$

where:

$FS_{III}$  denotes fatigue-to-static joint effectiveness factor; and

$FL^{JOINT}$  denotes fatigue limit for the SL, SNO or single lap joint; and

$UTS^{JOINT}$  denotes static ultimate tensile strength of the SL, SNO or single lap joint.

The SL, representing “perfect” joints, was the most effective in converting its static strength to fatigue endurance for the  $[0]_8$  and  $[0/\pm\theta/90]_s$ , at approximately 50-60% (Table 12), implying that 50-60% of the static strength can be utilized under low cycle fatigue for specimens exhibiting dominant adherend failure (Quasi-static failure modes: Figure 16 and Fatigue failure modes: Figure 20) regardless of differences in the stacking sequence effectiveness. The  $[0]_8$  single lap and SNO joints have similar fatigue-to-static effectiveness (Table 12) since non-dominant cohesive fracture with interface failure was predominant for both under monotonic and cyclic loading (Quasi-static failure modes: Figures 17 and 18. Fatigue failure modes: Figures 21 and 22).

For the  $[0/\pm\theta/90]_s$  family, the SL was most effective in converting static ultimate strength to fatigue endurance, followed by the SNO, and then the single lap joints. The  $[0/\pm$

$\theta/90]_s$  SNO joints consistently showed an improvement in performance of approximately 10-15% when converting static ultimate strength to fatigue endurance as compared to the  $[0/\pm\theta/90]_s$  single lap joints (Table 12). This improvement in performance was due largely to the increase in amount of fiber-dominated failure from the SNO joints that failed under mixed type failure to the single lap joints that failed under dominant cohesive failure.

An approximate range between 20-30% to 50-60% in fatigue endurance could be converted from the static ultimate strength when failure types range between matrix-dominated failure, such as dominant cohesive failure, to fiber-dominated failure, such as dominant adherend failure. The fatigue-to-static effectiveness factor did not appear sensitive to the shift in failure type from non-dominant cohesive failure to non-dominant adherend failure as in the case of  $[0/\pm\theta/90]_s$  SNO joints, rather mixed type failure tend to yield at approximately 35-45% of the static ultimate strength. The fatigue-to-static effectiveness factor was also insensitive to stacking sequence effectiveness between  $[0]_8$  and  $[0/\pm\theta/90]_s$ .

### ***3.5 Chapter Summary***

The strength indicators were limited by parameters, such as stacking sequences, cyclic frequency, and loading direction, although a reliable trend was established for a family of lay-ups. The fatigue-to-static effectiveness indicator showed a consistent 50-60% for both the  $[0]_8$  and  $[0/\pm\theta/90]_s$  SL but its validity in other family of stacking sequences was not investigated. Similar to the quasi-static failure modes, the fracture state illustrated in the failure mode figures only captured predominant failure features across the SL, single lap, and SNO joints but damage initiators and critical damage mechanisms could not be ascertained from these post fracture figures. Although there was insufficient evidence to conclude that the mean UTS from single panel and from multiple panels under monotonic loading were different, a significant amount of scatter near the FL was observed under cyclic loading, indicating the extent of scatter under fatigue for the IM7/8551-7 material system.

## CHAPTER IV

### QUASI-STATIC ACOUSTIC EMISSION COUNT PEAKS OBSERVED AS FATIGUE LIMIT INDICATOR

Quasi-static Acoustic Emission (AE) counts measures the elastic energy emitted by the specimen as it deforms during monotonic loading. A quasi-static cumulative AE count at each loading is taken as the sum of all the acoustic events (counts) up to that quasi-static load, while a quasi-static cumulative AE count peak, or AE count peak for short, refers to a sudden increase in the AE counts due to significant damage emitted at that particular stress level. Three distinct count peaks were identified for the IM7/8551-7  $[0/\pm\theta/90]_s$  SL, single lap, and SNO joints. With a sufficient number of specimens, these AE count peaks were found to occur repetitively at similar stress levels, suggesting the significance of these damage mechanisms. An onset of AE events refers to a computed average loading where AE events was first measured by the sensor.

The parametric AE study presented represents data collected from a single transducer. Due to limitations in processing and successful utilization of fatigue AE data, particularly for composite materials, analysis of fatigue AE data was not conducted in this study. Instead the significance of the quasi-static damage mechanisms, represented by the AE count peaks, were explored under fatigue.

When the AE count peaks were correlated to fatigue performance on the S-N curve, either the onset of AE events (indicating damage) or the first AE count peak was observed to be FL indicators for the IM7/8551-7  $[0/\pm\theta/90]_s$  family of SL and SNO joints cycled at a frequency of 5 Hz, R of 0.1 and fatigue run-out defined at  $1 \times 10^6$  cycles. For the IM7/8551-7  $[0]_8$ , the onset of AE events was observed to be a FL indicator for the SL.



**Table 13:** Straight laminates: Quasi-static cumulative AE count peaks for IM7/8551-7  $[0]_8$  and  $[0/\pm\theta/90]_s$

	$[0]_8$	$[0/\pm 30/90]_s$	$[0/\pm 45/90]_s$	$[0/\pm 60/90]_s$
<b>Onset of AE events</b>	1544	424	260	288
<b>First AE Peak</b>	—	530	480	400
<b>Second AE Peak</b>	—	630	560	450 – 510
<b>Third AE Peak</b>	—	680 – 770	620 – 740	545 – 645

*AE count values are in MPa.*

*Onset of AE events is a computed average based on all accepted test specimens.*

#### 4.1 Quasi-static Cumulative AE Count Peaks

The experimental setup for the AE data acquisition system is detailed in Appendix A. An onset of AE events, computed as an average across all tested specimens, as well as three distinct AE count peaks were identified for the  $[0/\pm\theta/90]_s$  SL, single lap, and SNO joints. However, significantly fewer count peaks were identified for the  $[0]_8$  due to more abrupt quasi-static fracture as a result of lack of  $\theta^\circ$  plies in the stacking sequence. For the  $[0]_8$  SL, only an onset of AE events was identified; for the  $[0]_8$  single lap and SNO joints, an onset of AE events and one AE count peak were identified. The stress values for the onset of AE events and first, second, and third quasi-static cumulative AE count peaks for the IM7-8551/7  $[0]_8$  and  $[0/\pm\theta/90]_s$  SL, single lap, and SNO joints were obtained from a minimum of five tested specimens and summarized in Tables 13, 14 and 15, respectively. Dashes in Tables 13-15 denote the lack of an observed AE count peak. A scatter plot of all the AE count peaks, including onset of AE events and first, second, and third AE count peak, for  $[0]_8$  and  $[0/\pm\theta/90]_s$  SL, single lap, and SNO joints is provided in Figure 25. Summary plots of quasi-static cumulative AE counts and quasi-static AE counts versus stresses for individual specimens are provided in Appendix C.

The AE count peak was also observed to occur over a range of stress values rather than at a single specific loading for some stacking sequences and configurations, particularly for the third AE count peak (Tables 13-15). This scatter was largely attributed to increase in complexity of the failure mechanisms or the joint design of fiber-dominated adherend fracture for the  $[0/\pm 45/90]_s$  SL and SNO joints [95]. However, a similar scatter observed in the

**Table 14:** Single lap joints: Quasi-static cumulative AE count peaks for IM7/8551-7  $[0]_8$  and  $[0/\pm\theta/90]_s$

	$[0]_8$	$[0/\pm 30/90]_s$	$[0/\pm 45/90]_s$	$[0/\pm 60/90]_s$
<b>Onset of AE events</b>	742	346	354	259
<b>First AE Peak</b>	750 – 810	380	350	350
<b>Second AE Peak</b>	–	440	480	380 – 420
<b>Third AE Peak</b>	–	480 – 550	580	440 – 475

*AE count values are in MPa.*

*Onset of AE events is a computed average based on all accepted test specimens.*

**Table 15:** Single nested overlap joints: Quasi-static cumulative AE count peaks for IM7/8551-7  $[0]_8$  and  $[0/\pm\theta/90]_s$

	$[0]_8$	$[0/\pm 30/90]_s$	$[0/\pm 45/90]_s$	$[0/\pm 60/90]_s$
<b>Onset of AE events</b>	916	223	301	313
<b>First AE Peak</b>	1100 – 1220	400	375	380
<b>Second AE Peak</b>	–	480	400	400 – 440
<b>Third AE Peak</b>	–	525 – 590	520 – 620	480 – 600

*AE count values are in MPa.*

*Onset of AE events is a computed average based on all accepted test specimens.*

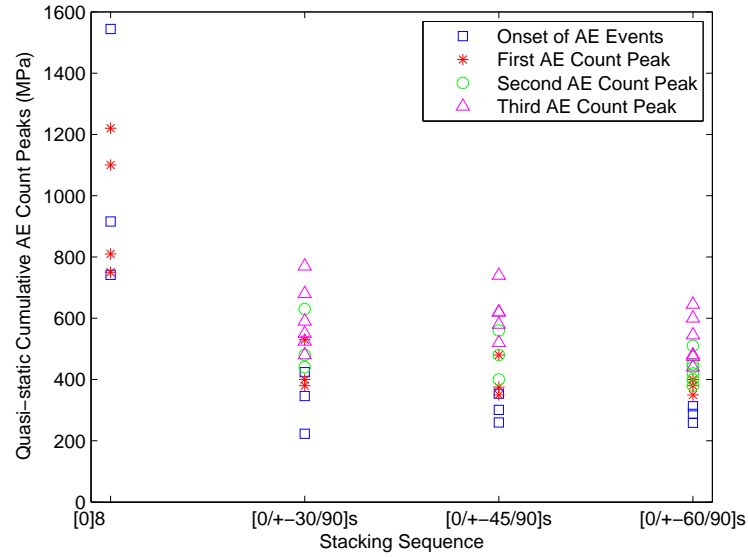


**Figure 25:** Scatter plot of quasi-static AE count peaks (onset of AE events, first AE count peak, second AE count peak and third AE count peak) for IM7/8551-7  $[0]_8$  and  $[0/\pm\theta/90]_s$

$[0]_8$ ,  $[0/\pm 30/90]_s$  and  $[0/\pm 60/90]_s$  configurations was more likely a result of manufacturing variation because a limited number of specimens were used.

In Figure 25, the onset of AE events and first, second, and third AE count peaks for the  $[0]_8$  and  $[0/\pm \theta/90]_s$  SL, single lap, and SNO joints were plotted against the stacking sequences. Each AE count peak was observed to occur within distinct ranges of stresses for the  $[0/\pm \theta/90]_s$  SL, single lap, and SNO joints. Assuming a similar failure mechanism for the  $[0/\pm \theta/90]_s$  family, the occurrence of distinct ranges of AE count peaks suggested similar damage type recurring at these loadings. This will be further investigated in Chapter 5.

Neither the AE counts, the cumulative AE counts, nor the AE count peaks were successful in differentiating between fiber-dominated and matrix-dominated failure observed in monotonic loading of the  $[0/\pm \theta/90]_s$  SL and single lap joints, respectively. The cumulative AE counts, however, did indicate a significant increase in counts for S2-glass/E773FR  $[0/\pm 45/90]_s$  where extensive fiber splitting was observed throughout the joints [97]. The current AE data acquisition technique requires a significant amount of fiber activity and hence, a significant amount of elastic energy for successful quantification with the cumulative AE counts.

## ***4.2 Observed Fatigue Limit Indicators for the $[0/\pm \theta/90]_s$ Family***

AE count peaks were observed to be FL indicators when the quasi-static damage mechanisms represented by AE count peaks were correlated to fatigue performance. The merit in using AE count peaks as quick estimates of FL is the significant reduction in extensive effort required for both fatigue AE data collection and analysis and to reliably characterize a S-N curve. However, due to the difference in rate of damage accumulation between monotonic and cyclic loading, the conditions under which adequate FL indicators could be expected will be further explored in the Chapter 5. Talreja (1985) [89] concluded that the FL for any laminate could be determined by the first cracking mechanism and thus, for a laminate with  $90^\circ$  plies, the FL would be governed by the strain at which transverse cracking first occurred. While the onset of AE events and/or first AE count peak likely determined the

first cracking mechanism, a definite correlation between the first cracking mechanism and the AE count peaks was not extensively investigated in this work.

For fatigue at frequency of 5 Hz, R of 0.1, and fatigue run-out of  $1 \times 10^6$  cycles, the failure type observed under low cyclic loading has a dominant effect on the observation of AE count peaks as FL indicators. Specifically, some amount of fiber-dominated activity under low cyclic loading was necessary for observed FL indicators while matrix-dominated failure under low cyclic loading resulted in no observed FL indicators.

#### 4.2.1 Straight Laminates

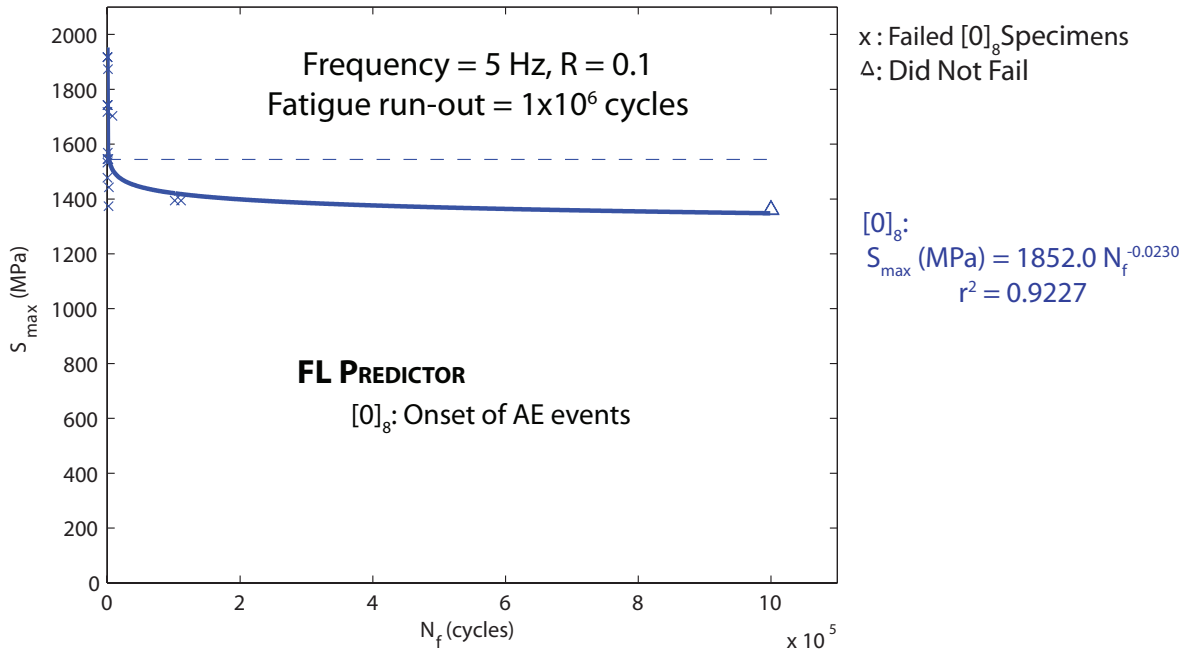
The  $[0]_8$  and  $[0/\pm\theta/90]_s$  SL failed under fiber-dominated adherend fracture under cyclic loading at a frequency of 5 Hz, R of 0.1, and fatigue run-out of  $1 \times 10^6$  cycles (Figure 20). This resulted in observed FL indicators for the  $[0]_8$  and  $[0/\pm\theta/90]_s$  SL. Figure 26a and Figure 26b illustrate the FL indicators for the IM7/8551-7  $[0]_8$  and  $[0/\pm\theta/90]_s$  SL on a constant amplitude tension-tension linear scale S-N curve, respectively. The onset of AE events was observed to be FL indicators for the  $[0/\pm 30/90]_s$  and  $[0]_8$  SL whereas the first AE count peak was observed to be FL indicators for the  $[0/\pm 45/90]_s$  and  $[0/\pm 60/90]_s$  SL.

#### 4.2.2 Single Lap Joints

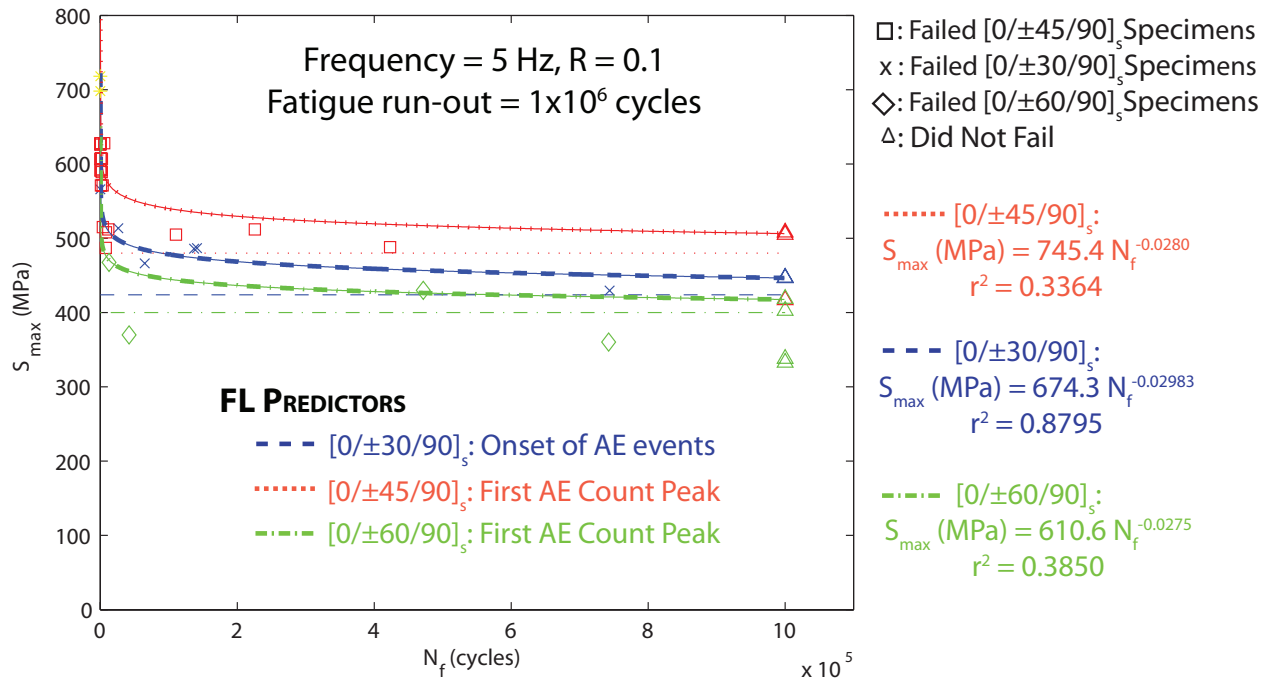
The  $[0]_8$  single lap joints failed under cohesive fracture with increased amount of interface failure observed at high loadings (Figure 21a). The  $[0/\pm\theta/90]_s$  single lap joints failed under cohesive fracture regardless of high or low loadings (Figure 21b). The matrix-dominated failure observed at low loadings resulted in no observed FL indicators for the  $[0]_8$  or the  $[0/\pm\theta/90]_s$  single lap joints. Figure 27a and Figure 27b illustrate this lack of observed FL indicators with any of the AE count peaks for the  $[0]_8$  and  $[0/\pm\theta/90]_s$  single lap joints, respectively, on a constant amplitude tension-tension linear scale S-N curve.

#### 4.2.3 Single Nested Overlap Joints

The  $[0]_8$  SNO joints failed under cohesive fracture with increased amount of interface failure at high loadings (Figure 22a), similar to the  $[0]_8$  single lap joints. The  $[0/\pm 30/90]_s$  and  $[0/\pm 60/90]_s$  SNO joints failed under non-dominant cohesive failure with interface failure

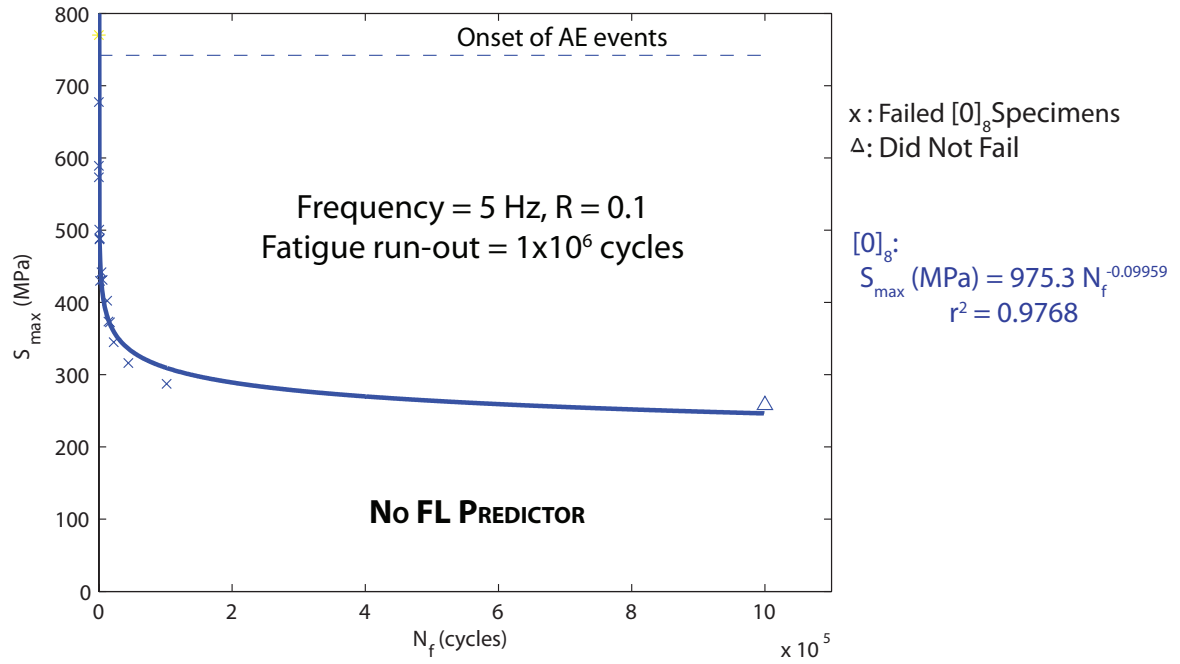


(a) [0]<sub>s</sub>

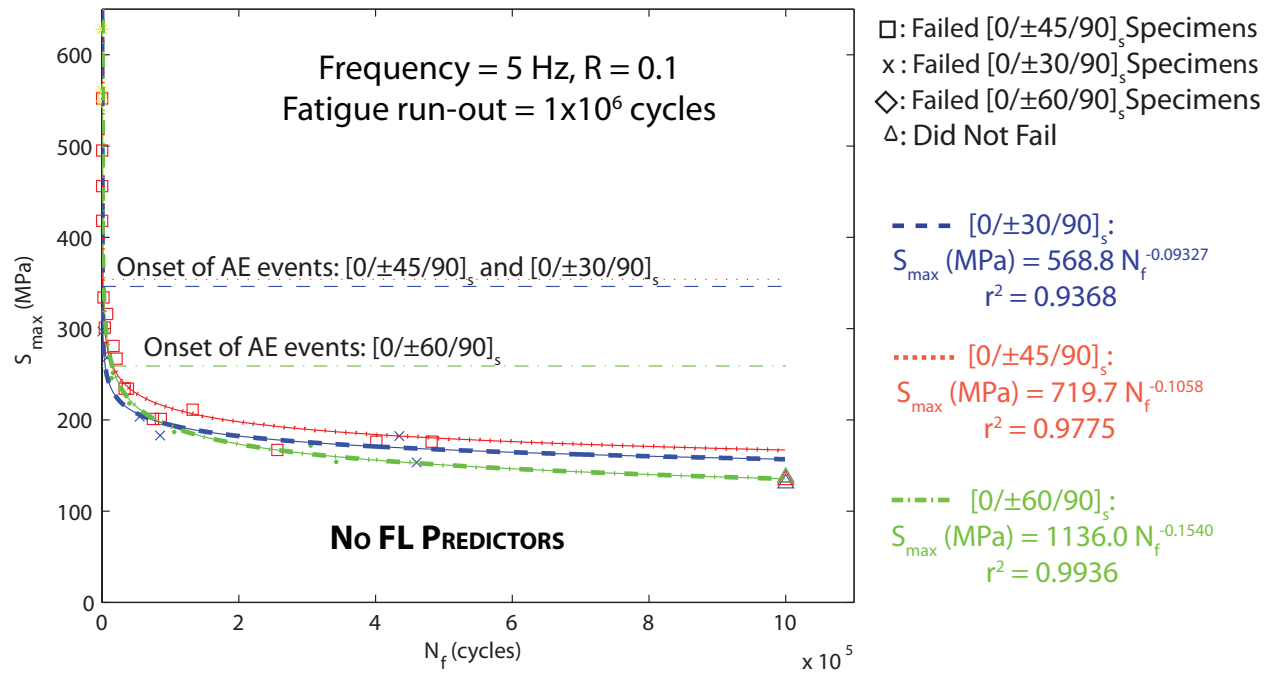


(b) [0/ ± θ/90]<sub>s</sub>

**Figure 26:** Straight laminates: FL indicators and S-N curve on a linear scale (frequency = 5 Hz, R = 0.1 and fatigue run-out =  $1 \times 10^6$  cycles) and observed fatigue limit indicators for IM7/8551-7 [0/ ± θ/90]<sub>s</sub> and [0]<sub>s</sub>



(a)  $[0]_8$



(b)  $[0/\pm \theta/90]_s$

**Figure 27:** Single lap joints: FL indicators and S-N curve on a linear scale (frequency = 5 Hz, R = 0.1 and fatigue run-out =  $1 \times 10^6$  cycles) and observed fatigue limit indicators for IM7/8551-7  $[0/\pm \theta/90]_s$  and  $[0]_8$

**Table 16:** Quasi-static cumulative AE count peaks for IM7/8551-7  $[45/0/-45/90]_s$  straight laminates, single lap and single nested overlap joints

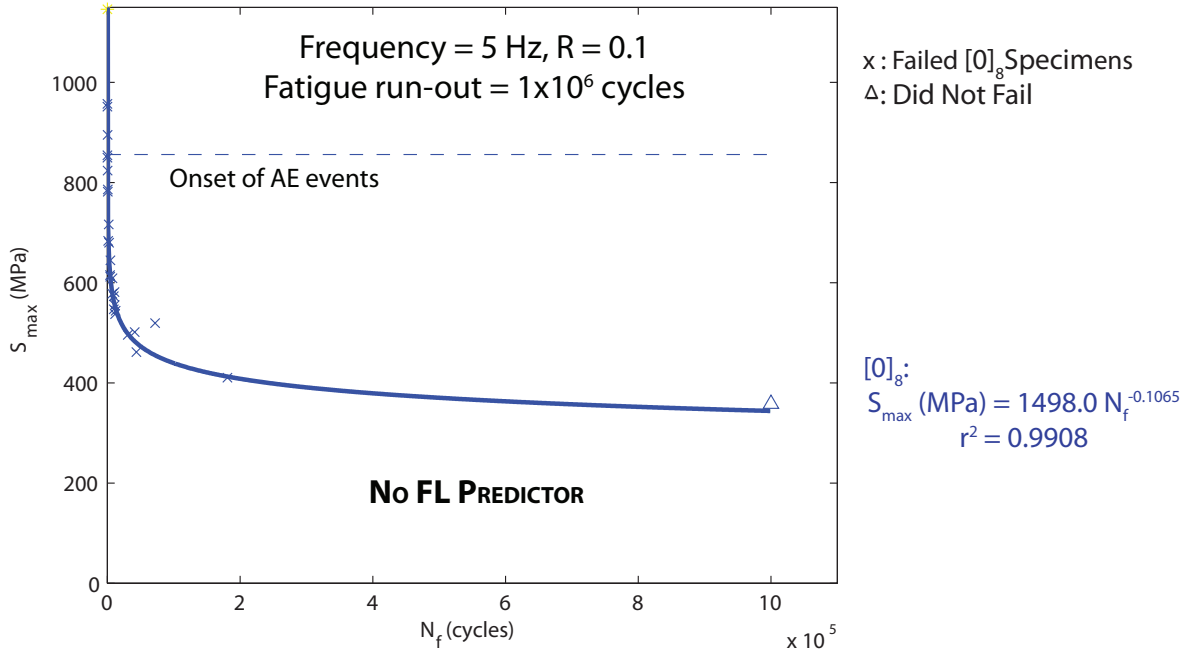
	Straight Laminates	Single Lap Joints	SNO Joints
Onset	463	328	366
First AE Peak	520	360	460
Second AE Peak	570	420	550
Third AE Peak	610	515	630

at all loadings (Figure 22b), while the  $[0/\pm 45/90]_s$  SNO joints only failed under non-dominant cohesive failure with interface failure at low loadings. Similar to the  $[0]_8$  single lap joints, the matrix-dominated cohesive fracture at low loadings resulted in no observed FL indicators. However, with the increase in fiber-dominated failure for the  $[0/\pm \theta/90]_s$  SNO joints, FL indicators were observed. Figure 28a illustrates the lack of a FL indicator for the  $[0]_8$  SNO joints while Figure 28b illustrates the FL indicators for the  $[0/\pm \theta/90]_s$  SNO joints on a constant amplitude tension-tension linear scale S-N curve. The onset of AE events was observed to be FL indicators for the  $[0/\pm \theta/90]_s$  SNO joints exhibiting similar failure modes at low loadings.

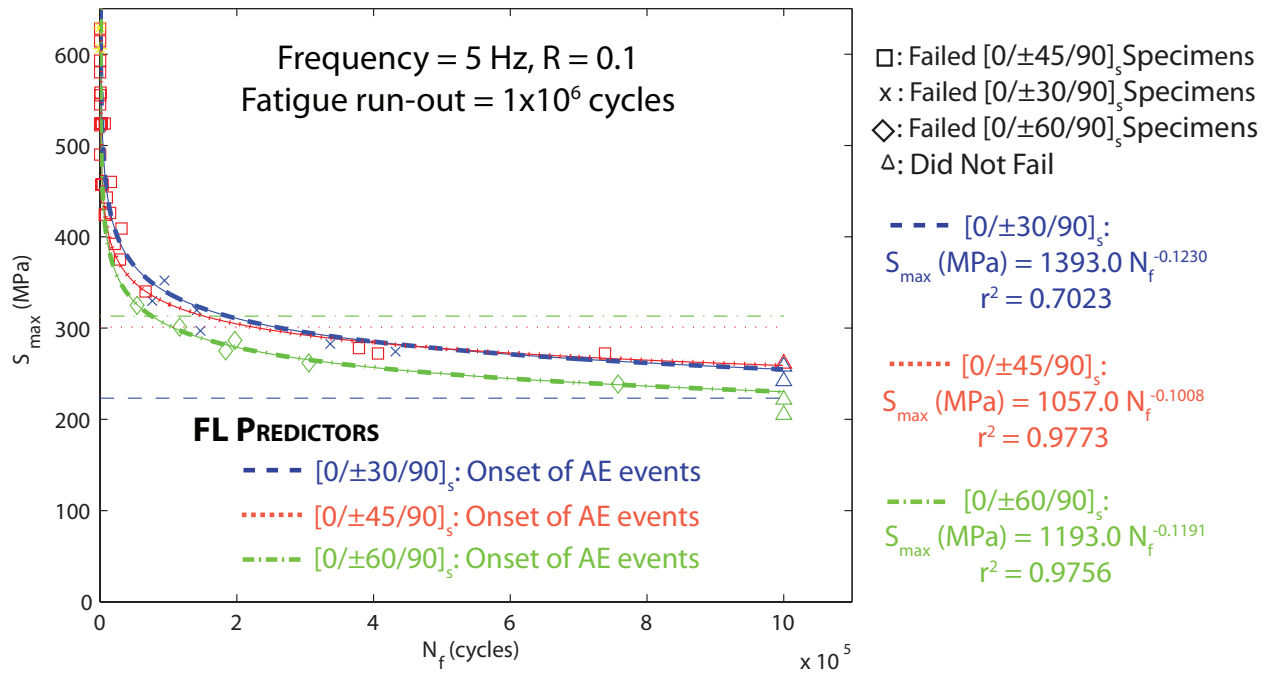
### 4.3 *Difference in Rate of Damage Accumulation under Quasi-static and Fatigue with Increased Frequency*

The validity of AE count peaks as FL indicators for fiber-dominated failure type observed under low cyclic loading was further investigated at a different cycling frequency. The frequency was increased from 5 Hz to 10 Hz for the  $[45/0/-45/90]_s$  SL, single lap, and SNO joints, while fatigue run-out was increased from  $1 \times 10^6$  cycles to  $1 \times 10^7$  cycles. This lay-up was chosen to isolate ED in the  $90^\circ/90^\circ$  interface and will be discussed in Chapter 6.

The AE count peaks for the  $[45/0/-45/90]_s$  SL, single lap, and SNO joints are provided in Table 16. These AE count peaks also fall within the ranges of stress values for the  $[0/\pm \theta/90]_s$  SL, single lap, and SNO joints illustrated in Figure 25. The semi-logarithmic S-N curve for the  $[45/0/-45/90]_s$  SL, single lap, and SNO joints is provided in Figure 29.



(a)  $[0]_8$



(b)  $[0/\pm \theta/90]_s$

**Figure 28:** Single nested overlap joints: FL indicators and S-N curve on a linear scale (frequency = 5 Hz, R = 0.1 and fatigue run-out =  $1 \times 10^6$  cycles) and observed fatigue limit indicators for IM7/8551-7  $[0/\pm \theta/90]_s$  and  $[0]_8$



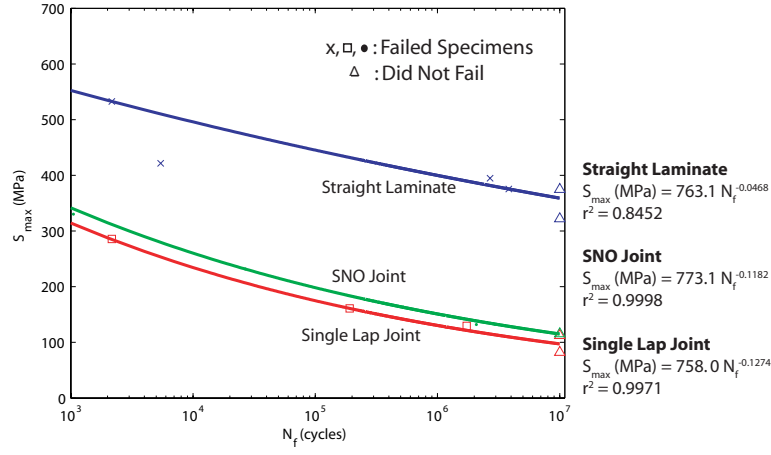
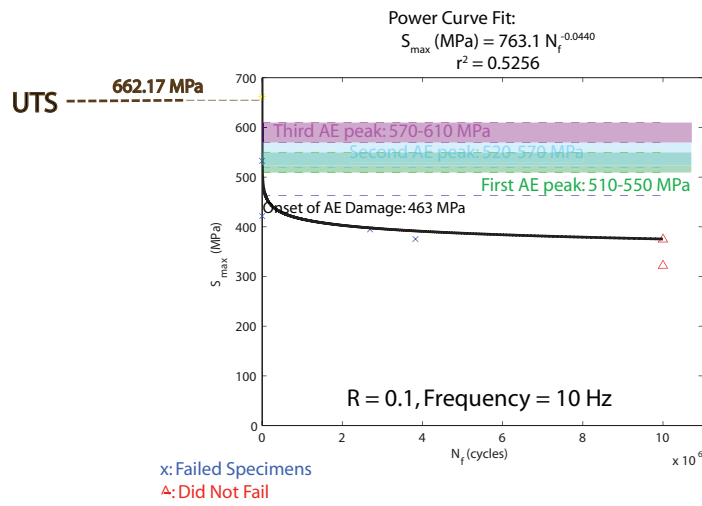


**Figure 29:** Semi-logarithmic S-N curve for IM7/8551-7 [45/0/−45/90]<sub>s</sub> straight laminates, single lap and single nested overlap joints (Frequency = 10 Hz, R = 0.1, Fatigue run-out =  $1 \times 10^7$  cycles)

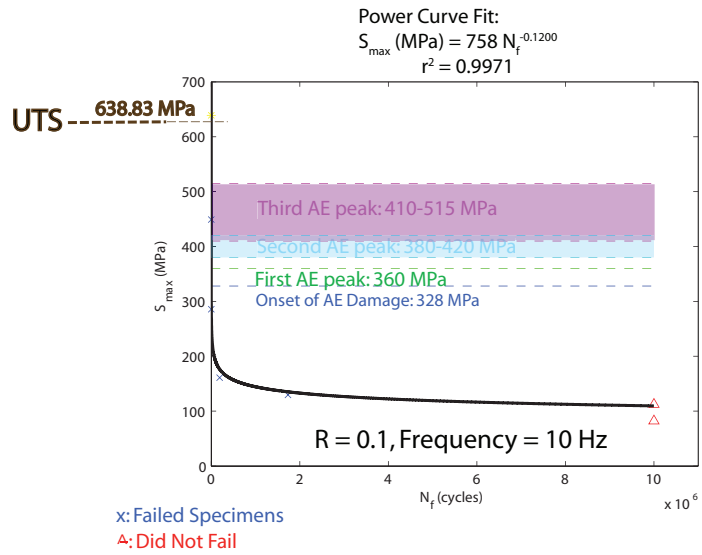
While FL indicators were observed for the SL (Figure 26) and SNO joints (Figure 28b) cycled at 5 Hz, more deviation was observed for the [45/0/−45/90]<sub>s</sub> lay-up cycled at 10 Hz. For fiber-dominated failure exhibited by both the [45/0/−45/90]<sub>s</sub> SL and SNO joints, an approximate FL indicator was observed for the SL but not the SNO joints. For matrix-dominated failure similar to the [0/±θ/90]<sub>s</sub> single lap joints, no FL indicators were observed, as expected. The linear S-N curve and the corresponding AE count peaks, illustrating the approximate FL indicator for [45/0/−45/90]<sub>s</sub> SL and the lack of FL indicators for [45/0/−45/90]<sub>s</sub> single lap and SNO joints, are provided in Figure 30a, 30b, and 30c, respectively.

#### 4.4 Conditions for Quasi-static Cumulative AE Count Peaks as Fatigue Limit Indicators

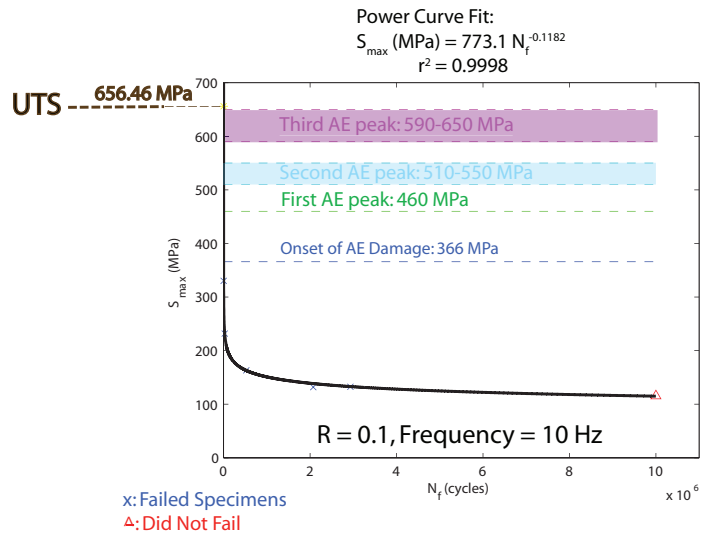
The observation of quasi-static AE count peaks as FL indicators correlated with the amount of fiber activity observed at low cyclic loadings and matrix-dominated failure would not yield any FL indicators regardless of loading frequency or stacking sequence. This implied some amount of similarity in the elastic energy measured by the AE transducer at the onset of AE events or the first AE count peak and that near the fatigue limit, whereas the brittle matrix failure was totally independent of the AE count peaks. In this study, fiber-dominated



(a) Linear S-N curve and AE Count Peaks for straight laminates



(b) Linear S-N curve and AE Count Peaks for single lap joints



(c) Linear S-N curve and AE Count Peaks for single nested overlap joints

**Figure 30:** Constant amplitude tension-tension S-N curve on a linear scale for IM7/8551-7 [45/0/ - 45/90]<sub>s</sub>

failure included failure modes such as adherend fracture and interface failure while matrix-dominated failure included cohesive fracture. Although no FL indicators were observed for the IM7/8551-7  $[0]_8$  and  $[0/\pm\theta/90]_s$  single lap joints, a FL indicator was observed for the S2/E773FR  $[0/\pm\theta/90]_s$  single lap joints, which failed under non-dominant cohesive failure with interface failure at low cyclic loading. The FL indicator was observed to be between the onset of AE event and the first AE count peak [97].

Either the onset of AE events or the first AE count peak was observed to be FL indicators for the  $[0]_8$  and  $[0/\pm\theta/90]_s$  SL, whereas the onset of AE events was observed to be FL indicators for the  $[0/\pm\theta/90]_s$  SNO joints. The significance of the onset of AE events and the first AE count peak will be investigated in Chapter 5. Although the failure types at low cyclic loadings were sufficient to determine possible FL indicators at frequency of 5 Hz, R of 0.1, and fatigue run-out of  $1 \times 10^6$  cycles, the failure types were insufficient in determining whether the onset of AE events or the first AE count peak would be a more likely FL indicator. In S2/E773FR SL and SNO joints, where a significant amount of fiber splitting occurred throughout the specimen, the FL indicator was observed to be between the onset of AE event and the first AE count peak [97].

The cyclic frequency was also an important factor in determining whether AE count peaks could be used as FL indicators. When the difference in rate of damage accumulation between quasi-static and fatigue was increased from 5 Hz to 10 Hz, the fiber activity observed for both the  $[45/0/-45/90]_s$  SL and SNO joints resulted in only an approximate FL indicator for the  $[45/0/-45/90]_s$  SL and no FL indicator for the  $[45/0/-45/90]_s$  SNO joints. Therefore, quasi-static cumulative AE count peaks could be used as quick estimates for fiber-dominated failure types at FL only under low frequency, noting that increasing deviation occurs with increasing cyclic frequency. Although this conclusion is limited in scope, the difficulties in processing and utilizing fatigue acoustic emission data and possible savings in time and effort still give merit to exploring the conditions where quasi-static cumulative AE count peaks are valid as FL indicators.

## ***4.5 Chapter Summary***

Quasi-static AE count peaks were observed to be FL indicators for fiber-dominated failure observed near the FL. Quasi-static AE count peaks measure the energy release in fiber fracture and interactions, and hence, were applicable in correlating adherend fracture but not cohesive fracture. Additionally, quasi-static fatigue limit predictors could only be observed under lower cyclic frequency because damage propagation differed significantly from the quasi-static case when the frequency was increased.

## CHAPTER V

### FATIGUE DAMAGE INITIATION AND PROPAGATION OF THE $[0/\pm 45/90]_S$ AND $[45/0/-45/90]_S$

The quasi-static and fatigue strength characterization of the  $[0]_S$  and  $[0/\pm\theta/90]_S$  family were assessed based on post-mortem examination of fracture modes in Chapters 2 and 3, respectively. The damage initiation and propagation of composite joints under fatigue will be discussed in this chapter. Due to the failure nature of composite joints and defined fatigue run-out, the damage initiation and propagation will be investigated under low Maximum cyclic Load ( $L_{max}$ ) and high Number of cycles to Failure ( $N_f$ ) and high  $L_{max}$  and low  $N_f$ , instead of monitoring the damage all through fatigue run-out. Two approaches were used to investigate the fatigue damage initiation and propagation of IM7/8551-7 SL, single lap, and SNO joints. The first approach explored the fatigue damage initiation and propagation under low  $L_{max}$  and high  $N_f$  near the fatigue limit, whereas the second approach explored the fatigue damage initiation and propagation under high  $L_{max}$  and low  $N_f$ .

In the first damage monitoring approach, the IM7/8551-7  $[0/\pm 45/90]_S$  and  $[45/0/-45/90]_S$  specimens were used to correlate damage types under distinctive monotonic loading defined by significant AE count peaks with damage types at the FL. This approach also further explored the validity of AE count peaks observed as FL indicators for the IM7/8551-7  $[0/\pm\theta/90]_S$  family of SL and SNO joints cycled at a frequency of 5 Hz, R of 0.1, and fatigue run-out defined at  $1 \times 10^6$  cycles, as discussed in Chapter 4. The  $[0/\pm 45/90]_S$  and  $[45/0/-45/90]_S$  lay-ups were chosen to isolate ED in the  $90^\circ/90^\circ$  interface, further discussed in Chapter 6.

The second fatigue damage monitoring approach employed an Infrared Thermoelastic Stress Analysis (IR-TSA) technique, which detects temperature changes emitted from the surface of a cyclically loaded specimen to characterize the fatigue damage propagation in terms of colored stress contour plots. This approach also explored the extent of ED in the

90°/90° interface observed in the  $[0/\pm\theta/90]_s$  SL and  $[0/\pm 45/90]_s$  SNO joints (Chapter 3) through a visualization of the stress contour during fatigue. The IM7/8551-7  $[0/\pm 45/90]_s$  SL, single lap and SNO joints were tested at a frequency of 5 Hz and a R of 0.2.

### ***5.1 First Approach: Damage Type Comparison with Quasi-static Cumulative AE Count Peaks***

This approach examined the fatigue damage initiation and propagation at low  $L_{max}$  and high  $N_f$  defined at the FL. Based on the observed FL indicators, the type of damage accumulated at these AE count peaks were investigated and compared against the type of damage accumulated at the FL. These AE count peaks represent significant AE events, including the onset of AE and the first, second, and third AE count peaks. The  $[0/\pm 45/90]_s$  was compared against FL at a frequency of 5 Hz, R of 0.1, and fatigue run-out of  $1 \times 10^6$  cycles, while the  $[45/0/-45/90]_s$  was compared against FL at a frequency of 10 Hz, R of 0.1, and fatigue run-out of  $1 \times 10^7$  cycles. The occurrence of these AE count peaks at distinct ranges of stresses (Figure 25) could imply specific load dependent damage types, such as matrix cracking, delamination, fiber breakage, and fiber pullout.

Each specimen was loaded quasi-statically until each AE count peak and then examined under a digital microscope. As there was no significant damage observed on the surfaces of the specimens prior to ultimate failure, the longitudinal cross-sectional area was examined to identify the accumulated damage types. Each specimen was also cut along the mid-width plane to examine the consistency of the identified damage types on the longitudinal cross-sectional area across the width of the specimen.

#### **5.1.1 Damage Type Comparison at 5 Hz: $[0/\pm 45/90]_s$**

In order to validate if the observation of quasi-static AE count peaks as FL indicators were due to similarity of damage types, the damage types at the AE count peaks were compared against damage types at the FL for the  $[0/\pm 45/90]_s$  SL, single lap, and SNO joints cycled at a frequency of 5 Hz. The identified damage types for the  $[0/\pm 45/90]_s$  SL, single lap, and SNO joints are summarized and illustrated in Tables 17-19, and, Figures 31-33, respectively. The horizontal arrow line in Tables 17-19, denotes the prevalence of a given damage type

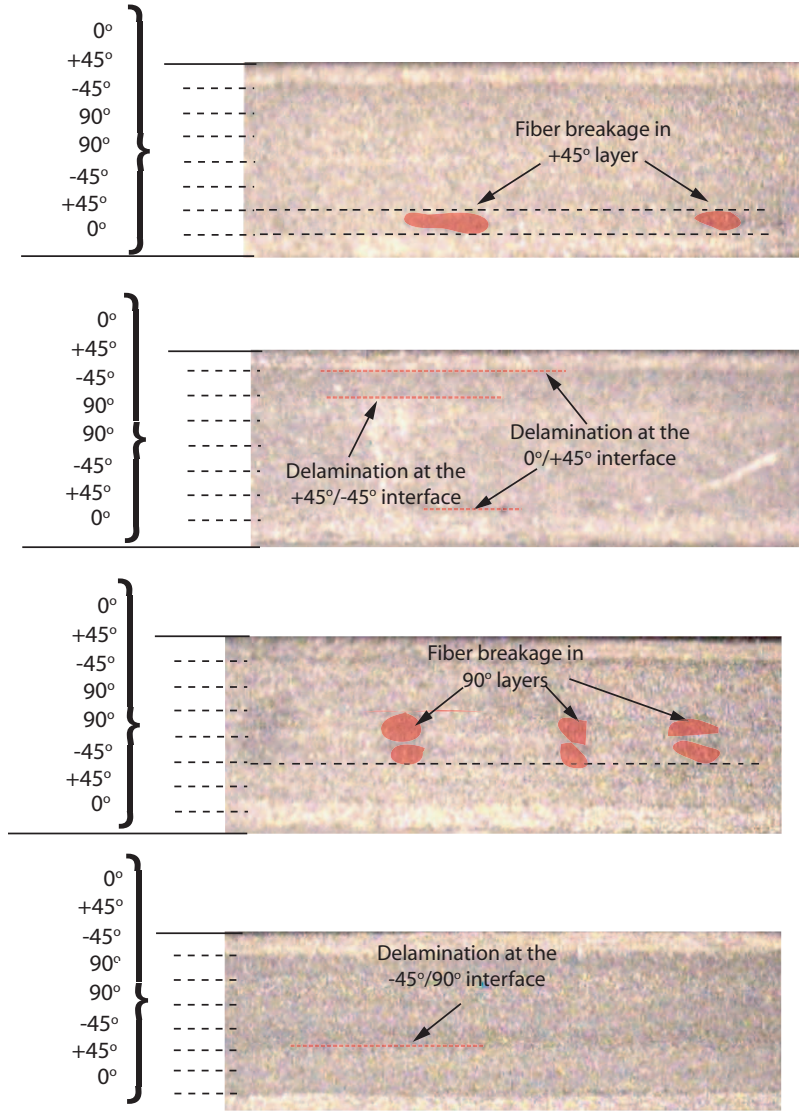
**Table 17:** Straight laminates: Damage type comparison at fatigue frequency of 5 Hz for IM7/8551-7  $[0/\pm 45/90]_s$  at AE count peaks and fatigue limit

	<b>Fatigue Limit</b> (475 MPa)	<b>Damage Onset</b> (260 MPa)	<b>First AE Peak</b> (480 MPa)	<b>Second AE Peak</b> (560 MPa)	<b>Third AE Peak</b> (620-740 MPa)
<b>Delamination</b>					
• $0^\circ/45^\circ$ interface	×				
• $+45^\circ/-45^\circ$ interface	×				
• $-45^\circ/90^\circ$ interface	×				
<b>Fiber Breakage</b>					
• $+45^\circ$ layer					
• $90^\circ$ layer					
<b>Matrix Cracking</b>					
• $90^\circ$ layer	×				

observed across the AE count peaks within the pertinent range, while the “x” denotes that a particular damage type was observed.

For the SL, fiber breakage in the  $+45^\circ$  layer and delamination at the  $0^\circ/45^\circ$  and  $+45^\circ/-45^\circ$  interfaces were observed upon onset of AE events (Table 13: onset 260 MPa). As loading increased to the first AE count peak (Table 13: first 480 MPa), the damage propagated to fiber breakage in the  $90^\circ$  layer and delaminated at the  $-45^\circ/90^\circ$  interface. These damage types continued to accumulate through the second and third AE counts peaks (Table 13: second 560 MPa; third 620-740 MPa) until ultimate failure. At the fatigue limit (Figure 23c: Specimens that did not fail indicated with blue triangles), delamination across the same three interfaces ( $0^\circ/45^\circ$ ,  $+45^\circ/-45^\circ$ , and  $-45^\circ/90^\circ$ ) was observed. However, instead of fiber breakage, matrix cracking was observed in the  $90^\circ$  layer.





For the single lap joints, delamination was observed at the  $0^\circ/45^\circ$  and  $+45^\circ/-45^\circ$  interfaces upon onset of AE events (Table 14: onset 354 MPa). Damage propagated to fiber breakage in the  $-45^\circ$  layer and  $90^\circ$  layer as loading approached the first and second AE count peaks, respectively (Table 14: first 350 MPa; second 480 MPa). These damage



**Figure 31:** Damage types at AE count peaks and at fatigue limit (frequency = 5 Hz,  $R = 0.1$ , fatigue run-out =  $1 \times 10^6$ ) for IM7/8551-7  $[0/\pm 45/90]_s$  straight laminates  
*The damage types illustrated have been highlighted to enhance clarity.*



**Table 18:** Single lap joints: Damage type comparison at fatigue frequency of 5 Hz for IM7/8551-7  $[0/\pm 45/90]_s$  at AE count peaks and fatigue limit

	Fatigue Limit (150 MPa)	Damage Onset (354 MPa)	First AE Peak (350 MPa)	Second AE Peak (480 MPa)	Third AE Peak (580 MPa)
<b>Delamination</b>					
● 0°/45° interface	×				
● +45°/-45° interface	×				
<b>Fiber Breakage</b>					
● -45° layer					
● 90° layer					

types continued to accumulate through the third AE count peak (Table 14: third 580 MPa) until ultimate failure. At the fatigue limit (Figure 23c: Specimens that did not fail indicated with red triangles), delamination was also observed across the two interfaces ( $0^\circ/45^\circ$  and  $+45^\circ/-45^\circ$ ). However, since the single lap joints failed under cohesive fracture within the overlap length, failure was sudden due to the brittle nature of the matrix. Therefore, no matrix cracking or fiber breakage was observed.

Damage was more extensive in the SNO joints with delamination at all interfaces ( $0^\circ/45^\circ$ ,  $+45^\circ/-45^\circ$ ,  $-45^\circ/90^\circ$ , and  $90^\circ/90^\circ$ ) and fiber breakage in the  $-45^\circ$  layer upon onset of AE events (Table 15: onset 301 MPa). Fiber breakage in the  $90^\circ$  layer was observed close to the second AE count peak (Table 15: second 400 MPa) while delamination at the fifth interface, the  $0^\circ/0^\circ$  overlap joint region, was observed close to the third AE count peak (Table 15: third 520-620 MPa). At the fatigue limit (Figure 23c: Specimens that did not fail indicated with green triangles), delamination was observed in three of the five interfaces under monotonic loading ( $0^\circ/45^\circ$ ,  $+45^\circ/-45^\circ$ , and  $-45^\circ/90^\circ$ ). Since damage was more distributed throughout the SNO joints compared to the single lap joint, fatigue failure was not limited to only cohesive fracture within the overlap joint region, and matrix cracking, instead of fiber breakage, was observed in the  $90^\circ$  layer.

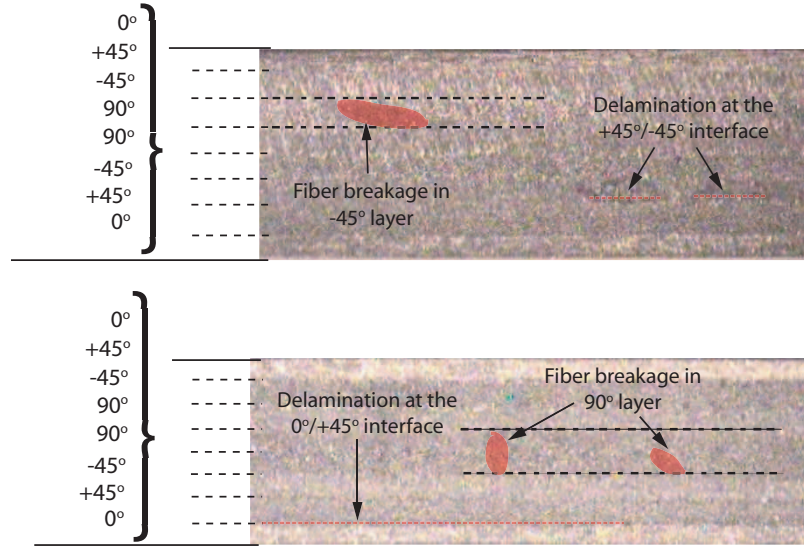


**Figure 32:** Damage types at AE count peaks and at fatigue limit (frequency = 5 Hz, R = 0.1, fatigue run-out =  $1 \times 10^6$ ) for IM7/8551-7  $[0/\pm 45/90]_s$  single lap joints  
*The damage types illustrated have been highlighted to enhance clarity.*

**Table 19:** Single nested overlap joints: Damage type comparison at fatigue frequency of 5 Hz for IM7/8551-7  $[0/\pm 45/90]_s$  at AE count peaks and fatigue limit

	Fatigue Limit (250 MPa)	Damage Onset (301 MPa)	First AE Peak (375 MPa)	Second AE Peak (400 MPa)	Third AE Peak (520-620 MPa)
<b>Delamination</b>					
• $0^\circ/45^\circ$ interface	×				
• $+45^\circ/-45^\circ$ interface	×				
• $-45^\circ/90^\circ$ interface	×				
• $90^\circ/90^\circ$ interface					
• $0^\circ/0^\circ$ interface (overlap joint region)					×
<b>Fiber Breakage</b>					
• $-45^\circ$ layer					
• $90^\circ$ layer					
<b>Matrix Cracking</b>					
• $90^\circ$ layer	×				

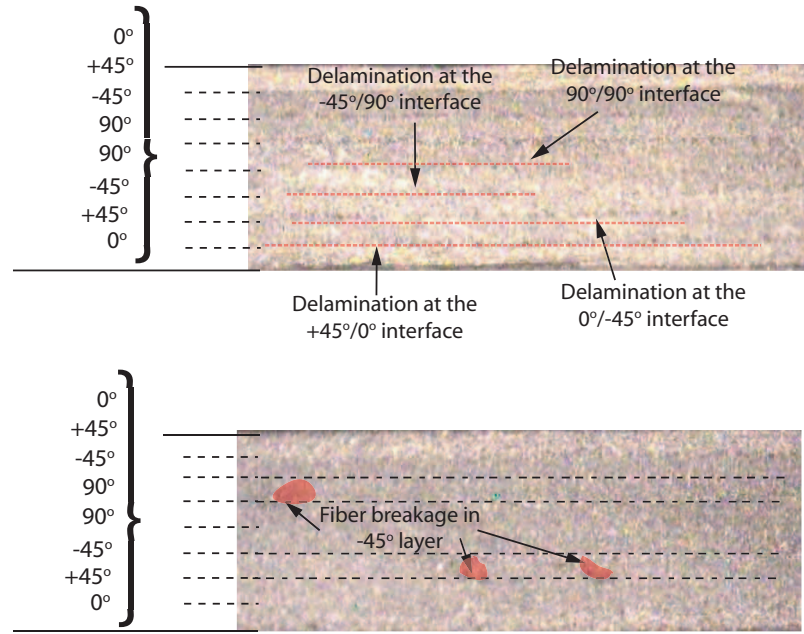


**Figure 33:** Damage types at AE count peaks and at fatigue limit (frequency = 5 Hz,  $R = 0.1$ , fatigue run-out =  $1 \times 10^6$ ) for IM7/8551-7  $[0/\pm 45/90]_s$  single nested overlap joints. The damage types illustrated have been highlighted to enhance clarity.

### 5.1.2 Damage Type Comparison at 10 Hz: $[45/0/-45/90]_s$

In Chapter 4, only an approximate FL indicator was observed for  $[45/0/-45/90]_s$  SL when the rate of damage accumulation between quasi-static and fatigue was enhanced by increasing the cyclic frequency from 5 Hz to 10 Hz. A comparison of damage types at the distinctive loading defined by AE count peaks and at the FL for  $[45/0/-45/90]_s$  SL, single lap, and SNO joints cycled at a frequency of 10 Hz was conducted as the AE count peaks still lay within similar range of stress values as that illustrated in Figure 25.

However, since the initiation of most damage types occurred between the onset and the first AE count peak, only the damage types accumulated at these two AE count peaks were examined for the  $[45/0/-45/90]_s$  SL, single lap, and SNO joints. The damage types for the  $[45/0/-45/90]_s$  SL, single lap, and SNO joints are summarized and illustrated in Tables 20-22 and Figures 34-36, respectively.

For the SL, delamination in the  $45^\circ/0^\circ$  and  $0^\circ/-45^\circ$  interfaces accompanied by matrix cracking in the  $90^\circ$  layer was observed upon onset of AE events (Table 16: onset 463 MPa).

**Table 20:** Straight laminates: Damage type comparison at fatigue frequency of 10 Hz for IM7/8551-7  $[45/0/-45/90]_s$  at AE count peaks and fatigue limit

	<b>Fatigue Limit</b> (370 MPa)	<b>Damage Onset</b> (463 MPa)	<b>First AE Peak</b> (520 MPa)
<b>Delamination</b>			
• $+45^\circ/0^\circ$ interface	×	→	
• $0^\circ/-45^\circ$ interface	×	→	
<b>Fiber Breakage</b>			
• $+90^\circ$ layer	×		
<b>Matrix Cracking</b>			
• $+90^\circ$ layer	×	→	

These damage types continued with no additional damage as loading increased to the first AE count peak (Table 16: first 520 MPa). At the fatigue limit (Figure 29: Specimens that did not fail indicated with blue triangles), delamination across two interfaces ( $45^\circ/0^\circ$  and  $0^\circ/-45^\circ$ ) and matrix cracking in the  $90^\circ$  layer were observed. In addition to the matrix cracking in the  $90^\circ$  layer, fiber breakage in the  $90^\circ$  layer was also observed.

For the single lap joints, delamination across all the four interfaces ( $45^\circ/0^\circ$ ,  $0^\circ/-45^\circ$ ,  $-45^\circ/90^\circ$ , and  $90^\circ/90^\circ$ ) and fiber breakage in the  $90^\circ$  layer were observed upon the onset of AE events (Table 16: onset 328 MPa). These damage types continued as the loading approached the first AE count peak (Table 16: first 360 MPa). At the fatigue limit (Figure 29: Specimens that did not fail indicated with red triangles), delamination was also observed across the same four interfaces ( $45^\circ/0^\circ$ ,  $0^\circ/-45^\circ$ ,  $-45^\circ/90^\circ$ , and  $90^\circ/90^\circ$ ). However, no fiber breakage or matrix cracking was observed at the fatigue limit, similar to the  $[0/\pm 45/90]_s$  single lap joints.

For the SNO joints, only delamination across all the four interfaces ( $45^\circ/0^\circ$ ,  $0^\circ/-45^\circ$ ,  $-45^\circ/90^\circ$ , and  $90^\circ/90^\circ$ ) was observed at onset of AE events (Table 16: onset 366 MPa) and continued through the first AE count peak (Table 16: first 460 MPa). At the fatigue limit (Figure 29: Specimens that did not fail indicated with green triangles), delamination was

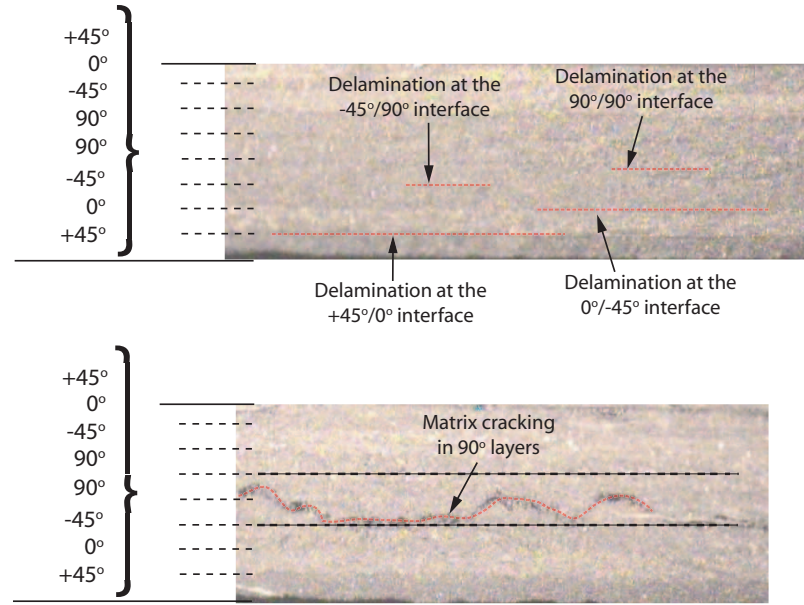


**Figure 34:** Damage types at AE count peaks and at fatigue limit (frequency = 10 Hz, R = 0.1, fatigue run-out =  $1 \times 10^7$ ) for IM7/8551-7  $[45/0/-45/90]_s$  straight laminates  
*The damage types illustrated have been highlighted to enhance clarity.*

**Table 21:** Single lap joints: Damage type comparison at fatigue frequency of 10 Hz for IM7/8551-7  $[45/0/-45/90]_s$  at AE count peaks and fatigue limit

	Fatigue Limit (110 MPa)	Damage Onset (328 MPa)	First AE Peak (360 MPa)
<b>Delamination</b>			
• $+45^\circ/0^\circ$ interface	×	→	→
• $0^\circ/-45^\circ$ interface	×	→	→
• $-45^\circ/90^\circ$ interface	×	→	→
• $90^\circ/90^\circ$ interface	×	→	→
<b>Fiber Breakage</b>			
• $+90^\circ$ layer		→	→

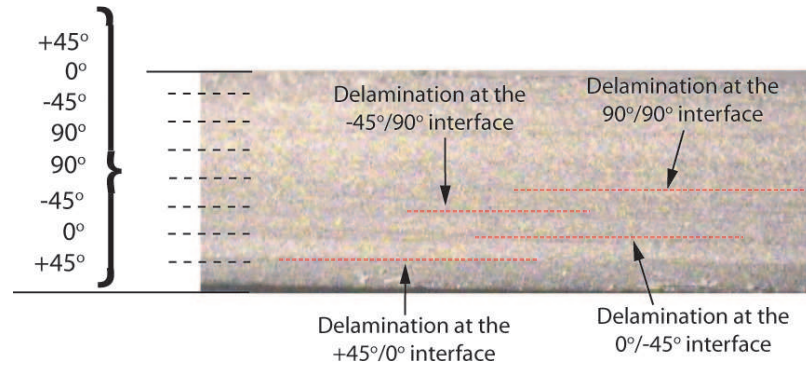


**Figure 35:** Damage types at AE count peaks and at fatigue limit (frequency = 10 Hz,  $R = 0.1$ , fatigue run-out =  $1 \times 10^7$  The damage types illustrated have been highlighted to enhance clarity.) for IM7/8551-7 [45/0/ - 45/90]<sub>s</sub> single lap joints

**Table 22:** Single nested overlap joints: Damage type comparison at fatigue frequency of 10 Hz for IM7/8551-7 [45/0/ - 45/90]<sub>s</sub> at AE count peaks and fatigue limit

	Fatigue Limit (125 MPa)	Damage Onset (366 MPa)	First AE Peak (460 MPa)
<b>Delamination</b>			
• +45°/0° interface	×	→	→
• 0°/-45° interface	×	→	→
• -45°/90° interface	×	→	→
• 90°/90° interface	×	→	→

also observed in all four interfaces identified under monotonic loading (45°/0°, 0°/ - 45°, -45°/90°, and 90°/90°). No additional matrix cracking or fiber breakage was observed.

## 5.2 Damage Types Correlated to Fatigue Limit Indicators

From the damage type assessment of the [0/ ± 45/90]<sub>s</sub> SL, single lap and SNO joints, the initiation of most damage types (delamination between interfaces, fiber breakages and matrix cracking) tended to occur during the onset of AE events or the first AE count peak, whereas the interaction of these damage types accounting for the more critical damages that eventually contributed to ultimate failure tended to occur during the second and third AE count peaks.

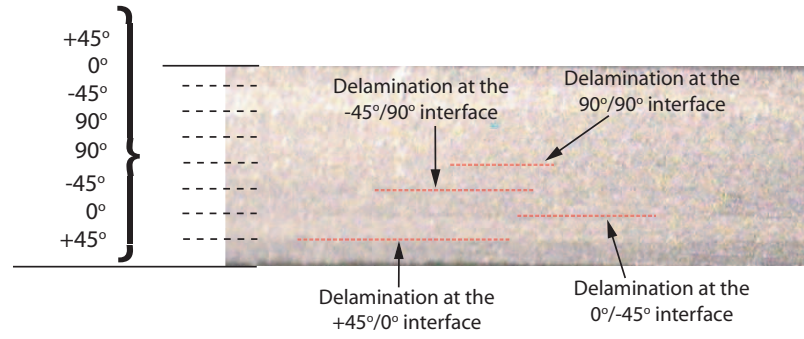


**Figure 36:** Damage types at AE count peaks and at fatigue limit (frequency = 10 Hz,  $R = 0.1$ , fatigue run-out =  $1 \times 10^7$ ) for IM7/8551-7  $[45/0/-45/90]_s$  single nested overlap joints. The damage types illustrated have been highlighted to enhance clarity.

As FL indicators were observed either at the onset of AE events or the first AE count peak (Chapter 4), the FL indicators were concluded to have a stronger dependence on quasi-static damage type initiation than on quasi-static damage interaction and propagation. When the cyclic frequency increased to 10 Hz, the intensified difference in damage propagation at the FL resulted in a lesser dependence on either the quasi-static damage type initiation or the quasi-static damage interaction and propagation; hence, more deviation was observed in the FL prediction for similar fiber-dominated failure modes at the FL.

Delamination was observed in the outer two interfaces ( $[0/\pm 45/90]_s$ :  $0^\circ/+45^\circ$  and  $+45^\circ/-45^\circ$ ,  $[45/0/-45/90]_s$ :  $+45^\circ/0^\circ$  and  $0^\circ/-45^\circ$ ) for all the SL, single lap and SNO joints, whereas delamination in subsequent interfaces depended on the specific joint configurations. Both the  $[0/\pm 45/90]_s$  and  $[45/0/-45/90]_s$  SNO joints were prone to delamination across all the interfaces. As opposed to fiber breakage observed under monotonic loading, matrix cracking in the corresponding layers were more commonly observed at the FL, with the exception of the  $[45/0/-45/90]_s$  SL and single lap joints.

In both the 5 Hz and 10 Hz results, the quasi-static cumulative AE count peaks appeared to be possible FL indicators when the matrix cracking in the  $90^\circ$  plies was observed in the FL specimens. The  $[0/\pm 45/90]_s$  and  $[45/0/-45/90]_s$  single lap joints that failed under matrix-dominated cohesive fracture under low cyclic loadings did not exhibit matrix cracking. The significance of matrix cracking observed at FL as a necessary condition for

FL estimation with quasi-static cumulative AE count peak was not further validated with multiple specimens.

### ***5.3 Second Approach: Damage propagation with Infrared Thermoelastic Stress Analysis Techniques***

This approach examined the fatigue damage initiation and propagation at higher cyclic stress and at lower number of cycles to failure to visualize the damage mechanism in a local region, using Infrared Thermoelastic Stress Analysis Techniques (IR-TSA) to monitor the damage during fatigue testing. This technique has been used in studies [30, 31, 38] to generate a quantitative IR-TSA correlation between the TSA signal and the sum of in-plane strains on cyclically loaded composite specimens, although in this approach only a qualitatively representation of the fatigue damage propagation was sought.

The IR-TSA technique was used to monitor the full-field fatigue damage propagation at select stress levels of the  $[0/\pm 45/90]_s$  SL, single lap, and SNO joints, to qualitatively ascertain the extent of ED in the  $90^\circ/90^\circ$  interface observed based on earlier fatigue studies. The constant amplitude tension-tension fatigue was cycled at a frequency of 5 Hz and a R of 0.2, with the maximum stress for each joint configuration set at approximately 80% of its UTS to allow the IR-TSA to record an adequate number of frames within a reasonable time. The fatigue failure modes under high and low loadings were examined through post mortem of the failed specimens. The IR-TSA setup and details is included in Appendix A.

#### **5.3.1 Damage propagation at Frequency = 5 Hz and R = 0.2: Graphite/epoxy $[0/\pm 45/90]_s$**

The fatigue damage propagation of the  $[0/\pm 45/90]_s$  SL, single lap, and SNO joints are shown in Figures 37a, 37b, and 37c, respectively.

The SL (Figure 20) failed under dominant adherend fracture with an increase in  $90^\circ/90^\circ$  interface delamination and matrix cracking observed as loading was increased. This was also observed in the fatigue damage propagation shown in Figure 37a. The amount of ED in the  $90^\circ/90^\circ$  interface increased significantly, indicated by a reduction in stress (Figure 37a: Blue region), as the number of cycles increases until ultimate failure under adherend



fracture.

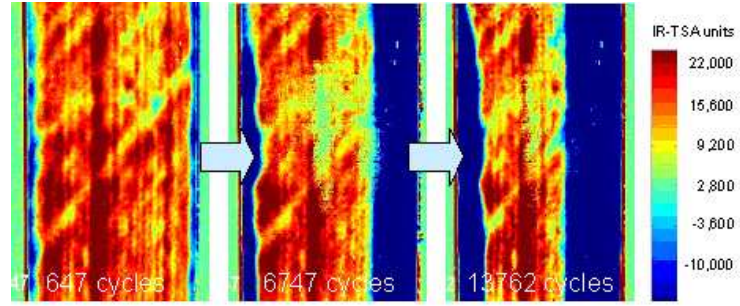
All the single lap joints (Figure 21) failed under dominant cohesive fracture. As loading increases, more irregular fracture lines were observed width-wise along the tapered end. In observing the propagation of fatigue damage, delamination initiated from the tapered end of the overlap joint region and propagated inwards across the  $0^\circ/0^\circ$  overlap joint interface (Figure 37b): Blue region) until ultimate failure under cohesive fracture.

The SNO joints (Figure 22) failed under non-dominant cohesive failure with interface failure at lower loadings and non-dominant adherend failure at higher loadings. Similar to the observed failure modes, a mix of both effects from SL and single lap joints were observed in the fatigue damage propagation of SNO joints. An increasing amount of ED in the  $90^\circ/90^\circ$  interface (Figure 37c: Blue region) and an increasing amount of  $0^\circ/0^\circ$  interface delamination (Figure 37c: Green region) was observed at higher number of cycles. The specimen eventually failed under non-dominant cohesive fracture within the overlap length. This was also in agreement with the fatigue failure modes (Figure 22) and the S-N curve (Figure 23c) comparison of the SL, single lap, and SNO joints. The SNO joints exhibited both adherend fracture similar to the SL and cohesive fracture similar to the single lap joints. The fatigue strength was compared with the SL and single lap joints as the upper and lower bounds, respectively.

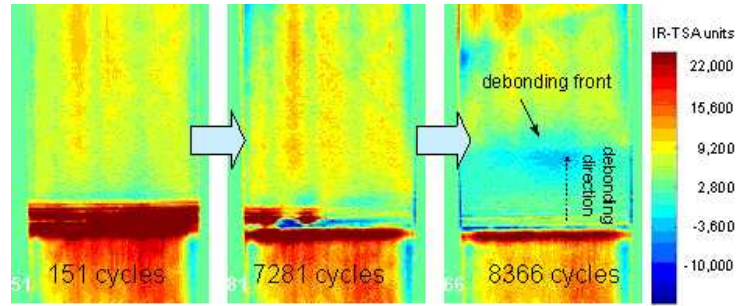
The IR-TSA technique was able to qualitatively differentiate the fatigue damage propagation and their failure modes in terms of the stress distribution, including cohesive fracture and free-edge delamination. However, due to the failure nature of co-cured composite joints and the limited region of focus for the IR-TSA technique, the exact fracture mechanism was not captured.

## ***5.4 Chapter Summary***

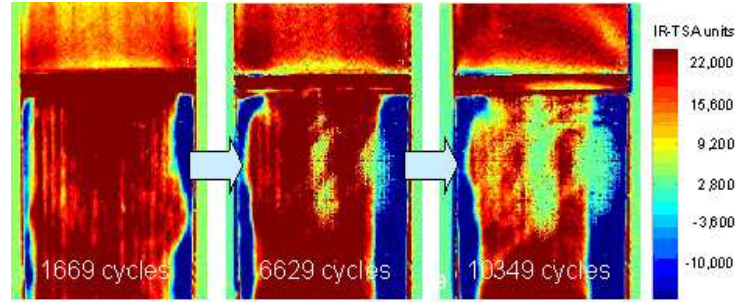
Based on the damage type correlation study, the onset of AE events and the first AE count peak represented the initiation of most damage types, whereas the second and third AE count peaks represented the interaction of damage types. As FL indicators were observed either at the onset of AE events or the first AE count peak, the FL indicators were concluded



(a) Straight laminates:  $\sigma_{max} \approx 0.8$  UTS,  $N_f = 13977$



(b) Single lap joints:  $\sigma_{max} \approx 0.6$  UTS,  $N_f = 8452$



(c) Single nested overlap joints:  $\sigma_{max} \approx 0.8$  UTS,  $N_f = 10363$

**Figure 37:** Infrared TSA images showing fatigue damage propagation for IM7/8551-7 straight laminates, single lap and single nested overlap joint (frequency = 5 Hz,  $R = 0.2$ )

to have a stronger dependence on quasi-static damage type initiation than on quasi-static damage interaction and propagation. IR-TSA was successful in qualitative assessment of composite joints, identifying joint failure modes such as cohesive fracture and extent of free-edge delamination.

## STRENGTH STUDY OF QUASI-ISOTROPIC LAY-UP WITH REDUCED EDGE DELAMINATION

In Chapters 2 and 3, free-Edge Delamination (ED) in the  $90^\circ/90^\circ$  interface was observed in the IM7/8551-7  $[0/\pm\theta/90]_s$  SL under both monotonic (Figure 16) and cyclic (Figure 20) loading and the extent of delamination for fatigued IM7/8551-7  $[0/\pm 45/90]_s$  SL was monitored with IR-TSA in Figure 37a. The IM7/8551-7  $[0/\pm 45/90]_s$  lay-up was also prone to ED in the  $90^\circ/90^\circ$  interface for T300/5208 under monotonic loading [1, 2]. Based on these observations and the earlier damage assessment study, a joint strength study was proposed by minimizing the effect of ED under monotonic and cyclic loading. The location of the  $90^\circ$  ply from the midplane has a significant effect in generating an opening/closing mode [1, 2] and on the quasi-static tensile strength [71]. ED in the midplane was minimized through reordering of the plies in the IM7/8551-7  $[0/\pm 45/90]_s$  quasi-isotropic lay-up, based on Armanios et al. (1989) [1, 2]. In considering only practical lay-ups with  $45^\circ$  plies on the surface for impact protection, two lay-ups were used in this chapter, the IM7/8551-7  $[45/0/-45/90]_s$  and  $[45/90/-45/0]_s$ , which optimizes and minimizes ED in the midplane, respectively. The IM7/8551-7  $[45/0/-45/90]_s$  lay-up was also used in the damage type assessment in Chapter 5, while the IM7/8551-7  $[45/90/-45/0]_s$  lay-up was only proposed in this chapter. The extent of minimized ED in the midplane between the IM7/8551-7  $[45/90/-45/0]_s$  and  $[0/\pm 45/90]_s$  SL was also illustrated with S2/E773FR using IR-TSA technique. The effect of minimized ED on failure modes and specimen width was also investigated.

### ***6.1 Effect of Stacking Sequence on Free-edge Delamination***

The plies in the symmetric eight-ply quasi-isotropic lay-up were reordered to minimize the ED observed in the midplane of  $[0/\pm 45/90]_s$  SL. In reordering the stacking sequence,

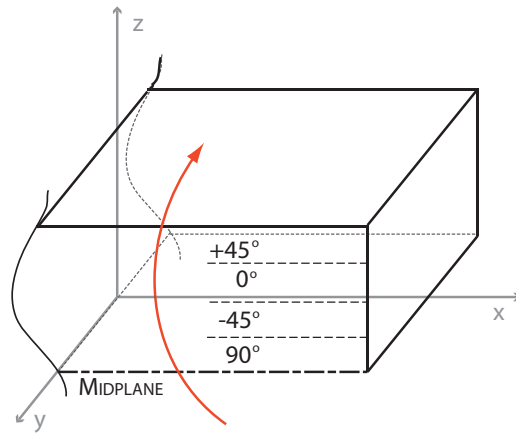
the  $45^\circ$  plies were moved to the outer surfaces for impact loading, while the  $90^\circ$  plies, which had higher stresses in the y-direction, were moved further away from the midplane to generate a larger moment arm for a resultant closing peel stress moment in the y-direction. Hence,  $[45/90/-45/0]_s$  resulted in a closing mode that minimizes edge delamination while  $[45/0/-45/90]_s$  resulted in an opening mode that optimizes edge delamination. Figure 38 illustrates this opening and closing midplane modes for the optimized and minimized edge delamination stacking sequence based on the conclusion drawn from the sublaminates analysis in Armanios et al. (1989) [1, 2]. This resulting opening/closing midplane mode for any laminate could be computed from classical lamination theory.

### 6.1.1 Quasi-static Comparison of Free-Edge Delamination in Straight Laminates

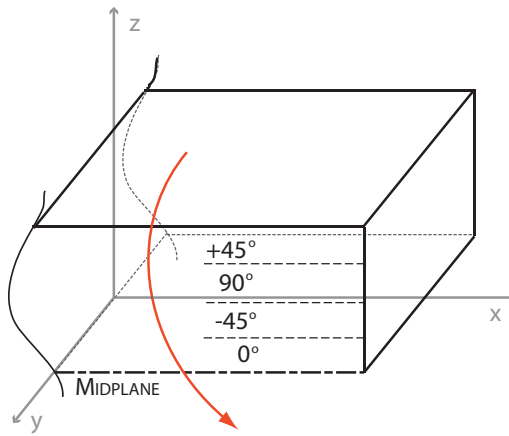
The quasi-static strength of IM7/8551-7  $[45/90/-45/0]_s$ ,  $[0/\pm 45/90]_s$ , and  $[45/0/-45/90]_s$  SL were compared to determine the effect of ED in the midplane based on reordering ply orientations in the laminate.  $[0/\pm 45/90]_s$  was among the  $[0/\pm \theta/90]_s$  family of joints studied in earlier chapters, where ED in the  $90^\circ/90^\circ$  was most predominant under both monotonic and cyclic loading, while  $[45/0/-45/90]_s$  and  $[45/90/-45/0]_s$  were the ED optimized and ED minimized stacking sequence, respectively, based on Armanios et al. (1989) [1, 2].  $[45/0/-45/90]_s$  SL was also used in the damage type assessment in Chapter 5.

The UTS comparison for IM7/8551-7  $[45/90/-45/0]_s$ ,  $[0/\pm 45/90]_s$ , and  $[45/0/-45/90]_s$  SL are illustrated in Figure 39. The standard deviations for each averaged UTS value is also plotted as error bars on the same figure. Based on a 1-way ANOVA with p-value of 0.0035, there was sufficient evidence to conclude that the mean UTS values for the three lay-ups were significantly different, with the  $[45/0/-45/90]_s$ , the ED optimized lay-up, at approximately 8% lower than the UTS of the  $[0/\pm 45/90]_s$  and the  $[45/90/-45/0]_s$ , the ED minimized lay-up, at approximately 15% higher than the UTS of the  $[0/\pm 45/90]_s$ . This was in agreement with the results presented in O'Brien (1984) [71].

The quasi-static failure mode comparison for  $[45/90/-45/0]_s$ ,  $[0/\pm 45/90]_s$ , and  $[45/0/-45/90]_s$  SL is shown in Figure 40 in order of increasing ED observed in the midplane. As mentioned in previous chapters, these post fracture failure mode figures were not able to



**OPENING MODE**  
OPTIMIZED EDGE DELAMINATION



**CLOSING MODE**  
MINIMIZED EDGE DELAMINATION

**Figure 38:** Opening and closing midplane modes for the optimized and minimized edge delamination stacking sequence, respectively

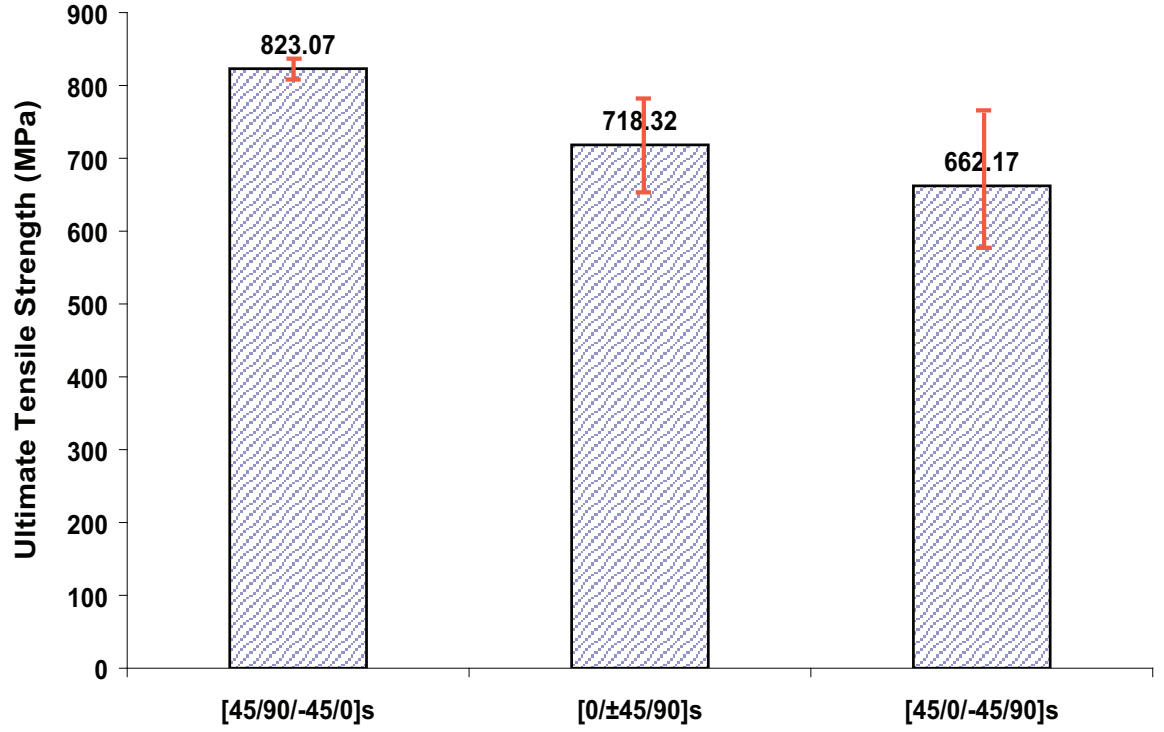
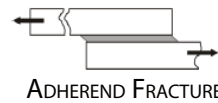


**Figure 39:** Quasi-static tensile strength comparison for  $[45/90/-45/0]_s$ ,  $[0/\pm 45/90]_s$  and  $[45/0/-45/90]_s$   
*Standard deviation of quasi-static tests plotted as error bars*

identify critical damage initiators leading to failure. Although  $[0/\pm 45/90]_s$  SL exhibited the most predominant ED in the  $90^\circ/90^\circ$  interface among the  $[0/\pm \theta/90]_s$  family, the ED optimized  $[45/0/-45/90]_s$  lay-up exhibited even more ED in the  $90^\circ/90^\circ$  interface. A comparison of the extent of ED illustrated with IR-TSA on S2-glass/epoxy will be presented in a later section.

CATEGORIZED FAILURE TYPE:  
DOMINANT ADHEREND FAILURE



INCREASING AMOUNT OF FREE-EDGE DELAMINATION IN MIDPLANE



**Figure 40:** Quasi-static failure mode comparison for IM7/8551-7 (IM7/8551-7)  $[45/90/-45/0]_s$ ,  $[0/\pm 45/90]_s$  and  $[45/0/-45/90]_s$   
Adherend fracture sketch taken from Heslehurst and Hart-Smith [49]



### 6.1.2 Effect of Minimized Edge Delamination on Strength under Monotonic and Cyclic Loading

The UTS comparison for IM7/8551-7  $[45/90/-45/0]_s$  and  $[0/\pm 45/90]_s$  SL, single lap, and SNO joints are illustrated in Figure 41, while the weighted non-linear least square power curve fitted S-N curves on a linear and semi-logarithmic scale are presented Figure 42. The linear scale plot shows a better comparison of the differences in the fatigue limit. A summary of the FL values is also provided in Table 23. The quasi-static failure mode comparison for the IM7/8551-7  $[45/90/-45/0]_s$  and  $[0/\pm 45/90]_s$  SL, single lap, and SNO joints is illustrated in Figure 40, Figure 43a, and Figure 43b, respectively while the fatigue failure mode comparison is illustrated in Figure 44.

An improvement in quasi-static strength of 15% was observed for the ED minimized  $[45/90/-45/0]_s$  SL, while the improvement for the single lap joints was 5%. The significant improvement in SL was attributed to the minimized ED, whereas the smaller difference in single lap joints was due to the increased interface failure since quasi-static failure of  $[0/\pm 45/90]_s$  single lap joints was dominated by matrix strength under cohesive failure. Contrary to earlier prediction of a corresponding improvement in quasi-static strength in the SNO joints, a difference of 8% was observed in the  $[45/90/-45/0]_s$  SNO joints, indicating that the extent of ED in quasi-static fracture was minimal. There was sufficient evidence, based on a 1-way ANOVA table, to conclude a difference in the average UTS between  $[45/90/-45/0]_s$  and  $[0/\pm 45/90]_s$  single lap and SNO joints, but the difference of 5% and 8%, respectively, were within the scatter of the data and therefore, not significant enough to conclude a definite comparison.

A decrease in fatigue endurance of 14% and 12% was observed for the ED minimized  $[45/90/-45/0]_s$  SL and SNO joints, respectively. As there was no significant differences observed in the fatigue failure mode (SL: Figure 44a and SNO: Figure 44c) or in the extent of ED between the two compared lay-ups,  $[45/90/-45/0]_s$  and  $[0/\pm 45/90]_s$ , the decrease in fatigue performance was attributed to differences in failure mechanism arising from the differences in stacking sequence. An unexpected large improvement of 43% in fatigue endurance was observed for the the proposed  $[45/90/-45/0]_s$  single lap joints.

**Table 23:** Fatigue limit comparison for IM7/8551-7  $[45/90/-45/0]_s$  and  $[0/\pm 45/90]_s$  joints

	$[45/90/-45/0]_s$	$[0/\pm 45/90]_s$
<b>Straight laminates</b>	410	475
<b>Single lap joints</b>	215	150
<b>SNO joints</b>	220	250

*FL values are in MPa.*

This improvement in fatigue endurance could also be attributed to the increase in fiber-dominated activity observed in the fatigue failure modes (Figure 44) as the  $45^\circ/45^\circ$  overlap joint interface in  $[45/90/-45/0]_s$  resulted in significant interface failure. With the improved fatigue endurance due to increased fiber-dominated activity, the  $[45/90/-45/0]_s$  single lap and SNO joints were observed to exhibit similar fatigue endurance (Figure 42).

Unlike the  $[0/\pm 45/90]_s$  SL, where a significant amount of ED in the  $90^\circ/90^\circ$  interface was observed at low cyclic loading, the  $[45/90/-45/0]_s$  SL did not exhibit ED in the  $0^\circ/0^\circ$  interface. However, delamination in the  $90^\circ/-45^\circ$  interfaces was consistently observed in the  $[45/90/-45/0]_s$  SL regardless of cyclic loading (Figure 44a).

The strength improvement of laminates and joints relied on different factors due to differences in failure mechanism. Although minimizing ED resulted in significant quasi-static strength improvement for SL, a corresponding improvement was not observed in SNO joints. The lack of improvement under fatigue for both laminates and joints suggested that ED was not a critical failure mechanism under fatigue. Increasing fiber-dominated activity at the overlap interface for single lap joints did result in improved quasi-static and fatigue performance.

## 6.2 *IR-TSA Damage Monitoring for S2-glass/epoxy $[45/90/-45/0]_s$*

The IR-TSA technique adopted in Chapter 5 was used to monitor the extent of ED in the midplane for S2-glass/epoxy  $[0/\pm 45/90]_s$  and  $[45/90/-45/0]_s$  SL, single lap and SNO joints.

The constant amplitude tension-tension fatigue was cycled at a frequency of 5 Hz and a R of 0.2, with the maximum stress for each joint configuration set to allow the IR-TSA to

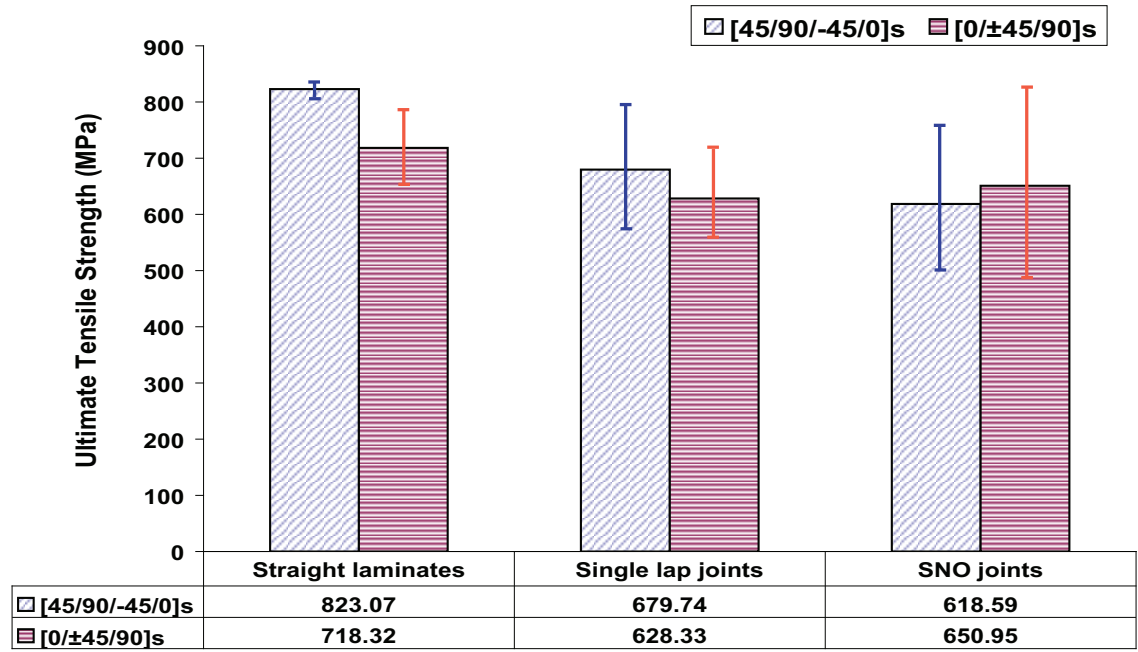


**Figure 41:** UTS comparison of IM7/8551-7  $[45/90/-45/0]_s$  and  $[0/\pm 45/90]_s$  straight laminates, single lap and SNO joints  
Standard deviation of quasi-static tests plotted as error bars

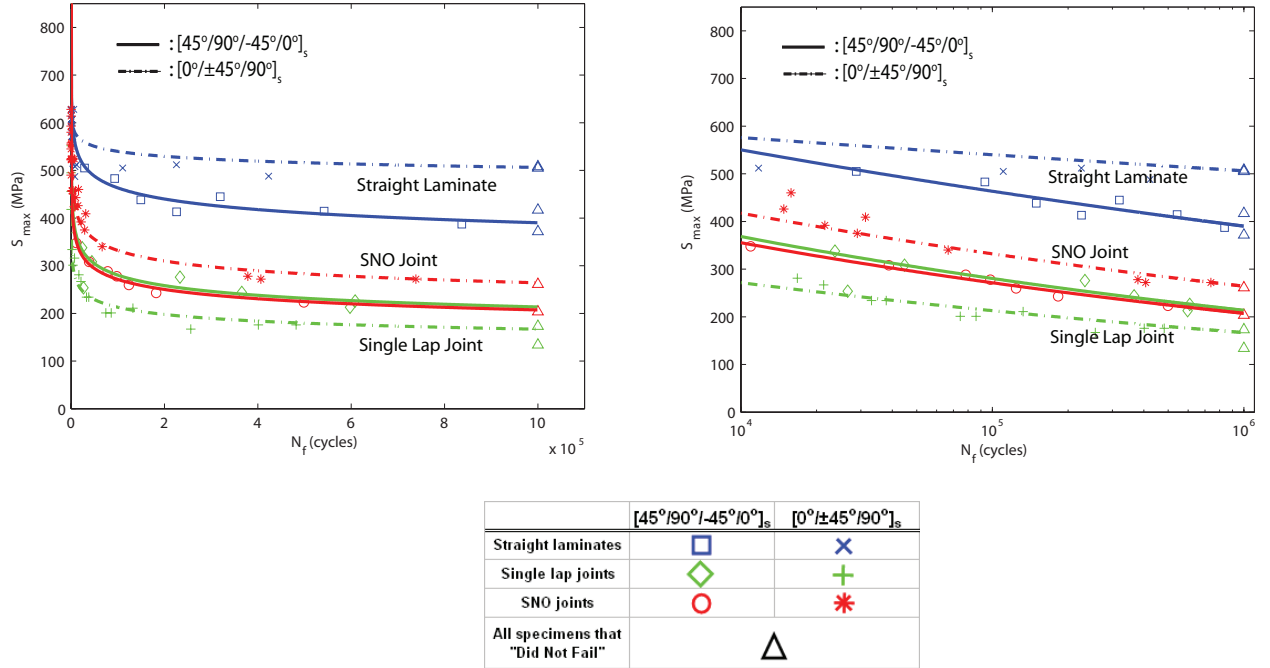
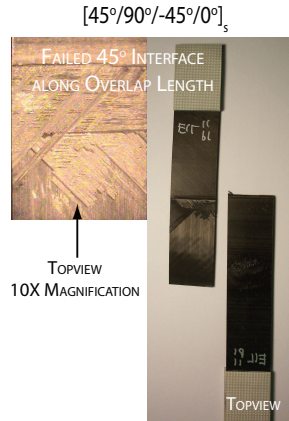
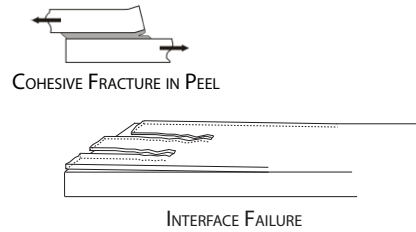
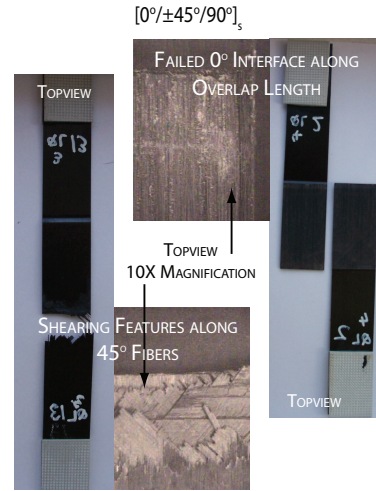
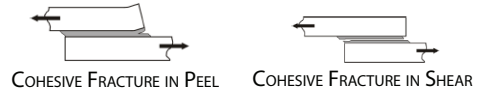


**Figure 42:** Fatigue limit comparison of IM7/8551-7  $[45/90/-45/0]_s$  and  $[0/\pm 45/90]_s$  straight laminates, single lap and SNO joints on a linear and a semi-logarithmic scale

CATEGORIZED FAILURE TYPE:  
NON-DOMINANT COHESIVE FAILURE AND INTERFACE FAILURE

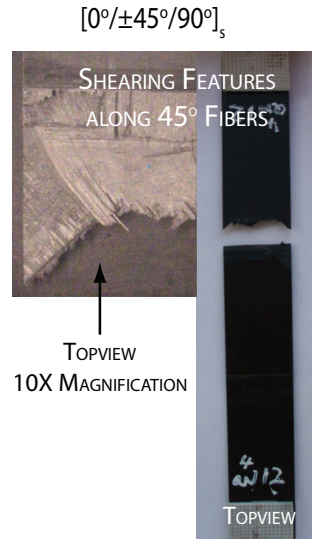
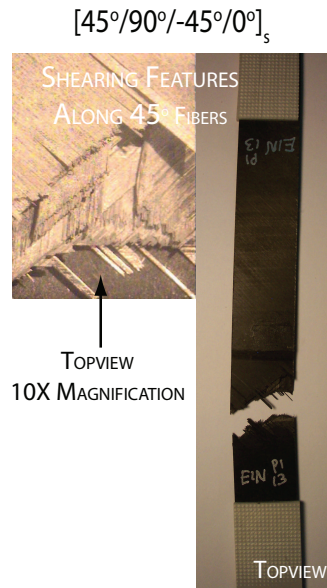
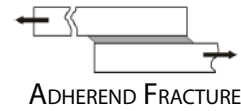


CATEGORIZED FAILURE TYPE:  
DOMINANT COHESIVE FAILURE



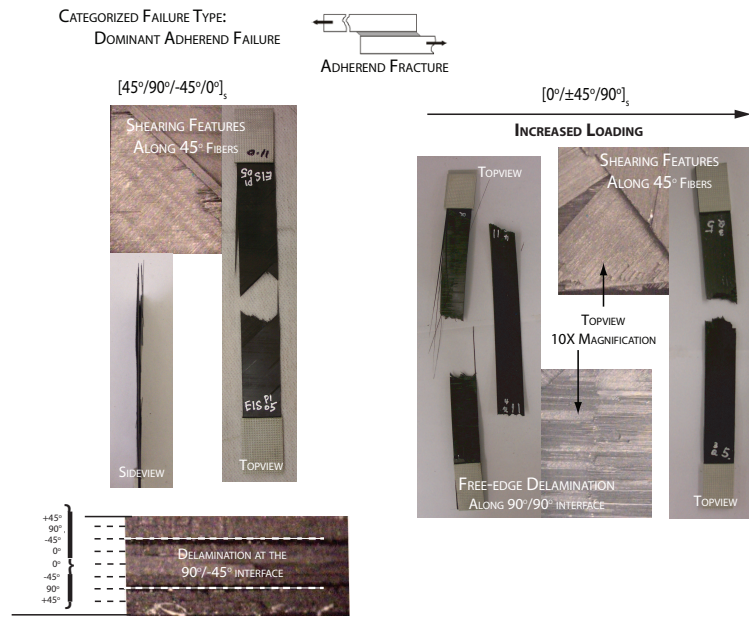
(a) Single lap joints

CATEGORIZED FAILURE TYPE:  
NON-DOMINANT ADHEREND FAILURE

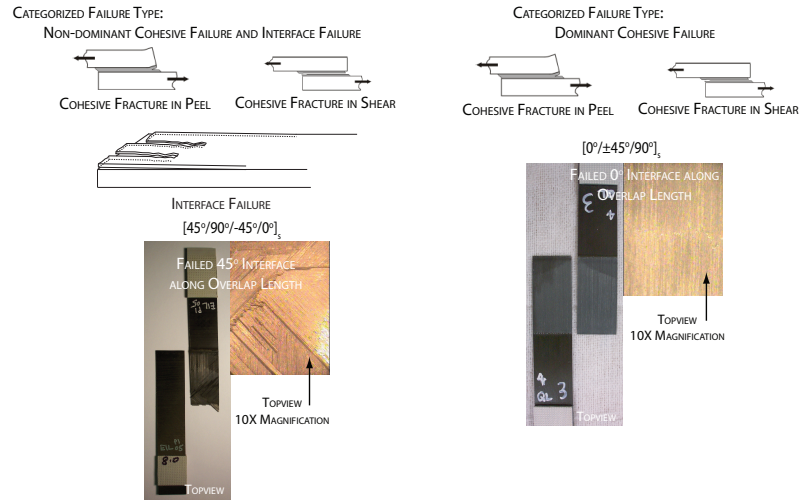


(b) Single nested overlap joints

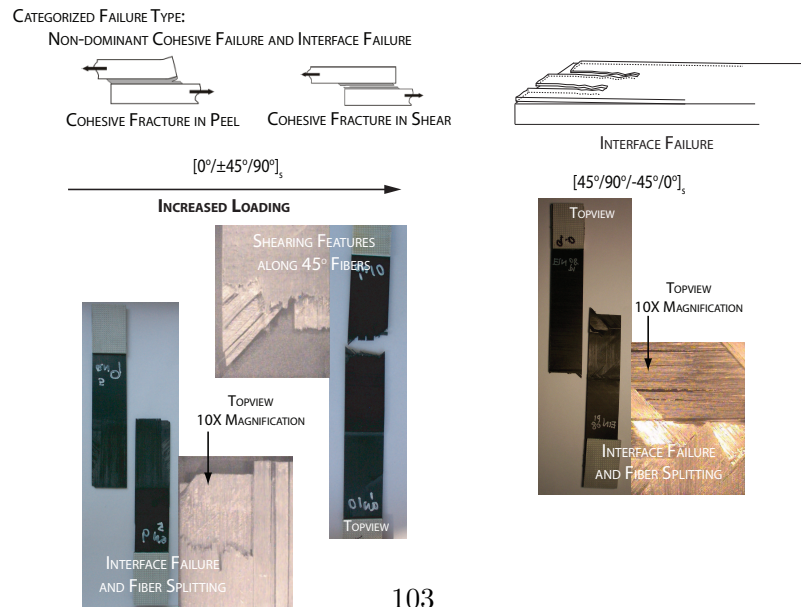
**Figure 43:** Quasi-static failure mode comparison for IM7/8551-7 (IM7/8551-7)  $[45/90/-45/0]_s$  and  $[0/\pm 45/90]_s$   
*Adherend fracture and cohesive fracture sketch taken from Heslehurst and Hart-Smith [49]*



(a) Straight laminates



(b) Single lap joints



(c) Single nested overlap joints

**Figure 44:** Fatigue failure mode comparison for IM7/8551-7 (IM7/8551-7)  $[45^\circ/90^\circ/-45^\circ/0^\circ]_s$  and  $[0^\circ/\pm 45^\circ/90^\circ]_s$

*Adherend fracture and cohesive fracture sketch taken from Heslehurst and Hart-Smith [49]*

**Table 24:** Material properties for S2-glass/epoxy (Cytec S2/E773FR)

$E_{11}$	$E_{22}$	Ply Thickness	$G_{12} = G_{13}$	$\nu_{12} = \nu_{13}$
48.36 GPa	12.53 GPa	0.22 mm	4.51 GPa	0.30
<i>ASTM D 3039-0012 for the tensile properties</i>				
<i>ASTM D 3518-9413 (reapproved 2001) for the shear properties</i>				

**Table 25:** UTS for S2/E773FR  $[0/\pm 45/90]_s$ 

	SL	Single lap joints	SNO joints
<b>Average</b>	568.83	146.63	226.68
<b>Maximum</b>	612.696	179.418	295.591
<b>Minimum</b>	463.634	126.772	201.505
<b>Standard Deviation</b>	49.171	14.347	27.908
<b>Coefficient of Variation (%)</b>	8.64	9.78	12.31

*UTS values are in MPa.*

record an adequate number of frames within a reasonable time. The material properties for S2/E773FR were characterized based on ASTM standards and provided in Table 24. The Average, Maximum, Minimum, Standard Deviation and CV for S2-glass/epoxy  $[0/\pm 45/90]_s$  SL, single lap, and SNO joints are provided in Table 25. These UTS values were used as a reference for setting the maximum cyclic stress for the IR-TSA technique.

The IR-TSA fatigue damage propagation images and failure modes for  $[0/\pm 45/90]_s$  and  $[45/90/-45/0]_s$  SL, single lap and SNO joints are illustrated in Figures 45, 46 and 47, respectively. The fatigue damage propagation for the S2-glass/epoxy  $[0/\pm 45/90]_s$  joints (Figures 45a, 46a and 47a) were mostly similar to their graphite/epoxy counterparts (Figures 37), with the exception of some minor damage types, such as fiber splitting, that were more prone to the S2-glass/epoxy material system.

The SL failed under dominant adherend fracture (Figure 45c), similar to the graphite/epoxy counterpart, with more extensive ED and fiber splitting in the  $90^\circ/90^\circ$  interface, indicating that ED was particularly significant in the S2-glass/epoxy  $[0/\pm 45/90]_s$  SL. A significant increase in the amount of ED in the  $90^\circ/90^\circ$  interface (Figure 45a: Yellow and green regions) was observed with increasing number of cycles in the S2-glass/epoxy  $[0/\pm 45/90]_s$  SL. In addition to ED, fiber splitting (Figure 45a: Cyan region) initiating from the sides of the specimen was also observed with the specimen failing ultimately under adherend

fracture. For the  $[45/90/-45/0]_s$ , ED in the  $90^\circ/90^\circ$  interface (Figure 45b: Blue region) was significantly reduced, although some local stress concentrations initiated from the sides (Figure 45b: Blue and red regions) as the number of cycles increased.

All the single lap joints (Figure 46c) failed under dominant cohesive fracture. As loading increased, more extensive fiber splitting in the overlap length along the  $0^\circ/0^\circ$  interface was observed. In the fatigue damage propagation, both lay-ups showed delamination initiating from the tapered end of the overlap length propagating inwards (Figures 46a and 46b: Blue and cyan regions) until ultimate failure. No ED was observed in the adherends or the overlap length.

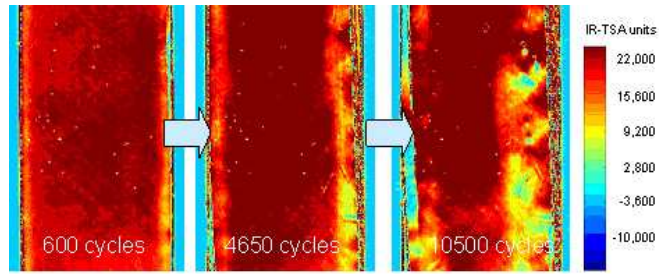
The S2-glass/epoxy SNO joints for both  $[0/\pm 45/90]_s$  and  $[45/90/-45/0]_s$  failed under non-dominant cohesive failure (Figures 47a and 47b: Blue and cyan regions), with a significant amount of interface failure observed along the overlap length as loading increased (Figure 47c) [96]. The interface failure occurred across a few adjacent layers of plies, with more regions of stress concentration (Figures 47a and 47b: Red regions) as compared to the single lap joint cases. There was no ED observed in S2-glass/E773FR SNO joints as compared to the IM7/8551-7 SNO joints due to the difference in material properties.

Although the effect of reduced ED in the  $90^\circ/90^\circ$  interface on the fatigue life of the joints was not quantified, the  $[45/90/-45/0]_s$  SL illustrated with the S2-glass/epoxy system showed significant reduction in ED in the  $90^\circ/90^\circ$  interface as compared to the  $[0/\pm 45/90]_s$  SL. An improvement in  $N_f$  was also observed for the  $[45/90/-45/0]_s$  in comparison to the  $[0/\pm 45/90]_s$  (Figures 45, 46 and 47), although this observed increase in  $N_f$  should not be inferred in general for the two lay-ups because only one specimen of each was tested.

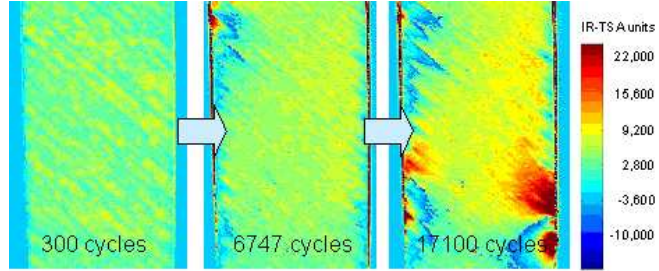
### **6.3 Effect of Specimen Width in $[45/90/-45/0]_s$ Free-edge Delamination Minimized Lay-up**

The UTS values for 1.0 inch, 1.5 inch and 2.0 inch wide  $[45/90/-45/0]_s$  SL are compared in Figure 48, while the S-N curves, along with their weighted non-linear least square power curve fits are illustrated on a linear and a semi-logarithmic scale in Figure 49. The power curve fits, obtained from the Matlab curve fitting toolbox, are given in Eqs. 10. The



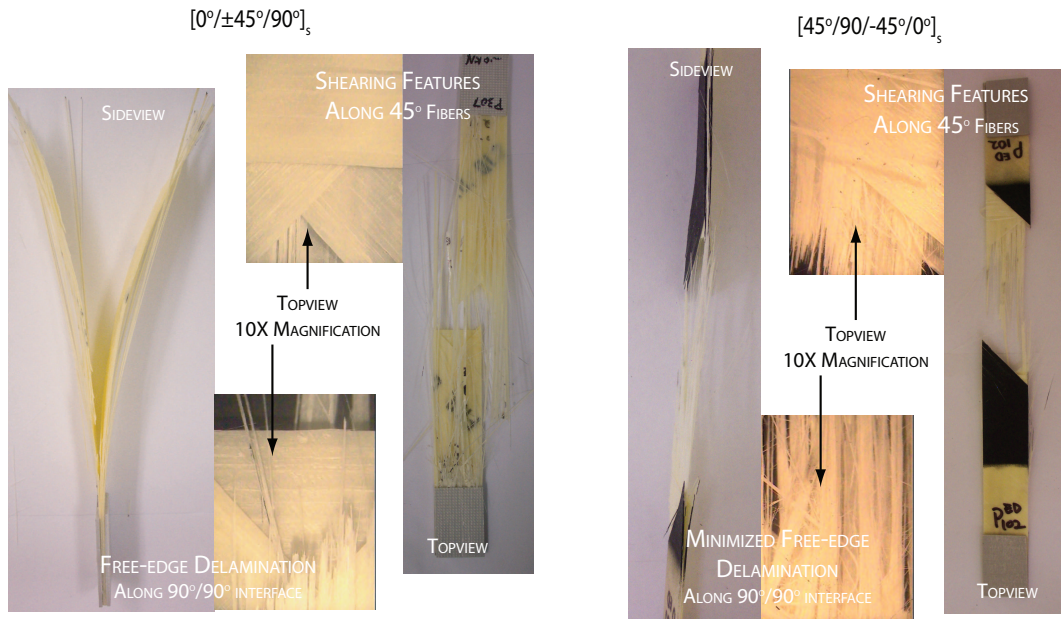


(a)  $[0/\pm 45/90]_s$ :  $\sigma_{max} \approx 0.4 \text{ UTS}([0/\pm 45/90]_s)$ ,  $N_f = 12537$



(b)  $[45/90/-45/0]_s$ :  $\sigma_{max} \approx 0.4 \text{ UTS}([0/\pm 45/90]_s)$ ,  $N_f = 23753$

CATEGORIZED FAILURE TYPE:  
DOMINANT ADHEREND FAILURE WITH SIGNIFICANT FIBER SPLITTING

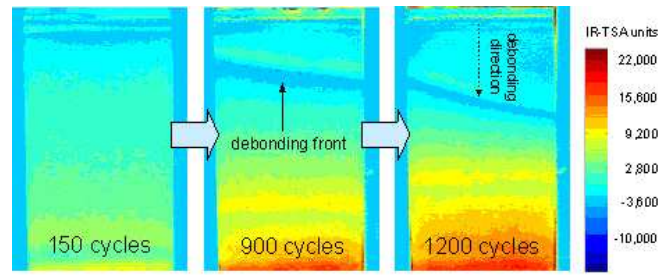


Adherend Fracture figure caption taken from Heslehurst and Hart-Smith (2002)

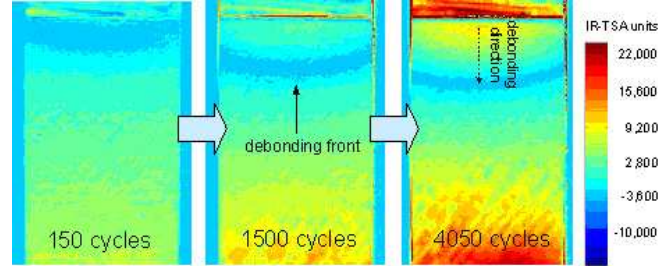
(c) Fatigue failure modes for S2/E773FR  $[0/\pm 45/90]_s$  and  $[45/90/-45/0]_s$ .

**Figure 45:** Straight laminates: Infrared TSA images showing fatigue damage propagation comparison and fatigue failure modes between  $[0/\pm 45/90]_s$  and  $[45/90/-45/0]_s$  S2/E773FR cycled at a frequency of 5 Hz and a R of 0.2





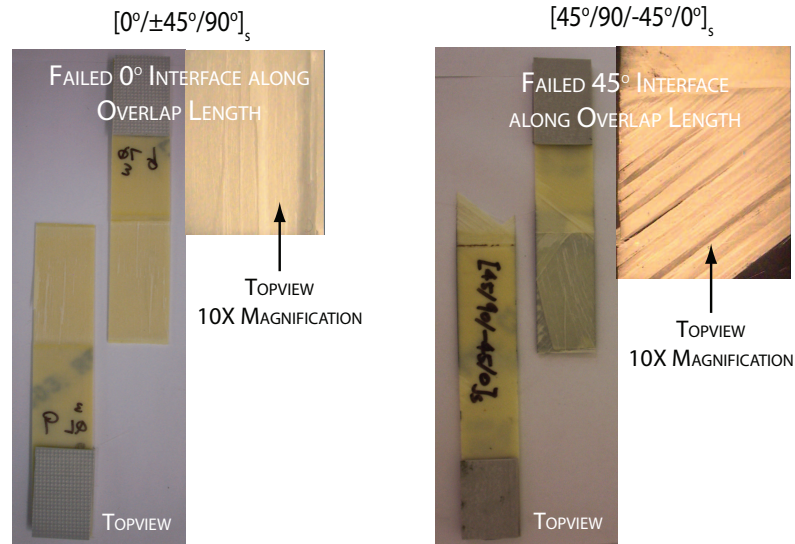
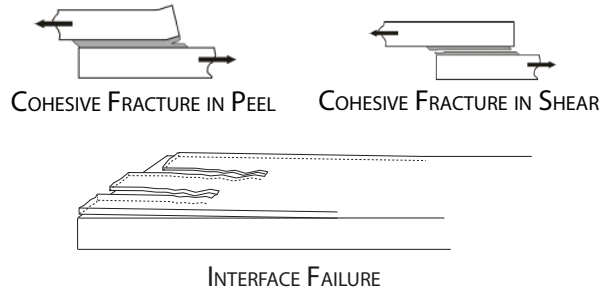
(a)  $[0/\pm 45/90]_s$ :  $\sigma_{max} \approx 0.8 \text{ UTS}([0/\pm 45/90]_s)$ ,  $N_f = 1286$



(b)  $[45/90/-45/0]_s$ :  $\sigma_{max} \approx 0.8 \text{ UTS}([0/\pm 45/90]_s)$ ,  $N_f = 4314$

#### CATEGORIZED FAILURE TYPE:

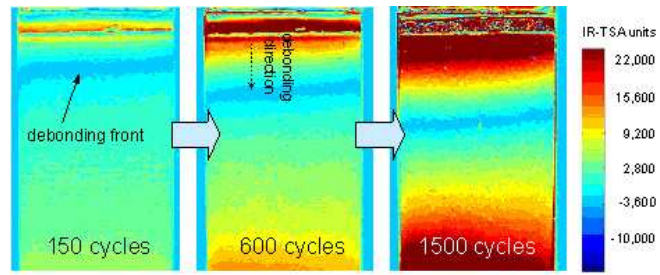
##### NON-DOMINANT COHESIVE FAILURE AND INTERFACE FAILURE



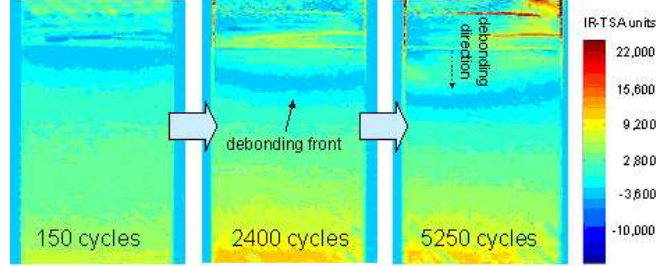
Cohesive Fracture figure caption taken from Heslehurst and Hart-Smith (2002)

(c) Fatigue failure modes for S2/E773FR  $[0/\pm 45/90]_s$  and  $[45/90/-45/0]_s$ .

**Figure 46:** Single lap joints: Infrared TSA images showing fatigue damage propagation comparison and fatigue failure modes between  $[0/\pm 45/90]_s$  and  $[45/90/-45/0]_s$  S2/E773FR cycled at a frequency of 5 Hz and a R of 0.2<sup>107</sup>



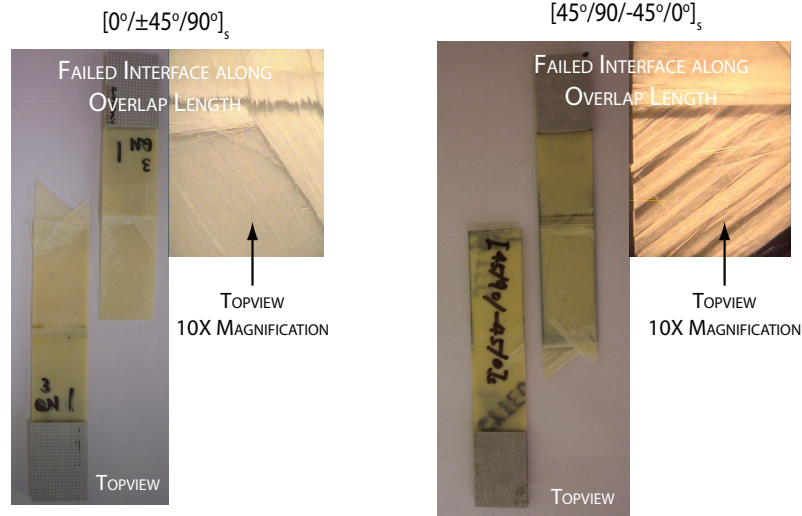
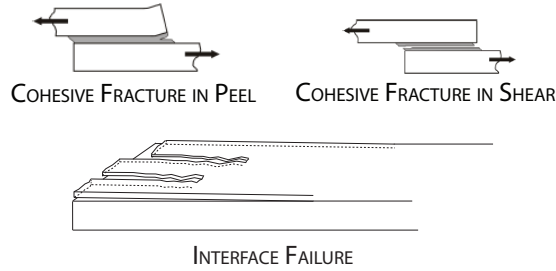
(a)  $[0/\pm 45/90]_s$ :  $\sigma_{max} \approx 0.8 \text{ UTS}([0/\pm 45/90]_s)$ ,  $N_f = 2120$



(b)  $[45/90/-45/0]_s$ :  $\sigma_{max} \approx 0.8 \text{ UTS}([0/\pm 45/90]_s)$ ,  $N_f = 5774$

#### CATEGORIZED FAILURE TYPE:

##### NON-DOMINANT COHESIVE FAILURE AND INTERFACE FAILURE



Cohesive Fracture figure caption taken from Heslehurst and Hart-Smith (2002)

(c) Fatigue failure modes for S2/E773FR  $[0/\pm 45/90]_s$  and  $[45/90/-45/0]_s$ .

**Figure 47:** Single nested overlap joints: Infrared TSA images showing fatigue damage propagation comparison and fatigue failure modes between  $[0/\pm 45/90]_s$  and  $[45/90/-45/0]_s$  S2/E773FR cycled at a frequency of 5 Hz and a R of 0.2

approximate fatigue limits are 410 MPa, 400 MPa, and 440 MPa for 1.0 inch, 1.5 inch, and 2.0 inch  $[45/90/-45/0]_s$  SL, respectively. The quasi-static and fatigue failure mode comparisons for 1.0 inch, 1.5 inch, and 2.0 inch  $[45/90/-45/0]_s$  SL are illustrated in Figures 50 and 51, respectively.

The extent of ED in the  $0^\circ/0^\circ$  interface was minimal as specimen width increased in the  $[45/90/-45/0]_s$  SL under both monotonic and cyclic loading (Quasi-static: Figure 50 and Fatigue: Figure 51). The minimized effect of ED in this lay-up resulted in quasi-static tensile strength that was independent of specimen width. A 1-way ANOVA table was performed to validate that there was also no significant difference in the UTS with increased specimen width. A significant amount of delamination at the  $90^\circ/-45^\circ$  interface was observed in this lay-up under fatigue, although the extent of this delamination was also independent of the specimen width. The effect of this delamination on fatigue endurance was also independent of the specimen width, as illustrated in the S-N curves (Figure 49).

Based on these results, ED in the midplane and delamination at the  $90^\circ/-45^\circ$  interface were both localized failure mechanisms that depended on parameters such as stacking sequence rather than width for both monotonic and cyclic loading.

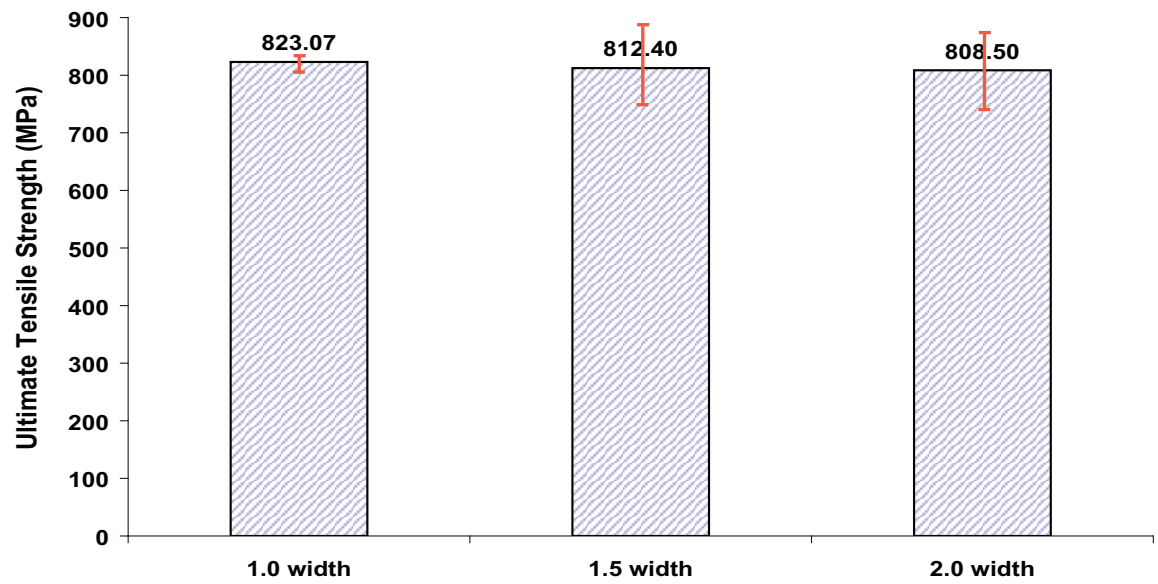


**Figure 48:** UTS comparison of IM7/8551-7 1.0 inch, 1.5 inch and 2.0 inch wide  $[45/90/-45/0]_s$  straight laminates  
*Standard deviation of quasi-static tests plotted as error bars*

### 1.0 inch width

$$S_{\max} \text{ (MPa)} = 1095 N_f^{-0.07469}$$
$$r^2 = 0.8617$$

### 1.5 inch width

$$S_{\max} \text{ (MPa)} = 910.3 N_f^{-0.06197}$$
$$r^2 = 0.8821$$

### 2.0 inch width

$$S_{\max} \text{ (MPa)} = 570.6 N_f^{-0.02092}$$
$$r^2 = 0.1936$$

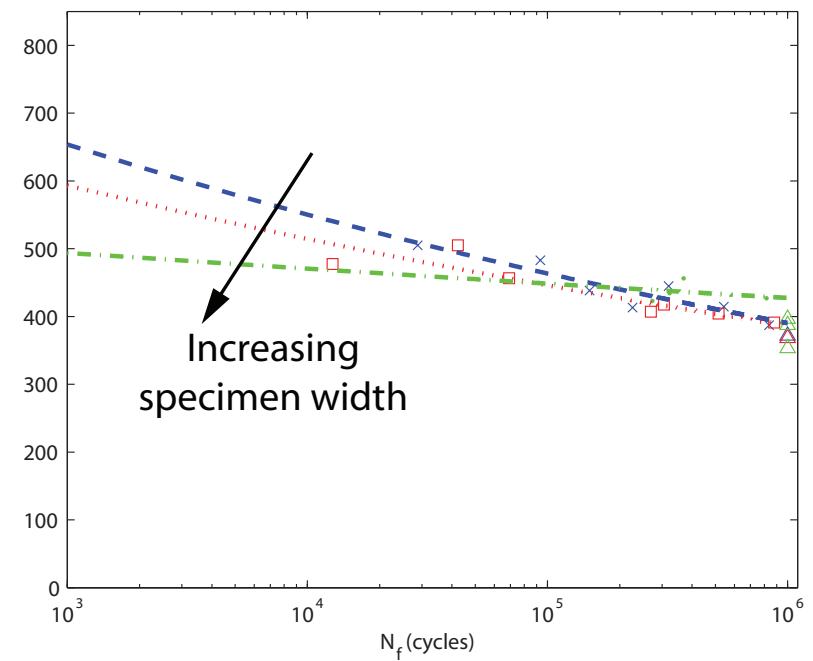
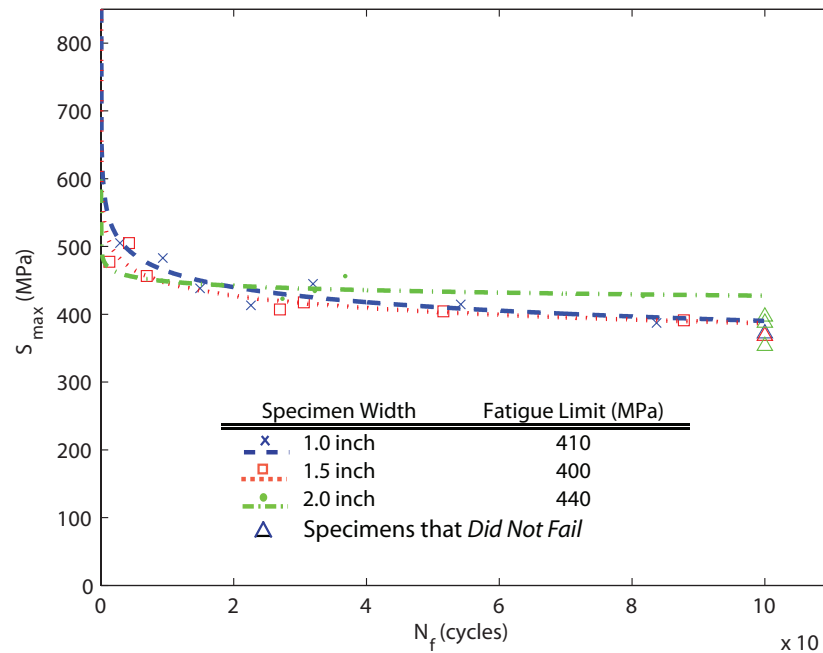


**Figure 49:** S-N curve on a linear scale and a semi-logarithmic scale for IM7/8551-7 1.0 inch, 1.5 inch and 2.0 inch wide  $[45/90/-45/0]_s$  straight laminates

CATEGORIZED FAILURE TYPE:  
DOMINANT ADHEREND FAILURE

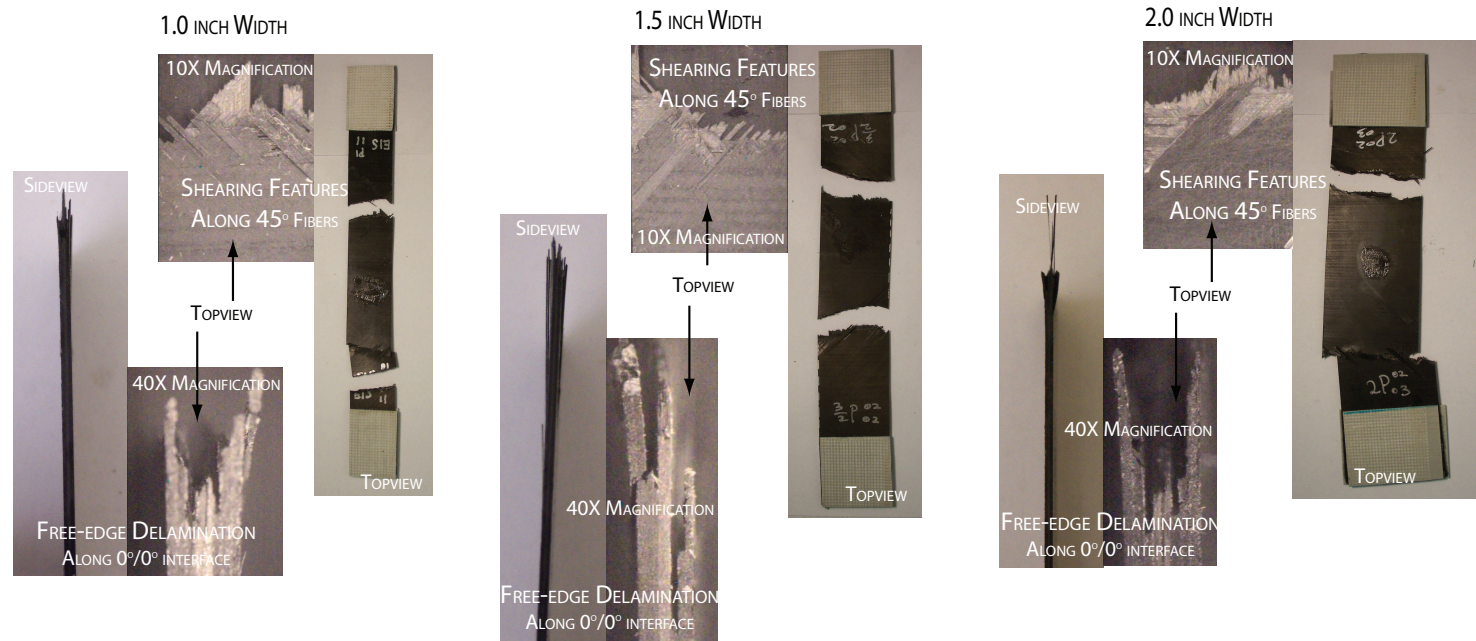
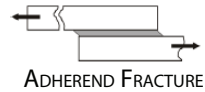


**Figure 50:** Quasi-static failure mode comparison for IM7/8551-7 (IM7/8551-7) 1.0 inch, 1.5 inch and 2.0 inch width  $[45/90/-45/0]_s$  straight laminates

*Adherend fracture sketch taken from Heslehurst and Hart-Smith [49]*



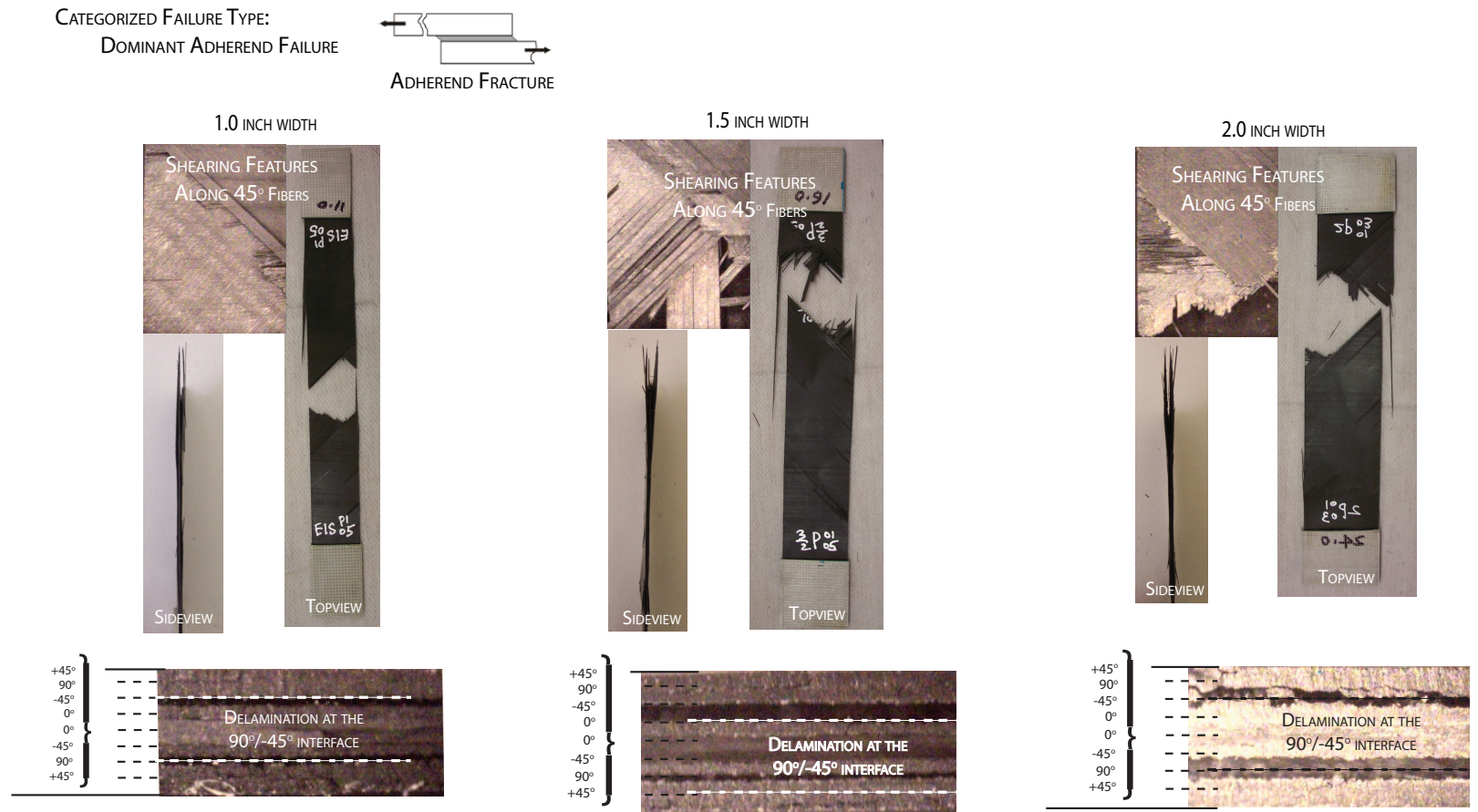


**Figure 51:** Fatigue failure mode comparison for 1.0 inch, 1.5 inch and 2.0 inch width IM7/8551-7 (IM7/8551-7)  $[45/90/-45/0]_s$  straight laminates under cyclic loading at frequency of 5 Hz, R of 0.1 and fatigue run-out at  $1 \times 10^6$  cycles  
*Adherend fracture sketch taken from Heslehurst and Hart-Smith [49]*

$$1.0 \text{ inch width} : S_{max} = 1095.0 N_f^{-0.07469}, \quad r^2 = 0.8617 \quad (10a)$$

$$1.5 \text{ inch width} : S_{max} = 910.3 N_f^{-0.06197}, \quad r^2 = 0.8821 \quad (10b)$$

$$2.0 \text{ inch width} : S_{max} = 570.6 N_f^{-0.02092}, \quad r^2 = 0.1936 \quad (10c)$$

## 6.4 Chapter Summary

The effect of suppressing free-edge delamination on joint strength was investigated under both monotonic and cyclic loading. Free-edge delamination was suppressed through reordering of the stacking sequence for eight-ply symmetric quasi-isotropic laminate to generate a closing mode in the midplane. A 15% improvement in UTS was observed for the free-edge delamination suppressed [45/90/ - 45/0]<sub>s</sub> SL as compared to the [0/ ± 45/90]<sub>s</sub> SL. However, no improvement was observed for the SNO joints, indicating that free-edge delamination was a critical failure mechanism for the SL but not the SNO joints. Suppressing free-edge delamination had no effect on the fatigue limit of both configurations. Although free-edge delamination was a critical failure mechanism for the SL, both the UTS and FL were found to be independent of specimen width for the [45/90/ - 45/0]<sub>s</sub> SL.



## CHAPTER VII

# CONCLUSION AND RECOMMENDATIONS FOR FUTURE WORK

### 7.1 *Conclusions*

This investigation complements two previous research efforts originated by *Coates and Armanios (2000, 2001)*, and expanded upon by *Cao and Dancila (2003, 2004)*, to characterize the SNO joint concept response under quasi-static and fatigue loading by expanding upon the lay-up configurations evaluated, and more importantly by investigating the effect of ply-swap lay-up modifications upon free edge delaminations in the joint region.

Previous work on the SNO joint concept compared quasi-static results within a single panel of manufactured specimens. The statistical reliability of the UTS based on specimens from multiple panels was assessed in this study through a comparison with the  $[0/\pm 45/90]_s$  single panel results from *Cao and Dancila (2003, 2004)*. In comparing the UTS, the multiple panel results showed a difference of 1% in standard deviation for single lap joints and a 6% difference in standard deviation for the SNO joints. The former was attributed to the consistency of the observed dominant cohesive fracture, while the increase in scatter for the latter was attributed to the increase in complexity for the fiber-dominated non-dominant adherend fracture. Despite the moderate statistic deviations observed for the single lap and SNO joints under monotonic loading, a significant amount of scatter near the FL was observed for these configurations under cyclic loading, indicating the extent of scatter under fatigue for the IM7/8551-7 material system.

To further ascertain the improvement in strength of the SNO joint over the single lap joint, the influence of stacking sequences was also investigated in this study. In previous investigations, only the  $[0]_8$  and the  $[0/\pm 45/90]_s$  lay-up was studied. The present work expanded the investigation to  $[0/\pm \theta/90]_s$ ,  $[45/90/-45/0]_s$ , and  $[45/0/-45/90]_s$  families.

For the  $[0/\pm\theta/90]_s$  family, the quasi-static strength compared at approximately 5-10% whereas the fatigue endurance showed an improvement of approximately 20-25%. The strength improvement of an eight-ply symmetric quasi-isotropic SNO joint over single lap joint was also assessed through three variations of the stacking sequence, namely,  $[0/\pm 45/90]_s$ ,  $[45/90/-45/0]_s$ , and  $[45/0/-45/90]_s$ . Similar to the  $[0/\pm\theta/90]_s$  family, the quasi-static strength compared at approximately 5-10%. However, no improvement was observed in the fatigue limit for  $[45/90/-45/0]_s$ .

While the influence of free-edge delamination on the stiffness and strength of SL has been studied extensively, its effect on joints that exhibit similar fiber-dominated failure has not been documented. In this work, the effect of suppressing free-edge delamination on joint strength was investigated under both monotonic and cyclic loading. Free-edge delamination was suppressed through reordering of the stacking sequence for eight-ply symmetric quasi-isotropic laminate to generate a closing mode in the midplane. A 15% improvement in UTS was observed for the free-edge delamination suppressed  $[45/90/-45/0]_s$  SL as compared to the  $[0/\pm 45/90]_s$  SL. However, no improvement was observed for the SNO joints, indicating that free-edge delamination was a critical failure mechanism for the SL but not the SNO joints. Suppressing free-edge delamination had no effect on the fatigue limit of either configuration.

The use of infrared thermoelastic stress analysis technique as a non-destructive evaluation tool has been studied for SL. In this work, IR-TSA was successful in qualitative assessment of composite joints, identifying joint failure modes, such as cohesive fracture and extent of free-edge delamination. Quantitative use of this technique on composite joints requires more study, particularly on more complex stacking sequences.

Based on the work done by Cao and Dancila (2003, 2004) [13, 12] and the current study, there is limited success with single transducer parametric AE study of composite joint coupon because of significant interference in the measured elastic waves. Sources of interference include reflection from coupon edges and refraction across the laminate. The stacking sequence, particularly within the overlap region, and the large transducer diameter relative to the coupon width further contaminate the measured elastic waves.

## ***7.2 Recommendations for Future Work***

Based on the results and understanding generated through this investigation, it is recommended that future research efforts focus on the following topics:

- 1) A computational, finite element method based investigation combining a micromechanics-type approach with appropriate composite material failure criteria in order to analyze the mechanical response and failure of single lap and SNO joints with lay-ups corresponding to those evaluated in the present experimental investigation. A correlation of results with those presently reported will provide insight into the predictive capability of the computational approach with respect to both the strength and the failure mechanisms involved. The influence of lay-up on the free-edge delamination of SNO joints can also be computationally investigated and results can be correlated with those presently reported.
- 2) A quantitative assessment of composite joints using the IR-TSA technique.
- 3) An investigation between the number of nested layers and overlap region length, which is expected to result in reduction of the overlap region length.
- 4) Extension of the SNO concept for post-cured bonded joints.

## APPENDIX A

### EQUIPMENT SETUP AND COUPON MANUFACTURING

The equipment setup, the joint configurations, the nested concept and manufacturing details are described in this appendix.

#### *A.1 Equipment and Testing Setup*

The quasi-static and fatigue testing were performed under load control on an MTS servo-hydraulic testing machine with a load cell of 50 kN capacity. Table 26 lists the tuning parameters on the MTS testing machine. The equipment setup for the acoustic emission study discussed in Chapters 4 and 5 is illustrated in Figure 52. The acoustic emission events were detected with a DiSP Acoustic Emission (AE) Workstation from Physical Acoustics to track the damage accumulated in the specimen during quasi-static loading. The quasi-static cumulative AE count peaks were monitored as fatigue limit predictors and a set of conditions for the validity of this hypothesis were investigated.

The infrared thermoelastic stress analysis used to monitor the progression of fatigue damage used a DeltaTherm DT1500 infrared-red (IR) camera with high temperature resolution (approximately 1mK). The loading signal from the MTS servo-hydraulic testing machine was used to synchronize the IR quantitative data acquisition to obtain the in-phase images with the mechanical loading, integrated over a 30 seconds duration [38]. This integration duration time was chosen to capture the IR images under semi-adiabatic conditions achieved from the cyclic loading. Fully adiabatic conditions during in-situ fatigue damage monitoring are difficult to achieve, especially under a low cycle fatigue protocol. However, with a short integration time (30 seconds or less at a 5 Hz frequency) and a fast rate of data accumulation, satisfactory semi-adiabatic results can be obtained. This setup is illustrated in Figure 53.

**Table 26:** MTS tuning parameters: PIDF load control values

Control Mode	Value
<b>Proportional (P) Gain</b>	20.0
<b>Integral (I) Gain</b>	6.0
<b>Derivative (D) Gain</b>	0.0
<b>Feed Forward (F) Gain</b>	0.0
<b>Forward Loop (FL) Filter</b>	300 Hz

For post-mortem examination of failed specimens, a National (DC3-420T) digital microscope with a 0.4 mega pixel built-in camera and up to 40X magnification was used. This setup is illustrated in Figure 54.

## ***A.2 Composite Manufacturing***

Similar co-cured manufacturing procedure is also detailed in Coates (2001) [25] and Cao (2004) [14].

### **A.2.1 Curing Cycle**

Graphite/epoxy (IM7/8551-7) unidirectional prepreg from Hexcel Corporation and S2-glass/epoxy (S2-glass/E773FR) unidirectional prepreg from Cytec Engineered Materials were used in this investigation. The curing follows the manufacturer's suggested cycle with a maximum temperature of  $350^{\circ}F$  ( $177^{\circ}C$ ) and a maximum pressure of 85 psi (586054 Pa) for the IM7/8551-7 and a maximum temperature of  $265^{\circ}F$  ( $129^{\circ}C$ ) and a maximum pressure of 85 psi (586054 Pa) for the S2-glass/E773FR. The curing cycle, depicted in Figure 55, is approximately 5 hours for the IM7/8551-7 and approximately 4 hours for the S2-glass/E773FR.

### **A.2.2 Co-cured composite joints**

Unidirectional prepreg with different fiber orientations ( $0^{\circ}$ ,  $30^{\circ}$ ,  $45^{\circ}$ ,  $60^{\circ}$  and  $90^{\circ}$ ) were cut, laid up by hand and placed in a 13x17 inches (33x43 cm) aluminum mold as illustrated in Figure 56. The mold was then vacuum bagged and placed in a horizontal 20x36 inches (51x91 cm) workspace autoclave, depicted in Figure 57. The vacuum bagging procedure

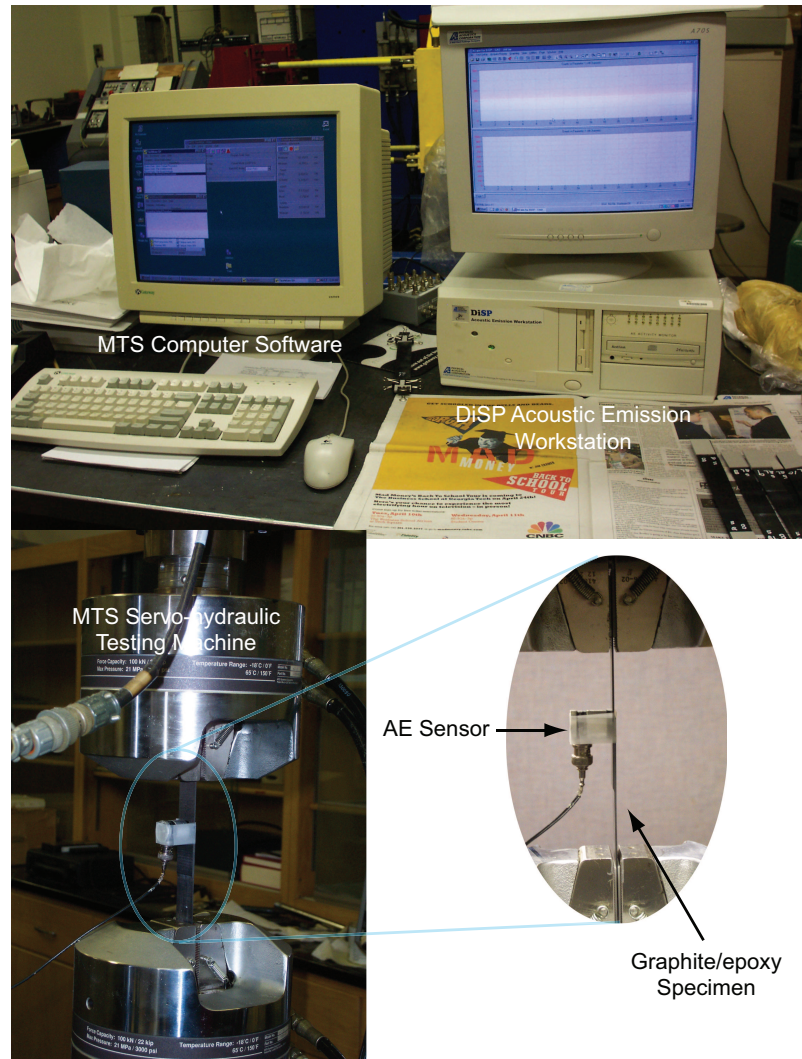


**Figure 52:** AE workstation and MTS servo-hydraulic testing machine setup

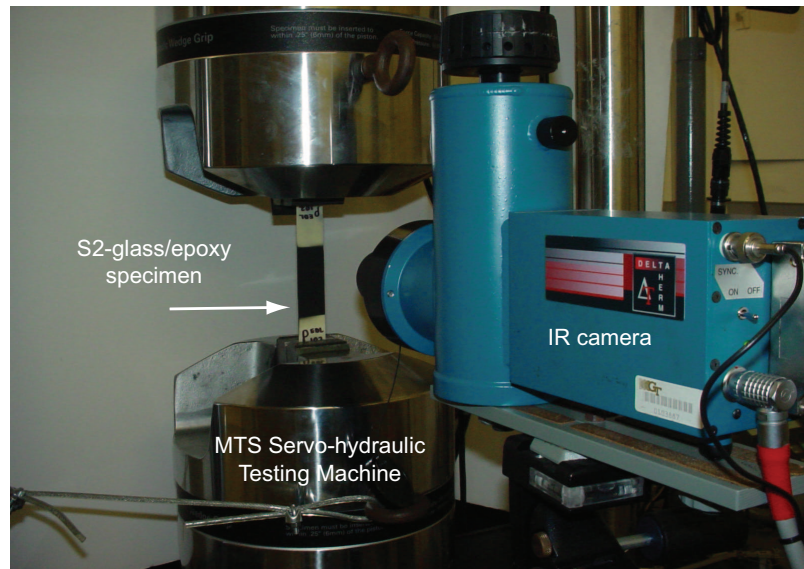


**Figure 53:** IR camera and MTS servo-hydraulic testing machine setup

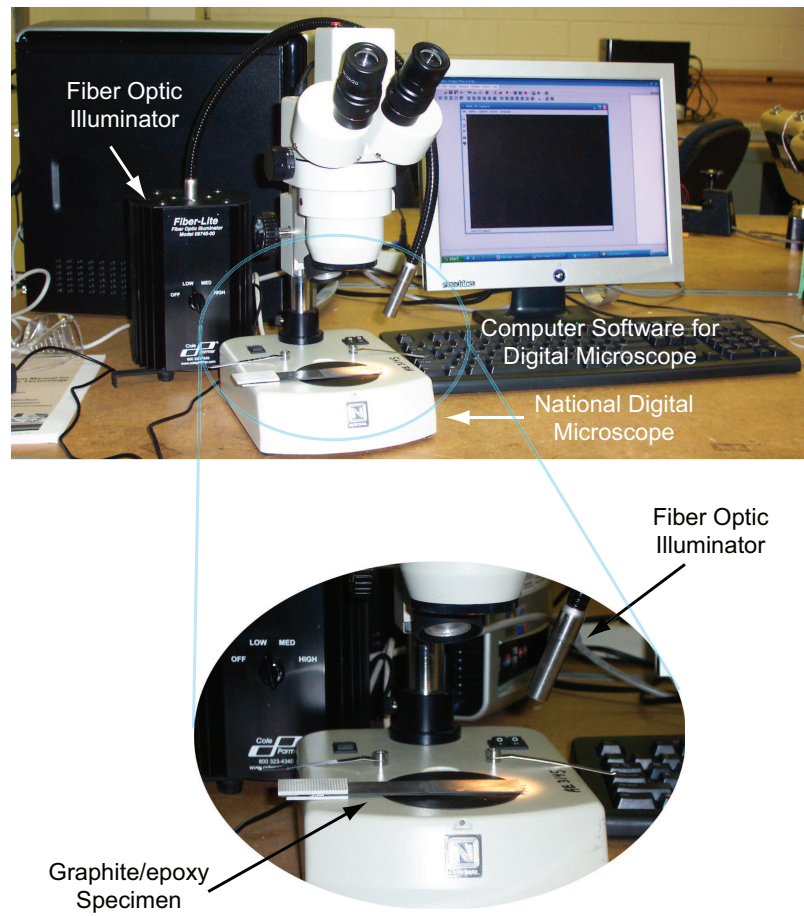
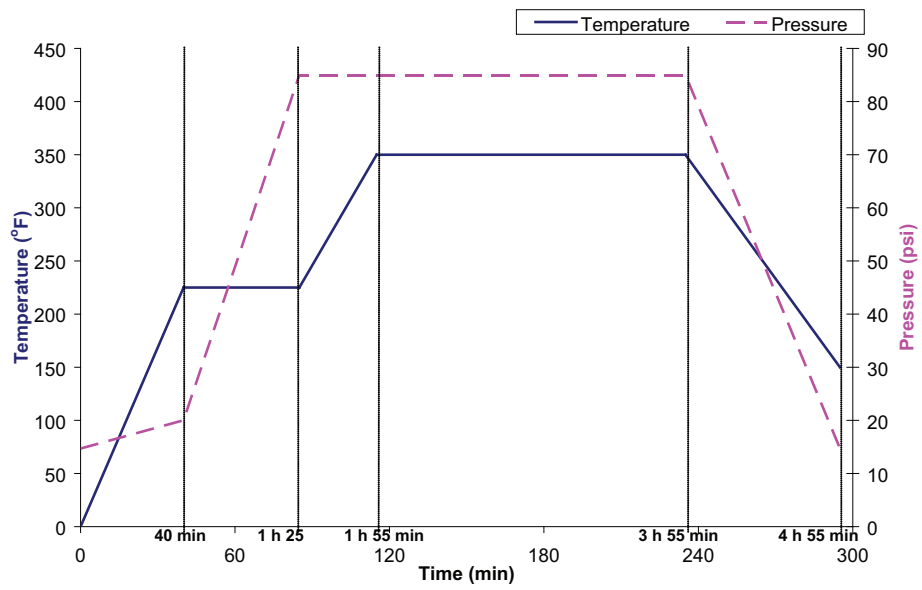
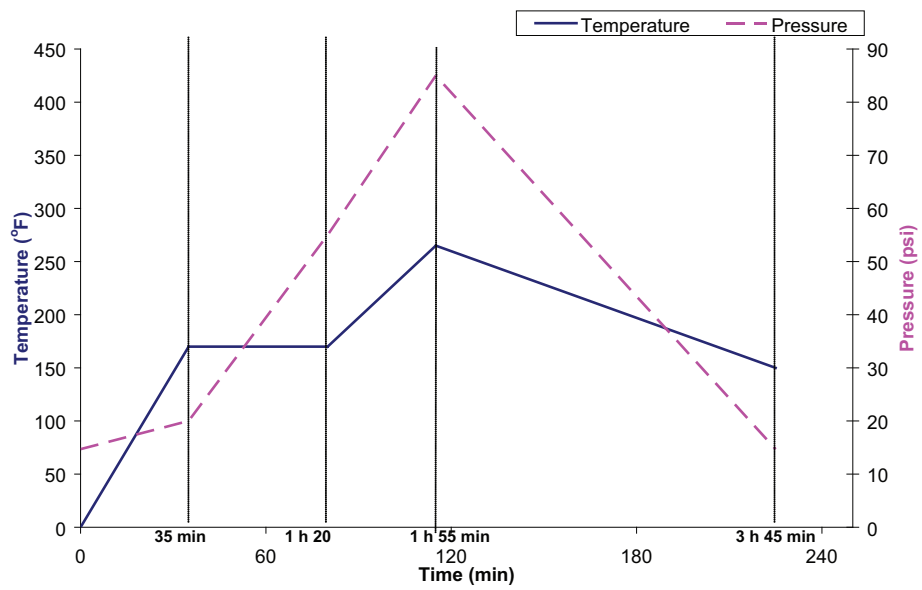


**Figure 54:** *National* digital microscope



(a) Graphite/epoxy IM7/8551-7



(b) S2-glass/epoxy S2-glass/E773FR

**Figure 55:** Curing cycle for IM7/8551-7 and S2-glass/E773FR



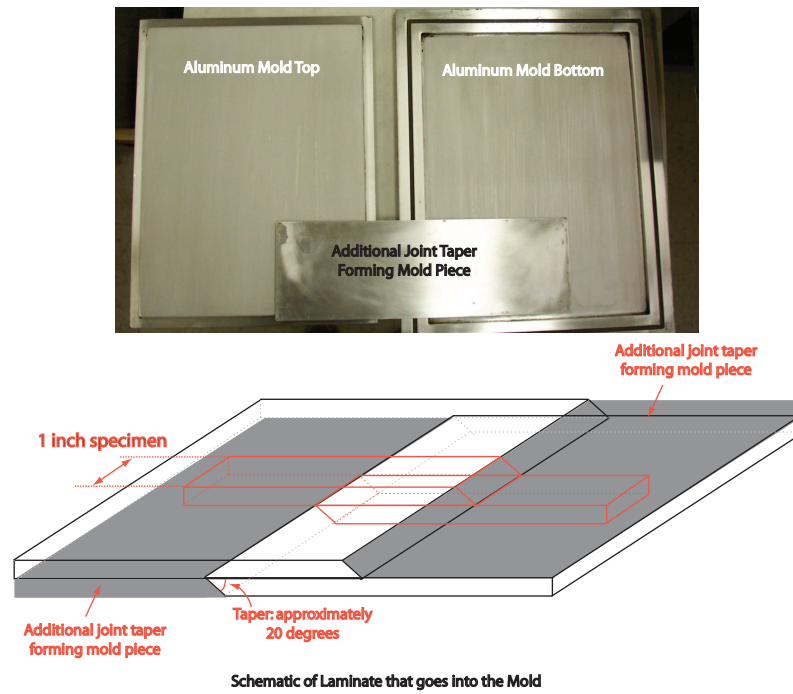


**Figure 56:** Co-cured composite joint mold

follows a general method for composite prepreg.

Both the single lap (Figure 1b) and SNO (Figure 1c) joints used in this investigation are co-cured with no additional layer of adhesive. The SNO joint is derived from the single lap joint through overlapping/interleafing of adjoining top/bottom adherend plies. An approximate  $20^\circ$  taper was built-in the single lap and the SNO joints by slightly displacing each adjacent ply. The taper minimizes stress singularity at the end of the overlap length, which exacerbates cohesive fracture in peel. This tapered angle is also reflected on the additional piece of mold for the joint as illustrated in Figure 56.

### ***A.3 Load Path Eccentricity***

Fiber-glass tabs were used to improve surface contact and prevent slipping between the coupons and the grips of the testing machines. Tabs of equal thickness are used on the SL (Figure 1a). However, because of the inherent geometry of the single lap (Figure 1b) and SNO joints (Figure 1c), fiber-glass tabs of unequal thickness, as depicted in Figure 59, were used to reduce load eccentricity resulting in premature failure. Figure 58 illustrates this development of peel stress in single lap joints.



**Figure 57:** *American Autoclave* with a 20x36 inches horizontal workspace

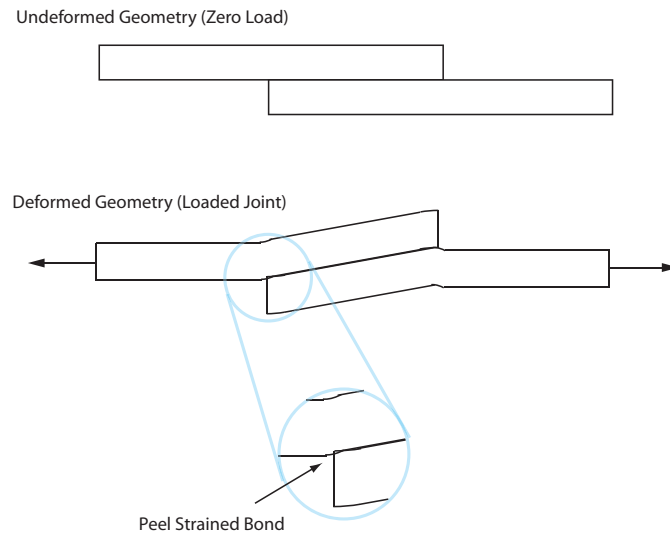


**Figure 58:** Development of peel stresses due to eccentricity in single lap joints

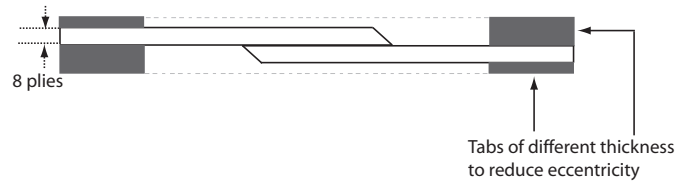


**Figure 59:** Fiberglass tabs of different thickness to reduce eccentricity in load path

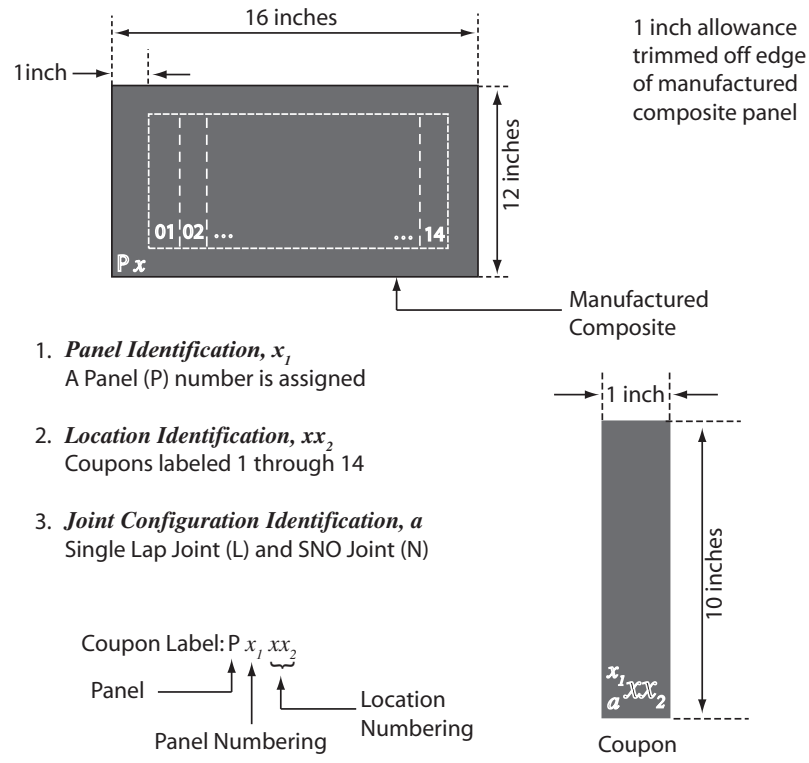


**Figure 60:** Specimen labeling

#### A.4 Specimen Labeling

Composite materials have significantly lower thermal conductivity than the mold material, which is typically made of aluminum. This temperature gradient across the laminate and the mold can result in laminate thickness variation during curing. In order to minimize this effect, specimens were manufactured in panels instead of individually. Manufacturing specimens in panels also reduce the inconsistency of the hand lay-up method in stacking up each specimen individually.

Fourteen one-inch (2.54 cm) wide coupons were cut from each manufactured panel. Each specimen was identified as  $Px_1xx_2$  denoted by its panel number and location along the panel, respectively, as illustrated in Figure 60. Additional subscripts were used to differentiate between the lay-up and configuration. Table 27 shows the nomenclature used for the lay-up and configuration identification. Coupons cut from the edges of the panel were discarded due to their non uniform thickness. Coupons with 3-5% variation in either thickness or width were discarded, as well.

**Table 27:** Nomenclature used for lay-up and configuration identification

<b>Configuration Nomenclature</b>	
S	Straight laminates
L	Single lap joints
N	Single nested overlap joints

<b>Lay-up Nomenclature</b>	
U	$[0]_8$
30	$[0/\pm 30/90]_s$
Q	$[0/\pm 45/90]_s$
60	$[0/\pm 60/90]_s$
EDH	$[45/0/-45/90]_s$
EDL	$[45/90/-45/0]_s$

## APPENDIX B

### SUMMARY OF ULTIMATE STRENGTH FOR QUASI-STATIC TEST SPECIMENS

The Average, Maximum, Minimum, Standard Deviation and Coefficient of Variation (CV) for the Ultimate Tensile Load (UTL) and the Ultimate Tensile Stress (UTS) under quasi-static loading for SL, single lap and SNO joints for each set of results are provided in this appendix. An average nominal cross-sectional area for each panel was used in computing the UTS values. Specimens that failed too close to the end tabs were discarded from the results and marked with an “x” in the Accept/Reject column. The average, standard deviation and CV values listed under this column were computed based on discarding the reject joints. In computing the stress values, the average nominal cross-sectional area for each panel and the nominal cross-section area for each specimen was used for multiple and single panel results, respectively.

The individual UTS values for IM7/8551-7  $[0]_s$  and  $[0/\pm\theta/90]_s$  family of SL, single lap and SNO joints used in behavior characterization (Chapters 2 and 3) are provided in Tables 28-39. The individual UTS values for IM7/8551-7  $[45/0/-45/90]_s$  SL, single lap and SNO joints used in fatigue damage initiation and propagation (Chapter 5) are provided in Tables 40-42. The individual UTS values for S2/E773FR  $[0/\pm 45/90]_s$  and IM7/8551-7  $[45/90/-45/0]_s$  SL, single lap and SNO joints used in the joint strength improvement (Chapter 6) study are provided in Tables 43-50.

**Table 28:** Straight laminates (IM7/8551-7 [0]<sub>8</sub>): Summary of quasi-static test specimens

Coupon	Load (kN)	Stress (MPa)	Accept\Reject
<b>Panel 1:</b> <i>Average Nominal Cross-sectional Area = 29.4 mm<sup>2</sup></i>			
P102	65.340	2225.64	✓
P103	73.500	2503.59	✓
P111	70.705	2408.39	✓
<b>Panel 2:</b> <i>Average Nominal Cross-sectional Area = 29.1 mm<sup>2</sup></i>			
P202	59.298	2036.96	✓
P208	54.711	1879.39	✓
P212	49.119	1687.30	✓
<b>Panel 3:</b> <i>Average Nominal Cross-sectional Area = 28.7 mm<sup>2</sup></i>			
P302	65.925	2297.83	✓
P307	50.094	1746.04	✓
P311	62.760	2187.52	✓
<b>Minimum</b>	49.119	1687.296	
<b>Maximum</b>	73.500	2503.590	
<b>Average</b>	61.27	2108.07	
<b>Standard Deviation</b>	8.649	289.016	
<b>Coefficient of Variation (%)</b>	14.12	13.71	

**Table 29:** Single lap joints (IM7/8551-7 [0]<sub>8</sub>): Summary of quasi-static test specimens

Coupon	Load (kN)	Stress (MPa)	Accept\Reject
<b>Panel 1:</b> <i>Average Nominal Cross-sectional Area = 34.0 mm<sup>2</sup></i>			
P101	17.368	511.50	×
P105	28.433	837.38	✓
P112	27.034	796.17	✓
<b>Panel 2:</b> <i>Average Nominal Cross-sectional Area = 34.9 mm<sup>2</sup></i>			
P201	22.908	656.57	✓
P208	28.538	817.93	✓
P212	26.296	753.67	✓
<b>Panel 3:</b> <i>Average Nominal Cross-sectional Area = 34.8 mm<sup>2</sup></i>			
P304	26.907	773.34	✓
P312	26.475	760.93	✓
P313	26.698	767.34	✓
<b>Minimum</b>	17.368	511.503	
<b>Maximum</b>	28.538	837.377	
<b>Average</b>	25.63	741.65	26.66 770.42
<b>Standard Deviation</b>	3.498	100.214	1.737 54.451
<b>Coefficient of Variation (%)</b>	13.65	13.51	6.51 7.07

**Table 30:** SNO joints (IM7/8551-7 [0]<sub>s</sub>): Summary of quasi-static test specimens

	Coupon	Load (kN)	Stress (MPa)	Accept\Reject
<b>Panel 1:</b>	<i>Average Nominal Cross-sectional Area = 29.4 mm<sup>2</sup></i>			
	P101	27.711	941.94	✓
	P104	35.291	1199.60	×
	P110	36.394	1237.10	✓
<b>Panel 2:</b>	<i>Average Nominal Cross-sectional Area = 27.9 mm<sup>2</sup></i>			
	P202	33.966	1216.54	✓
	P204	33.727	1207.98	✓
	P212	31.725	1136.28	✓
<b>Panel 3:</b>	<i>Average Nominal Cross-sectional Area = 29.3 mm<sup>2</sup></i>			
	P301	34.338	1174.00	✓
	P306	35.187	1203.03	✓
	P312	30.690	1049.28	✓
<b>Minimum</b>		27.711	941.945	
<b>Maximum</b>		36.394	1237.095	
<b>Average</b>		33.23	1151.75	
<b>Standard Deviation</b>		2.722	96.706	
<b>Coefficient of Variation (%)</b>		8.19	8.40	

**Table 31:** Straight laminates (IM7/8551-7 [0/ ± 30/90]<sub>s</sub>): Summary of quasi-static test specimens

	Coupon	Load (kN)	Stress (MPa)	Accept\Reject
<b>Panel 1:</b>	<i>Average Nominal Cross-sectional Area = 29.6 mm<sup>2</sup></i>			
	P101	23.285	846.95	✓
	P102	24.746	825.77	✓
	P103	23.443	757.13	✓
	P112	22.499	742.70	✓
	P113	23.489	854.21	✓
<b>Minimum</b>		22.499	742.695	
<b>Maximum</b>		24.746	854.212	
<b>Average</b>		23.49	805.35	
<b>Standard Deviation</b>		0.807	51.928	
<b>Coefficient of Variation (%)</b>		3.43	6.45	



**Table 32:** Single lap joints (IM7/8551-7  $[0/\pm 30/90]_s$ ): Summary of quasi-static test specimens

Coupon	Load (kN)	Stress (MPa)	Accept\Reject
<b>Panel 1:</b> <i>Average Nominal Cross-sectional Area = 29.8 mm<sup>2</sup></i>			
P101	15.645	574.15	✓
P102	16.758	549.88	✓
P103	17.000	560.71	✓
P107	15.525	523.49	✓
P108	14.794	488.54	✓
Minimum	15.525	523.489	
Maximum	16.758	574.154	
Average	15.98	549.17	
Standard Deviation	0.680	25.340	
Coefficient of Variation (%)	4.26	4.61	

**Table 33:** SNO joints (IM7/8551-7  $[0/\pm 30/90]_s$ ): Summary of quasi-static test specimens

Coupon	Load (kN)	Stress (MPa)	Accept\Reject
<b>Panel 1:</b> <i>Average Nominal Cross-sectional Area = 29.5 mm<sup>2</sup></i>			
P101	18.482	670.08	✓
P102	18.267	623.50	✓
P103	17.937	598.07	✓
P112	16.108	535.52	✓
P113	17.160	601.34	✓
Minimum	16.108	535.525	
Maximum	18.482	670.077	
Average	17.59	605.70	
Standard Deviation	0.969	48.639	
Coefficient of Variation (%)	5.51	8.03	

**Table 34:** Straight laminates (IM7/8551-7 [0/  $\pm$  45/90]<sub>s</sub>): Summary of quasi-static test specimens

	Coupon	Load (kN)	Stress (MPa)	Accept\Reject	
Panel 1:	Average Nominal Cross-sectional Area = 28.8 mm <sup>2</sup>				
	P105	21.244	738.23	✓	
	P106	19.021	660.98	✓	
	P107	19.751	686.35	✓	
	P111	20.760	721.41	✓	
	P112	20.748	721.00	✓	
Panel 2:	Average Nominal Cross-sectional Area = 28.0 mm <sup>2</sup>				
	P202	20.749	740.84	×	
	P203	20.570	734.45	✓	
Panel 3:	Average Nominal Cross-sectional Area = 28.7 mm <sup>2</sup>				
	P302	21.761	759.16	×	
	P303	20.990	732.26	✓	
Panel 4:	Average Nominal Cross-sectional Area = 28.7 mm <sup>2</sup>				
	P401	22.012	766.53	×	
	P402	22.249	774.79	✓	
	P412	20.898	727.74	✓	
	P413	19.699	727.74	✓	
Minimum		19.021	660.984		
Maximum		22.249	774.786		
Average		20.80	726.90	20.59	718.32
Standard Deviation		0.925	32.967	0.910	32.489
Coefficient of Variation (%)		4.45	4.54	4.42	4.52

**Table 35:** Single lap joints (IM7/8551-7  $[0/\pm 45/90]_s$ ): Summary of quasi-static test specimens

Coupon	Load (kN)	Stress (MPa)	Accept\Reject
<b>Panel 1:</b> <i>Average Nominal Cross-sectional Area = 26.3 mm<sup>2</sup></i>			
<i>P101</i>	15.279	581.20	✓
<i>P102</i>	14.930	567.93	✓
<i>P105</i>	17.508	665.99	✓
<i>P112</i>	16.005	608.82	✓
<i>P113</i>	16.462	626.20	✓
<b>Panel 2:</b> <i>Rejected ∴ poor surface texture and dryness</i>			
<b>Panel 3:</b> <i>Average Nominal Cross-sectional Area = 29.9 mm<sup>2</sup></i>			
<i>P301</i>	18.210	608.87	✓
<i>P302</i>	20.534	686.57	✓
<i>P312</i>	20.294	678.55	✓
<i>P313</i>	17.425	582.62	✓
<b>Panel 4:</b> <i>Average Nominal Cross-sectional Area = 28.5 mm<sup>2</sup></i>			
<i>P401</i>	16.907	593.61	✓
<i>P402</i>	18.517	650.14	✓
<i>P412</i>	19.259	676.19	✓
<i>P413</i>	18.273	641.57	✓
<b>Minimum</b>	14.294	567.925	
<b>Maximum</b>	20.534	686.570	
<b>Average</b>	17.66	628.33	
<b>Standard Deviation</b>	1.282	39.421	
<b>Coefficient of Variation (%)</b>	7.26	6.27	

**Table 36:** SNO joints (IM7/8551-7 [0/  $\pm$  45/90]<sub>s</sub>): Summary of quasi-static test specimens

	Coupon	Load (kN)	Stress (MPa)	Accept\Reject	
Panel 1:	Average Nominal Cross-sectional Area = 29.3 mm <sup>2</sup>				
	P101	17.700	603.38	✓	
	P102	17.027	580.43	✓	
	P103	18.248	622.09	✓	
	P104	21.005	716.06	×	
	P105	21.258	724.69	✓	
	P106	19.828	675.92	✓	
	P112	18.267	622.72	✓	
Panel 2:	Average Nominal Cross-sectional Area = 28.7 mm <sup>2</sup>				
	P201	16.559	577.91	×	
	P205	22.765	794.52	✓	
	P212	20.203	705.11	✓	
Panel 3:	Average Nominal Cross-sectional Area = 30.6 mm <sup>2</sup>				
	P301	15.754	514.25	✓	
	P302	16.225	529.62	✓	
	P312	18.307	597.58	✓	
	P313	17.347	566.25	✓	
Panel 4:	Rejected ∴ poor surface texture and dryness				
Panel 5:	Average Nominal Cross-sectional Area = 29.4 mm <sup>2</sup>				
	P501	21.500	731.99	✓	
	P502	23.011	783.44	✓	
	P512	20.029	681.91	✓	
	P513	20.013	681.37	✓	
Minimum		15.754	514.254		
Maximum		23.011	794.520		
Average		19.17	650.51	19.22	650.95
Standard Deviation		2.215	83.128	2.209	84.816
Coefficient of Variation (%)		11.56	12.78	11.50	13.03

**Table 37:** Straight laminates (IM7/8551-7 [0/  $\pm$  60/90]<sub>s</sub>): Summary of quasi-static test specimens

Coupon	Load (kN)	Stress (MPa)	Accept\Reject
<b>Panel 1:</b> <i>Average Nominal Cross-sectional Area = 30.1 mm<sup>2</sup></i>			
P101	20.062	707.98	✓
P102	19.309	633.72	✓
P111	21.899	702.94	✓
P112	21.546	705.87	✓
P113	20.292	739.71	✓
<b>Minimum</b>	19.309	633.717	
<b>Maximum</b>	21.899	739.713	
<b>Average</b>	20.62	698.05	
<b>Standard Deviation</b>	1.076	38.918	
<b>Coefficient of Variation (%)</b>	5.22	5.58	

**Table 38:** Single lap joints (IM7/8551-7 [0/  $\pm$  60/90]<sub>s</sub>): Summary of quasi-static test specimens

Coupon	Load (kN)	Stress (MPa)	Accept\Reject
<b>Panel 1:</b> <i>Average Nominal Cross-sectional Area = 29.0 mm<sup>2</sup></i>			
P101	15.277	558.87	✓
P102	16.248	554.38	✓
P111	15.516	525.60	✓
P112	16.306	567.61	✓
P113	16.002	586.37	✓
<b>Minimum</b>	15.277	554.381	
<b>Maximum</b>	16.306	567.606	
<b>Average</b>	15.94	560.29	
<b>Standard Deviation</b>	0.578	6.725	
<b>Coefficient of Variation (%)</b>	3.63	1.20	

**Table 39:** SNO joints (IM7/8551-7  $[0/\pm 60/90]_s$ ): Summary of quasi-static test specimens

Coupon	Load (kN)	Stress (MPa)	Accept\Reject
<b>Panel 1:</b> <i>Average Nominal Cross-sectional Area = 28.8 mm<sup>2</sup></i>			
P101	19.012	689.96	✓
P102	18.305	638.87	✓
P111	17.733	611.11	✓
P112	18.002	624.45	✓
P113	14.782	581.69	✓
<b>Minimum</b>	14.782	581.693	
<b>Maximum</b>	19.012	689.957	
<b>Average</b>	17.57	629.21	
<b>Standard Deviation</b>	1.628	39.974	
<b>Coefficient of Variation (%)</b>	9.27	6.35	

**Table 40:** Straight laminates (IM7/8551-7  $[45/0/-45/90]_s$ ): Summary of quasi-static test specimens

Coupon	Load (kN)	Stress (MPa)	Accept\Reject
<b>Panel 1:</b> <i>Average Nominal Cross-sectional Area = 29.7 mm<sup>2</sup></i>			
P106	19.761	668.97	✓
P108	20.505	29.06	✓
P112	18.500	30.23	✓
<b>Minimum</b>	18.500	611.962	
<b>Maximum</b>	20.505	705.577	
<b>Average</b>	19.59	662.17	
<b>Standard Deviation</b>	1.014	47.177	
<b>Coefficient of Variation (%)</b>	5.17	7.12	

**Table 41:** Single lap joints (IM7/8551-7 [45/0/ – 45/90]<sub>s</sub>): Summary of quasi-static test specimens

Coupon	Load (kN)	Stress (MPa)	Accept\Reject
<b>Panel 1:</b> <i>Average Nominal Cross-sectional Area = 33.7 mm<sup>2</sup></i>			
P102	19.507	638.50	✓
P107	19.995	643.33	✓
P108	14.744	483.08	×
P111	19.502	634.68	✓
P112	16.499	553.95	×
<b>Minimum</b>	19.502	634.678	
<b>Maximum</b>	19.995	643.331	
<b>Average</b>	19.67	638.83	
<b>Standard Deviation</b>	0.283	4.337	
<b>Coefficient of Variation (%)</b>	1.44	0.68	

**Table 42:** SNO joints (IM7/8551-7 [45/0/ – 45/90]<sub>s</sub>): Summary of quasi-static test specimens

Coupon	Load (kN)	Stress (MPa)	Accept\Reject
<b>Panel 1:</b> <i>Average Nominal Cross-sectional Area = 30.0 mm<sup>2</sup></i>			
P101	18.247	638.63	✓
P103	20.097	661.34	✓
P107	18.761	629.09	✓
P111	20.502	681.56	✓
P112	19.244	653.84	✓
<b>Minimum</b>	18.247	629.085	
<b>Maximum</b>	20.502	681.563	
<b>Average</b>	19.37	652.89	
<b>Standard Deviation</b>	0.930	20.399	
<b>Coefficient of Variation (%)</b>	4.80	3.12	

**Table 43:** Straight laminates (S2/E773FR  $[0/\pm 45/90]_s$ ): Summary of quasi-static test specimens

Coupon	Load (kN)	Stress (MPa)	Accept\Reject
<b>Panel 1:</b> <i>Average Nominal Cross-sectional Area = 46.9 mm<sup>2</sup></i>			
P102	28.012	596.947	✓
P105	28.751	612.696	✓
P109	28.255	602.142	✓
<b>Panel 2:</b> <i>Average Nominal Cross-sectional Area = 45.9 mm<sup>2</sup></i>			
P201	24.504	534.425	✓
P206	27.513	600.066	✓
P207	26.504	578.063	✓
P211	26.255	572.612	✓
P212	21.258	463.634	✓
<b>Panel 3:</b> <i>Average Nominal Cross-sectional Area = 45.7 mm<sup>2</sup></i>			
P301	22.742	497.857	✓
P303	27.006	591.199	✓
P310	27.748	607.444	✓
<b>Minimum</b>	21.258	463.634	
<b>Maximum</b>	28.751	612.696	
<b>Average</b>	26.23	568.83	
<b>Standard Deviation</b>	2.411	49.171	
<b>Coefficient of Variation (%)</b>	9.19	8.64	



**Table 44:** Single lap joints (S2/E773FR  $[0/\pm 45/90]_s$ ): Summary of quasi-static test specimens

Coupon	Load (kN)	Stress (MPa)	Accept\Reject
<b>Panel 1:</b> <i>Average Nominal Cross-sectional Area = 46.2 mm<sup>2</sup></i>			
P101	7.001	151.366	✓
P104	6.757	146.095	✓
P108	6.752	145.996	✓
<b>Panel 2:</b> <i>Average Nominal Cross-sectional Area = 45.9 mm<sup>2</sup></i>			
P201	6.507	141.665	✓
P205	8.241	179.418	✓
P210	6.249	136.058	✓
<b>Panel 3:</b> <i>Average Nominal Cross-sectional Area = 45.4 mm<sup>2</sup></i>			
P302	6.761	149.084	✓
P308	5.750	126.772	✓
P310	6.495	143.202	✓
<b>Minimum</b>	5.750	126.772	
<b>Maximum</b>	8.241	179.418	
<b>Average</b>	6.72	146.63	
<b>Standard Deviation</b>	0.676	14.347	
<b>Coefficient of Variation (%)</b>	10.05	9.78	

**Table 45:** SNO joints (S2/E773FR [0/  $\pm$  45/90]<sub>s</sub>): Summary of quasi-static test specimens

	Coupon	Load (kN)	Stress (MPa)	Accept\Reject
<b>Panel 1:</b>	<i>Average Nominal Cross-sectional Area = 51.1 mm<sup>2</sup></i>			
	P103	10.499	205.615	✓
	P106	10.502	205.675	✓
	P110	11.002	215.463	✓
<b>Panel 2:</b>	<i>Average Nominal Cross-sectional Area = 44.9 mm<sup>2</sup></i>			
	P204	10.000	222.739	✓
	P206	10.249	228.306	✓
	P209	11.248	250.538	✓
<b>Panel 3:</b>	<i>Average Nominal Cross-sectional Area = 52.2 mm<sup>2</sup></i>			
	P302	11.504	220.553	✓
	P305	10.510	201.505	✓
	P308	10.746	206.032	✓
<b>Panel 4:</b>	<i>Average Nominal Cross-sectional Area = 44.8 mm<sup>2</sup></i>			
	P401	13.253	295.591	✓
	P407	11.504	256.573	✓
	P411	9.484	211.537	✓
<b>Minimum</b>		9.484	201.505	
<b>Maximum</b>		13.253	295.591	
<b>Average</b>		10.88	226.68	
<b>Standard Deviation</b>		0.959	27.908	
<b>Coefficient of Variation (%)</b>		8.82	12.31	

**Table 46:** Straight laminates (1.0 inch width IM7/8551-7 [45/90/ − 45/0]<sub>s</sub>): Summary of quasi-static test specimens

Coupon	Load (kN)	Stress (MPa)	Accept\Reject
<b>Panel 1:</b> <i>Average Nominal Cross-sectional Area = 28.4 mm<sup>2</sup></i>			
P101	22.022	816.87	✓
P102	23.279	815.67	✓
P111	23.765	820.86	✓
P112	24.587	833.89	✓
P113	22.751	828.04	✓
<b>Minimum</b>	22.022	815.675	
<b>Maximum</b>	24.587	833.890	
<b>Average</b>	23.28	823.07	
<b>Standard Deviation</b>	0.975	7.742	
<b>Coefficient of Variation (%)</b>	4.19	0.94	

**Table 47:** Straight laminates (1.5 inch width IM7/8551-7 [45/90/ − 45/0]<sub>s</sub>): Summary of quasi-static test specimens

Coupon	Load (kN)	Stress (MPa)	Accept\Reject
<b>Panel 2:</b> <i>Average Nominal Cross-sectional Area = 42.7 mm<sup>2</sup></i>			
P201	28.785	773.62	✓
P202	37.059	834.16	✓
P203	30.017	663.34	✓
P204	36.518	829.43	✓
<b>Minimum</b>	28.785	773.618	
<b>Maximum</b>	37.059	834.159	
<b>Average</b>	34.12	812.40	
<b>Standard Deviation</b>	4.629	33.672	
<b>Coefficient of Variation (%)</b>	13.57	4.14	

**Table 48:** Straight laminates (2.0 inch width IM7/8551-7 [45/90/ − 45/0]<sub>s</sub>): Summary of quasi-static test specimens

Coupon	Load (kN)	Stress (MPa)	Accept\Reject
<b>Panel 1:</b> <i>Average Nominal Cross-sectional Area = 57.6 mm<sup>2</sup></i>			
P201	45.749	802.96	✓
P202	47.338	765.88	✓
P203	46.098	822.36	✓
P204	46.675	842.80	✓
Minimum	45.749	765.877	
Maximum	47.338	842.799	
Average	46.47	808.50	
Standard Deviation	0.696	32.741	
Coefficient of Variation (%)	1.50	4.05	

**Table 49:** Single lap joints (1.0 inch width IM7/8551-7 [45/90/ − 45/0]<sub>s</sub>): Summary of quasi-static test specimens

Coupon	Load (kN)	Stress (MPa)	Accept\Reject
<b>Panel 1:</b> <i>Average Nominal Cross-sectional Area = 28.8 mm<sup>2</sup></i>			
P101	16.500	602.944	✓
P102	19.004	666.036	✓
P111	19.249	652.557	✓
P112	21.499	729.133	✓
P113	20.744	748.051	✓
Minimum	16.500	602.944	
Maximum	21.499	748.051	
Average	19.40	679.74	
Standard Deviation	1.924	59.014	
Coefficient of Variation (%)	9.92	8.68	

**Table 50:** SNO joints (1.0 inch width IM7/8551-7  $[[45/90/-45/0]_s]$ ): Summary of quasi-static test specimens

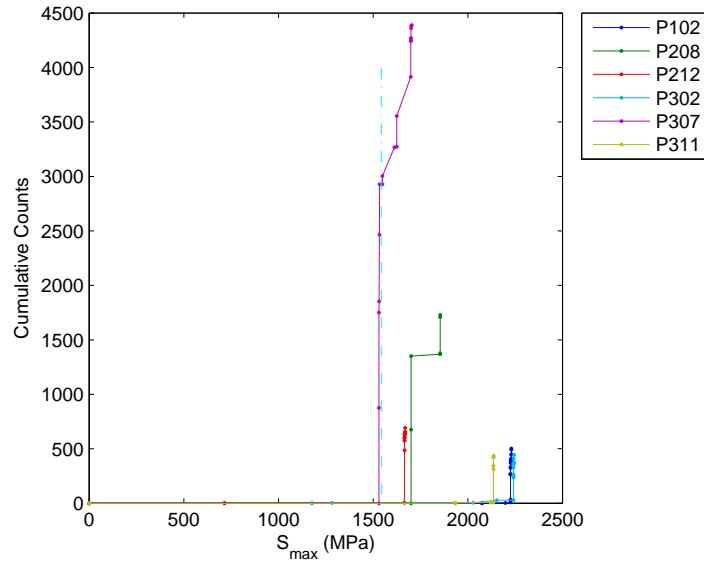
	Coupon	Load (kN)	Stress (MPa)	Accept\Reject
<b>Panel 1:</b>	<i>Average Nominal Cross-sectional Area = 28.8 mm<sup>2</sup></i>			
	<i>P101</i>	11.004	418.134	×
	<i>P102</i>	15.749	534.886	✓
	<i>P111</i>	17.748	604.562	✓
	<i>P112</i>	19.246	651.180	✓
	<i>P113</i>	18.996	683.740	✓
<b>Minimum</b>		11.004	534.886	
<b>Maximum</b>		19.246	683.740	
<b>Average</b>		16.55	618.59	
<b>Standard Deviation</b>		3.394	64.575	
<b>Coefficient of Variation (%)</b>		20.51	10.44	

## APPENDIX C

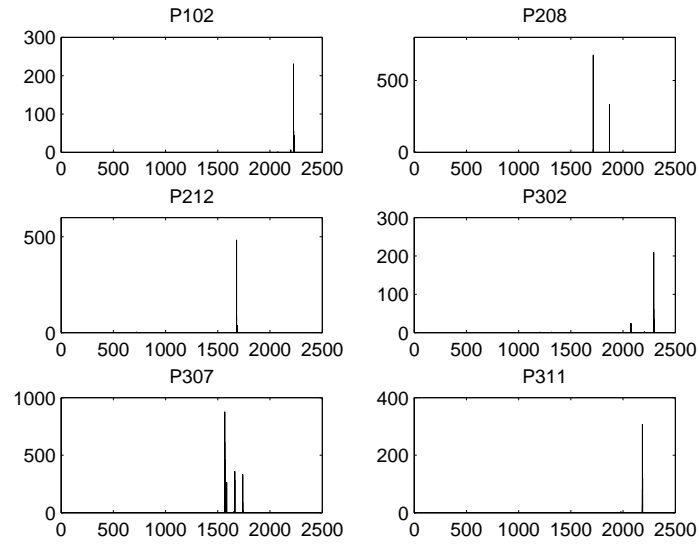
### SUMMARY OF ACOUSTIC EMISSION COUNTS UNDER QUASI-STATIC LOADING

The AE data collected during quasi-static loading is provided in this appendix. The AE data is separated into cumulative AE counts vs. stress and AE counts vs. stress for each of the SL, single lap and SNO joints. The onset of AE events refers to the stress level where damage is first detected by the acoustic equipment. A cumulative AE count at each loading is taken as the sum of all the acoustic events (counts) up till that quasi-static load, while a cumulative AE count peak refers to a sudden increase in the AE counts due to significant damage emitted at that particular stress level. The second and third AE count peak for the  $[0/\pm 30/90]_s$  and  $[0/\pm 60/90]_s$  lay-ups tend to occur over a range of stresses instead of distinctly at a specific stress level as that observed in the  $[0/\pm 45/90]_s$  because of the limited number of specimens tested for the former two lay-ups.

The summary for the family of IM7/8551-7  $[0]_s$  and  $[0/\pm \theta/90]_s$  family of SL, single lap and SNO joints used in behavior characterization (Chapters 2 and 3) are provided in Figures 61-72. The summary for IM7/8551-7  $[45/0/-45/90]_s$  SL, single lap and SNO joints used in fatigue damage initiation and propagation (Chapter 5) are provided in Figures 73-75. The summary for S2/E773FR  $[0/\pm 45/90]_s$  and IM7/8551-7  $[45/90/-45/0]_s$  SL, single lap and SNO joints used in the joint strength improvement (Chapter 6) study are provided in Figures 76-78.

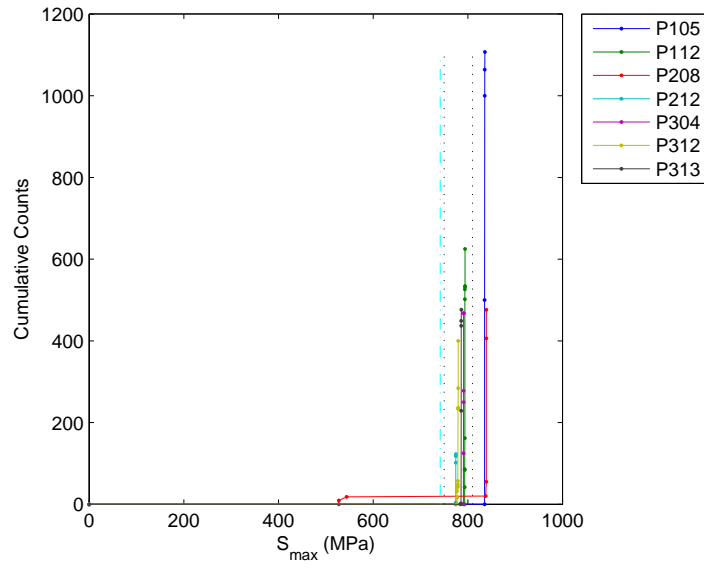


(a) Cumulative AE counts vs. stress (MPa) Onset: 1544 MPa.

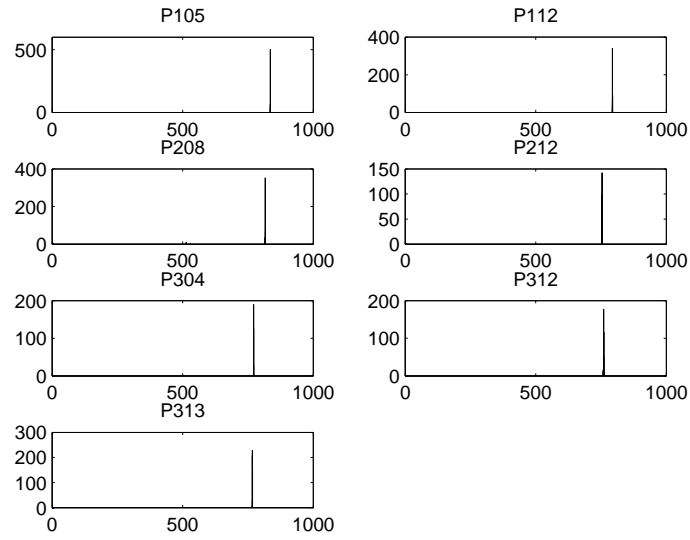


(b) AE Counts vs. stress (MPa)

**Figure 61:** Straight laminates (IM7/8551-7  $[0]_8$ ): Quasi-static acoustic emission  
*Onset of AE damage is a computed average based on all accepted quasi-static test specimens*



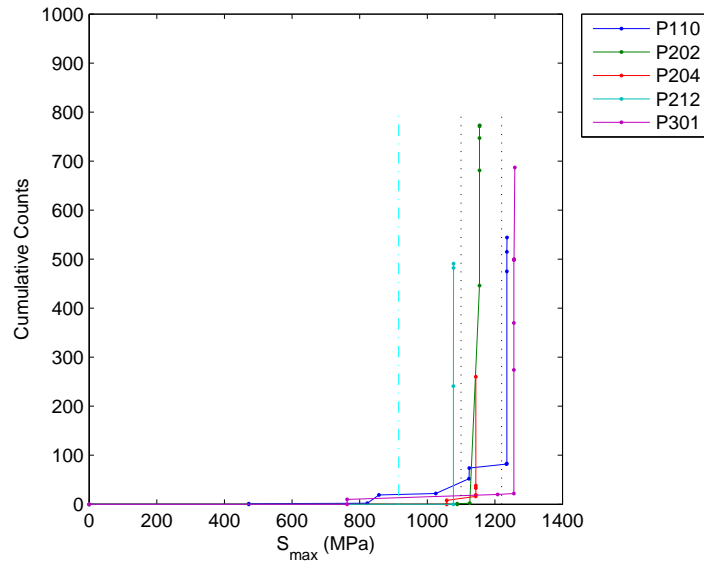
(a) Cumulative AE counts vs. stress (MPa)  
Onset: 742 MPa. First Peak Range: 750-810 MPa.



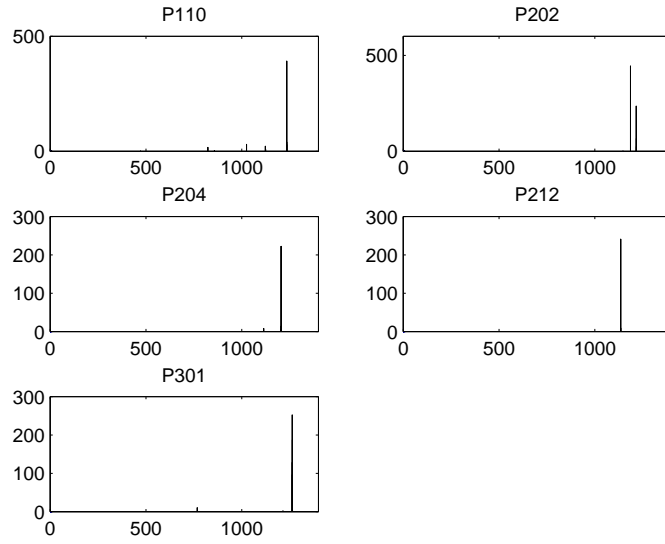
(b) AE counts vs. stress (MPa)

**Figure 62:** Single lap joints (IM7/8551-7  $[0]_8$ ): Quasi-static acoustic emission  
*Onset of AE damage is a computed average based on all accepted quasi-static test specimens*



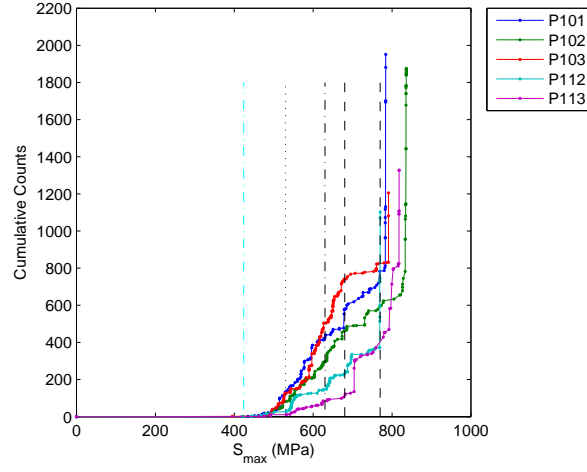


(a) Cumulative AE counts vs. stress (MPa)  
Onset: 916 MPa. First Peak Range: 1100-1220 MPa.

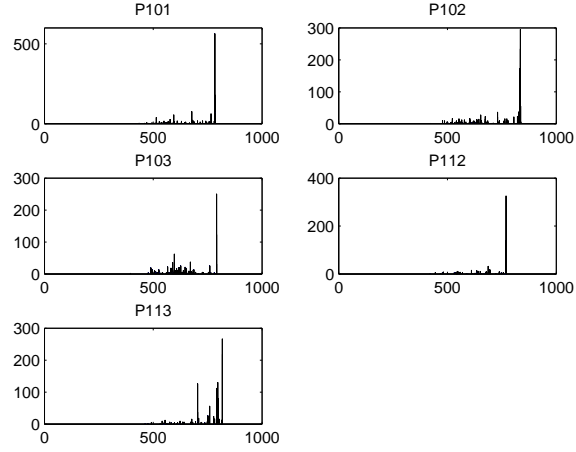


(b) AE counts vs. stress (MPa)

**Figure 63:** SNO joints (IM7/8551-7  $[0]_8$ ): Quasi-static acoustic emission  
*Onset of AE damage is a computed average based on all accepted quasi-static test specimens*

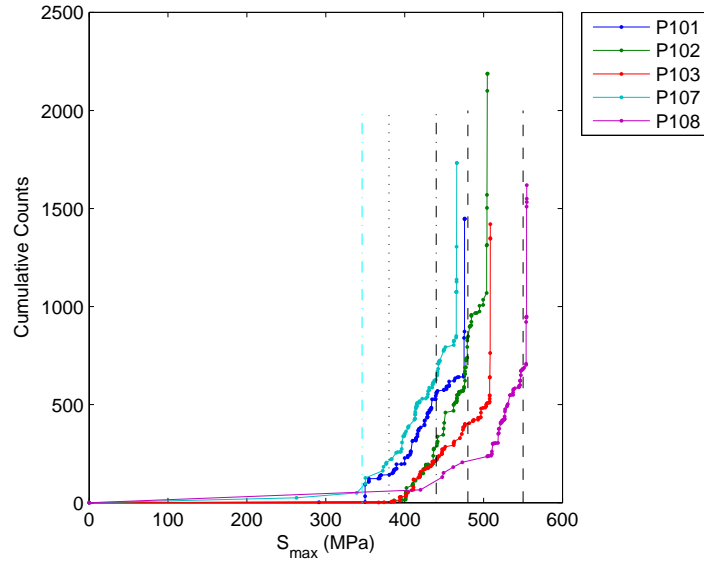


(a) Cumulative AE counts vs. stress (MPa)  
Onset: 424 MPa. First Peak: 530 MPa. Second Peak: 630 MPa. Third Peak Range: 680-770 MPa.

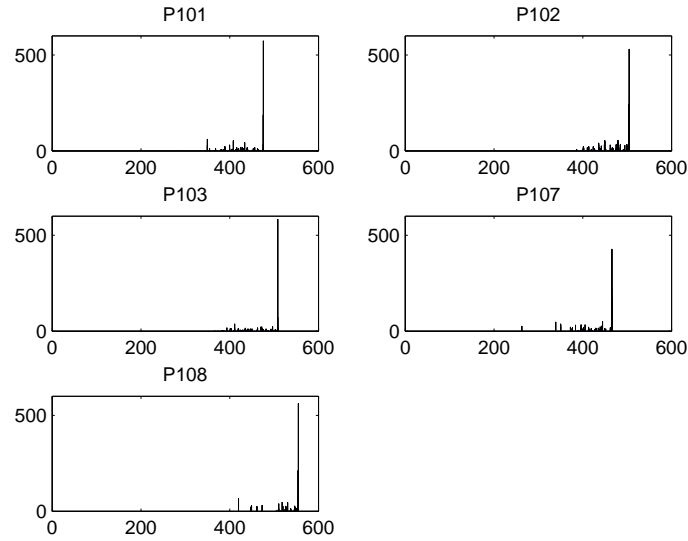


(b) AE counts vs. stress (MPa)

**Figure 64:** Straight laminates (IM7/8551-7  $[0/\pm 30/90]_s$ ): Quasi-static acoustic emission  
*Onset of AE damage is a computed average based on all accepted quasi-static test specimens*

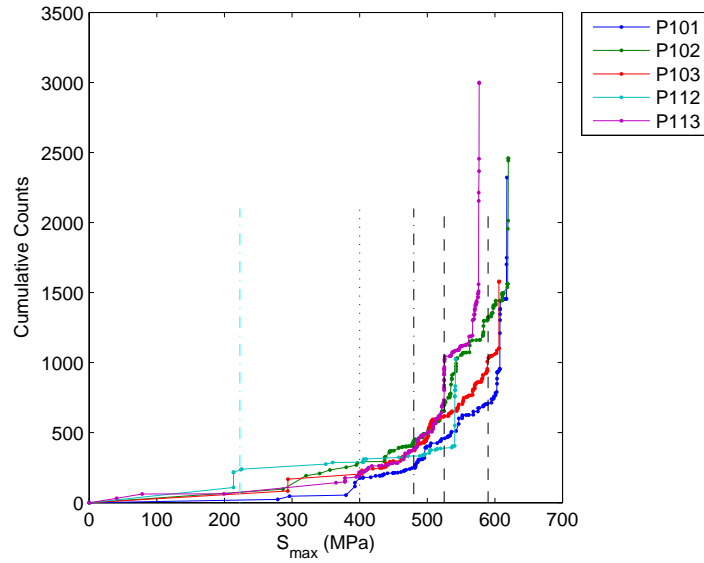


(a) Cumulative AE counts vs. stress (MPa)  
 Onset: 346 MPa. First Peak: 380 MPa. Second Peak: 440 MPa. Third Peak Range: 480-550 MPa.

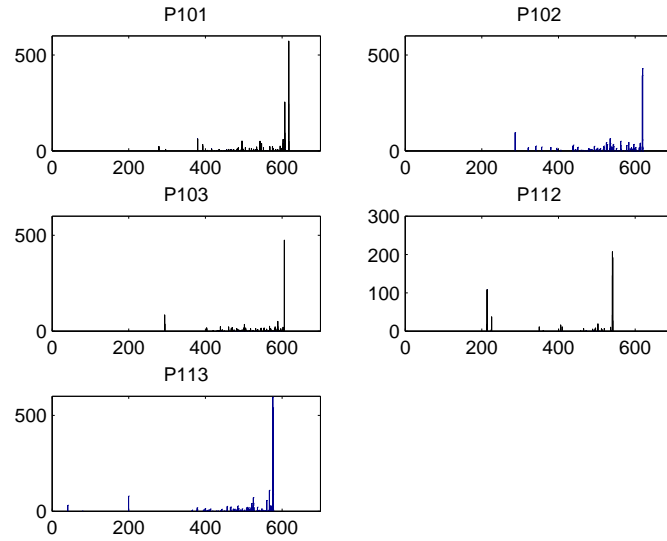


(b) AE counts vs. stress (MPa)

**Figure 65:** Single lap joints (IM7/8551-7  $[0/\pm 30/90]_s$ ): Quasi-static acoustic emission  
*Onset of AE damage is a computed average based on all accepted quasi-static test specimens*

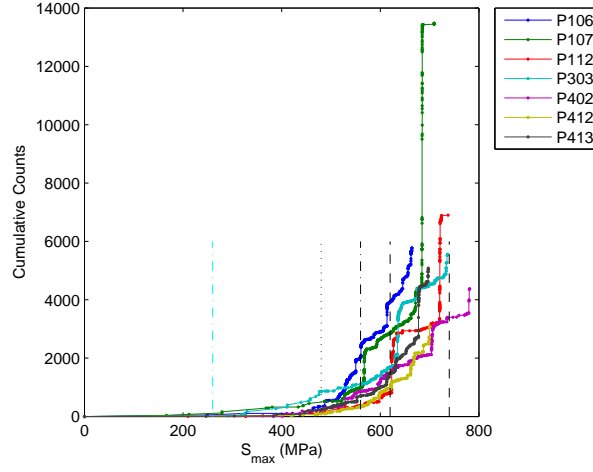


(a) Cumulative AE counts vs. stress (MPa)  
 Onset: 223 MPa. First Peak: 400 MPa. Second Peak: 480 MPa. Third Peak Range: 525-590 MPa.

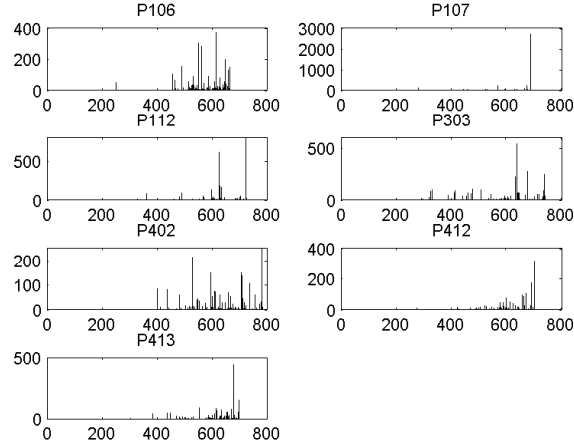


(b) AE counts vs. stress (MPa)

**Figure 66:** SNO joints (IM7/8551-7  $[0/\pm 30/90]_s$ ): Quasi-static acoustic emission  
*Onset of AE damage is a computed average based on all accepted quasi-static test specimens*

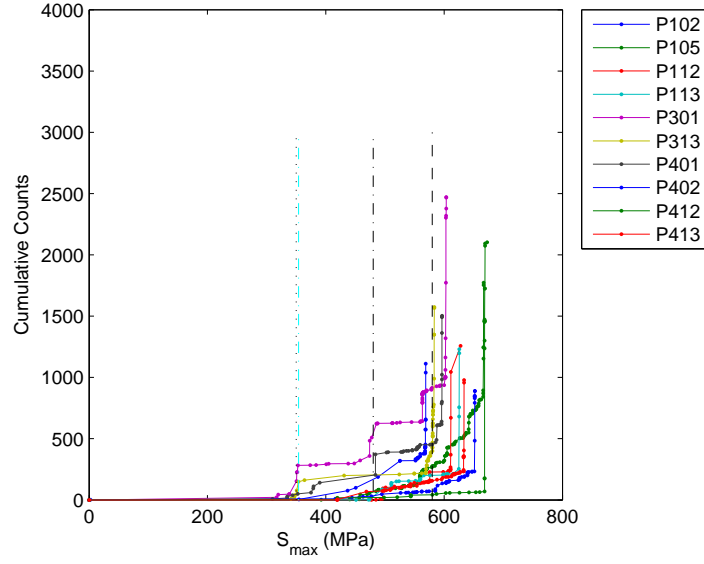


(a) Cumulative AE counts vs. stress (MPa)  
Onset: 260 MPa. First Peak: 480 MPa. Second Peak: 560 MPa. Third Peak Range: 620-740 MPa.

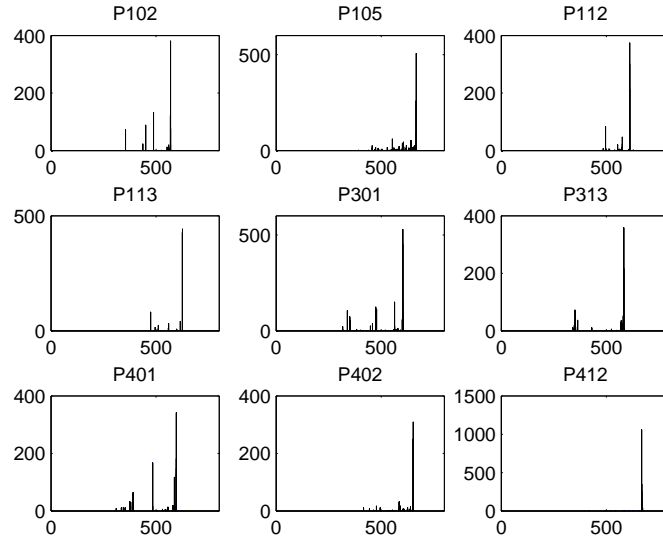


(b) AE counts vs. stress (MPa)

**Figure 67:** Straight laminates (IM7/8551-7  $[0/\pm 45/90]_s$ ): Quasi-static acoustic emission  
*Onset of AE damage is a computed average based on all accepted quasi-static test specimens*

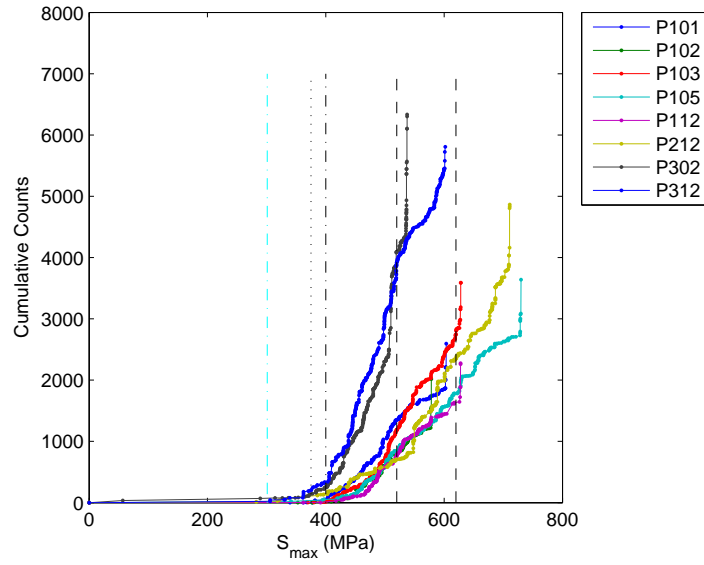


(a) Cumulative AE counts vs. stress (MPa)  
 Onset: 354 MPa. First Peak: 350 MPa. Second Peak: 480 MPa. Third Peak: 580 MPa.

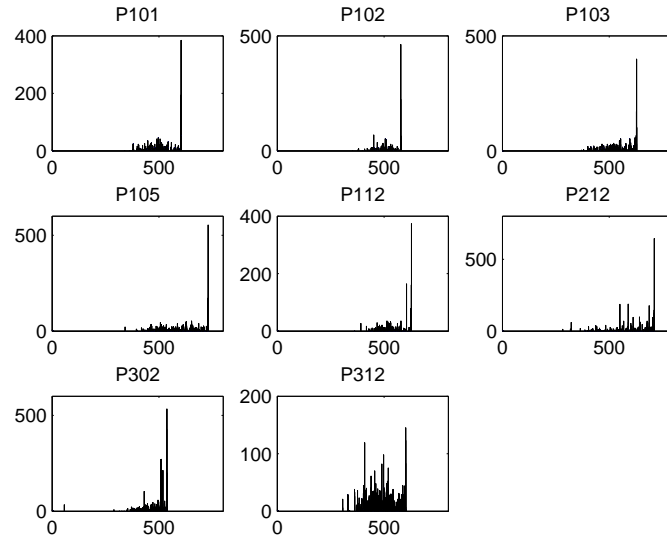


(b) AE counts vs. stress (MPa)

**Figure 68:** Single lap joints (IM7/8551-7  $[0/\pm 45/90]_s$ ): Quasi-static acoustic emission  
*Onset of AE damage is a computed average based on all accepted quasi-static test specimens*

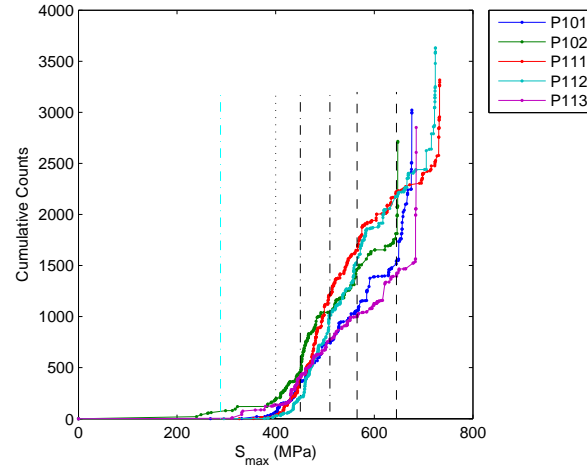


(a) Cumulative AE counts vs. stress (MPa)  
 Onset: 301 MPa. First Peak: 375 MPa. Second Peak: 400 MPa. Third Peak Range: 520-620 MPa.

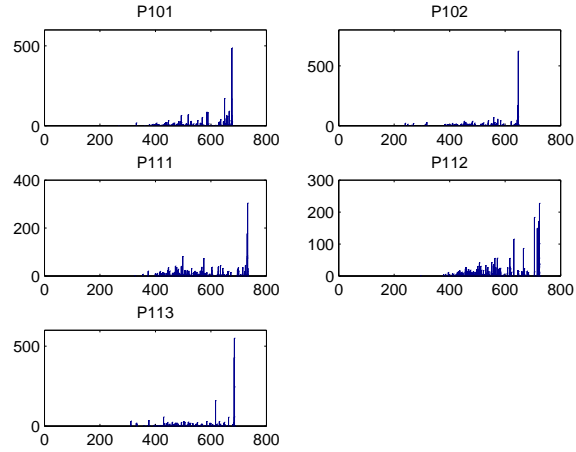


(b) AE counts vs. stress (MPa)

**Figure 69:** SNO joints (IM7/8551-7  $[0/\pm 45/90]_s$ ): Quasi-static acoustic emission  
*Onset of AE damage is a computed average based on all accepted quasi-static test specimens*



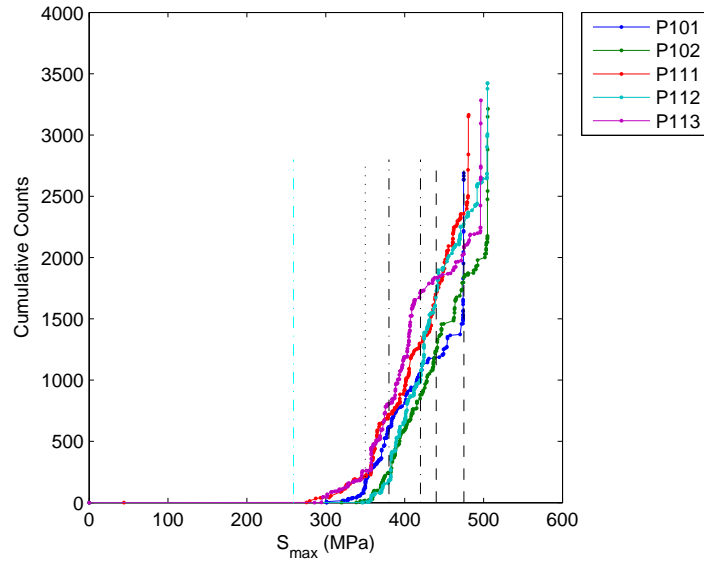
(a) Cumulative AE counts vs. stress (MPa)  
 Onset: 288 MPa. First Peak: 400 MPa. Second Peak Range: 450-510 MPa. Third Peak Range: 545-645 MPa.



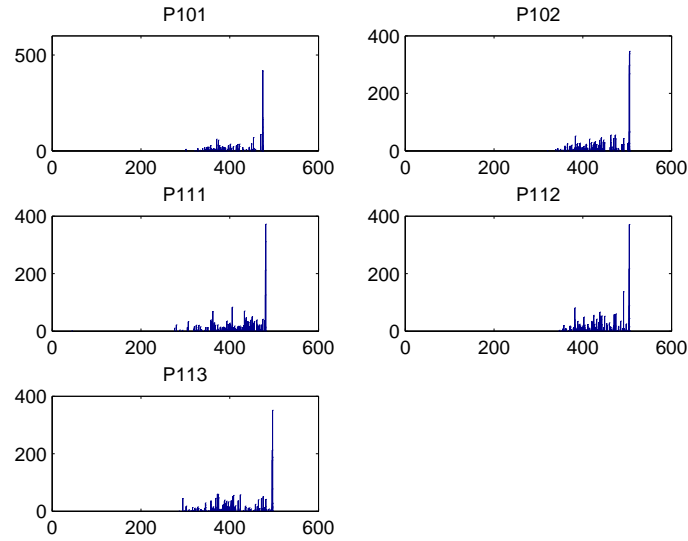
(b) AE counts vs. stress (MPa)

**Figure 70:** Straight laminates (IM7/8551-7  $[0/\pm 60/90]_s$ ): Quasi-static acoustic emission  
*Onset of AE damage is a computed average based on all accepted quasi-static test specimens*



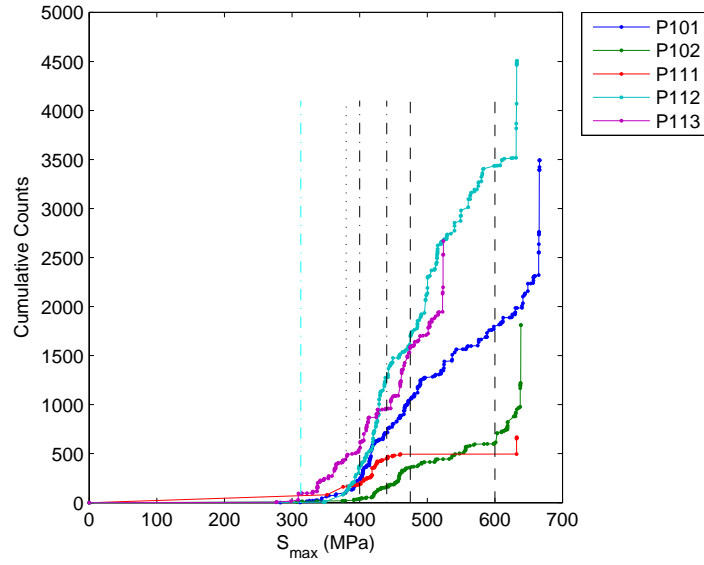


(a) Cumulative AE counts vs. stress (MPa)  
Onset: 259 MPa. First Peak: 350 MPa. Second Peak Range: 380-420 MPa.  
Third Peak Range: 440-475 MPa.

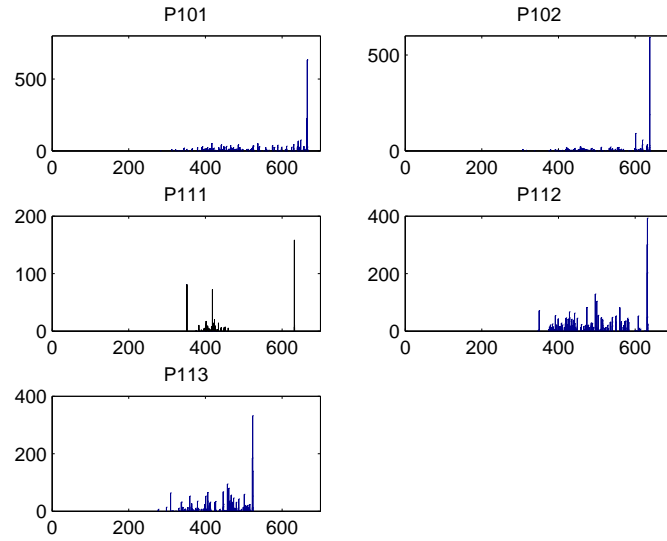


(b) AE counts vs. stress (MPa)

**Figure 71:** Single lap joints (IM7/8551-7  $[0/\pm 60/90]_s$ ): Quasi-static acoustic emission  
*Onset of AE damage is a computed average based on all accepted quasi-static test specimens*

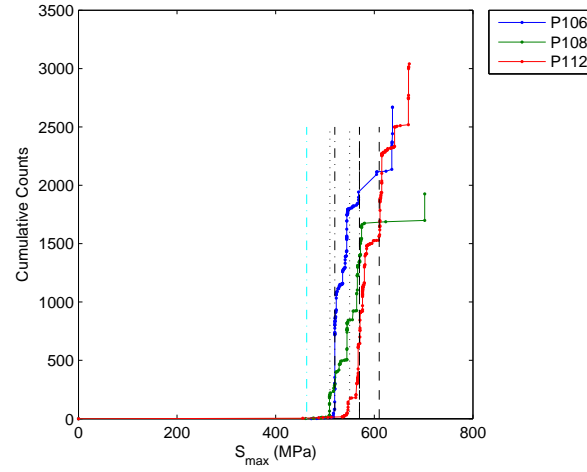


(a) Cumulative AE counts vs. stress (MPa)  
 Onset: 313 MPa. First Peak: 380 MPa. Second Peak Range: 400-440 MPa.  
 Third Peak Range: 480-600 MPa.

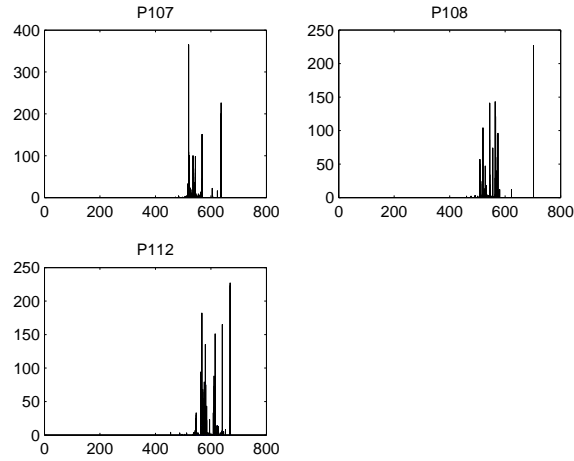


(b) AE counts vs. stress (MPa)

**Figure 72:** SNO joints (IM7/8551-7  $[0/\pm 60/90]_s$ ): Quasi-static acoustic emission  
*Onset of AE damage is a computed average based on all accepted quasi-static test specimens*

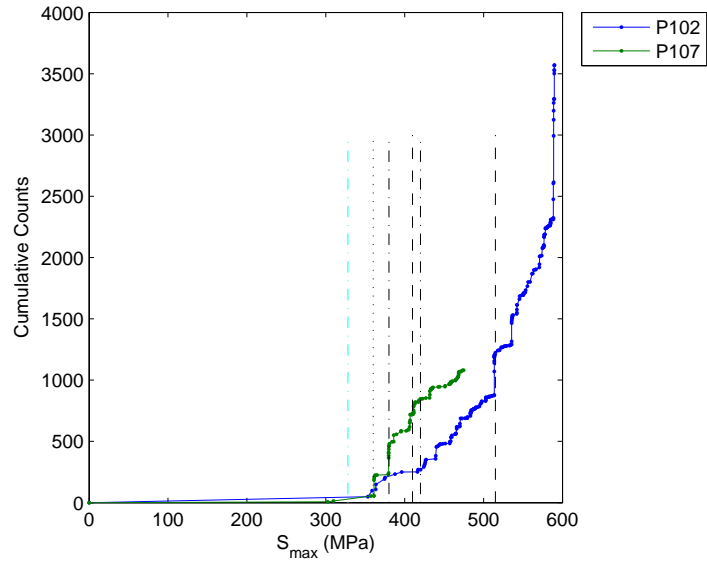


(a) Cumulative AE counts vs. stress (MPa)  
 Onset: 463 MPa. First Peak Range: 510-550 MPa. Second Peak Range: 520-570 MPa. Third Peak Range: 570-610 MPa.

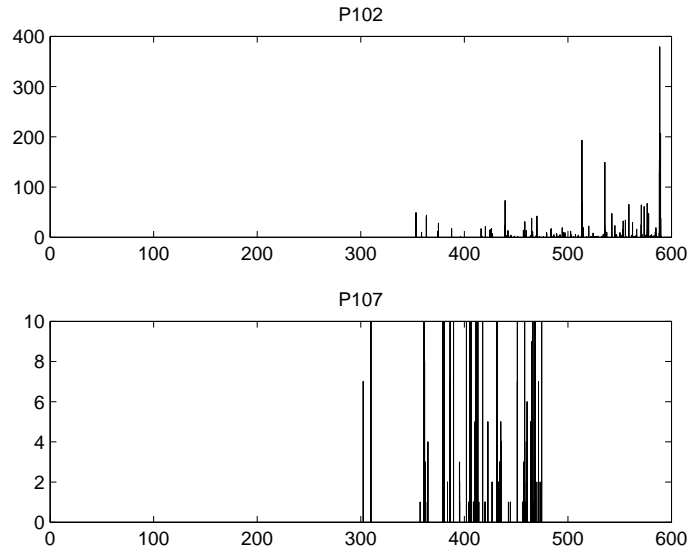


(b) AE counts vs. stress (MPa)

**Figure 73:** Straight laminates (IM7/8551-7  $[45/0/-45/90]_s$ ): Quasi-static acoustic emission  
*Onset of AE damage is a computed average based on all accepted quasi-static test specimens*

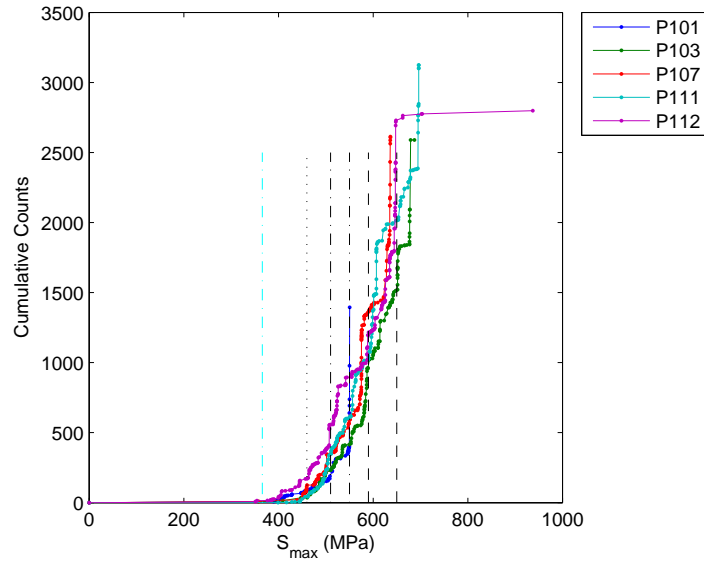


(a) Cumulative AE counts vs. stress (MPa)  
 Onset: 328 MPa. First Peak: 360 MPa. Second Peak Range: 380-420 MPa.  
 Third Peak Range: 410-515 MPa.

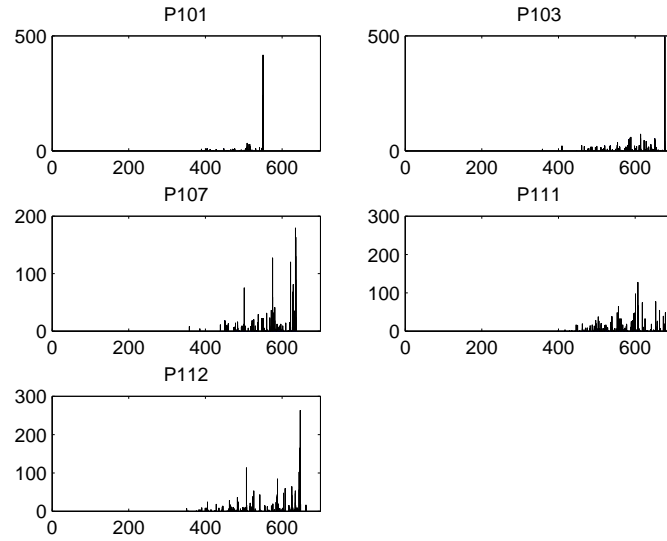


(b) AE counts vs. stress (MPa)

**Figure 74:** Single lap joints (IM7/8551-7 [45/0/ - 45/90]<sub>s</sub>): Quasi-static acoustic emission  
*Onset of AE damage is a computed average based on all accepted quasi-static test specimens*

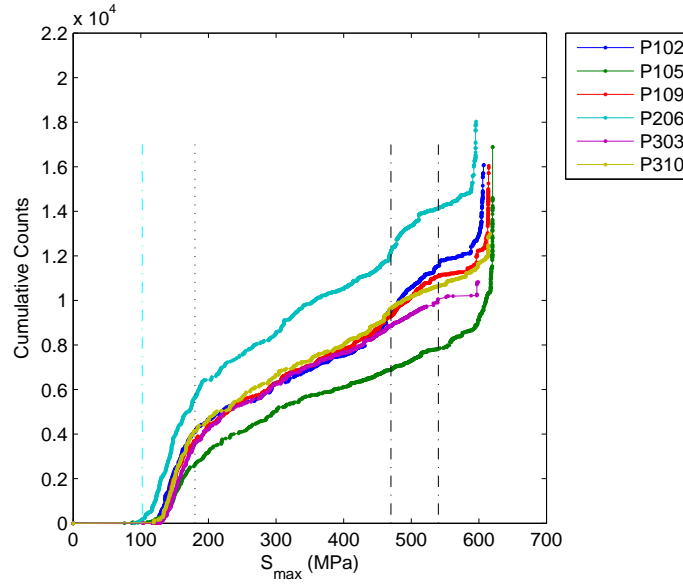


(a) Cumulative AE counts vs. stress (MPa)  
 Onset: 366 MPa. First Peak: 460 MPa. Second Peak Range: 510-550 MPa.  
 Third Peak Range: 590-650 MPa.

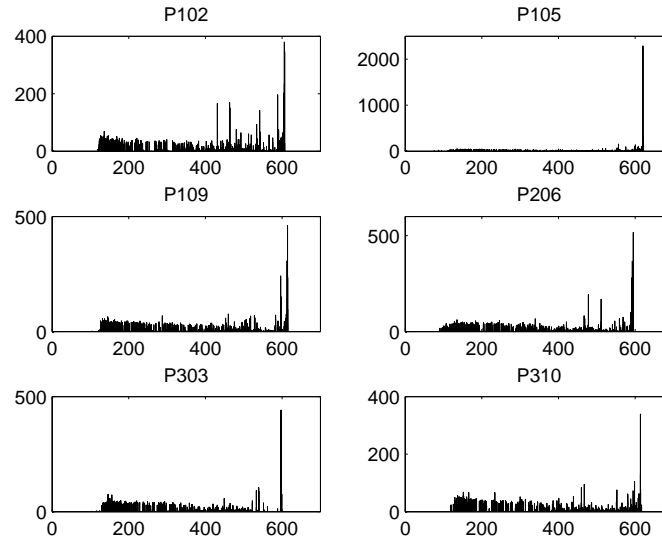


(b) AE counts vs. stress (MPa)

**Figure 75:** SNO joints (IM7/8551-7  $[45/0/-45/90]_s$ ): Quasi-static acoustic emission  
*Onset of AE damage is a computed average based on all accepted quasi-static test specimens*

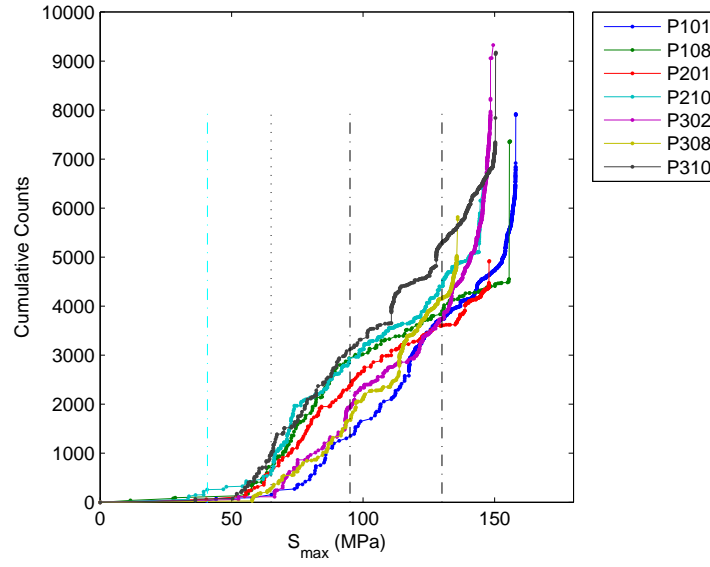


(a) Cumulative AE counts vs. stress (MPa)  
Onset: 102 MPa. First Peak: 180 MPa. Second Peak Range: 470-540 MPa.

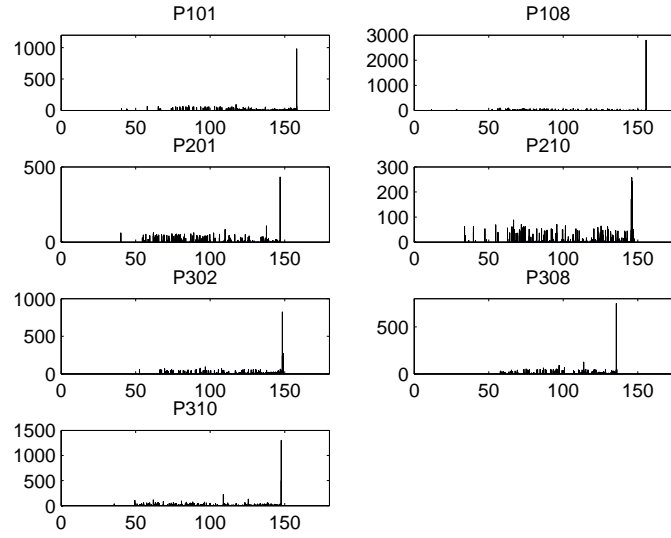


(b) AE counts vs. stress (MPa)

**Figure 76:** Straight laminates (S2/E773FR  $[0/\pm 45/90]$ ): Quasi-static acoustic emission  
*Onset of AE damage is a computed average based on all accepted quasi-static test specimens*

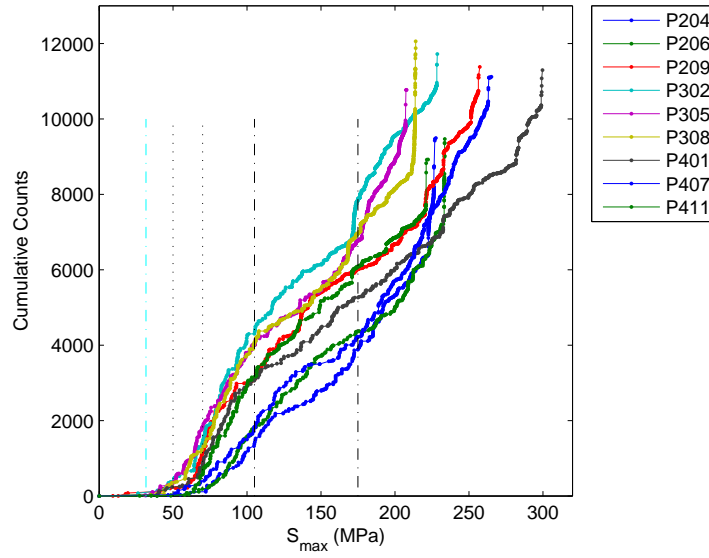


(a) Cumulative AE counts vs. stress (MPa)  
Onset: 41 MPa. First Peak: 65 MPa. Second Peak Range: 95-130 MPa.

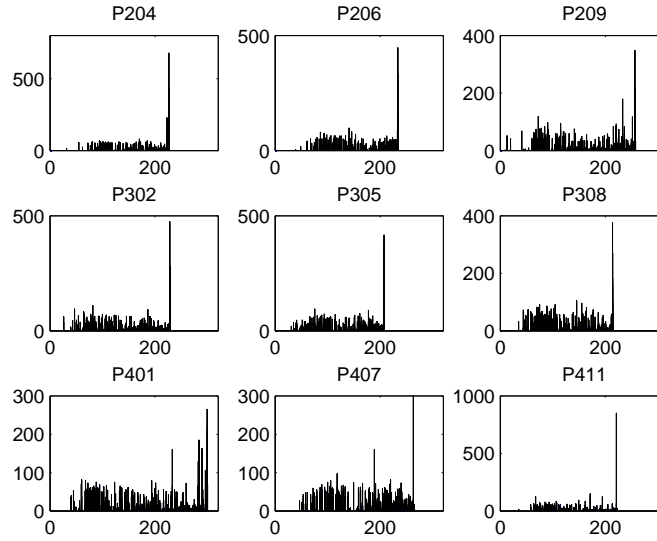


(b) AE counts vs. stress (MPa)

**Figure 77:** Single lap joints (S2/E773FR  $[0/\pm 45/90]$ ): Quasi-static acoustic emission  
*Onset of AE damage is a computed average based on all accepted quasi-static test specimens*



(a) Cumulative AE counts vs. stress (MPa)  
 Onset: 32 MPa. First Peak Range: 50-70 MPa. Second Peak Range: 105-175 MPa.



(b) AE counts vs. stress (MPa)

**Figure 78:** Straight laminates (S2/E773FR  $[0/\pm 45/90]$ ): Quasi-static acoustic emission  
*Onset of AE damage is a computed average based on all accepted quasi-static test specimens*



## APPENDIX D

### SUMMARY OF FATIGUE TEST SPECIMENS

The maximum cyclic load ( $L_{max}$ ), maximum cyclic stress ( $S_{max}$ ), number of cycles to failure ( $N_f$ ) under constant amplitude, tension-tension fatigue of R at 0.1 for SL, single lap and SNO joints are provided in this appendix. For computation of the  $S_{max}$  values, a panel average of the nominal cross-sectional area was used for the  $[0]_8$  IM7/8551-7 and  $[0/\pm 45/90]_s$  IM7/8551-7 and S2-glass/773FR, where multiple panels were tested, while an average for each individual specimen was used for the  $[0/\pm 30/90]_s$ ,  $[0/\pm 60/90]_s$ ,  $[45/0/-45/90]_s$  and  $[45/90/-45/0]_s$  IM7/8551-7, where only one panel was tested. Cyclic loading was carried out at a frequency of 5 Hz and a fatigue run-out of  $1 \times 10^6$  cycles for all the results except the AE study, which was conducted at a frequency of 10 Hz, R of 0.1 and a fatigue run-out of  $1 \times 10^7$  cycles.

A significant amount of scatter was observed in the  $N_f$  for the  $[0]_8$  IM7/8551-7 because of the difference in intensity of the failure mode, from adherend fracture with minimal fiber splitting to adherend fracture with “broom-like” fiber splitting.

The summary for the family of IM7/8551-7  $[0]_8$  and  $[0/\pm \theta/90]_s$  family of SL, single lap and SNO joints used in behavior characterization (Chapters 2 and 3) are provided in Tables 51-62. These results were conducted at a frequency of 5 Hz and a fatigue run-out of  $1 \times 10^6$  cycles. The summary for IM7/8551-7  $[45/0/-45/90]_s$  SL, single lap and SNO joints used in fatigue damage initiation and propagation (Chapter 5) are provided in Tables 63-65. These results were conducted at a frequency of 10 Hz and a fatigue run-out of  $1 \times 10^7$  cycles. The summary for S2/E773FR  $[0/\pm 45/90]_s$  and IM7/8551-7  $[45/90/-45/0]_s$  SL, single lap and SNO joints used in the joint strength improvement (Chapter 6) study are provided in Tables 66-68. These results were conducted at a frequency of 5 Hz and a fatigue run-out of  $1 \times 10^6$  cycles.

**Table 51:** Straight laminates (IM7/8551-7 [0]<sub>8</sub>): Summary of fatigue test specimens at 5 Hz with fatigue run-out at  $1 \times 10^6$  cycles

Specimen	$L_{max}$ (kN)	$S_{max}$ (MPa)	$N_f$ (Cycles)
P310	39.0	1359.36	$> 1.0 \times 10^6$
P109	40.0	1362.50	$> 1.0 \times 10^6$
P201	40.0	1374.05	1940
P308	40.0	1394.21	101576
P309	40.0	1394.21	111054
P210	42.0	1442.75	2310
P211	43.0	1477.10	227
P110	45.0	1532.81	254
P206	45.0	1545.80	1630
P207	45.0	1545.80	34
P306	45.0	1568.49	738
P101	50.0	1703.12	7635
P204	50.0	1717.56	168
P205	50.0	1717.56	17
P304	50.0	1742.76	623
P305	50.0	1742.76	272
P107	55.0	1873.43	965
P301	55.0	1917.04	481
P303	55.0	1917.04	185

*Average nominal cross-sectional area of each panel used for computation of stress values.*

*All specimens labeled with subscripts "SU".*

*No rejected specimens.*

**Table 52:** Single lap joints (IM7/8551-7 [0]<sub>s</sub>): Summary of fatigue test specimens at 5 Hz with fatigue run-out at  $1 \times 10^6$  cycles

Coupon	$L_{max}$ (kN)	$S_{max}(MPa)$	$N_f$ (Cycles)
P203	9.0	257.95	$> 1 \times 10^6$
P305	10.0	287.41	101873
P306	11.0	316.15	44256
P307	12.0	344.90	22323
P202	13.0	372.59	16704
P308	13.0	373.64	14372
P309	14.0	402.38	12538
P109	15.0	441.76	4097
P310	15.0	431.12	5653
P213	15.0	429.92	1884
P110	17.0	500.66	571
P211	17.0	487.24	968
P311	17.0	488.60	1601
P111	20.0	589.02	179
P210	20.0	573.22	276
P113	23.0	677.37	34
P209	23.0	659.20	0

*Average nominal cross-sectional area of each panel used for computation of stress values.*

*All specimens labeled with subscripts "LU".*

*No rejected specimens.*

**Table 53:** SNO joints (IM7/8551-7 [0]<sub>s</sub>): Summary of fatigue test specimens at 5 Hz with fatigue run-out at  $1 \times 10^6$  cycles

Coupon	$L_{max}$ (kN)	$S_{max}(MPa)$	$N_f$ (Cycles)
P209	10.0	358.16	$> 1 \times 10^6$
P302	12.0	410.27	180965
P303	13.5	461.56	43808
P213	14.0	501.43	41298
P214	14.5	519.34	71926
P304	14.5	495.75	30920
P211	15.0	537.25	11595
P206	15.5	555.15	11176
P111	16.0	543.87	12612
P210	16.0	573.06	9654
P313	16.0	547.03	9682
P109	17.0	577.86	7463
P205	17.0	608.88	7821
P311	17.0	581.22	10772
P108	18.0	611.85	4490
P209	18.0	644.70	4656
P307	18.0	615.41	4099
P308	20.0	683.79	1137
P207	20.0	716.33	2234
P107	20.0	679.83	2690
P106	23.0	781.81	586
P208	23.0	823.78	559
P305	23.0	786.36	595
P105	25.0	849.79	180
P203	25.0	895.41	482
P309	25.0	854.74	139
P103	28.0	951.77	71
P201	28.0	1002.86	0
P310	28.0	957.31	18

*Average nominal cross-sectional area of each panel used for computation of stress values.*

*All specimens labeled with subscripts "NU".*

*No rejected specimens.*

**Table 54:** Straight laminates (IM7/8551-7 [0/±30/90]<sub>s</sub>): Summary of fatigue test specimens at 5 Hz with fatigue run-out at  $1 \times 10^6$  cycles

Specimen	$L_{max}$ (kN)	$S_{max}$ (MPa)	$N_f$ (Cycles)
P106	13.0	446.40	$> 1.0 \times 10^6$
P110	13.5	429.66	743895
P108	13.5	466.23	64903
P107	14.0	486.71	141179
P111	14.0	447.35	$> 1.0 \times 10^6$
P109	14.5	485.89	137140
P105	15.0	513.42	26215
P104	17.0	565.80	266

*Individual nominal cross-sectional area of each specimen used for computation of stress values.*

*All specimens labeled with subscripts “S30”.*

*No rejected specimens.*

**Table 55:** Single lap joints (IM7/8551-7 [0/±30/90]<sub>s</sub>): Summary of fatigue test specimens at 5 Hz with fatigue run-out at  $1 \times 10^6$  cycles

Specimen	$L_{max}$ (kN)	$S_{max}$ (MPa)	$N_f$ (Cycles)
P113	4.0	137.09	$> 1.0 \times 10^6$
P110	4.0	130.41	$> 1.0 \times 10^6$
P111	4.5	153.17	460037
P112	5.0	182.16	434776
P109	5.5	182.89	84789
P106	6.0	203.53	55042
P105	8.0	268.10	7174
P104	10.0	296.77	814

*Individual nominal cross-sectional area of each specimen used for computation of stress values.*

*All specimens labeled with subscripts “L30”.*

*No rejected specimens.*

**Table 56:** SNO joints (IM7/8551-7  $[0/\pm 30/90]_s$ ): Summary of fatigue test specimens at 5 Hz with fatigue run-out at  $1 \times 10^6$  cycles

Specimen	$L_{max}$ (kN)	$S_{max}$ (MPa)	$N_f$ (Cycles)
$P107$	7.0	241.96	$> 1.0 \times 10^6$
$P109$	7.5	257.90	$> 1.0 \times 10^6$
$P106$	8.0	274.21	432302
$P108$	8.5	282.60	336828
$P104$	9.0	297.02	147020
$P110$	9.5	319.55	141409
$P105$	10.0	329.69	76409
$P111$	10.5	352.10	94269

*Individual nominal cross-sectional area of each specimen used for computation of stress values.*

*All specimens labeled with subscripts “N30”.*

*No rejected specimens.*

**Table 57:** Straight laminates (IM7/8551-7  $[0/\pm 45/90]_s$ ): Summary of fatigue test specimens at 5 Hz with fatigue run-out at  $1 \times 10^6$  cycles

Specimen	$L_{max}$ (kN)	$S_{max}$ (MPa)	$N_f$ (Cycles)	Accept/Reject
<i>P104</i>	12.0	417.00	$> 0.15 \times 10^6$	✓
<i>P101</i>	14.0	486.50	8126	✓
<i>P411</i>	14.0	487.53	423291	✓
<i>P408</i>	14.5	504.94	110514	✓
<i>P403</i>	14.5	504.94	$> 1.0 \times 10^6$	✓
<i>P406</i>	14.6	508.42	$> 1.0 \times 10^6$	✓
<i>P409</i>	14.6	508.42	8438	✓
<i>P405</i>	14.7	511.90	225815	✓
<i>P410</i>	14.7	511.90	11764	✓
<i>P404</i>	14.8	515.39	3839	✓
<i>P109</i>	16.0	556.00	249	×
<i>P205</i>	16.0	571.28	3551	✓
<i>P211</i>	16.0	571.28	867	✓
<i>P204</i>	16.5	589.13	2213	✓
<i>P102</i>	17.0	590.75	161	✓
<i>P206</i>	17.0	606.98	2331	✓
<i>P209</i>	17.0	606.98	534	✓
<i>P210</i>	17.0	606.98	1170	✓
<i>P212</i>	17.0	606.98	1090	✓
<i>P304</i>	17.0	593.06	693	×
<i>P310</i>	17.0	593.06	3024	×
<i>P311</i>	17.0	593.06	1495	✓
<i>P108</i>	18.0	625.50	2	✓
<i>P110</i>	18.0	625.50	63	✓
<i>P207</i>	18.0	642.69	82	×
<i>P208</i>	18.0	642.69	144	×
<i>P305</i>	18.0	627.95	587	✓
<i>P306</i>	18.0	627.95	5799	✓
<i>P307</i>	18.0	627.95	17	×
<i>P309</i>	18.0	627.95	581	✓

*Average nominal cross-sectional area of each panel used for computation of stress values.*

**Table 58:** Single lap joints (IM7/8551-7  $[0/\pm 45/90]_s$ ): Summary of fatigue test specimens at 5 Hz with fatigue run-out at  $1 \times 10^6$  cycles

Specimen	$L_{max}$ (kN)	$S_{max}$ (MPa)	$N_f$ (Cycles)
P311	4.0	133.74	$> 1.0 \times 10^6$
P308	5.0	167.18	256483
P408	5.0	175.55	401186
P409	5.0	175.55	482034
P305	6.0	200.61	86090
P309	6.0	200.61	74541
P403	6.0	210.66	132488
P304	7.0	234.05	33045
P310	7.0	234.05	37851
P303	8.0	267.49	21341
P410	8.0	280.88	16762
P307	9.0	300.92	4101
P411	9.0	315.99	7350
P306	10.0	334.36	2125
P110	11.0	418.43	109
P111	11.0	418.43	99
P108	12.0	456.47	57
P109	12.0	456.47	72
P106	13.0	494.51	11
P107	13.0	494.51	36
P103	14.5	551.57	15
P104	14.5	551.57	16

*Average nominal cross-sectional area of each panel used for computation of stress values.*

*All specimens labeled with subscripts "LQ".*

*No rejected specimens.*



**Table 59:** SNO joints (IM7/8551-7 [0/  $\pm$  45/90]<sub>s</sub>): Summary of fatigue test specimens at 5 Hz with fatigue run-out at  $1 \times 10^6$  cycles

Specimen	$L_{max}$ (kN)	$S_{max}$ (MPa)	$N_f$ (Cycles)
P605	7.5	260.98	$> 1.0 \times 10^6$
P503	8.0	272.37	738631
P504	8.0	272.37	406707
P606	8.0	278.38	378808
P505	10.0	340.46	66738
P506	11.0	374.51	29031
P507	11.5	391.53	21568
P508	12.0	408.55	31273
P509	12.5	425.58	14813
P303	13.0	424.36	6944
P304	13.0	424.36	8582
P510	13.0	442.60	9984
P511	13.5	459.62	15831
P305	14.0	457.00	3751
P306	14.0	457.00	2409
P310	14.0	457.00	2192
P207	15.0	523.51	14
P208	15.0	523.51	2340
P209	15.0	523.51	1932
P210	15.0	523.51	6901
P307	15.0	489.64	81
P311	15.0	489.64	83
P110	16.0	545.44	216
P111	16.0	545.44	196
P206	16.0	558.41	573
P308	16.0	552.29	51
P108	17.0	579.53	14
P109	17.0	579.53	45
P204	17.0	593.31	11
P309	17.0	554.93	1
P107	18.0	613.62	41
P202	18.0	628.21	1
P203	18.0	628.21	1
P211	18.0	628.21	2

*Average nominal cross-sectional area of each panel used for computation of stress values.*

*All specimens labeled with subscripts "NQ".*

*No rejected specimens.*

**Table 60:** Straight laminates (IM7/8551-7 [0/±60/90]<sub>s</sub>): Summary of fatigue test specimens at 5 Hz with fatigue run-out at  $1 \times 10^6$  cycles

Specimen	$L_{max}$ (kN)	$S_{max}$ (MPa)	$N_f$ (Cycles)
P106	10.0	332.73	$> 1.0 \times 10^6$
P104	10.5	338.00	$> 1.0 \times 10^6$
P105	11.0	360.40	742510
P103	11.5	369.94	42116
P107	12.5	418.70	$> 1.0 \times 10^6$
P110	12.5	402.57	$> 1.0 \times 10^6$
P109	13.0	429.97	471786
P108	14.0	467.52	12938

*Individual nominal cross-sectional area of each specimen used for computation of stress values.*

*All specimens labeled with subscripts “S60”.*

*No rejected specimens.*

**Table 61:** Single lap joints (IM7/8551-7 [0/±60/90]<sub>s</sub>): Summary of fatigue test specimens at 5 Hz with fatigue run-out at  $1 \times 10^6$  cycles

Specimen	$L_{max}$ (kN)	$S_{max}$ (MPa)	$N_f$ (Cycles)
P106	10.0	332.73	$> 1.0 \times 10^6$
P104	10.5	338.00	$> 1.0 \times 10^6$
P105	11.0	360.40	742510
P103	11.5	369.94	42116
P107	12.5	418.70	$> 1.0 \times 10^6$
P110	12.5	402.57	$> 1.0 \times 10^6$
P109	13.0	429.97	471786
P108	14.0	467.52	12938

*Individual nominal cross-sectional area of each specimen used for computation of stress values.*

*All specimens labeled with subscripts “L60”.*

*No rejected specimens.*

**Table 62:** SNO joints (IM7/8551-7  $[0/\pm 60/90]_s$ ): Summary of fatigue test specimens at 5 Hz with fatigue run-out at  $1 \times 10^6$  cycles

Specimen	$L_{max}$ (kN)	$S_{max}$ (MPa)	$N_f$ (Cycles)
P106	6.0	205.02	$> 1.0 \times 10^6$
P107	6.5	221.71	$> 1.0 \times 10^6$
P105	7.0	238.46	757935
P108	7.5	261.67	305436
P104	8.0	275.06	183865
P110	8.5	286.35	197396
P103	9.0	301.03	116523
P109	9.5	324.89	54097

*Individual nominal cross-sectional area of each specimen used for computation of stress values.*

*All specimens labeled with subscripts "N60".*

*No rejected specimens.*

**Table 63:** Straight laminates (IM7/8551-7  $[45/0/-45/90]_s$ ): Summary of fatigue test specimens at 10 Hz with fatigue run-out at  $1 \times 10^7$  cycles

Specimen	$L_{max}$ (kN)	$S_{max}$ (MPa)	$N_f$ (Cycles)
P103	10.0	322.13	$> 1.0 \times 10^6$
P109	11.0	374.77	$> 1.0 \times 10^6$
P104	11.5	375.52	3827795
P111	12.0	394.80	2693817
P102	13.0	421.68	5441
P101	15.5	532.76	2166

*Individual nominal cross-sectional area of each specimen used for computation of stress values.*

*All specimens labeled with subscripts "SEDH".*

*No rejected specimens.*

**Table 64:** Single lap joints (IM7/8551-7 [45/0/ – 45/90]<sub>s</sub>): Summary of fatigue test specimens at 10 Hz with fatigue run-out at  $1 \times 10^7$  cycles

Specimen	$L_{max}$ (kN)	$S_{max}$ (MPa)	$N_f$ (Cycles)
P105	2.5	82.17	$> 1.0 \times 10^6$
P104	3.5	112.45	$> 1.0 \times 10^6$
P106	4.0	129.74	1732557
P110	5.0	161.02	191228
P109	8.5	285.54	2165
P103	14.0	449.05	1

*Individual nominal cross-sectional area of each specimen used for computation of stress values.*

*All specimens labeled with subscripts “LEDH”.*

*No rejected specimens.*

**Table 65:** SNO joints (IM7/8551-7 [45/0/ – 45/90]<sub>s</sub>): Summary of fatigue test specimens at 10 Hz with fatigue run-out at  $1 \times 10^7$  cycles

Specimen	$L_{max}$ (kN)	$S_{max}$ (MPa)	$N_f$ (Cycles)
P104	3.5	115.52	$> 1.0 \times 10^6$
P108	4.0	132.00	2075534
P109	4.0	132.52	2932788
P105	5.0	163.15	524887
P110	7.0	231.92	26826
P106	10.0	330.28	1049

*Individual nominal cross-sectional area of each specimen used for computation of stress values.*

*All specimens labeled with subscripts “NEDH”.*

*No rejected specimens.*

**Table 66:** Straight laminates (S2/E773FR [0/  $\pm$  45/90]<sub>s</sub>): Summary of fatigue test specimens at 5 Hz with fatigue run-out at  $1 \times 10^6$  cycles

Coupon	$L_{max}$ (kN)	$S_{max}$ (MPa)	$N_f$ (Cycles)
P202	7.0	152.67	$> 1 \times 10^6$
P104	8.0	170.49	845858
P203	8.0	174.48	358101
P304	8.0	175.13	428040
P111	9.0	191.80	54826
P209	9.0	196.29	105445
P312	9.0	197.02	10315
P103	9.5	202.45	59116
P205	9.5	207.20	79431
P302	9.5	207.97	32649
P107	10.0	213.11	74819
P208	10.0	218.10	55561
P306	10.0	218.92	92970
P106	11.0	234.42	44802
P204	11.0	239.91	17658
P311	11.0	240.81	22689
P110	12.0	255.73	11424
P307	12.0	277.04	17142
P112	13.0	277.04	1659
P305	13.0	284.59	6732
P308	13.0	284.59	9626
P108	15.0	319.66	2720
P210	15.0	327.15	1399
P309	15.0	328.37	2683
P101	18.0	383.59	368

*Average nominal cross-sectional area of each panel used for computation of stress values.*

*All specimens labeled with subscripts "SQ".*

*No rejected specimens.*

**Table 67:** Single lap joints (S2/E773FR  $[0/\pm 45/90]_s$ ): Summary of fatigue test specimens at 5 Hz with fatigue run-out at  $1 \times 10^6$  cycles

Specimen	$L_{max}$ (kN)	$S_{max}$ (MPa)	$N_f$ (Cycles)
P109	2.0	43.24	$> 1.0 \times 10^6$
P202	2.0	43.54	$> 1.0 \times 10^6$
P107	2.5	54.06	396192
P203	2.5	54.43	264912
P207	2.5	54.43	192500
P209	2.5	54.43	323053
P309	2.5	55.12	330305
P106	3.0	64.87	60403
P206	3.0	65.32	26391
P211	3.0	65.32	71960
P304	3.0	66.15	33859
P307	3.0	66.15	68924
P103	3.5	75.68	53680
P110	3.5	75.68	20755
P204	3.5	76.20	12444
P301	3.5	77.17	15491
P306	3.5	77.17	20603
P105	4.0	86.49	4151
P208	4.0	87.09	3867
P303	4.0	88.20	4102
P102	4.5	97.30	1561
P305	4.5	99.22	1184

*Average nominal cross-sectional area of each panel used for computation of stress values.*

*All specimens labeled with subscripts "LQ".*

*No rejected specimens.*

**Table 68:** SNO joints (S2/E773FR  $[0/\pm 45/90]_s$ ): Summary of fatigue test specimens at 5 Hz with fatigue run-out at  $1 \times 10^6$  cycles

Specimen	$L_{max}$ (kN)	$S_{max}$ (MPa)	$N_f$ (Cycles)
<i>P111</i>	3.0	58.75	$> 1.0 \times 10^6$
<i>P304</i>	3.0	57.52	$> 1.0 \times 10^6$
<i>P404</i>	3.0	66.91	744827
<i>P104</i>	3.5	68.54	311237
<i>P107</i>	3.5	68.54	146869
<i>P202</i>	3.5	77.96	636608
<i>P309</i>	3.5	67.10	716262
<i>P405</i>	3.5	78.06	190846
<i>P409</i>	3.5	78.06	160017
<i>P108</i>	4.0	78.33	47328
<i>P112</i>	4.0	78.33	72982
<i>P205</i>	4.0	89.10	91331
<i>P306</i>	4.0	76.69	158339
<i>P402</i>	4.0	89.22	105631
<i>P403</i>	4.0	89.22	91466
<i>P412</i>	4.0	89.22	18508
<i>P105</i>	4.5	88.13	22711
<i>P109</i>	4.5	88.13	16619
<i>P201</i>	4.5	100.24	174195
<i>P303</i>	4.5	86.28	28005
<i>P408</i>	4.5	100.37	28111
<i>P102</i>	5.0	97.92	47522
<i>P207</i>	5.0	111.38	20150
<i>P301</i>	5.0	95.86	13050
<i>P410</i>	5.0	111.52	14661
<i>P101</i>	6.0	117.50	1571
<i>P203</i>	6.0	133.65	4233
<i>P208</i>	6.0	133.65	20707
<i>P307</i>	6.0	115.04	5599
<i>P406</i>	6.0	133.82	3093

*Average nominal cross-sectional area of each panel used for computation of stress values.*

*All specimens labeled with subscripts "NQ".*

*No rejected specimens.*

**Table 69:** Straight laminates (1.0 inch width IM7/8551-7 [45/90/ − 45/0]<sub>s</sub>): Summary of fatigue test specimens at 5 Hz with fatigue run-out at  $1 \times 10^6$  cycles

Specimen	$L_{max}$ (kN)	$S_{max}$ (MPa)	$N_f$ (Cycles)
P106	10.5	371.70	$> 1.0 \times 10^6$
P105	11.0	387.31	837143
P107	11.5	414.50	542153
P104	12.0	412.59	226125
P108	12.5	444.82	319599
P103	13.0	438.37	149493
P109	13.5	482.99	93300
P110	14.5	505.07	28768

*Individual nominal cross-sectional area of each specimen used for computation of stress values.*

*All specimens labeled with subscripts “SEDL”.*

*No rejected specimens.*



**Table 70:** Straight laminates (1.5 inch width IM7/8551-7 [45/90/ – 45/0]<sub>s</sub>): Summary of fatigue test specimens at 5 Hz with fatigue run-out at  $1 \times 10^6$  cycles

Specimen	$L_{max}$ (kN)	$S_{max}$ (MPa)	$N_f$ (Cycles)
P106	15.0	368.25	$> 1.0 \times 10^6$
P105	16.0	391.05	878177
P104	17.0	404.22	515922
P108	17.5	407.14	269610
P103	18.0	417.45	305692
P101	19.0	477.47	12730
P102	20.0	456.42	69161
P107	21.0	505.14	42334

*Individual nominal cross-sectional area of each specimen used for computation of stress values.*

*All specimens labeled with subscripts “SEDL”.*

*No rejected specimens.*

**Table 71:** Straight laminates (2.0 inch width IM7/8551-7 [45/90/ – 45/0]<sub>s</sub>): Summary of fatigue test specimens at 5 Hz with fatigue run-out at  $1 \times 10^6$  cycles

Specimen	$L_{max}$ (kN)	$S_{max}$ (MPa)	$N_f$ (Cycles)
P102	22.0	353.23	$> 1.0 \times 10^6$
P104	22.5	387.59	$> 1.0 \times 10^6$
P105	23.0	396.53	$> 1.0 \times 10^6$
P101	23.0	422.87	273468
P103	24.0	434.50	322354
P106	25.0	426.93	816648
P107	26.0	456.18	368148
P108	27.0	449.42	91713

*Individual nominal cross-sectional area of each specimen used for computation of stress values.*

*All specimens labeled with subscripts “SEDL”.*

*No rejected specimens.*

**Table 72:** Single lap joints (1.0 inch width IM7/8551-7 [45/90/ − 45/0]<sub>s</sub>): Summary of fatigue test specimens at 5 Hz with fatigue run-out at  $1 \times 10^6$  cycles

Specimen	$L_{max}$ (kN)	$S_{max}$ (MPa)	$N_f$ (Cycles)
P108	5.0	173.12	$> 1.0 \times 10^6$
P107	6.0	212.73	597474
P109	6.5	226.22	608593
P106	7.0	244.08	365672
P110	7.5	253.79	26606
P105	8.0	276.12	233382
P104	9.0	308.21	44702
P103	10.0	337.81	23662

*Individual nominal cross-sectional area of each specimen used for computation of stress values.*

*All specimens labeled with subscripts “LEDL”.*

*No rejected specimens.*

**Table 73:** SNO joints (1.0 inch width IM7/8551-7 [45/90/ – 45/0]<sub>s</sub>): Summary of fatigue test specimens at 5 Hz with fatigue run-out at  $1 \times 10^6$  cycles

Specimen	$L_{max}$ (kN)	$S_{max}$ (MPa)	$N_f$ (Cycles)
P104	6.0	203.53	$> 1.0 \times 10^6$
P109	6.5	223.28	498338
P107	7.0	243.30	182315
P106	7.5	259.82	124138
P105	8.0	277.87	98288
P110	8.5	288.41	78302
P108	9.0	307.64	38780
P103	10.0	347.63	10949

*Individual nominal cross-sectional area of each specimen used for computation of stress values.*

*All specimens labeled with subscripts “NEDL”.*

*No rejected specimens.*

## REFERENCES

- [1] ARMANIOS, E. A. and REHFELD, L. W., "Sublaminar analysis of interlaminar fracture in composites: Part I -analytical model," *Journal of Composites Technology & Research*, vol. 11, pp. 135–146, Winter 1989.
- [2] ARMANIOS, E. A., REHFELD, L. W., RAJU, I. S., and O'BRIEN, T. K., "Sublaminar analysis of interlaminar fracture in composites: Part II -applications," *Journal of Composites Technology & Research*, vol. 11, pp. 147–153, Winter 1989.
- [3] ASHCROFT, I. A., GILMORE, R. B., and SHAW, S. J., "Cyclic fatigue and environmental effects with adhesively bonded joints," *83rd Meeting of the AGARD SMP on "Bolted/Bonded Joints in Polymeric Composites"*, pp. 14(1)–14(9), Florence, Italy, 2-3 September 1996.
- [4] ATIVITAVAS, N., POTHISIRI, T., and FOWLER, T. J., "Identification of fiber-reinforced plastic failure mechanisms from acoustic emission data using neural networks," *Journal of Composite Materials*, vol. 40, no. 3, pp. 193–226, 2006.
- [5] AWERBUCH, J., ECKLES, W. F., and ERDMAN, D. L., "Detection of failure progression in cross-ply graphite/epoxy during fatigue through acoustic emission," tech. rep., Flight Dynamics Laboratory, Wright Research and Development Center, Air Force Systems Command, Wright-Patterson Air Force Base, Ohio 45433-6553, WRDC-TR-89-3087, November 1989.
- [6] AWERBUCH, J. and GHAFARI, S., "Monitoring progression of matrix splitting during fatigue loading through acoustic emission in notched unidirectional graphite/epoxy composite," *Journal of Reinforced Plastics and Composites*, vol. 7, pp. 245–264, May 1988.
- [7] BAKUCKAS, J. G., PROSSER, W. H., and JOHNSON, W. S., "Monitoring damage growth in titanium matrix composites using acoustic emission," *Journal of Composite Materials*, vol. 28, no. 4, pp. 305–328, 1994.
- [8] BHAT, C., BHAT, M. R., and MURTHY, C. R. L., "Acoustic emission characterization of failure modes in composites with ANN," *Composite Structures*, vol. 61, pp. 213–220, 2003.
- [9] BHAT, C., BHAT, M. R., and MURTHY, C. R. L., "Characterization of failure modes in CFRP composites -an ANN approach," *Journal of Composite Materials*, vol. 42, no. 3, pp. 257–276, 2008.
- [10] BLOM, A., ANSELL, H., NYMAN, T., and SCHON, J., "Fatigue of composite airframe structures," *Proceedings of the International Conference on Fatigue of Composites*, 3-5 June, Paris 1997.

- [11] BOURCHAK, M., FARROW, I. R., BOND, I. P., ROWLAND, C. W., and MENAN, F., "Acoustic emission energy as a fatigue damage parameter for CFRP composites," *International Journal of Fatigue*, vol. 29, pp. 457–470, 2007.
- [12] CAO, C. and DANCILA, D. S., "Differentiation of damage and failure mechanisms of co-cured fiber-reinforced composite joints using acoustic emission," *45<sup>th</sup> AIAA/ASME/ASCE/AHS/ASC Structures, Structural Dynamics and Materials Conference*, Palm Springs, CA April 19-22 2004.
- [13] CAO, C. and DANCILA, D., "Damage and failure analysis of co-cured fiber-reinforced composite joints with unidirectional lay-up," *44<sup>th</sup> AIAA/ASME/ASCE/AHS/ASC Structures, Structural Dynamics and Materials Conference*, Norfolk, VA April 7-10 2003.
- [14] CAO, C., "Damage and failure analysis of co-cured fiber-reinforced composite joints," *School of Aerospace Engineering, Georgia Institute of Technology*, Directed by D. Stefan Dancila 2004.
- [15] CAO, C. and DANCILA, D. S., "Characterization of damage and failure mechanisms of co-cured fiber-reinforced composite joints under quasi-static, tensile loading," *Journal of ASTM International*, vol. 2, pp. 1–25, September 2005.
- [16] CAO, C. and DANCILA, D. S., "Differentiation of damage and failure mechanisms of co-cured fiber-reinforced composite joints using acoustic emission," *Journal of ASTM International*, vol. 2, pp. 1–24, February 2005.
- [17] CHAN, W. S., REHFELD, L. W., and O'BRIEN, T. K., "Analysis, prediction, and prevention of edge delamination in rotor system structures," *Proceedings of the 43rd Annual Forum of the American Helicopter Society*, vol. St. Louis, Missouri, May 18-20 1987.
- [18] CHANG, F. K., "The effect of pin load distribution on the strength of pin loaded holes in laminated composites," *Journal of Composite Materials*, vol. 20, pp. 401–408, 1986.
- [19] CHANG, F. K., SCOTT, R. A., and SPRINGER, G. S., "Strength of mechanically fastened composite joints," *Journal of Composite Materials*, vol. 16, pp. 470–493, 1982.
- [20] CHANG, F. K., SCOTT, R. A., and SPRINGER, G. S., "Failure of composite laminates containing pin loaded holes -method of solution," *Journal of Composite Materials*, vol. 18, pp. 255–277, 1984.
- [21] CHEN, W. H. and YEH, J. T., "Three-dimensional finite element analysis of static and dynamic contact problems with friction," *Composite Structures*, vol. 35, pp. 341–352, 1990.
- [22] COATES, C. and ARMANIOS, E., "Testing and prediction of co-cured composite single lap joints with modified interface under cyclic loading," *Proceedings of the 16<sup>th</sup> Annual ASC Technical Conference*, Virginia Polytechnic Institute and State University Blacksburg, VA September 9-12 2001.

- [23] COATES, C. and ARMANIOS, E. A., "Assessment of nested overlap and transverse interfacial layer in co-cured composite single lap joints," *Proceedings of the Fifteenth Annual ASC/ASTM D-30 Technical Conference*, Texas A & M University, Texas, Sept 24-27 2000.
- [24] COATES, C. W. and ARMANIOS, E. A., "Monotonic and fatigue response of co-cured composite lap joints with modified interfaces," *Proceedings of American Helicopter Society 56<sup>th</sup> Annual Forum*, Virginia Beach, VA May 2-4 2000.
- [25] COATES, C. W., "New concepts for strength enhancement of co-cured composite single lap joints," *School of Aerospace Engineering, Georgia Institute of Technology*, Directed by Erian A. Armanmios 2001.
- [26] CREWS, J. H., J., "Bolt-bearing fatigue of a graphite/epoxy laminate," *Joining of Composite Materials, ASTM STP 749*, pp. 131-144, Kedward, K. T., Ed., American Society for Testing and Materials 1981.
- [27] Department of Defense Handbook, MIL-HDBK-17-3F, *Composite Materials Handbook*, 17 June 2002. Volume 3: Polymer Matrix Composites Materials Usage, Design and Analysis.
- [28] DULIEU-BARTON, J. M., EMERY, T. R., QUINN, S., and CUNNINGHAM, P. R., "A temperature correction methodology for quantitative thermoelastic stress analysis and damage assessment," *Measurement Science and Technology*, vol. 17, pp. 1627-1637, Institute of Physics Publishing 2006.
- [29] DZENIS, Y. A. and QIAN, J., "Analysis of microdamage evolution histories in composites," *International Journal of Solids and Structures*, vol. 38, pp. 1831-1854, 2001.
- [30] EL-HAJJAR, R. and HAJ-ALI, R., "A quantitative thermoelastic stress analysis method for pultruded composites," *Composites Science and Technology*, pp. 967-978, 2003.
- [31] EL-HAJJAR, R. and HAJ-ALI, R., "IR-thermography for strain analysis in pultruded fiber reinforced plastics," *Experimental Techniques*, vol. 28, no. 9, pp. 967-978, 2004.
- [32] ELY, T. M. and HILL, E. v. K., "Longitudinal splitting and fiber breakage characterization in graphite epoxy using acoustic emission data," *Materials Evaluation*, pp. 288-294, February 1995.
- [33] ERIKSSON, L. I., "Contact stresses in bolted joints of composite laminates," *Composite Structures*, vol. 6, pp. 57-75, 1986.
- [34] FOWLER, T. J., BLESSING, J. A., and CONLISK, P. J., "New directions in testing," *3rd International Symposium on Acoustic Emission from Composite Materials AECM-3*, p. 1627, Paris, France, July 1721 1989.
- [35] GAMSTEDT, E. K. and TALREJA, R., "Fatigue damage mechanisms in unidirectional carbon-fibre-reinforced plastics," *Journal of Materials Science*, vol. 34, pp. 2535-2546, 1999.
- [36] GOLAND, M. and REISSNER, E., "Stresses in cemented joints," *Journal of Applied Mechanics*, vol. 11, pp. A17-A27, 1944.

- [37] GYEKENYESI, A. L. and MORSCHER, G. N., "Evaluating the mechanical behavior of notched siC/siC composites using thermoelastic stress analysis," *Proceedings of SPIE*, vol. 5405, pp. 456–465, edited by Douglas D. Burleigh, K. Elliott Cramer, G. Raymond Peacock, Thermosense XXVI 2004.
- [38] HAJ-ALI, R., WEI, B. S., JOHNSON, S., and EL-HAJJAR, R., "Thermoelastic and infrared-thermography methods for surface strains in cracked orthotropic composite materials," *Engineering Fracture Mechanics*, vol. 75, pp. 58–75, 2008.
- [39] HART-SMITH, L. J., "Design and analysis of adhesive-bonded joints," tech. rep., Douglas Aircraft Company, McDonnell Douglas Corporation, Paper 6059A, USAF Conference Proceedings AFFDL-TR-72-130, Presented to Air Force Conference on Fibrous Composites in Flight Vehicle Design, Dayton, Ohio, pp 813-856, September 1972.
- [40] HART-SMITH, L. J., "Adhesive bonded double lap joints," *NASA CR-112235*, vol. Douglas Aircraft Company, Jan 1973.
- [41] HART-SMITH, L. J., "Adhesive bonded scarf and stepped-lap joints," *NASA CR-112237*, vol. NASA Langley Contractor Report, 1973.
- [42] HART-SMITH, L. J., "Bolted joints in graphite-epoxy laminates," tech. rep., Douglas Aircraft Company, NASA CR-144899, Jan 1977.
- [43] HART-SMITH, L. J., *Mechanically-Fastened Joints for Advanced Composites - Phenomenological Considerations and Simple Analyses*, vol. pp. 543-574 of *Lenoe, E. M., Oplinger, D. W. and Burke, J. J., Ed. Fibrous Composites in Structural Design*, 4<sup>th</sup> Conference on Fibrous Composites in Structural Design: Plenum Press, 1980.
- [44] HART-SMITH, L. J., "Differences between adhesive behavior in test coupons and structural joints," *ASTM Adhesive Committee D-14 Meeting*, vol. Douglas Aircraft Company paper 7066, Phoenix, Arizona 1981.
- [45] HART-SMITH, L. J., "Design methodology for bonded-bolted composites joints," tech. rep., Douglas Aircraft Company, AFWAL-TR-81-3154, Feb 1982.
- [46] HART-SMITH, L. J., *Design and Analysis of Bolted and Riveted Joints in Fibrous Composite Structures*, vol. pp. 227-269 of *Matthews, J. L., Ed. Joining Fibre-Reinforced Plastics*: Elsevier, 1987.
- [47] HART-SMITH, L. J., "Joints," *Engineered Materials Handbook -Composites*, vol. 1, pp. 479–495, ASM International 1987.
- [48] HASHIN, Z., "Analysis of orthogonally cracked laminates under tension," *Journal of Applied Mechanics*, vol. 54, pp. 872–879, December 1987.
- [49] HESLEHURST, R. B. and HART-SMITH, L. J., "The science and art of structural adhesive bonding," *SAMPE Journal*, vol. 38, pp. 60–71, March/April 2002.
- [50] HOSKIN, B. C. E. and BAKER, A. A. E., *Composite Materials for Aircraft Structures*. AIAA Education Series, 1986.

- [51] IREMAN, T., "Three-dimensional stress analysis of bolted single-lap composite joints," *Composite Structures*, vol. 43, pp. 195–216, 1998.
- [52] KRADINOV, V., BARUT, A., MADENCI, E., and AMBUR, D. R., "Bolted double-lap composite joints under mechanical and thermal loading," *International Journal of Solids and Structures*, vol. 38, pp. 7801–7837, 2001.
- [53] LACKMAN, L. M. and PAGANO, N. L., "On the prevention of delamination in composite laminates," *AAIAA/ASME/SAE 15<sup>th</sup> Structures, SDM Conference*, Paper No. 74-355 1974.
- [54] LEE, Y. J. and CHEN, W. H., "Study on the failure behavior of bolted connections in vessel made of GFRP laminates," *Journal of the Society of Naval Architects of Japan*, vol. 169, pp. 467–476, 1991.
- [55] LEONE, F. A. J., OZEVIN, D., MOSINYI, B., BAKUCKAS, J. G. J., AWERBUCH, J., LAU, A., and TAN, T.-M., "Detecting damage in full-scale honeycomb sandwich composite curved fuselage panels through frequency response," *Proceedings of SPIE*, vol. 6934, no. 693405, 2008.
- [56] LI, J. and O'BRIEN, T. K., "Analysis of the hygrothermal effects and parametric study of the edge crack torsion (ECT) mode III test layups," *Composite Materials: Fatigue and Fracture (6th Volume), ASTM STP 1285*, pp. 409–431, E. A. Armanios, Ed., American Society for Testing and Materials 1997.
- [57] MACKIN, T. J. and ROBERTS, M. C., "Evaluation of damage evolution in ceramic-matrix composites using thermoelastic stress analysis," *Journal of American Ceramic Society*, vol. 83, no. 2, pp. 337–343, 2000.
- [58] MACKIN, T. J. and VERNON, P. J., "Detecting sub-surface cracking in laminated membranes using infrared imaging," *Polymer Composites*, vol. 22, pp. 752–761, December 2001.
- [59] MADENCI, E., SERGEEV, B., SHIPILOV, Y., and SCOTTI, S., "Analysis of double-lap composite joints with multiple-row bolts under combined mechanical and thermal loading," *International Conference on Joining and Repair of Plastics and Composites*, pp. 55–64, The Institution of Mechanical Engineers, London, England 1999.
- [60] MADENCI, E., SHKARAYEV, S., and SERGEEV, B., "Analysis of composite laminates with multiple fasteners," tech. rep., Report to the Federal Aviation Administration, University of Arizona, Tucson, AZ, 1997.
- [61] MADENCI, E., SHKARAYEV, S., SERGEEV, B., OPLINGER, D. W., and SHYPRYKEVICH, P., "Analysis of composite laminates with multiple fasteners," *International Journal of Solids and Structures*, vol. 35, pp. 1793–1811, 1998.
- [62] MANGALGIRI, P. D. and DATTA GURU, B., "A large orthotropic plate with misfit pin under arbitrary oriented biaxial loading," *Composite Structures*, vol. 6, pp. 271–281, 1986.
- [63] MARSHALL, I. H., ARNOLD, W. S., WOOD, J., and MOUSLEY, R. F., "Observations on bolted connections in composite structures," *Composite Structures*, vol. 13, pp. 133–151, 1989.



- [64] MILLER, R. and MCLNTIRE, P., "Nondestructive testing handbook (2nd edition)," *Volume 5 Acoustic Emission Testing*, American Society for Nondestructive Testing 1987.
- [65] NAIK, R. A. and CREWS, J. H., "Stress analysis method for a clearance-fit bolt under bearing loads," *AIAA Journal*, vol. 24, pp. 1348–1353, 1986.
- [66] NAIRN, J., "Microcracking, microcrack-induced delamination, and longitudinal splitting of advanced composite structures," NASA Report 4472 1992.
- [67] NELSON, W. D., BUNIN, B. L., and HART-SMITH, L. J., "Critical joints in large composite aircraft structure," *Proceedings of 6<sup>th</sup> Conference on Fibrous Composites in Structural Design*, pp. II(1)–II(38), AMMRC MS 83-2, Army Materials and Mechanics Research Center 1983.
- [68] O'BRIEN, T. K., "Characterization of delamination onset and growth in a composite laminate," *Damage in Composite Materials, ASTM STP 775*, pp. 140–167, K. L. Reifsnider, Ed., American Society for Testing and Materials 1982.
- [69] O'BRIEN, T. K., "Analysis of local delaminations and their influence on composite laminate behavior," *Delamination and Debonding of Materials, ASTM STP 876*, pp. 282–297, W. S. Johnson, Ed., American Society for Testing and Materials, Philadelphia 1985.
- [70] O'BRIEN, T. K., RIGAMONTI, M., and ZANOTTI, C., "Tension fatigue analysis and life prediction for composite laminates," *International Journal of Fatigue*, vol. 11, no. 6, pp. 379–393, 1989.
- [71] O'BRIEN, T. K., "The effect of delamination on the tensile strength of unnotched quasi-isotropic, graphite/epoxy laminates," *Proceedings of the 1982 Joint Conference on Experimental Mechanics*, vol. 1, pp. 236–243, May 23–28, Oahu-Maui, Hawaii 1984.
- [72] OPLINGER, D. W., "On the structural behavior of mechanically fastened joints in composite structures," *Fibrous Composites in Structural Design*, pp. 575–602, Plenum Press, New York 1980.
- [73] OPLINGER, D. W., "Bolted joints in composites structures -an overview," *83<sup>rd</sup> Meeting of the AGARD SMP on Bolted/Bonded Joints in Polymeric Composites*, pp. 1(1)–1(11), Florence, Italy, 2–3 September 1996.
- [74] PARKER, R. T., "Mechanical fastener selection," *Engineered Materials Handbook - Composites*, vol. 1, pp. 706–708, ASM International 1987.
- [75] POON, C., "Literature review on the design of mechanically fastened composite joints," *AGARD Conference Proceedings No. 427*, Madrid, Spain, 27–29 April 1987.
- [76] POON, C. and XIONG, Y., "Bolted joint technology in composite structures - analytical tools development," *83<sup>rd</sup> Meeting of the AGARD SMP on Bolted/Bonded Joints in Polymeric Composites*, pp. 2(1)–2(11), Florence, Italy, 2–3 September 1996.
- [77] RAMAMURTHY, T. S., "Recent studies on the behaviour of interference fit pins in composite plates," *Composite Structures*, vol. 13, pp. 81–99, 1989.

- [78] RAMKUMAR, R. L., SAETHER, E. S., and APPA, K., "Strength analysis of laminated and metallic plates bolted together by many fasteners," tech. rep., Air Force Flight Dynamics Laboratory, Report AFWAL-TR-86-3034 1986.
- [79] REIFSNIDER, K., "Fatigue behavior of composite materials," *International Journal of Fracture*, vol. 16, pp. 563–583, 1980.
- [80] REIFSNIDER, K. L., "The mechanics of fatigue in composite laminates," *Composite Materials: Proceedings of Japan-U.S. Conference*, pp. 563–583, Ed. Kawata, K. and Akasaka, T. 1981.
- [81] REIFSNIDER, K. L., HENNEKE, E. G., and STINCHCOMB, W. W., "Delamination in quasi-isotropic graphite-epoxy laminates," *Composite Materials: Testing and Design (4<sup>th</sup> Conference)*, *ASTM STP 617*, pp. 93–105, American Society for Testing and Materials 1977.
- [82] REIFSNIDER, K. L. and STINCHCOMB, W. W., "A critical-element model of the residual strength and life of fatigue-loaded composite coupons," *Proceedings of the Symposium of Composite Materials: Fatigue and Fracture*, Dallas, TX, 24-25 October 1984.
- [83] ROWLANDS, R. E., RAHMAN, M. U., WILKINSON, T. L., and CHIANG, Y. I., "Single- and multiple-bolted joints in orthotropic materials," *Composites*, pp. 273–279, 1982.
- [84] RYBICKI, E. F., SCHMUESER, D. W., and FOX, J., "An energy release rate approach for stable crack growth in the free-edge delamination problem," *Journal of Composite Materials*, vol. 11, pp. 470–487, October 1977.
- [85] SALPEKAR, S. A. and K., O. T., "Analysis of matrix cracking and local delamination in  $(0/\theta/-\theta)_s$  graphite epoxy laminates under tensile load," *Journal of Composites Technology & Research*, vol. 15, pp. 95–100, Summer 1993.
- [86] SALPEKAR, S. A. and O'BRIEN, T. K., "Combined effect of matrix cracking and free edge on delamination," *Composite Materials: Fatigue and Fracture (3rd Volume)*, *ASTM STP 1110*, pp. 287–311, T. K. O'Brien, Ed., American Society for Testing and Materials, Philadelphia 1991.
- [87] SHOKRIEH, M. M., "Failure of laminated composite pinned connections," *Master Engineering Thesis*, McGill University, Montreal, Canada 1991.
- [88] TALREJA, R., "Fatigue of composite materials: Damage mechanisms and fatigue life diagrams," *Proceedings of Royal Society of London*, vol. A378, pp. 461–475, 1981.
- [89] TALREJA, R., "Transverse cracking and stiffness reduction in composite laminates," *Journal of Composite Materials*, vol. 19, pp. 355–375, 1985.
- [90] TALREJA, R., "Continuum modeling of the development of intralaminar cracking in composite laminates," *Proceedings of the 7<sup>th</sup> International Conference on Fracture (ICF7)*, Houston, TX, 20-24 March 1989.

- [91] TALREJA, R., "Modeling of damage development in composites using internal variables concepts," *Proceedings of the Winter Annual Meeting*, Boston, MA, 13-18 December 1989.
- [92] TALREJA, R., "Fatigue of fiber composites," *Materials Science and Technology*, vol. Chapter 13, pp. 584–607, Weinheim 1993.
- [93] TALREJA, R., "A synergistic damage mechanics approach to durability of composite material systems," *Progress in Durability Analysis of Composite Systems*, pp. 117–129, Edited by A. Cardon, H. Fukuda, K. L. Reifsnider, A. A. Baikema 1996.
- [94] TALREJA, R., "Fatigue of polymer matrix composites," *Comprehensive Composite Materials*, vol. 2, pp. 529–552, Oxford: Elsevier 2000.
- [95] TAN, X. and ARMANIOS, E., "Comparison of co-cured composite joint strength under fatigue loading," *Proceedings of 21<sup>st</sup> Annual Technical Conference of the American Society for Composites*, Dearborn, MI, September 17-20 2006.
- [96] TAN, X. and ARMANIOS, E., "Damage assessment of co-cured composite joint strength under quasi-static and fatigue loading," *48<sup>th</sup> AIAA/ASME/ASCE/AHS/ASC Structures, Structural Dynamics, and Materials Conference*, Honolulu, Hawaii, April 23-26 2007.
- [97] TAN, X. and ARMANIOS, E., "Damage initiation and propagation of co-cured composite joint under fatigue loading," *AHS 63<sup>rd</sup> Annual Forum and Technology Display*, Virginia Beach, VA, May 1-3 2007.
- [98] TAN, X. and ARMANIOS, E., "Strength of quasi-isotropic co-cured composite joints under quasi-static and fatigue loading," *Journal of ASTM International*, 2007.
- [99] TSAI, C. L., DANIEL, I. M., and LEE, J.-W., "Progressive matrix cracking of crossply composite laminates under biaxial loading," *Proceedings of the Symposium, ASME Winter Annual Meeting*, vol. 34, pp. 9–18, Dallas, TX, 25-30 November 1990.
- [100] TSAI, P. and CHEN, W. H., "Finite element analysis of elastodynamic sliding contact problems with friction," *Composite Structures*, vol. 22, pp. 925–938, 1986.
- [101] VOLKERSEN, O., "Die nietkraftverteilung in zugbeanspruchten nietverbindungen mit konstanten laschenquerschnitten," in *Luftfahrtforschung* [27], pp. 4–47. Volume 3: Polymer Matrix Composites Materials Usage, Design and Analysis.
- [102] WASZCZAK, J. P. and CRUSE, T. A., "Failure mode and strength predictions of anisotropic bolt bearing specimens," *Journal of Composite Materials*, vol. 5, pp. 421–425, 1971.
- [103] WHITNEY, J. M. and NUISMER, R. J., "Stress fracture criteria for laminated composites containing stress concentrations," *Journal of Composite Materials*, vol. 8, pp. 253–263, 1974.
- [104] WILKINSON, T. L., ROWLANDS, R. E., and COOK, R. D., "An incremental finite-element determination of stresses around loaded holes in wood plates," *Composite Structures*, vol. 14, pp. 123–128, 1981.

- [105] WILLIAMS, J. and SCARDINO, W., "Adhesives selection," *Engineered Materials Handbook -Composites*, vol. 1, pp. 479–495, ASM International 1987.
- [106] WISNOM, M. R., KHAN, B., and HALLETT, S. R., "Size effects in unnotched tensile strength of unidirectional and quasi-isotropic carbon/epoxy composites," *Composite Structures*, vol. 84, pp. 21–28, 2008.
- [107] WONG, C. M. and MATTHEWS, F. L., "A finite element analysis of single and two-hole bolted joints in fibre reinforced plastic," *Journal of Composite Materials*, vol. 15, pp. 481–491, 1981.
- [108] XIONG, Y. and POON, C., "A design model for composite joints with multiple fasteners," tech. rep., Aeronautical Note IAR-AN-80, National Research Council, Canada, NRC no. 3216 1994.
- [109] YOGESWAREN, E. K. and REDDY, J. N., "A study of contact stresses in pin-loaded orthotropic plates," *Computing Structure*, vol. 30, pp. 1067–1077, 1988.
- [110] ZENG, Q. and SUN, C. T., "A new bonded composite wavy lap joint," *Proceedings of the 41<sup>st</sup> AIAA/ASME/ASCE/AHS/ASC SDM Conference*, April 2-6 2000.
- [111] ZENG, Q. and SUN, C. T., "Fatigue performance of a bonded wavy composite lap joint," *Proceedings of the 42<sup>nd</sup> AIAA/ASME/ASCE/AHS/ASC SDM Conference*, vol. Seattle, Washington, April 16-19 2001.
- [112] ZENG, Q. and SUN, C. T., "Novel design of a bonded lap joint," *Journal of AIAA*, vol. 39, pp. 1991–1996, 2001.
- [113] ZENG, Q. and SUN, C. T., "Fatigue performance of a bonded wavy composite lap joint," *Fatigue & Fracture Engineering Material Structures*, vol. 27, pp. 413–422, 2004.